https://theses.gla.ac.uk/

Theses Digitisation:

https://www.gla.ac.uk/myglasgow/research/enlighten/theses/digitisation/

This is a digitised version of the original print thesis.

Copyright and moral rights for this work are retained by the author

A copy can be downloaded for personal non-commercial research or study, without prior permission or charge

This work cannot be reproduced or quoted extensively from without first obtaining permission in writing from the author

The content must not be changed in any way or sold commercially in any format or medium without the formal permission of the author

When referring to this work, full bibliographic details including the author, title, awarding institution and date of the thesis must be given

Enlighten: Theses
https://theses.gla.ac.uk/
research-enlighten@glasgow.ac.uk

The Application of Resonance Ionisation Spectroscopy to III-V Semiconductor Surface and Depth Analysis.

Christopher John McLean

Department of Electronics and Electrical Engineering

University of Glasgow

Presented as a thesis for the degree of Doctor of Philosophy
in the University of Glasgow

© C J McLean 1990

ProQuest Number: 11007596

All rights reserved

INFORMATION TO ALL USERS
The quality of this reproduction is dependent upon the quality of the copy submitted.

In the unlikely event that the author did not send a complete manuscript
and there are missing pages, these will be noted. Also, if material had to be removed,
a note will indicate the deletion.

ProQuest 11007596

Published by ProQuest LLC (2018). Copyright of the Dissertation is held by the Author.

All rights reserved.
This work is protected against unauthorized copying under Title 17, United States Code
Microform Edition © ProQuest LLC.

ProQuest LLC.
789 East Eisenhower Parkway
P.O. Box 1346
Ann Arbor, MI 48106 – 1346

To

Mum and Dad

Acknowledgements.

I would like to thank the following people for their contributions and assistance during the period of the project and the production of this work:-

Dr. K. W. D. Ledingham, Laser Ionisation Studies group leader, for a continuous supply of advice, and confidence in my abilities,

Dr. J. H. Marsh and the Department of Electronics and Electrical Engineering for their initial interest and confidence in the project,

Dr. R. Jennings, Dr. R. P. Singhal, and Dr. D. T. Stewart for advice and helpful discussion on all aspects associated with the project,

my fellow reasearch colleagues Dr. A. Marshall, Dr M. Towrie Mr. I. Borthwick and Mr. A. P. Land for helpful discussions and suggestions, Mr. P. T. McCombes for computer associated aspects of the project and Mr. A. Clarke and Dr. Wang Li for their assistance with experimental work,

Mr. R. G. Maxwell and Mr. T. McCanny for technical support and advice,

Mr. R. Pallester for assistance with electronics,

Mr. T. Neil and the staff of the mechanical workshop (Department of Physics and Astronomy) for manufacture of instrument parts,

the SERC for financial support during the course of my study,

and finally, my family for the support and encouragement they have provided throughout.

Publications.

McLean C.J., Marsh J.H., Cahill J.W., Drysdale S.L.T., Jennings R., McCombes P.T., Land A.P., Ledingham K.W.D., Singhal R.P., Smyth M.H.C., Stewart D.T., Towrie M.,"Application of Resonant Ionisation Mass Spectrometry to Depth Profiling in III-V Semiconductor Devices", *Proceedings RIS 88*, p193, IOP publishing, 1988

McLean C.J., Marsh J.H., Land A.P., Clark A., Jennings R., Ledingham K.W.D., McCombes P.T., Marshall A., Singhal R.P., Towrie M.,"Resonant Laser Ablation", *Int. J. Mass Spectrom. Ion Proc.*, 96, 1990

Towrie M., Drysdale S.L.T., Houston C.M., Jennings R., Land A.P., Ledingham K.W.D., McCombes P.T., McLean C.J., Singhal R.P., Smyth M.H.C., Stewart D.T.,"The Glasgow Resonant Ionisation Mass Spectrometer", *Proceedings RIS 88*, p267 IOP publishing, 1988

McCombes P.T., Borthwick I. S., Drysdale S.L.T., Jennings R., Land A.P., Ledingham K.W.D., McLean C.J., Singhal R.P., Smyth M.H.C., Stewart D.T., Towrie M., "Preliminary Results from the Glasgow Resonant Ionisation Mass Spectrometer", presented as a poster at 'The Application of Lasers in Surface Science', Trieste, Italy 1988

Wang L., McLean C.J., Jennings R., Ledingham K.W.D., Singhal R.P.,"The Characteristics of Resonant Laser Ablation", to be published, proceedings RIS 90

McLean C.J., McCombes P.T., Jennings R., Ledingham K.W.D., Singhal R.P.,"Novel Ion Optics for Secondary Ion Suppression in Sputter Initiated Resonant Ionisation", to be published, Nuclear Instruments and Methods for Research.

McCombes P.T., Drysdale S.L.T., Jennings R., Land A.P., Ledingham K.W.D., McLean C.J., Singhal R.P., Smyth M.H.C., Stewart D.T., Towrie M., "The Glasgow Resonant Ionisation Mass Spectrometer", *proceedings IMSC XII*, 1988

Marshall A., Clark A., Jennings R., Ledingham K.W.D., McLean C.J., Singhal R.P.,"Resonant Two-Photon Ionisation of Aromatic Molecules: Wavelength Dependence and Fragmentation Patterns", to be published, Proceedings RIS 90

Towrie M., Drysdale S.L.T., Jennings R., Land A.P., Ledingham K.W.D., McCombes P.T., McLean C.J., Singhal R.P., Smyth M.H.C.,"Trace Analysis using a Commercial Resonant Ionisation Mass Spectrometer", *Int. J. Mass Spectrom. Ion Proc.*, 96, 1990

Summary

Resonance Ionisation Spectroscopy (RIS) is a relatively new analytical technique which is gaining increasing significance in the field of quantitative trace analysis. This work is principally concerned with the particular application of Resonance Ionisation Spectroscopy to surface and depth analysis of semiconductor material.

For any new technique to succeed amidst a plethora of competing, proven technologies, it must offer some added advantage. The introductory chapter assesses some of the common electron, ion and laser based techniques already in existence, with which RIS is in direct competition, stressing fundamental problems in use which limit their degree of success. As a preamble to Chapter 2, the process of Resonance Ionisation Spectroscopy is also introduced at this stage.

Chapter 2 deals with the physical principles behind RIS and its mass analysis derivative, RIMS, introducing the concept of atomically selective ionisation schemes used to discriminate between elements. A rate equation model, restricted to a three level system, allows determination of the necessary experimental conditions for efficient implementation of the process.

In its most common form, with regards to its application to solid sample analysis, RIS is applied in a post-ionisation mode, in which case ion sputtering or laser ablation are employed in the sample vaporisation process. Of the two methods, ion sputtering is by far the more versatile and better understood. Chapter 3 introduces the physical concepts of ion sputtering and erosion and includes the necessary theory for modelling of the experimental conditions. With regard to depth profiling in particular, the factors contributing to the broadening of known concentration profiles are described in detail.

A prerequisite for such analysis, is the ability to detect and recognise the species being analysed. To this end, a major portion of the project was devoted to the design and construction of a time-of-flight mass spectrometer, responsibility for which was placed solely upon the author. Chapter 4 deals specifically with the instrumentation aspect of the project, detailing the operational principles of a time-of-flight mass spectrometer, the various components of the analysis system constructed, the vacuum and laser systems, the ion optical assembly and the sputter ion gun to name but a few.

Chapter 5 is the first relating to actual experiments, and provides the basis for an estimate of the operational usefulness of the instrument. Both pulsed secondary ion (SIMS) and resonant ion (RIMS) analyses were carried out on Aluminium and Gallium by the author. The wavelength spectra allow an investigation of the effects of experimental parameters on the resonant process. Chapter 6 describes attempts at depth profiling of aluminium concentration through multilayered structures of GaAs and AlGaAs.

During the design stage, familiarity with the problems associated with the secondary ion background prevalent in these experiments, led the author to devise a novel approach to experimental procedure and ion optical design. Chapter 7 discusses the solution in detail, and produces experimental data and computer simulation as confirmation of the usefulness of the method.

Recent investigations by the author have led to the development of what has been termed Resonant Laser Ablation (RLA). Chapter 8 introduces this new concept which is derived from the combined mechanisms of laser ablation and resonant ionisation to offer enhancements in sensitivity and selectivity. The technique has generated a great deal of interest due to the possibilities it offers in the field of surface analysis. Experiments, carried out initially by the author and at a later stage in collaboration with Dr. Wang Li of the Department of Physics and Astronomy, on semiconductor and metal samples indicate that RLA may prove to be an interesting alternative technique to existing forms of laser spectrometry. Consequently RLA has become a subject for further investigations within the group.

Finally, Chapter 9 discusses briefly the project as a whole and describes some interesting future developments which should enhance the position of RIS/RIMS in the fields of spectrometry and surface analysis.

Contents

Page

Chapter 1. Introduction

Methods for Surface Analysis 1

Chapter 2. Resonance Ionisation Spectroscopy

Introduction 10
Physical Basis 11
RIMS 13
Rate Equations 13

Chapter 3. The Theory of Ion Sputtering and its Application to Depth Profiling

Introduction 18
Sputtering 19
Nature of Sputtered Particles 22
Incidence Angle Dependence 23
Energy Distribution of Sputtered particles 24
Angular Distribution of Sputtered Particles 24
Erosion Rate 24
Factors Affecting Depth Profiling 26
Depth Resolution 26
Recoil Mixing 27
Surface Roughness 28
Dynamic Range 30
Crater-Edge Effects 30
Redeposition 31
Residual Gas 31
Time of Flight Operation 32
Comparison of Performance in Depth Analysis 34

Chapter 4. Instrumentation

Introduction 36
Mass Spectrometer 36
Vacuum System 39
Ion Optics 41
Sample Vaporisation 43
Glasgow RIMS Instrument 45
Data Acquisition 46
System Triggering 47
Laser System 47
Excimer Laser 48
Dye Laser 48
Frequency Doubling 49
Laser Power Measurement 49
Optical Attenuator 50

Chapter 5. Resonant Ionisation of Gallium and Aluminium in a TOF Mass Spectrometer

Introduction 51
Experimental Arrangement 51
Results and Discussion 52
Gallium SIMS 52
Gallium RIMS 55
Aluminium SIMS 57
Aluminium RIMS 58

Chapter 6. Application of RIMS to Depth Profiling in III-V Semiconductors

Introduction 65
Experimental Arrangement 65
Results and Discussion 67
Conclusion 71

Chapter 7 **Secondary Ion (SIMS) Suppression During Resonant Ion Detection**

Introduction 73

Physical Basis 73

Implementation 74

Chapter 8. **Resonant Laser Ablation (RLA)**

Introduction 76

Laser Ablation 78

Experimental Arrangement 80

Results and Discussion 80

Effect of Angle of Incidence on RLA 82

Laser Power Density Effects in RLA 84

Conclusion 90

Chapter 9. **General Discussion and Future Developments** 93

Appendix A. **Spectrometer Resolution** 98

Appendix B. **Frequency Doubling** 101

Appendix C. **Transition Broadening Mechanisms**

Doppler Broadening 104

Collisional Broadening 106

Saturation (power) Broadening 106

References. 113

Chapter 1

Introduction

In recent years, many advances have been made in the technologies involved in crystal growth, in particular those techniques used in the manufacture of ultra-thin layered structures for use in new generations of optoelectronic devices. Typically these devices are constructed with extremely thin multiple layers which exhibit particular physical properties. They also demand a high degree of surface uniformity and low impurity levels.

The Quantum Well (QW) Heterostructure is an example of such devices being of particular use in the design of semiconductor lasers and waveguides constructed from III-V semiconductor materials [18][39][103]. Its principle of operation relies on what is termed the Quantum Size Effect (**QSE**), which requires that the depth dimension of the layers be comparable with, and typically much smaller than, the de Broglie wavelength for an electron (~500 Å).

The process of Molecular Beam Epitaxy (**MBE**) has come to the fore in the manufacture of these Quantum Well devices. MBE utilises beams of thermal atoms incident on a substrate to effect crystal growth. The atom fluxes can be varied independently, resulting in structures possessing abrupt concentration steps or precisely engineered concentration gradients either of the bulk materials or of dopants. Substrate rotation and temperature control results in surface coverage uniformity. Impurity concentrations are dependent on the purity of the atomic beams and on the quality of the vacuum during growth.

The operational characteristics of these devices are determined by the small dimension and quality of the structures. Improved performance therefore demands greater accuracy and smaller tolerances in the manufacturing process. On such a small scale it becomes difficult to monitor accurately the growth, and therefore analysis must be carried out on the final product to ensure the desired standards are attained.

The determination of an elemental concentration as a function of depth is commonly referred to as Depth Profiling. This is a feature of surface or thin-film analysis, where the exposed surface is analysed layer by layer after a process of erosion. The method of analysis itself introduces a smearing out effect on an abrupt concentration transition. The figure of merit attributed to a particular analytical process is known as its depth resolution, and is defined as the depth across which the measured concentration drops from 84% to 16% of its maximum value at an abrupt junction [35]. As the available resolution improves, the measured profile will resemble more accurately the true profile. For structural analysis of typical QW heterostructures, the depth resolution must be tens to hundreds of angstroms.

In order that the measured concentration at any exposed layer is representative of the true concentration at that depth, the information depth of the surface analysis technique must be confined to the surface layers alone. Information depth is defined as the depth which contributes ($1-e^{-1}$) or 63% of the signal and is equivalent to the mean free path of the information particle in the sample medium [118].

Methods for Surface Analysis.

Since there are many surface analysis techniques currently employed in depth profiling, it would seem reasonable at this stage to describe several of the most successful.

Firstly, there are the **electron spectrometries**, of which the most important are Auger Electron Spectroscopy (**AES**) and X-ray Photo-electron Spectroscopy (**XPS**) [118][9].

In AES (Figure 1.1), electron bombardment (typically 0.5 - 10 keV) of an atom causes the ejection of an inner electron. An outer electron then de-excites to the vacancy causing a second high lying electron to be ejected. This ejected "Auger" electron is characteristic of the emitting atom as the transferred energy E_e corresponds to a discrete transition within the atom, and is given by the expression:

$$E_e = E_p(Z) - \big(E_q(Z) + E_r(Z + \Delta)\big) - \phi_s \qquad (1.1)$$

where E_p, E_q, and E_r are the electronic energy levels of the atom, ϕ_s is the work

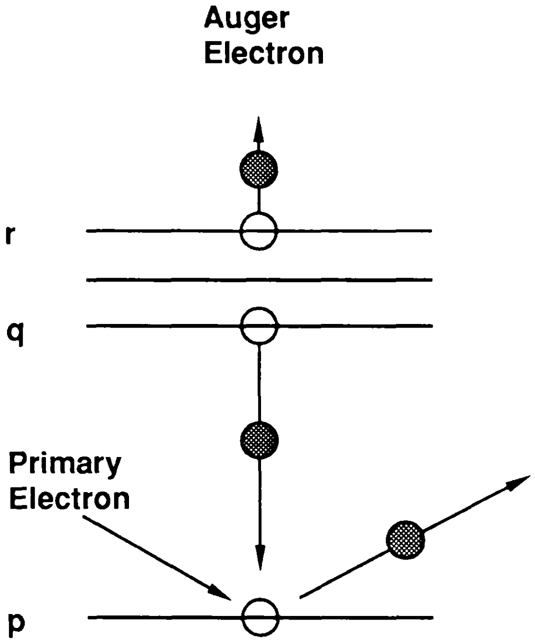
Auger
Electron
r
q
Primary
Electron
p

Figure 1.1 Schematic of AES process

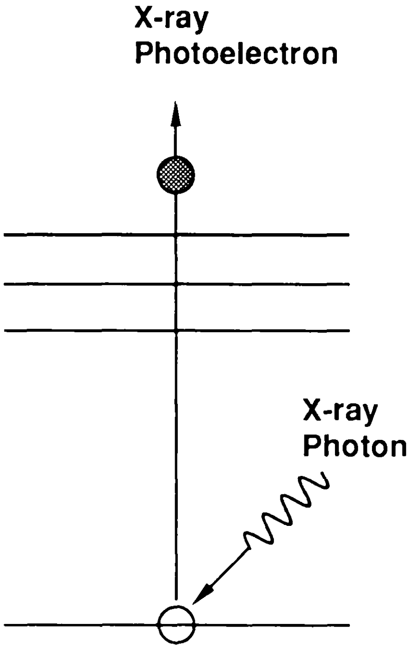
X-ray
Photoelectron
X-ray
Photon

Figure 1.2 Schematic of XPS process

function of the sample surface and Δ is the de-screening correction (i.e. the change in the effective charge of the nucleus due to the doubly-ionised state of the atom). The energies are measured with respect to the Fermi energy of the solid. All elements above He in the periodic table produce Auger electrons in the range 0 - 2 keV.

XPS (Figure 1.2) relies on X-ray induced ejection of a core electron from the atom, again at a discrete energy given by:

$$E_e = h\nu - E_p - \phi_s \qquad (1.2)$$

where E_p is the binding energy of the electron and ν the frequency of the X-rays.

In both processes, the intensity of the electron signal is proportional to the atomic concentration and hence they are both quantitative.

The information depth for AES and XPS is determined by the mean free path of the electrons escaping the surface, and is typically in the nanometre range or less.

The major advantage of electron spectrometries is that the analysis does not contribute to contamination of the ultra-high-vacuum (**UHV**) system, as is the case with the more destructive ion spectrometries which rely on the liberation of sample material through ion-solid interactions. Manipulation of the primary and secondary electrons is easily accomplished by electrostatic and magnetic lenses and deflectors. Detection can also be highly efficient.

For depth profiling by, for example, AES, the sample is continuously eroded by a low energy, unfocused ion beam while the electron beam impinges on the centre of the ion spot [66][68].

Another electron technique, different in principle, is the Scanning Transmission Electron Microscope (**STEM**) [73]. As its name suggests, information concerning the sample composition is gathered on the opposite face of the sample to the primary beam (Figure 1.3). Transmission intensity is limited by the mean free path of the electrons, restricting the use of the process to extremely thin samples which require careful preparation. Depth analysis must be carried out edge-on to the sample in imaging mode with resolution very much dependent on the spatial extent of the primary electron beam (~1nm).

As well as these electron spectrometries, there are numerous **ion spectrometries**. Of these, possibly the most surface selective of all analytical

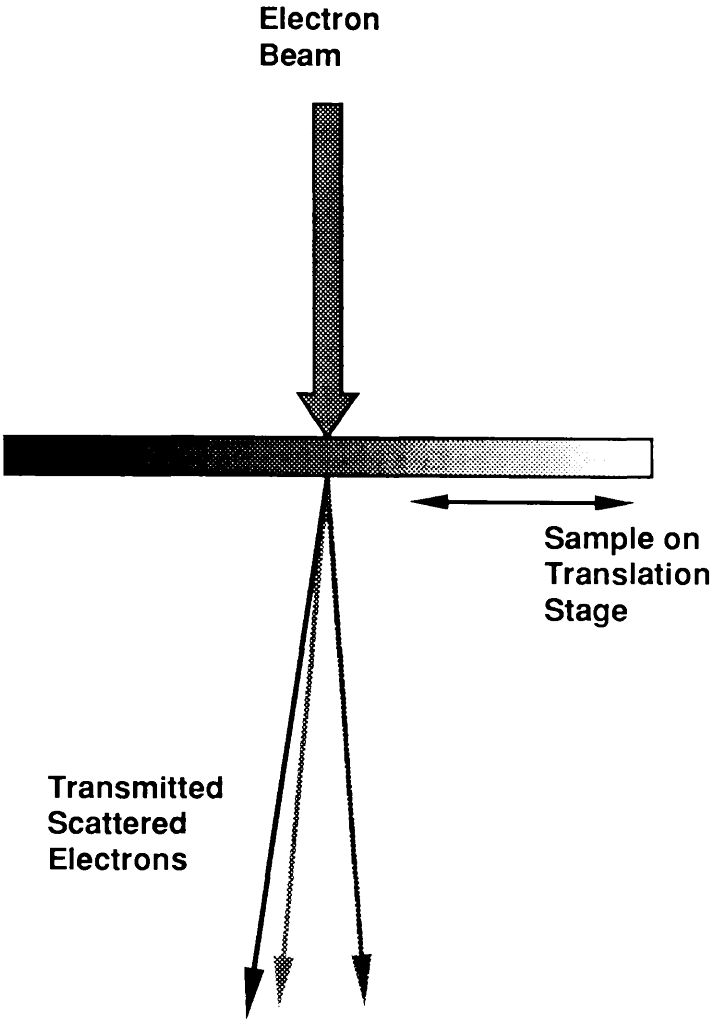
Electron Beam
Sample on Translation Stage
Transmitted Scattered Electrons

Figure 1.3 STEM experimental geometry

techniques is Low Energy Ion Scattering spectrometry (**LEIS**), also known as Ion Scattering Spectroscopy (**ISS**) [118][9][117][25].

The principle of LEIS involves a beam of low energy ions (0.2 - 3 keV), usually of an inert gas variety, incident on a solid surface at shallow incidence (Figure 1.4). A fraction of these ions are then scattered elastically in collisions with atoms on the surface. The identity of the scattering atoms is then revealed in the energy spectrum of the scattered ions [118][9][117].The energy E_{11} of these scattered ions can be given by the expression:

$$E_{11} = \frac{E_{10}}{(M_1 + M_2)^2} \cdot \left[M_1 \cos\Phi + \left(M_2^2 - M_1^2 \sin^2\Phi\right)^{1/2}\right]^2 \qquad (1.3)$$

where E_{10} is the initial energy of the projectile, and M_1 and M_2 the masses of the projectile and target atoms respectively. Φ is the scattering angle given by:

$$\Phi = \pi - (\Psi_i + \Psi_o) \qquad (1.4)$$

where Ψ_i andΨ_0 are the incident beam angle and the emission angle with respect to the surface normal. For a scattering angle of 90^0, as is frequently used, Equation (1.3) reduces to:

$$E_{11} = E_{10}(M_2 - M_1)(M_2 + M_1)^{-1} \qquad (1.5)$$

The extreme surface selectivity arises from the short mean free path of the ions in the sample ($\sim 10^{-4}$ nm). However, the overall sensitivity is limited by the high probability of the primaries being neutralised in inelastic collisions with surface atoms.

Another much used ion technique is High Energy Ion Scattering (**HEIS**) more commonly known as Rutherford Back Scattering (**RBS**) [118][9][25].

High energy, low Z primary ions in the range 1 to 5 MeV are used to obtain RBS spectra. The projectile ions back scattered in binary collisions with target atoms contain information on the mass and position of the target atom in their final energy and angle of ejection (Figure 1.5).

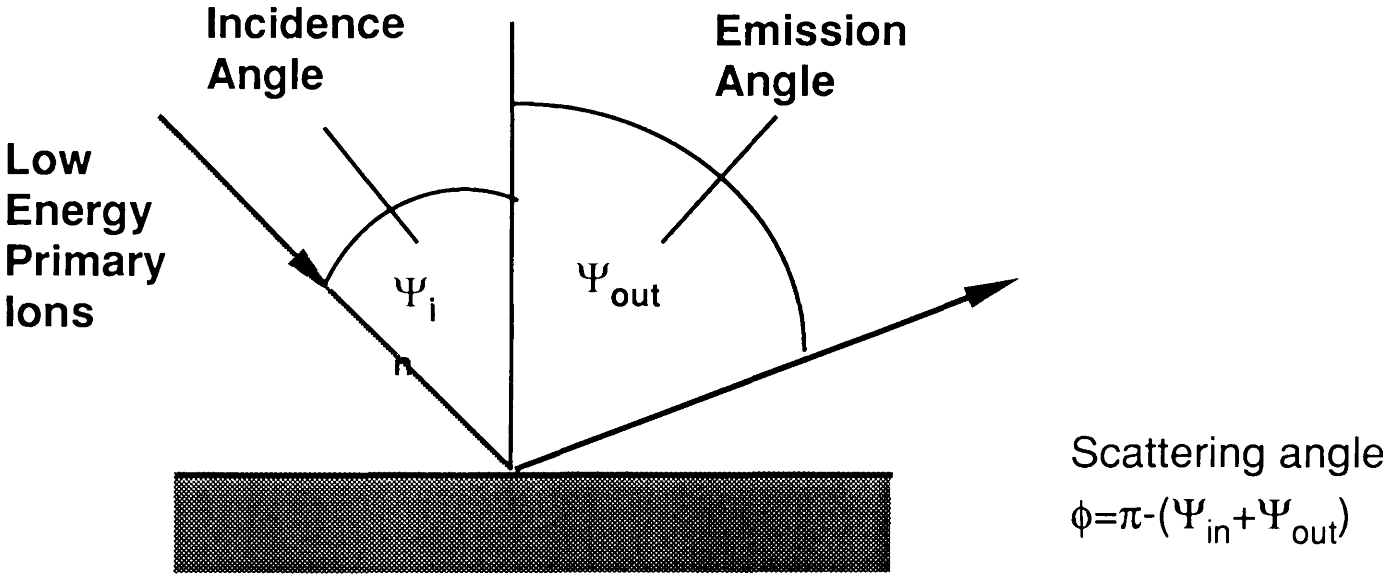
Incidence Angle
Emission Angle
Low Energy Primary Ions
Ψ_i
Ψ_{out}
n
Scattering angle
$\phi=\pi-(\Psi_{in}+\Psi_{out})$

Figure 1.4 LEIS experimental geometry

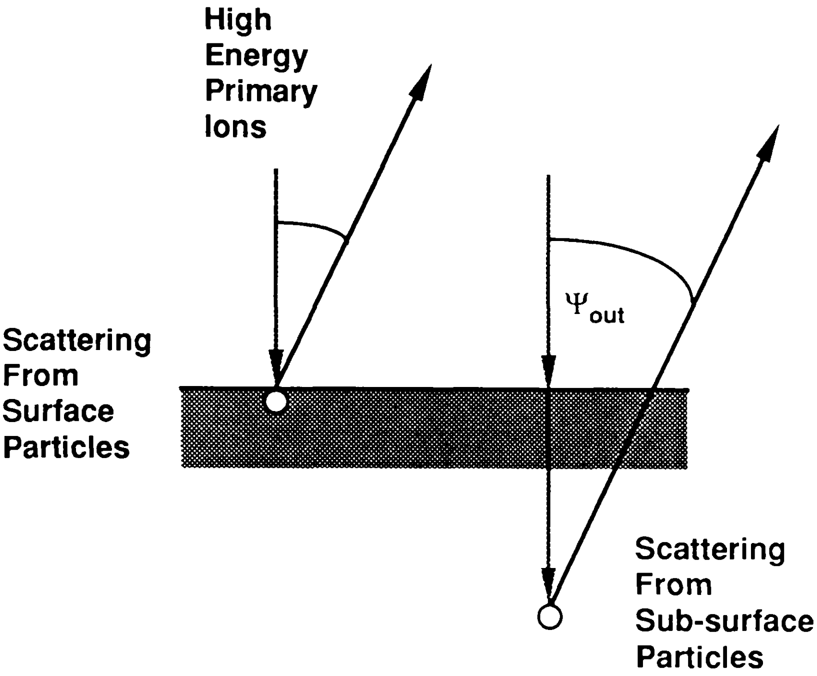
High Energy Primary Ions
Ψ_{out}
Scattering From Surface Particles
Scattering From Sub-surface Particles

Figure 1.5 HEIS/RBS experimental geometry

For primary ions incident normally, the energy of the backscattered particles can be derived from Equation (1.3) as:

$$E_{11} = \frac{E_{10}}{(M_1 + M_2)^2} \cdot \left\{ \left(M_2^2 - M_1^2 \sin^2 \Psi_o \right)^{1/2} - M_1 \cos \Psi_o \right\}^2 \qquad (1.6)$$

and hence the mass of the target can be calculated, with surface atoms heavier than the matrix giving higher scattering energies.

The backscattered ion loses energy in traversing to and from the target atom, and hence the energy spectrum also yields information on the depth, below the surface, of the scattering centre.

As depth and mass information appear simultaneously in the energy spectrum, this creates problems in the characterisation of samples of complex composition due to overlapping spectra. Therefore, RBS is only effectively applied to samples containing few elements.

HEIS is also often successfully applied to channelling studies. The channelling of projectile particles between the planes of atoms yields details of the crystalline quality or degree of amorphisation of the sample, and also allows an accurate determination of the locations of impurity atoms in the lattice.

Possibly the most important of the ion spectrometries is Secondary Ion Mass Spectrometry (**SIMS**), which has only really come into prominence in the last few decades but has rapidly established itself as an invaluable technique for ultra-trace, surface and depth analysis [118][25][23][116][117][7][8].

The action of a beam of ions of typically a few keV incident on a surface causes the ejection of secondary particles, either atomic or molecular in origin, a fraction of which are in a charged state. The analysis of these charged particles is the basis of SIMS (Figure 1.6).

The technique has achieved high sensitivities, better than parts per million (**PPM**), and can be made extremely surface selective by a wise choice of primary ion beam parameters. However, a major disadvantage is its susceptibility to matrix effects, i.e. the variation in the ion yield as a function of the sample composition, which reduces its effectiveness in quantitative analysis of samples of varying structural composition. Also, irrespective of the matrix, the ion fraction is never

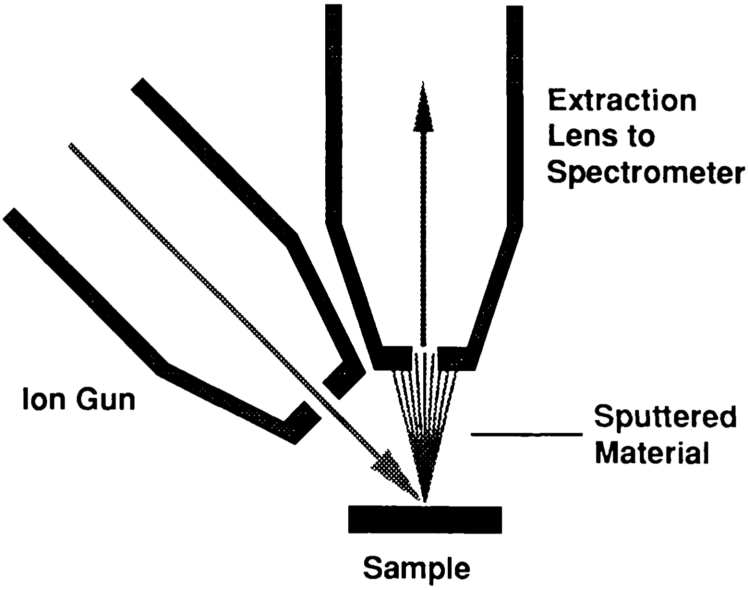
Extraction
Lens to
Spectrometer
Ion Gun
Sputtered
Material
Sample

Figure 1.6 SIMS experimental geometry

greater than about 10%. This is by far an upper limit with typical values several orders of magnitude less and is a strongly varying function of the experimental parameters, namely primary beam energy, primary ion type, and sample constituents.

A variation on SIMS, namely Secondary Neutral Mass Spectrometry (SNMS), involves analysis of the secondary neutral particles, which are, as mentioned, much more numerous [118][117][25]. A method of post-ionisation must therefore be employed to make effective use of the available material. This is usually accomplished by electron impact or laser interaction (Figure 1.7). Alternatively the sputtering process can be carried out in an rf generated plasma, post-ionisation again being by electron impact within the plasma [48]. Detection efficiency is not necessarily improved due to low ionisation efficiency, at most 1% [51], or reduced spectrometer acceptance for neutral particles, however matrix effects are significantly reduced. Quantitative SNMS analysis has also been shown to be less prone to effects caused by surface and residual gas contamination than is SIMS [107].

A further variation on the SIMS theme utilises a neutral primary beam (Fast Atom Bombardment **FAB**) and is often referred to as FAB-SIMS [118]. This allows for the use of higher extraction potentials thereby improving detection efficiency and mass resolution. Charging effects in insulating and semi-insulating samples which are compensated for in SIMS by the use of an auxiliary electron beam incident on the sample during analysis [122][88], are less of a problem [76].

Fundamental to SIMS analysis is the choice of primary ion. To avoid chemical reaction of the sample with primary implants, rare-gas ions are generally used. For improved sensitivity, electro-negative oxygen ions are employed as they enhance the positive ion yield [14] or alternatively, oxygen may be flowed across the sample surface during analysis to the same effect [16]. Similarly for the production of negative ions, Caesium primaries are often used [62]. In depth analysis, the determining factor in choosing a particular ion, for optimum depth resolution, may be its relative mass with respect to that of the target. In surface imaging mode, where a small spot size is required for high spatial resolution, space charge effects within the primary beam must also be considered.

In trace analysis the main limitations to detection sensitivity arise due to mass interference from isotopes of different elements, clusters, hydrocarbons, oxides etc., which may exist as surface contaminants, as residual gas molecules, or alternatively may result from the interaction of the elements in the sample with the primary ion

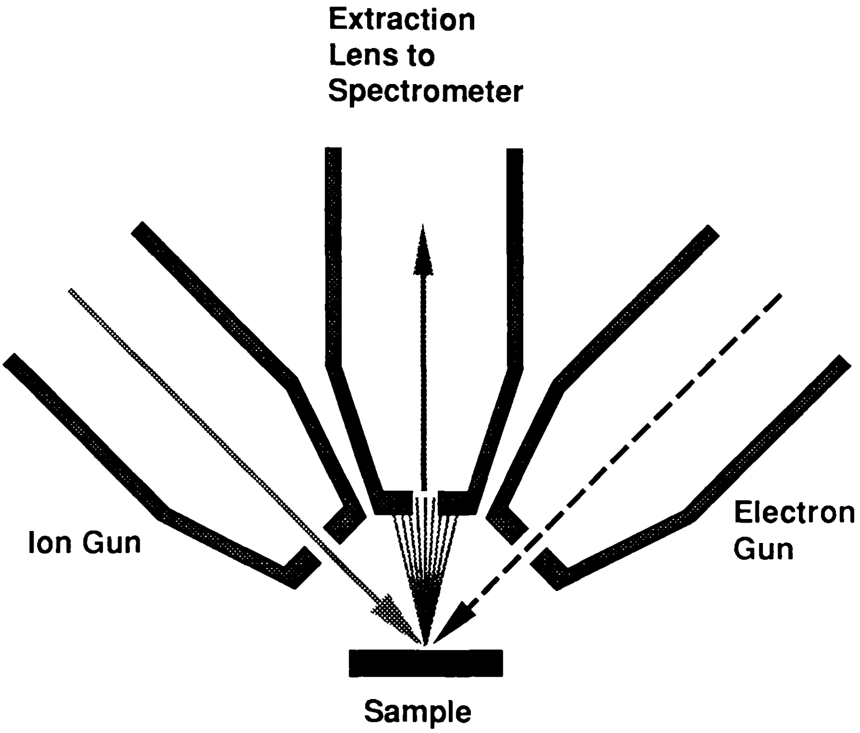
Extraction
Lens to
Spectrometer
Ion Gun
Electron
Gun
Sample

Figure 1.7 Electron gun SNMS experimental geometry

beam. Such interference effects can be resolved by the use of more costly high mass resolution spectrometers.

More recently, alternative analytical techniques, relying on the use of high power lasers in the ablation/desorption and/or post-ionisation processes have been successfully added to the long list of currently available and widely used techniques.

Laser Micro-Probe (**LMP**,"LIMA") analysis [118][55][56][25][10] utilises a tightly focused laser to vaporise and ionise solid samples, yielding material suitable for examination by accepted spectrometric means. Such devices generally operate in either a transmission mode (Figure 1.8(a)), in the case of very thin samples or coated sample grids, where the ablating laser perforates the sample, or in a surface reflection mode for thicker samples (Figure 1.8(b)). The latter geometry is particularly suited to surface imaging where the laser can be focused down to a spot ~ μm in diameter. The secondary ions are analysed using a time of flight mass analyser.

A further use of lasers is in the post-ionisation of ablated neutral material. Such material may be the result of ion sputtering (SNMS)(Figure 1.9), or the action of a primary ablating laser, and is of much use in the reduction of the matrix effects normally associated with ablation mechanisms.

Laser post-ionisation involves the absorption by an atom or molecule of multiple photons (Multi-Photon Ionisation (**MPI**)(Figure 1.10))[4][25][65][64], to excite and eventually ionise the particle. This generally requires a high photon flux to improve the ionisation efficiency.

One major advantage of using a laser as the probe-beam in preference to an ion beam, is that the laser does not interact with the electric fields normally present in the sample region, and consequently, much higher extraction potentials may be used which contribute to the overall transmission efficiency and mass resolution of the system. Furthermore lasers are not space charge limited and therefore the focus quality of the beam is diffraction limited and is not affected by the laser intensity.

Problems arise in the non-uniformity of the laser evaporation, presenting limitations in depth analysis.

The analysis of the ablated ions under laser microprobe assay is also prone to matrix effects in the ablation mechanism as are ion beams, and the variance of the ionisation potentials of the elements.

Detection sensitivity is also affected by mass interference of similar origin to

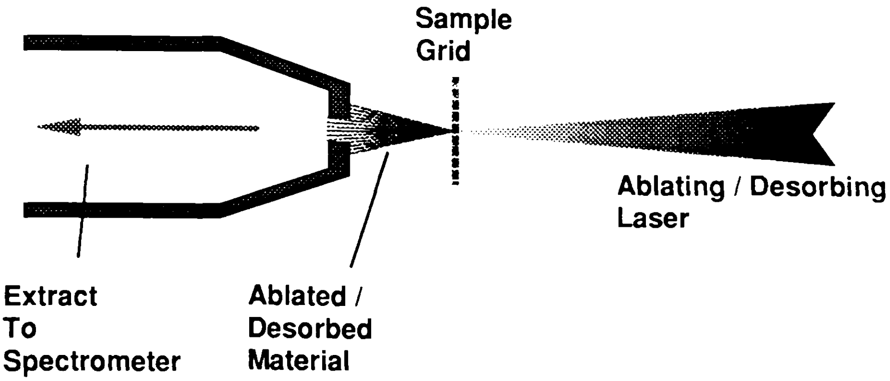
Sample
Grid
Ablating / Desorbing
Laser
Extract
To
Spectrometer
Ablated /
Desorbed
Material

Figure 1.8 (a) Transmission LMP experimental geometry

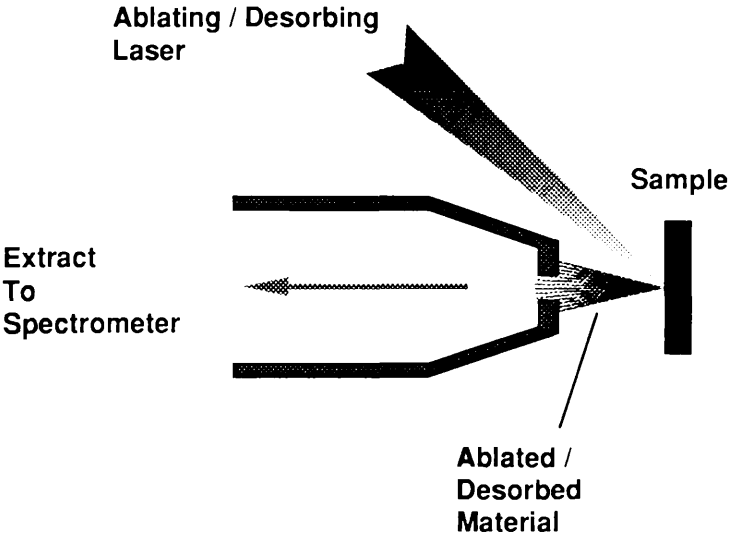
Ablating / Desorbing
Laser
Sample
Extract
To
Spectrometer
Ablated /
Desorbed
Material

Figure 1.8 (b) Reflection LMP experimental geometry

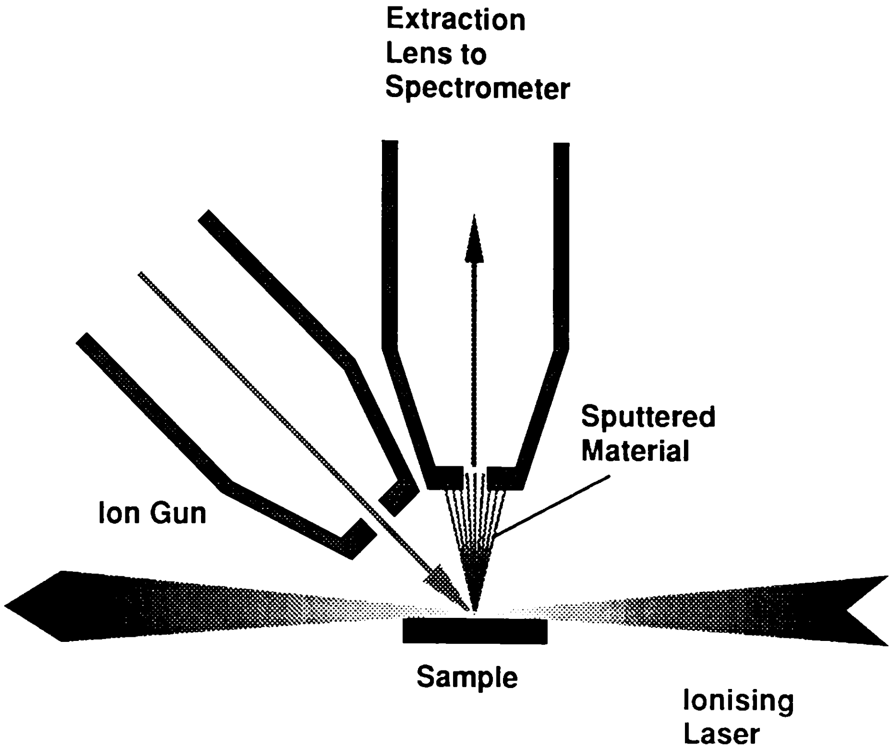
Extraction
Lens to
Spectrometer
Sputtered
Material
Ion Gun
Sample
Ionising
Laser

Figure 1.9 Laser post-ionisation (laser SNMS)

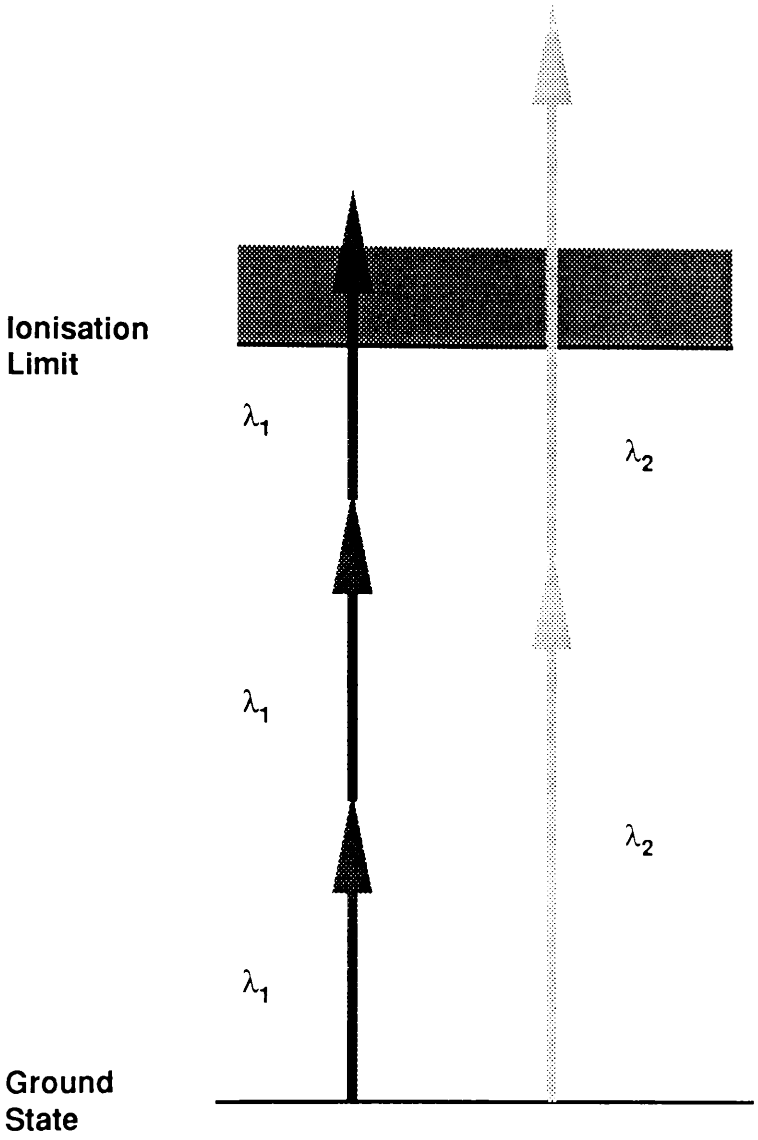
Ionisation Limit
λ_1
λ_2
λ_1
λ_2
λ_1
Ground State

Figure 1.10 Two and three photon MPI

those found in SIMS as the ionisation is generally non-selective, and may be severely restricted by surface contamination due to the ease of thermal desorption of surface particles.

This leads on to probably the most recent development in laser post-ionisation, namely Resonant Ionisation Spectroscopy (**RIS**), which utilises the tunable qualities of modern dye lasers to match real transitions within atoms and thereby achieve ionisation with high probability and atomic selectivity. Details of the mechanisms involved will be discussed in the following chapter, suffice it to say that RIS offers possibly the greatest scope for improvements in ultra-trace analysis of any of the aforementioned or other techniques.

All of the above techniques have their own particular advantages and disadvantages and it would therefore seem the logical step to combine techniques in order to combine the best qualities of the individual methods, to yield more information and a more accurate representation of the sample.

Multiple instruments are now widely in use operating with various combinations of electron and ion spectrometries [54].

An example of such an instrument may incorporate either AES or XPS in conjunction with SIMS.

Electron techniques, being less prone to matrix effects supply the quantitative information while SIMS supplies the major compositional information as well as the sensitivity.

Similarly, RBS is used in conjunction with SIMS. From RBS spectra an absolute depth scale can be derived, provided details concerning the ion-target interactions are known, i.e. interaction cross-sections and stopping powers. Again due to the relatively poor sensitivities attainable with RBS, SIMS is used to provide the missing sensitivity factor.

More recently, a combined SIMS/laser desorption instrument has been described [28].

The nature of this project concerns the application of Resonance Ionisation Mass Spectrometry (**RIMS**), to surface and 'in depth' analysis (depth profiling), in particular with respect to possible structural investigation of multilayer structures grown by MBE.

These initial experiments will involve analysis of only bulk material constituents, namely Ga and Al in GaAs/AlGaAs layers, in an attempt to recognise procedural difficulties which may be encountered and to determine the limitations of the apparatus used.

Chapter 2.

Resonance Ionisation Spectroscopy (RIS).

Introduction

The technique of **RIS** has been in widespread use now for little more than a decade, developed in the early seventies by Letokhov and co-workers in the USSR Academy of Sciences, and in the USA by Hurst and co-workers at Oak Ridge, as a consequence of improvements in laser technology, in particular the availability of powerful tunable sources.

The interest in RIS stems from its ability to selectively ionise a particular atom of interest with a high probability while effectively leaving the all others present in a neutral state. For this reason, it offers immense possibilities in the field of trace analysis.

In the early years of its development, much interest lay in its possibilities for application to isotope separation[3][13][115], in particular those of Uranium for use in nuclear reactors . However, its use has expanded into many other fields where trace analytical and spectroscopic investigations of the highest sensitivity are vital. Uses for RIS have been found in areas as diverse as high energy physics [57], medicine [99], and the electronics industry [19], to name but a few.

At present the first generation of commercial systems are beginning to appear on the market with future improvements in reliability and ease of use, dependent on further developments in laser technology and computer control.

Physical Basis.

In principle, RIS is very straightforward.

A typical atom has a structure of discrete energy states or levels, from the lowest energy ground state to the ionisation limit or continuum. Normally, the populations in these states are determined by a Boltzmann distribution, and therefore at room temperature, assuming a non-split ground state, the population in the ground state is effectively 100%. If a photon equal in energy to the difference between two states is incident on the atom, a transition may occur from the lower to the higher state. Further transition may then be made to higher lying states by subsequent photon interaction until sufficient energy is supplied to promote an electron into the ionisation continuum, thereby creating a positive ion and an unbound electron (Figure 2.1(a)).

Since every element has its own unique energy level scheme, a choice of photon energies, particular to the element of interest, results in the creation of what are termed 'Resonant' ions of that type. Furthermore the probability of ionising an atom of another element via non-resonant transitions is many orders of magnitude smaller. Resonant Ionisation is therefore extremely elementally selective, and in addition, can be made 100% efficient if sufficient photon flux is available.

However, not all transitions occur with the same probability, and in fact many are not normally allowed. The allowable transitions are determined by selection rules which arise from angular momentum conservation considerations within the atom under the influence of electric dipole radiation.

Due to the intrinsic spin of the photon, under absorption, the orbital angular momentum of the excited state electron must change by $1\hbar$. For a many electron atom, the electric dipole selection rules in atoms with LS coupling, for single photon absorption are [123]:

$$\Delta L = 0, \pm 1$$

$$\Delta S = 0$$

$$\Delta J = \pm 1, 0$$

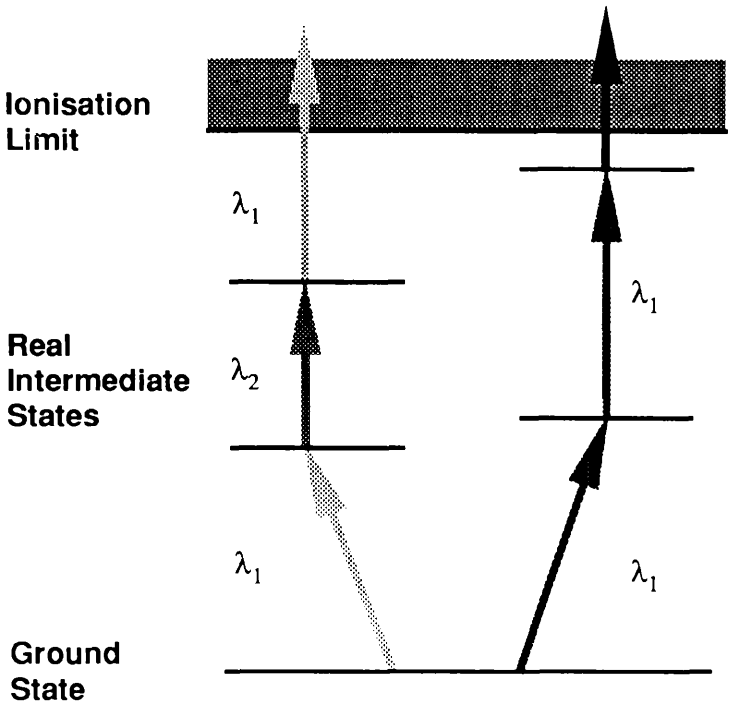
Ionisation Limit
Real Intermediate States
Ground State
λ_1
λ_2
λ_1
λ_1
λ_1

Figure 2.1 (a) Resonant multiphoton ionisation via real intermediate states

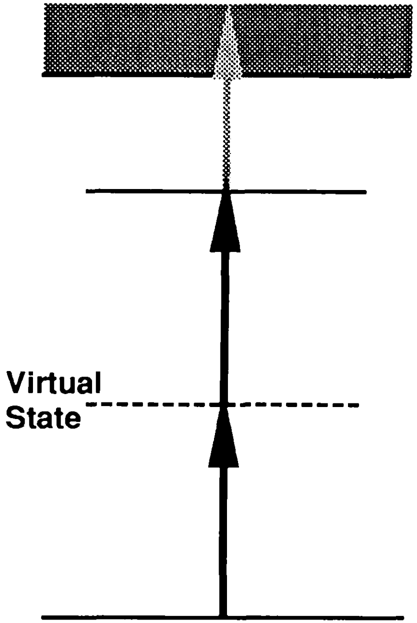
Virtual State

Figure 2.1 (b) Resonant multiphoton ionisation via a virtual intermediate state

$$J = \sum_i j_i = L + S = \sum_i l_i + \sum_i s_i$$

where l and s are the angular momentum quantum numbers defining the electron configuration.

Also, in an electric dipole transition the parity of the atomic wavefunction, defined by $(-1)^L$, must change.

As well as single photon transitions, excitation may occur between bound states under the action of two or more consecutive photons through what are known as virtual states (Figure 2.1(b)). This method allows transitions which break the dipole selection rules, but requireshigher photon fluxes due to the short lifetimes of these states. For the case of two photon interactions the selection rules are similarly defined as [61]:

$$\Delta L = 0, \pm 2$$

$$\Delta S = 0$$

$$\Delta J = 0, \pm 1, \pm 2$$

in which case parity is conserved.

Five main schemes have been suggested by Hurst et al. [42][43] (Figure 2.2) to enable resonant ionisation of all the elements, except He and Ne which have very high ionisation potentials. The application of these schemes to the elements is illustrated in the periodic table of Figure 2.3. However, these need not be adhered to rigorously as there are many more possibilities for most elements which may be more suitable to a particular experimental arrangement or samples of complex matrix which may contain elements with similar electronic structures. Thonnard et. al. [19] have illustrated how 39 of the elements can be resonantly ionised by the same laser arrangement, therefore allowing rapid switching between the elements under investigation, under computer control if necessary.

The simplest scheme requires a single photon to excite the electron into an upper level more than halfway to the continuum. A second photon of the same energy is then

The five basic Resonance Ionisation schemes

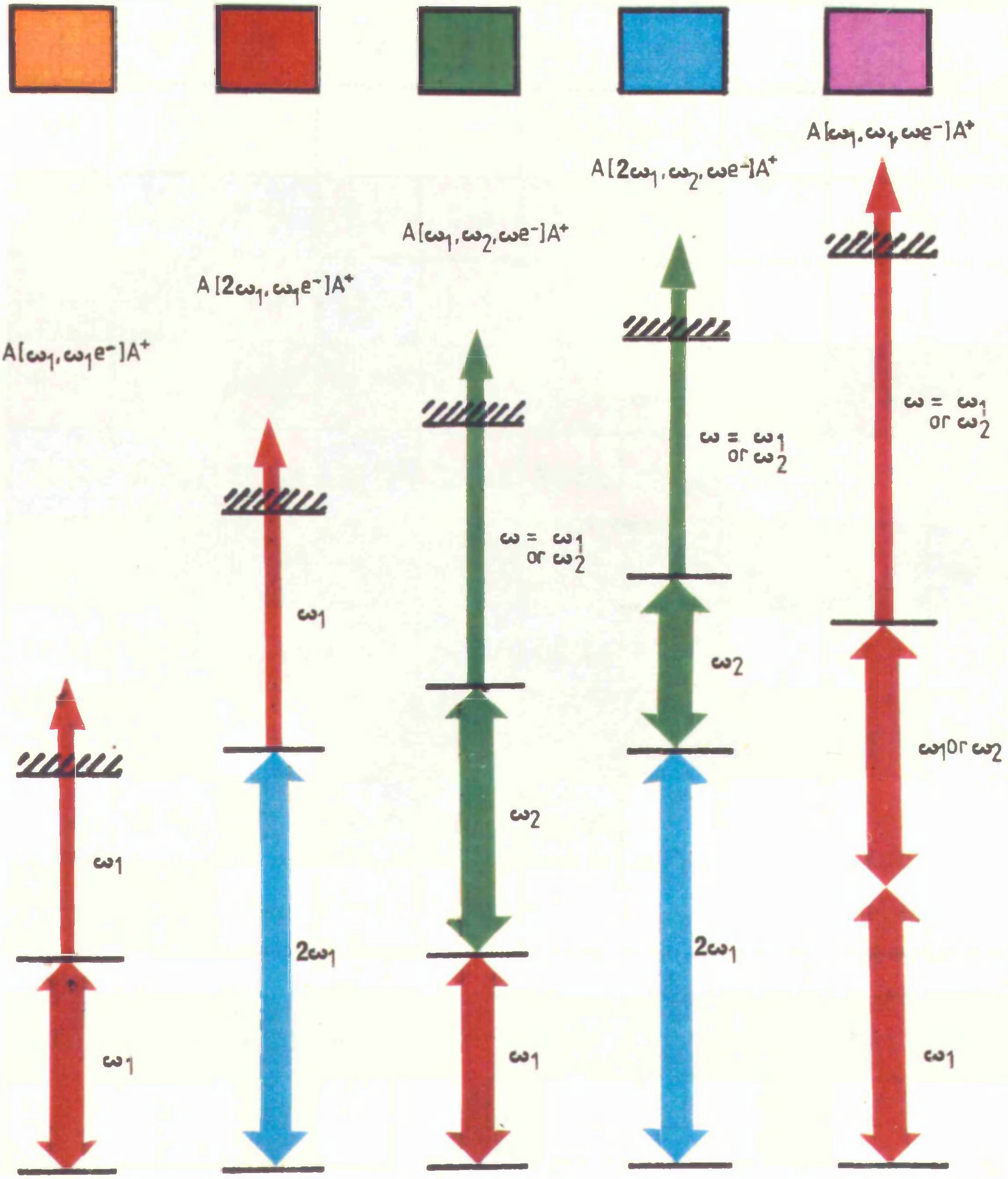
$A[\omega_1, \omega_1 e^-]A^+$
ω_1
ω_1
$A[2\omega_1, \omega_1 e^-]A^+$
ω_1
$2\omega_1$
$A[\omega_1, \omega_2, \omega e^-]A^+$
$\omega = \omega_1$ or ω_2
ω_2
ω_1
$A[2\omega_1, \omega_2, \omega e^-]A^+$
$\omega = \omega_1$ or ω_2
ω_2
$2\omega_1$
$A[\omega_1, \omega_1, \omega e^-]A^+$
$\omega = \omega_1$ or ω_2
ω_1 or ω_2
ω_1

Figure 2·2.

Application of the Resonance Ionisation schemes
to the periodic table

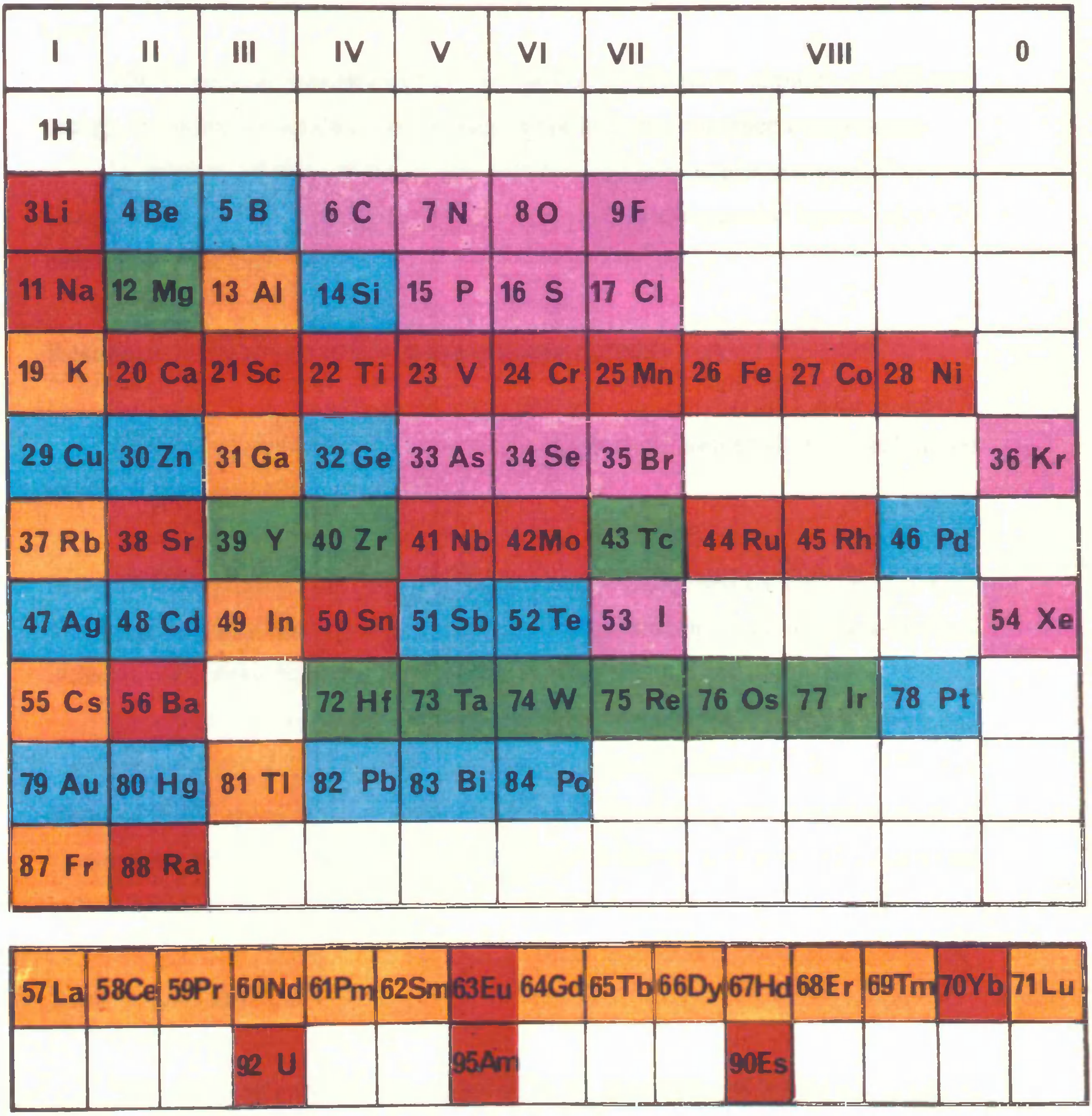

I	II	III	IV	V	VI	VII	VIII			0
1H										
3Li	4 Be	5 B	6 C	7 N	8 O	9 F				
11 Na	12 Mg	13 Al	14 Si	15 P	16 S	17 Cl				
19 K	20 Ca	21 Sc	22 Ti	23 V	24 Cr	25 Mn	26 Fe	27 Co	28 Ni	
29 Cu	30 Zn	31 Ga	32 Ge	33 As	34 Se	35 Br				36 Kr
37 Rb	38 Sr	39 Y	40 Zr	41 Nb	42Mo	43 Tc	44 Ru	45 Rh	46 Pd	
47 Ag	48 Cd	49 In	50 Sn	51 Sb	52 Te	53 I				54 Xe
55 Cs	56 Ba		72 Hf	73 Ta	74 W	75 Re	76 Os	77 Ir	78 Pt	
79 Au	80 Hg	81 Tl	82 Pb	83 Bi	84 Po					
87 Fr	88 Ra									

57 La	58Ce	59Pr	60Nd	61Pm	62Sm	63Eu	64Gd	65Tb	66Dy	67Hd	68Er	69Tm	70Yb	71 Lu
			92 U			95Am				90Es				

Figure 2·3

sufficient to cause ionisation.

A variation on this, for atoms of slightly higher ionisation potential , involves the use of a frequency doubled photon to effect the transition to the upper state followed by a photon of the original frequency for the ionisation step. This scheme was used in the analysis of Gallium and Aluminium in the experiments to be outlined later.

The remaining schemes utilise various combinations of photons of different energy, including the fundamental frequencies or frequency doubled components.

In order to achieve saturation of a resonant two photon process, typical photon fluxes of around 10^{26} photons cm^{-2} s^{-1} are required. Modern pulsed lasers can easily meet this requirement.

Resonant Ionisation Mass Spectrometry.(RIMS)

RIMS involves a coupling of the RIS process to the well established techniques of post-ionisation mass analysis [102].

Assuming all the isotopes of an element are simultaneously ionised by the resonant laser photons, the isotopic ratios can be determined by the spectrometer, assuming the mass resolution is sufficiently high, with improved accuracy due to a reduction in isobaric background effects.

Quadrupole mass spectrometers and sector instruments have been used with RIS although they are limited by their low transmission efficiencies ($\sim 10^{-1}$-10^{-4}) [51]. Time of flight mass spectrometers, either with or without the improvements of electrostatic and magnetic sectors, can however be ideally applied to RIS due to the pulsed nature of their operation.

Rate Equations

The use of population rate equations in the modelling of resonant ionisation, provides a simple and effective method of determining the conditions necessary for saturation of the ionisation process, whereby every atom of interest within the laser volume is ionised, and is generally applicable under conditions where the laser linewidth exceeds that of the atomic states.

The simplest resonant ionisation scheme can be viewed as a three level system

(Figure 2.4), the first and third levels being the ground state of the atom and the ionisation limit respectively. This being the case, the rate equations for the three levels are as follows:

$$\frac{dN_0}{dt} = -\sigma_a\Phi N_0 + \Gamma N_1 + \sigma_s\Phi N_1 \qquad (2.1)$$

$$\frac{dN_1}{dt} = \sigma_a\Phi N_0 - \Gamma N_1 - \beta N_1 - \sigma_s\Phi N_1 - \sigma_i\Phi N_1 \qquad (2.2)$$

$$\frac{dN_i}{dt} = \sigma_i\Phi N_1 \qquad (2.3)$$

where N_0, N_1, N_i, are the relative populations of the three states at time t, σ_a is the stimulated absorption cross-section, σ_s is the stimulated emission cross-section, and σ_i is the ionisation cross-section from the excited state. Γ is the spontaneous decay rate (equal to the reciprocal of the excited state lifetime), β is the rate of non-radiative decay to a state not contributing to the photoionisation process, and Φ is the photon flux (the number of photons per unit area per unit time).

Adding (2.1) and (2.2) gives:

$$\frac{dN_0}{dt} = -\frac{dN_1}{dt} - N_1\sigma_i\Phi - \beta N_1 \qquad (2.4)$$

Differentiating (2.2) with respect to t and substituting (2.4) yields:

$$\frac{d^2N_1}{dt^2} + \kappa\frac{dN_1}{dt} + \lambda^2 N_1 = 0 \qquad (2.5)$$

where

$$\kappa = \Gamma + \beta + (\sigma_a + \sigma_s + \sigma_i)\Phi \qquad (2.6)$$

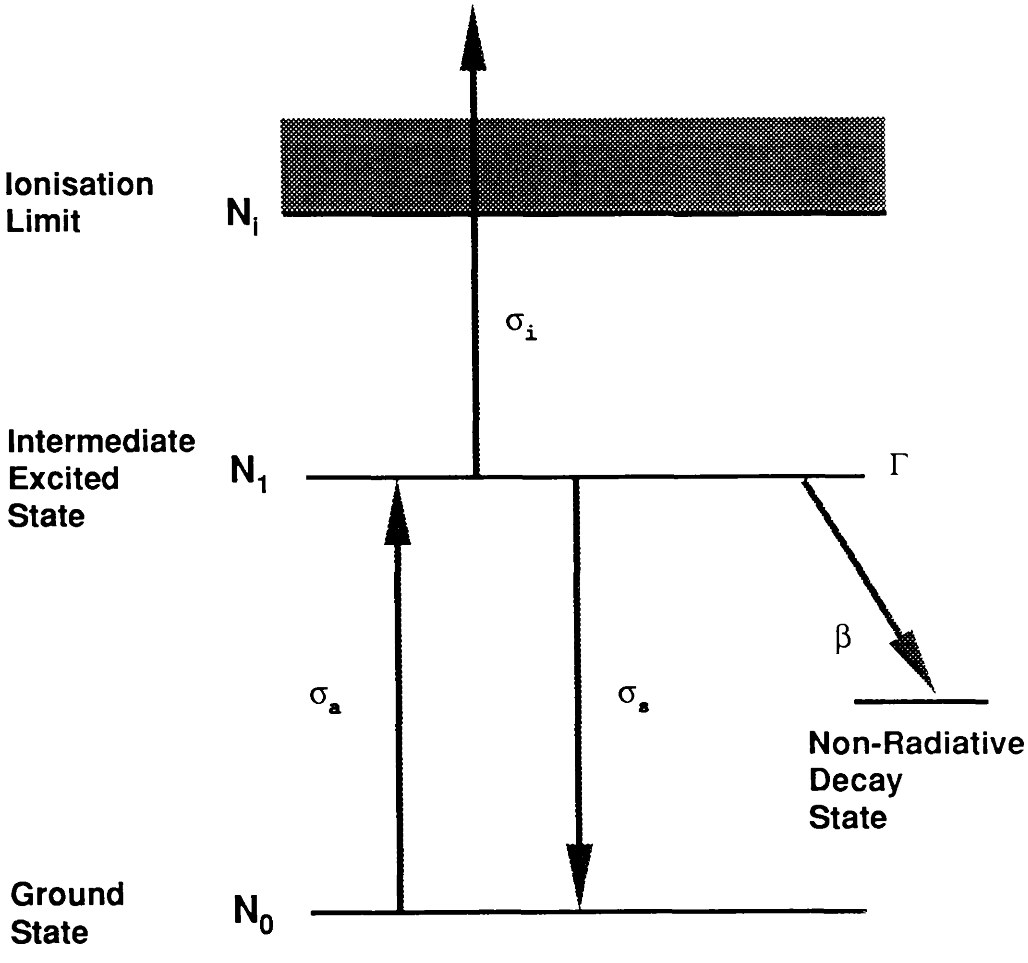
Ionisation Limit
N_i
σ_i
Intermediate Excited State
N_1
Γ
β
σ_a
σ_s
Non-Radiative Decay State
Ground State
N_0

Figure 2.4 Schematic of a three level system

and

$$\lambda^2 = \sigma_a\Phi(\beta + \sigma_i\Phi) \quad (2.7)$$

Equation (2.5) can then be solved to give the population of the excited state as:

$$N_1 = \frac{N_0\sigma_a\Phi}{\mu_2 - \mu_1}\left[e^{-\mu_1 t} - e^{-\mu_2 t}\right] \quad (2.8)$$

where:

$$\mu_1 = \frac{\kappa}{2} - \frac{1}{2}\sqrt{\kappa^2 - 4\lambda^2} \quad (2.9)$$

and

$$\mu_2 = \frac{\kappa}{2} + \frac{1}{2}\sqrt{\kappa^2 - 4\lambda^2} \quad (2.10)$$

For a narrow linewidth laser, tuned on resonance, the cross-sections for stimulated absorption and emission are very much larger than for ionisation (i.e $\sigma_a \sim \sigma_s \gg \sigma_i$). With the flux condition that the rate of excitation is large compared to the spontaneous decay rate (i.e. $\sigma_a\Phi \gg \Gamma+\beta$) then $\mu_2 \gg \mu_1$ and equation (2.8) becomes:

$$N_1 = \frac{N_0\sigma_a\Phi}{\mu_2}\left[e^{-\mu_1 t}\right] \quad (2.11)$$

with μ_2 now approximately equal to $2\Phi\sigma_a$.

Substituting Equation (2.11) into (2.3) and integrating wrt time over the pulse length of the laser T (assuming a square pulse) we get:

$$N_i = \frac{\sigma_i\Phi N_0}{2}\int_0^T e^{-\mu_1 t}dt \quad (2.12)$$

which yields:

$$N_i = N_0\left[1 - e^{-\mu_1 T}\right] \qquad (2.13)$$

From a binomial expansion of (2.9) and the condition that $\kappa \sim 2\Phi\sigma_a$ it can be shown that $\mu_1 = \sigma_a\Phi/2$.

Finally, if the condition holds that $\sigma_i\Phi T \gg 1$ (the fluence condition), then we have the result that $N_i = N_0$ (i.e. all atoms in the ground state at time $t = 0$ are ionised by the end of the laser pulse.). This is what is known as Saturation Ionisation.

Typical values for the above variables are $\sigma_a \sim \sigma_s \sim 10^{-14}\text{cm}^{-2}$; $\sigma_i \sim 10^{-17}\text{cm}^{-2}$; $\Gamma \sim 10^8\text{s}^{-1}$; $\beta \sim 10^6\text{s}^{-1}$ making an overall requirement of $\Phi \gg 10^{25}$. Therefore, for $\lambda \sim$ 500 nm and a laser pulse length of 10 ns, saturation occurs for a fluence > 4 mJ per mm^2.

The above conditions can be met by most commercially available dye lasers with the requirement of moderate focussing of the beam.

A more detailed discussion of the rate equation model can be found in the references which deal with a more complex four level system [91][92]

Due to possible difficulties arising in the saturation of the ionisation step, multistep excitation was proposed which involved excitation through a series of resonant steps to a high lying excited state very close to the ionisation limit of the atom. Ionisation is then achieved by an electric field pulse[60]. Similarly, ionisation from such energetic states may be enhanced via collisions with the atoms of a buffer gas, as in investigations of resonant effects in proportional counters [58][40]. In fact the first successful experiments on single atom detection were carried out in such proportional counter devices[41].

Collisional mechanisms within the buffer gas have the undesir able effect of broadening the resonant transitions (Appendix C), thereby reducing the spectral resolution attainable with such arrangements. Also the high operating pressure within the proportional chamber is not compatible with most types of mass spectrometer. For these reasons it has been more advantageous to adopt atomic beams as the source of material and either apply direct photo-ionisation, or employ field ionisation [5]. Being vacuum compatible atomic beams also allow for their use in conjunction with mass analysers prior to detection.

For analysis of solid samples, the process requires further sophistication with the need for controlled sample vaporisation. This is generally achieved using either a primary pulsed laser to ablate material from the surface or by the action of a beam of primary ions. The plume of vapour thus generated can then be intercepted by the resonant lasers [27][52][79][99][121][51], with the subsequently generated ions analysed and detected in a mass spectrometer. These aspects will be discussed in more detail in subsequent Chapters.

Chapter 3

The Theory of Ion Sputtering and its Application to Depth Profiling.

Introduction.

As already mentioned in Chapter 1, the need for reliable and accurate techniques for the characterisation of modern superlattice structures continues to increase, with advances in growth processes surpassing the abilities of presently "state of the art" analytical methods. In most cases, a balance has to be made between the requirements for high depth resolution and sensitivity. An exception to this rule is SIMS which displays PPM sensitivity while maintaining a depth resolution of some nm. SIMS does however have its own inherent problems.

In applying the popular surface analysis techniques to depth profiling, the common requirement is the continuous exposure of the sub-surface layers. This must be achieved at a constant rate with high spatial uniformity. The usual method employed is that of ion-erosion, with the exception of RBS which yields the depth information directly in the energy spectrum of the ions backscattered in collisions with deeper lying planes of atoms.

The following sections describe the major mechanisms involved in depth profiling, namely the process of ion erosion (sputtering), and the factors determining the ultimate depth resolution obtainable under a particular experimental arrangement. The great deal of material available on these subjects is beyond the scope of this work, however it is worthwhile to present the salient aspects, required for day to day depth analysis, relating to the physical and technical limitations arising.

Sputtering.

The ejection of particles from a solid by bombardment of the surface with energetic primary ions, is known as Sputtering. The physical mechanism responsible for this process is generally considered to be collisional, where incident primary ions colliding with target atoms on the surface, transfer a fraction of their energy and momentum. Further interactions occur until the primary particle comes to rest within the material or is backscattered to the surface. The target recoil particles set in motion also exhibit their own collisional pattern.

Such patterns, involving essentially binary interactions (i.e. interactions involving only two particles), are commonly referred to as collisional cascades (Figure 3.1). If, as a consequence of these cascades, sufficient energy is imparted to atoms on the surface, so as to overcome the surface binding potential of the solid, sputtering of target atoms is observed. For primary ions in the keV energy range, disordering of the sample due to these effects may occur over a depth of several hundreds of angstroms while sputtered particles in general only originate from the first few atomic layers, or tens of angstroms below the surface.

Using this idea of collision cascades, Sigmund developed a sputtering theory, explaining sputter yields (i.e. number of sputtered particles per incident ion) as well as the energy and angular distributions of secondary particles.

According to the theory of Sigmund [93][100][94][95][96], the number of recoil particles (i.e. from within the sample) arriving at the surface in the energy range E, E+dE in solid angle $d\Omega$, at an angle ψ to the surface normal is:

$$\frac{d^3N}{d\Omega dE} = \frac{3}{2\pi^3}\frac{\alpha S_n(E_p)}{C_0}\frac{\cos\psi}{E^2} \qquad (3.1)$$

where $S_n(E_p)$ is the nuclear stopping cross-section for primary particles of energy E_p, α is a factor dependent on the relative masses of projectile and target, and C_0 is a constant of the scattering cross-section.

For energies in the keV range, $C_0 = 1.8 \times 10^{-16}$ and [126]

$$\alpha \sim 0 \cdot 15 + 0 \cdot 13\left(\frac{M_2}{M_1}\right) \qquad (3.2)$$

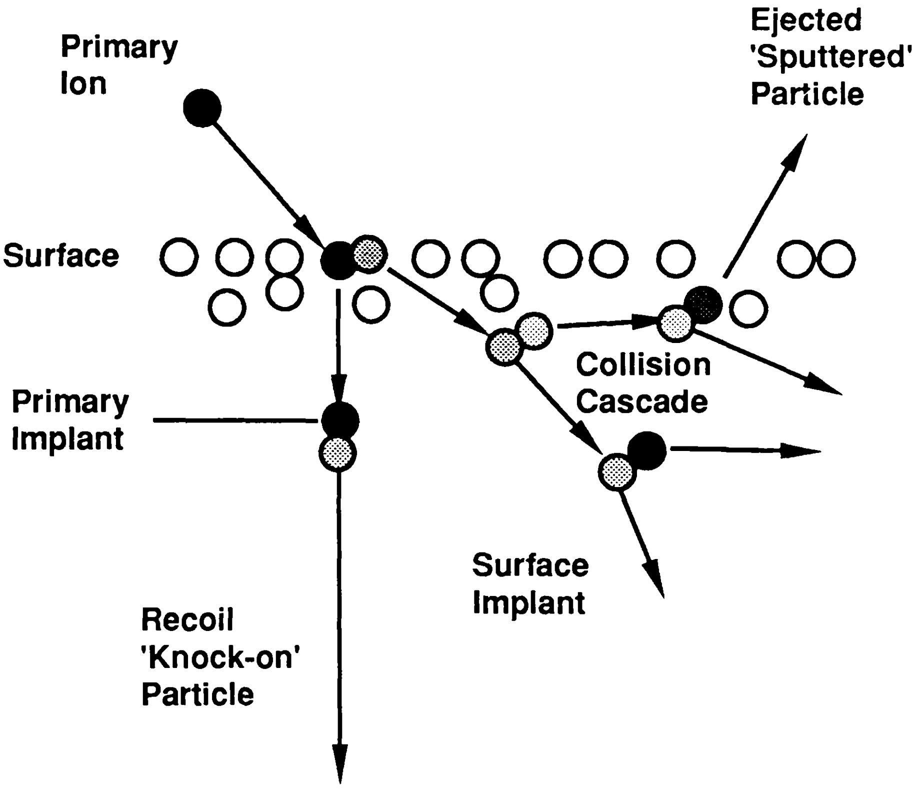
Primary
Ion
Ejected
'Sputtered'
Particle
Surface
Collision
Cascade
Primary
Implant
Surface
Implant
Recoil
'Knock-on'
Particle

Figure 3.1 Features of the interaction of fast ions with a solid sample
(Collision Cascades)

where M_1 and M_2 are the masses of the primary and secondary particles.

Assuming a planar potential barrier at the surface, integration of Equation (3.1) over all angles and energies $\geq U_s$ gives:

$$Y(E_p) = \frac{3}{4\pi^2 C_0} \frac{\alpha S_n(E_p)}{U_s} \tag{3.3}$$

where Y is the sputter yield, U_s is the surface binding potential of the solid, usually taken as the sublimation energy for most elements [127], and in the case of semiconductors as the energy required to break half the number of bonds in the bulk [2], and is typically a few electron volts. Inserting values for the various constants, Equation (3.3) becomes:

$$Y = \frac{0 \cdot 042\,[\text{Å}^{-2}]\,\alpha\, S_n[\text{eV}\,.\,\text{Å}^2]}{U_s[\text{eV}]} \tag{3.4}$$

where the nuclear stopping cross-section is given by:

$$S_n(E) = 4\pi Z_1 Z_2 e^2 a \left[\frac{M_1}{M_1 + M_2}\right] s_n(\varepsilon) \tag{3.5}$$

Z_1 and Z_2 being the atomic numbers of the primary and secondary species, and

$$a = 0 \cdot 8853\ a_0 \left(Z_1^{2/3} + Z_2^{2/3}\right)^{-1/2} \tag{3.6}$$

is the Lindhard screening radius [9] for the Thomas-Fermi interaction potential of atoms and ions. The term a_0 here, is the Bohr radius = 0.52915 Å.

In order to reduce the number of parameters the dimensionless reduced energy has been introduced and is defined by the expression:

$$\varepsilon = \frac{M_2 E}{M_1 + M_2} \cdot \frac{a}{Z_1 Z_2 e^2} \tag{3.7}$$

This is given for cgs units and by inserting the appropriate values can be re-expressed in terms of E in eV by:

$$\varepsilon = \frac{32 \cdot 5\ M_2\ E(\mathrm{keV})}{(M_1 + M_2)\, Z_1 Z_2 (Z_1^{2/3} + Z_2^{2/3})^{1/2}} \qquad (3.8)$$

This leads to Equation (3.5) being rewritten as

$$S_n(E) = 84 \cdot 77 \frac{Z_1 Z_2}{(Z_1^{2/3} + Z_2^{2/3})^{1/2}} \cdot \frac{M_1}{M_1 + M_2} \cdot s_n(\varepsilon) \quad [\mathrm{eV}\,.\,\mathrm{\AA}^2] \qquad (3.9)$$

where $s_n(\varepsilon)$ is the reduced stopping cross-section which has been expressed [120] by:

$$s_n(\varepsilon) = \frac{\frac{1}{2}\ln(1+\varepsilon)}{\varepsilon + 0.14\varepsilon^{0.42}} \qquad (3.10)$$

As an example, consider a 2keV beam of primary argon ions incident normally on a solid gallium surface. M_1 is taken as 40 amu, and M_2 as the average mass of the two gallium isotopes as 69.7 amu. The atomic numbers of the projectile and target are 18 and 31 respectively.

Substituting into Equation (3.8) gives the reduced energy as $\varepsilon = 0.0181$.

Using this value in Equation (3.10) yields $s_n(\varepsilon) = 0.204$.

Equation (3.9) then gives $S_n(E) = 859.22$ [eV.Å^2]

Finally, substituting all values into Equation (3.4) gives the sputter yield for argon on gallium as 5.04 sputtered particles per incident primary ion.

where $U_s(\mathrm{Ga}) = 2.7$ eV and α is calculated from Equation (3.2) to be 0.377.

Similarly for GaAs the various parameters can be calculated.

$\varepsilon = 0.0177$

$s_n(\varepsilon) = 0.202$

$S_n(E) = 852.59$

$\alpha = 0.385$

where the avarage atomic number and mass were taken as 32 and 72.32 respectively. Substituting into Equation (3.4) then yields 4.18 particles sputtered per incident ion.

Figure 3.2 shows how the sputter yield varies with the mass and energy of the primary particle, calculated from the Sigmund theory.

Nature of Sputtered Particles.

Of primary importance to sputter induced ion spectrometries, is the charge state of the particles liberated, whether as ions for SIMS analysis, or neutrals for methods of SNMS.

It is an accepted fact that the ion fraction generated is much smaller than the neutral fraction [51], with a severe dependence (up to a factor of 100), on the sample composition, thus creating obvious problems in the quantitative analysis of samples varying in matrix, without the introduction of multiple internal and/or external standards for comparison.

In order to make an accurate determination of the true composition from the secondary ion information, it becomes necessary to derive a physical model for the secondary ion formation.

A variety of such models have been proposed, although a general model applicable under all situations and combinations of primary and target material, does not exist as yet.

The most widely used model assumes the development of a plasma layer in the sample under ion bombardment, in which all particles are in a local thermodynamic equilibrium (LTE). The model is restricted to the presence of oxygen within the plasma [116].This however is often the case in SIMS analysis where oxygen is used as the primary beam or is introduced to enhance the positive ion production due to the electronegativity of its nature [1][52].

Under these conditions the degree of ionisation can be derived from the Saha-Eggert equation [9][1][14]:

$$\frac{n^+ n_e}{n^0} = \frac{2Z^+(T)}{Z^0(T)}\left(\frac{2\pi m_e kT}{h^2}\right)^{3/2} \exp\left(-\frac{E_i - \Delta E}{kT}\right) \tag{3.11}$$

where n^0, n^+, n_e are the number densities of the neutral particles, positive ions and electrons respectively, $Z^0(T)$, $Z^+(T)$ are the internal partition functions of the neutrals

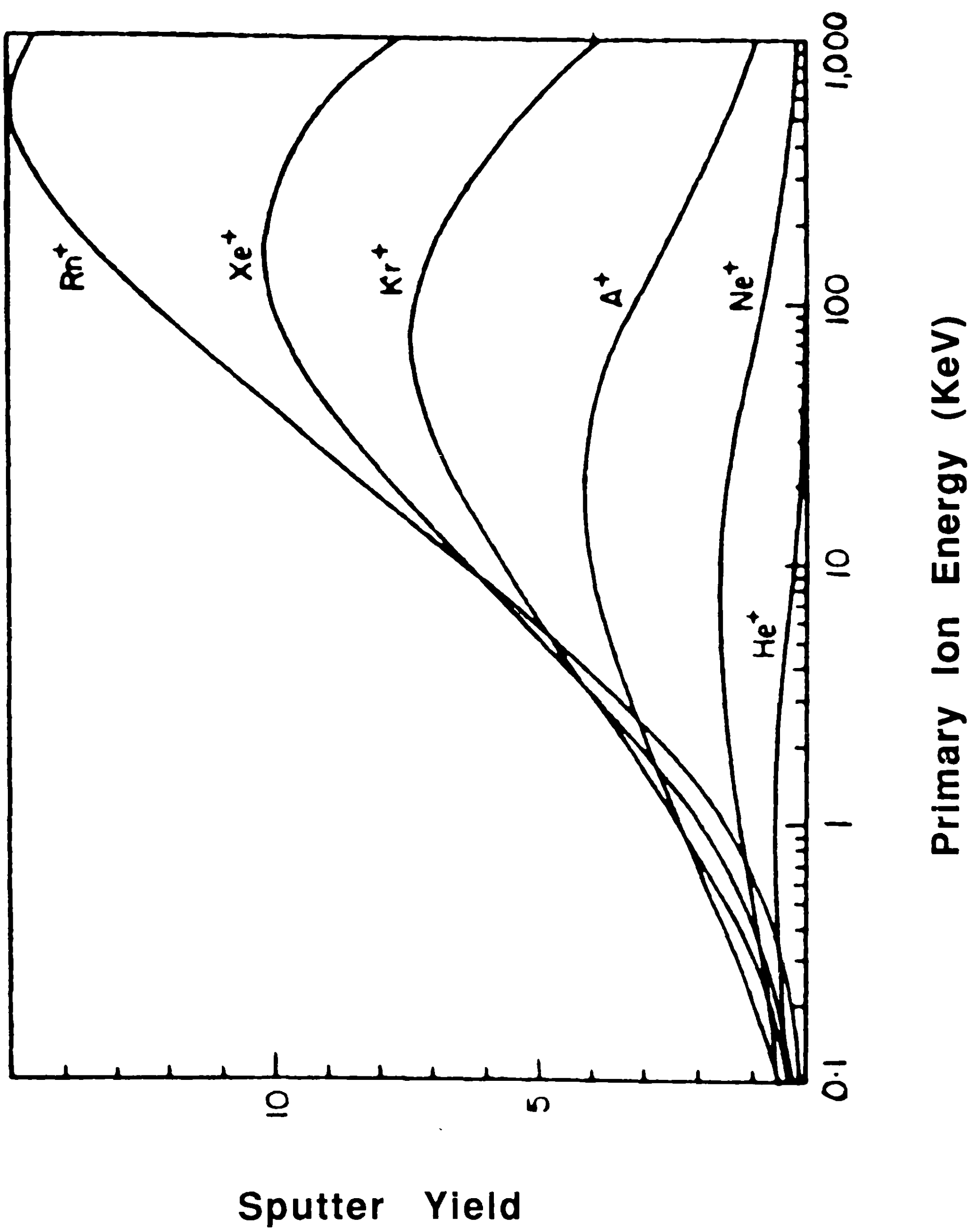

Figure 3.2 Sputter yield from Al as a function of energy and mass of projectile [93]

and positive ions [7], E_i is the first ionisation potential of the atom, T the plasma temperature, k Boltzmann's constant, h Planck's constant, m_e the electron mass and ΔE the depression of the ionisation energy due to charge and temperature effects in the plasma and is given by the Debye correction [112]:

$$\Delta E = e^3\left(\frac{8\pi n_e}{kT}\right)^{1/2} \tag{3.12}$$

where e is the electronic charge.

For multi-elememt systems, due to the unknown quantities T and n_e, at least two internal standards are still required in order for the true concentrations to be calculated. It can be shown [116] that the temperature T is not identified as the macroscopic temperature of the target, but is in effect related to the average kinetic energy available in the collision cascade .

Software packages such as CARISMA [1] have been developed specifically for this purpose using iterative methods to calculate the unknowns T and n_e from the internal standards and hence calculate the relative populations of all other elements present from the measured ion yields.

Incidence Angle Dependence.

The dependence of the incident angle of the primary beam on the sputter yield, for polycrystalline materials is given by [93][80][69]:

$$\frac{Y(\theta)}{Y(0)} = (\cos\theta)^{-f} \tag{3.13}$$

where Y(0) is the sputter yield at normal incidence, θ is the incident angle relative to the surface normal and f is a constant defined by the mass ratio (for $M_2/M_1 < 3$, $f = 5/3$). At oblique angles this relation breaks down as the reflection coefficient of the incident particles increases until a critical angle where the reflection is 1, in which case all incident particles are scattered from the surface atomic layer, none having sufficient energy perpendicular to the surface to overcome the potential barrier (Figure 3.3). Maxima in the sputter yield usually occur at between 60^0 and 70^0 to the normal [98].

Figure 3.3 Dependence of sputter yield on primary beam incidence angle for inert gas ions [9]

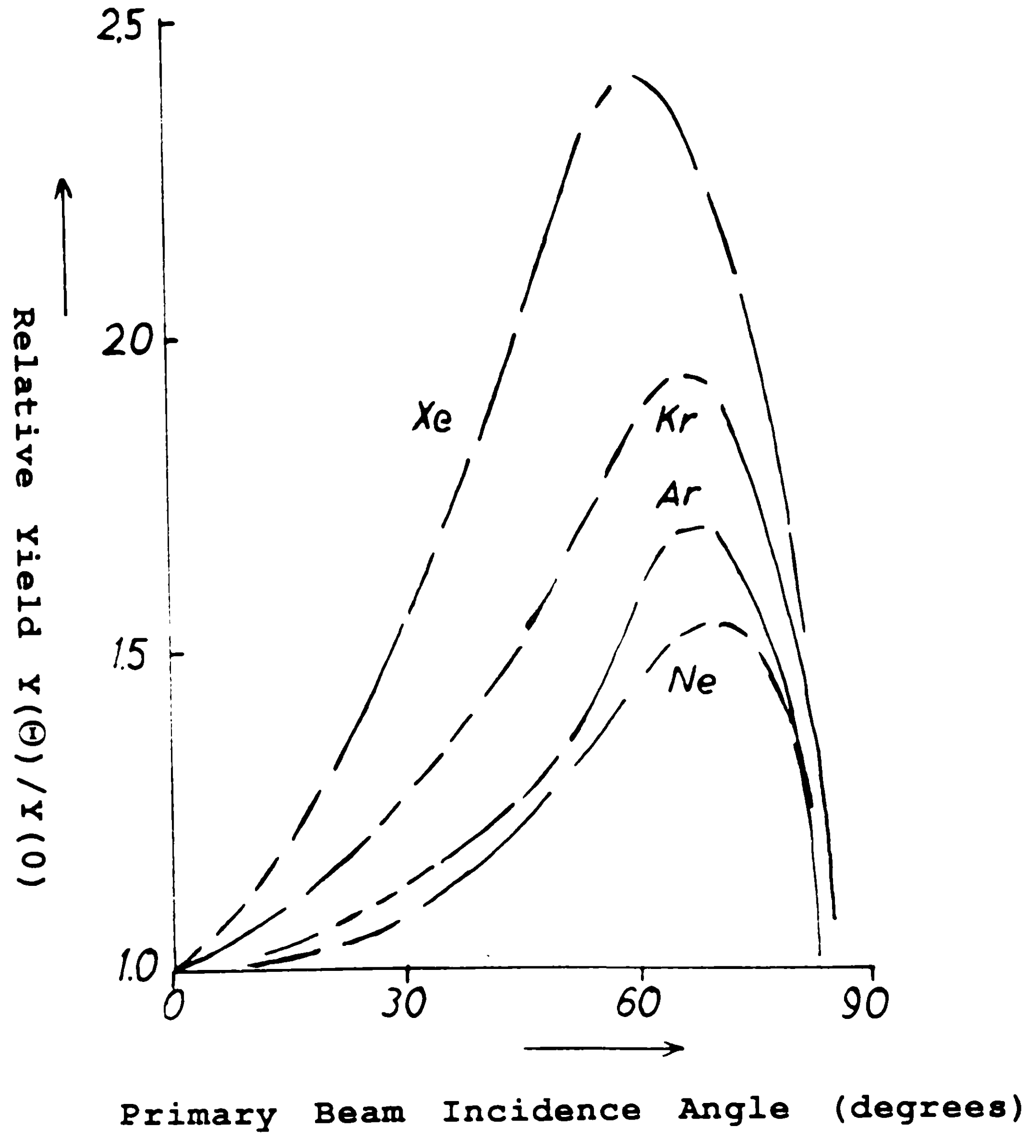

This however, is not necessarily the case for a monocrystalline target, where ions may be channelled by parallel crystal planes and penetrate farther into the crystal. At such incident angles, the sputter yield will be reduced.

Energy Distribution of Sputtered Particles.

Equation (3.1) can be integrated over a 2π solid angle to give the energy distribution of the sputtered particles as:

$$\frac{dN}{dE} = \frac{3}{2\pi^2}\frac{\alpha S_n(E_p)}{C_0}\frac{E}{(E + U_s)^3} \qquad (3.14)$$

which has a maximum at $E = U_s/2$, a linear increase at $E \ll U_s$ and a $1/E^2$ dependence at $E \gg U_s$. Figure 3.4 shows a series of curves corresponding to the sputtered energy distribution of various elements.

Angular Distribution of Sputtered Particles.

For polycrystalline materials, if one assumes that after a few collisions within the target the recoil atoms are moving essentially randomly through the medium, their distribution being therefore isotropic, then the angular distribution of the ejected material is effectively isotropic. The normal component of the secondary particle current then approximates a cosine distribution [80][106][98]. This holds for normal incidence. However, at oblique primary beam incidence, the preferential emission angle is shifted away from the normal in the direction of specular reflection of the primary ions [80], due to the formation of knock-on atoms with a large component of momentum parallel to the surface (Figure 3.5). Emission of these knock-on particles is then dependent on their component of momentum normal to the surface, determined by the primary ion energy, and the surface binding energy of the material [80].

Erosion Rate.

A prerequisite for depth analysis is the constant, continuous erosion of the sample at a rate dependent on the primary beam and the sample characteristics. This

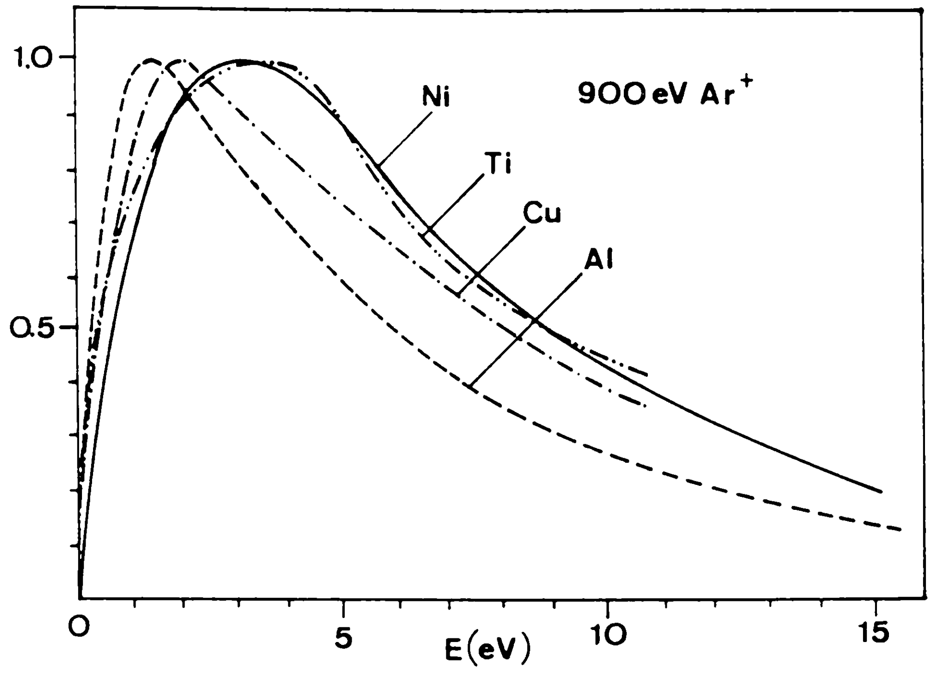

Figure 3.4 Kinetic energy distribution of particles sputtered from various samples. Primary beam 900eV argon ions. [9]

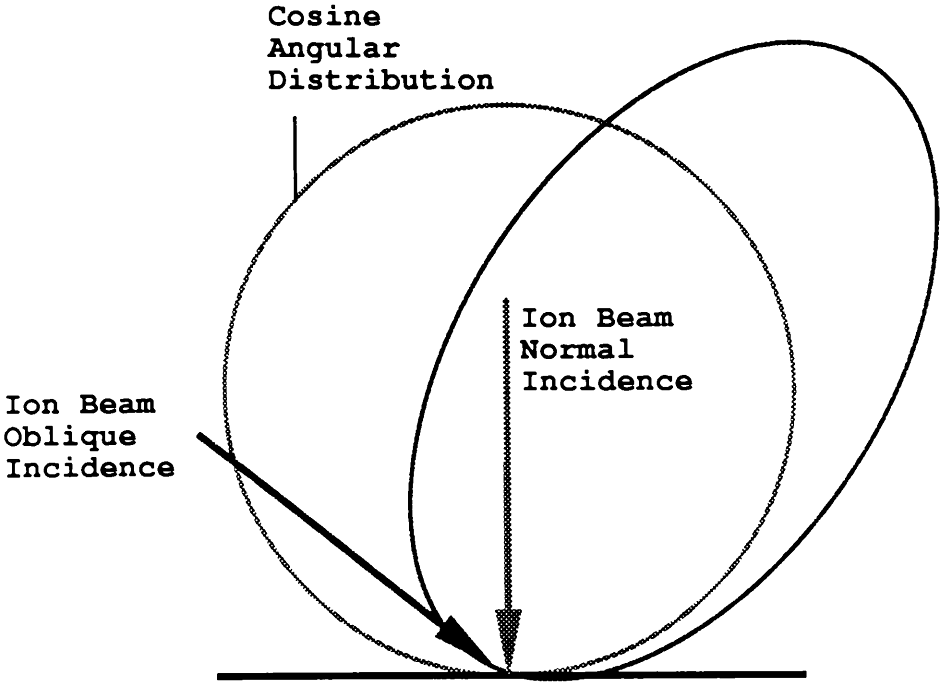
Cosine Angular Distribution
Ion Beam Normal Incidence
Ion Beam Oblique Incidence

Figure 3.5 Angular distribution of sputtered particles

erosion (sputter) rate is given by [9][35]:

$$z = 3 \cdot 755 \times 10^{-4} . \frac{M(\text{amu}) . j(\mu A / cm^3) . Y}{\rho(g / cm^3)} \tag{3.15}$$

in μm per hour.

Here j is the effective current density of the primary ion beam, M is the average mass, ρ the density, and Y the total sputter yield of the sample.

For the case of one major matrix component, the sputter rate is a constant, and the sputtered depth is simply the product of the sputter rate and the total time.

The target number density (atoms per cm^3) is given by

$$n_0 = \frac{\rho N_A}{M} \tag{3.16}$$

where N_A is Avogadro's constant . This can be substituted into equation (3.15) to simplify the expression if the information concerning the lattice construction is known.

As an example, GaAs has a Cubic Zinc Sulfide (Diamond) Structure with a lattice parameter *a* of approximately 5.67 Å. In each conventional cell there are 4 atoms of Ga and 4 of As. The number density can then be easily calculated as $8 \times 10^{24} / a^3(\text{Å}) = 4.39 \times 10^{22}$ cm^{-3}.

Equation (3.15) can be written as

$$\dot{z} = 3 \cdot 755 \times 10^{-4} . \frac{N_A . j . Y}{n_0} \tag{3.17}$$

and substituting the values for n_0 and N_A yields

$$\dot{z} \cong 5 \cdot 15 \times 10^{-3} . j . Y \tag{3.18}$$

Therefore, for a current density of 0.01 μA/cm^2 and a total sputter yield of 5 the sputter rate can be calculated to be ~2.58 x 10^{-4} μm/hour.

This relation (Equation (3.17)) holds for a uniform surface current density which can be better approximated by rastering of the ion beam. In this case, the current density, and hence the sputter rate, is reduced by the ratio of the spot size to the rastered area.

Erosion rate is usually easily controllable, and is variable over a wide range, with ion gun parameters. Generally there are considered to be two types of SIMS defined according to the ratio of the erosion time, t_M, of a monolayer of the sample to the recording time of a mass spectrum, t_A. The practically non-destructive 'static' SIMS mode arises for $t_M/t_A \gg 1$, while 'dynamic' SIMS, more suited to depth analysis arises for $t_M/t_A \leq 1$ [33].

Factors Affecting Depth Profiling.

The main experimental aspects responsible for accurate determination of depth concentration profiles are the depth resolution and the dynamic range. These are affected to varying degrees by instrumental factors and ion solid interactions within the target.

Depth Resolution.

Depth Resolution Δz is a measure of the quality of a depth profile. For a step-like concentration transition, the measured signal will be broadened by various experimental factors. The shape of the measured profile can be closely approximated by the function [35][9]:

$$I(z) = I_0\left[\tfrac{1}{2} - \tfrac{1}{2}\mathrm{erf}(z)\right] \qquad (3.19)$$

where the current drops from a maximum level I_0 to a minimum (Figure 3.6). The derivative of Equation (3.19) is a Gaussian error function. From the measured profile, the value for the depth resolution is defined in several ways; for example, the depth Δz across which the current drops from 95% to 5% of I_0 , or more commonly, the depth across 84% to 16% of the maximum, which corresponds to twice the standard deviation 2σ of the Gaussian distribution.

Figure 3.6 Depth resolution defined at a concentration step junction by an error function.

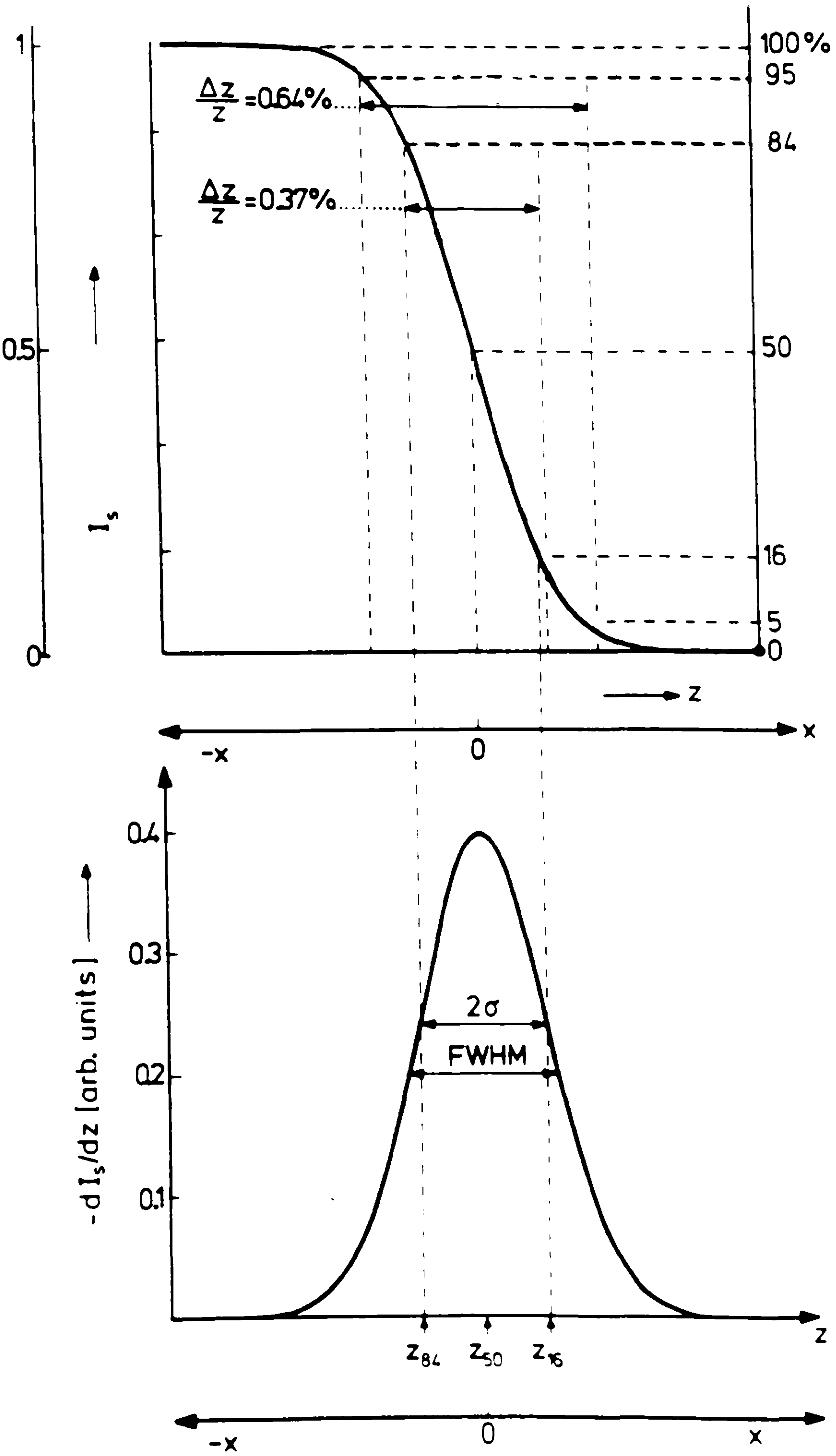

The total measured depth resolution Δz, is a function of all the contributions to the broadening from instrumental and physical parameters, and has been expressed [34][35] as:

$$\Delta z = \left(\sum_{j=1}^{n} \Delta z_j^2 \right)^{1/2} \tag{3.20}$$

where the Δz_j correspond to the contributions from such sources as atomic mixing, surface roughness, edge effects, the most important of which will be discussed in following sections.

Recoil Mixing.

There are two types of recoil mixing which take place under ion bombardment of a solid. Primary Recoil Mixing involves direct ion-target impact resulting in target atoms acquiring high momentum in the forward direction. These are generally small in number and non-isotropic. Although such mixing has some influence on the measured profile, including a possible shift in the distribution, the major mixing contribution arises from Cascade mixing i.e. profile broadening due to the development of collision cascades.

Andersen [2] has theoretically shown that a concentration δ-function is broadened by random collisions to a Gaussian function. Sigmund [97] then derived a general theory which predicts the effects of cascade and recoil mixing on the broadening and shifting of profiles. The theory goes on to show how the Full Width at Half Maximum (FWHM) of this function can be expressed by the dependence:

$$\Delta z \propto \left[\frac{E}{Y} \right]^{1/2} \tag{3.21}$$

where E and Y are defined as before.

For an abrupt concentration step this broadening can be assumed to be comparable with the depth resolution, hence the effects of experimental parameters can be concluded from the expression.

As Δz is proportional to $E^{1/2}$, the use of low primary energy (typically 3 to 5 keV) enhances the resolution. The sputter yield is dependent on the incident angle (Equation (3.13)) and hence at the angle corresponding to the maximum sputter yield, the effect on profile broadening is minimised. Y is also proportional to the constant α which is related to the mass ratio of target and projectile (Equation (3.2)). At energies ~keV, heavy projectiles reduce the effect of cascade mixing while improving the sputter yield.

Monte Carlo simulations of atomic mixing effects [46] compared with experimental corroboration [45] confirm these predictions of increased broadening due to higher energy primaries and steeper incidence.

High energy primary ions also have a tendency to generate structural defects within the crystal which enhance the diffusion rate [29], again leading to a broadening of the profile.

Surface Roughness

Deterioration of the depth resolution can also result from the initial surface roughness of the sample. For surface features smaller than the spot size of the primary ion beam, sputtered material may originate from different exposed layers within the beam spot. Also, sputtering may occur at different rates due to a variation in the angle of incidence at different points on the surface (Figure 3.7). This can then lead to an enhancement of the roughness, implying a worsening of the measured broadening with depth. Inhomogeneities in the sample, whether already present or ion bombardment induced, also lead to the development of surface roughness and cone formation (Figure 3.8).

Obviously some care has to be taken in the preparation of samples to ensure the minimum of surface contamination and lack of large particles on the surface which may cause a shadowing of the surface to the primary ions.

To an extent the effect of surface roughness can be reduced by the use of multiple ion beams at different orientations or sample rotation during sputtering. Alternatively the introduction of oxygen during the sputtering process can lead to the formation of quasi-amorphous oxides which sputter more uniformly over the surface due to a reduction in channelling of the projectiles, resulting in a suppression of cone formation and incident ion orientation dependence [105]. Similar observations have

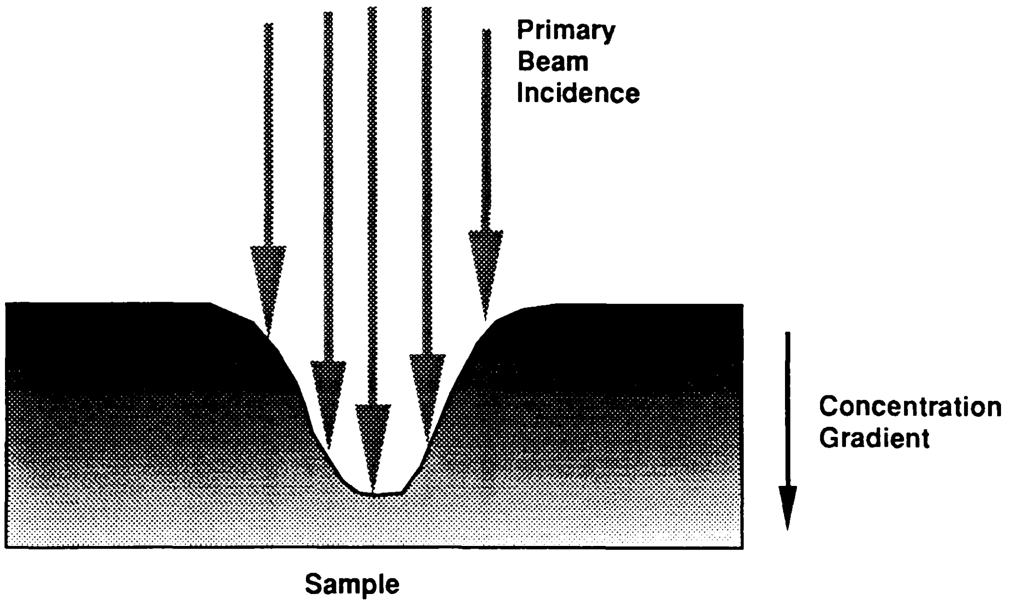
Primary
Beam
Incidence
Concentration
Gradient
Sample

Figure 3.7 Non-uniform crater formation due to the radial profile of the ion beam, resulting in sputtered material originating from various depths

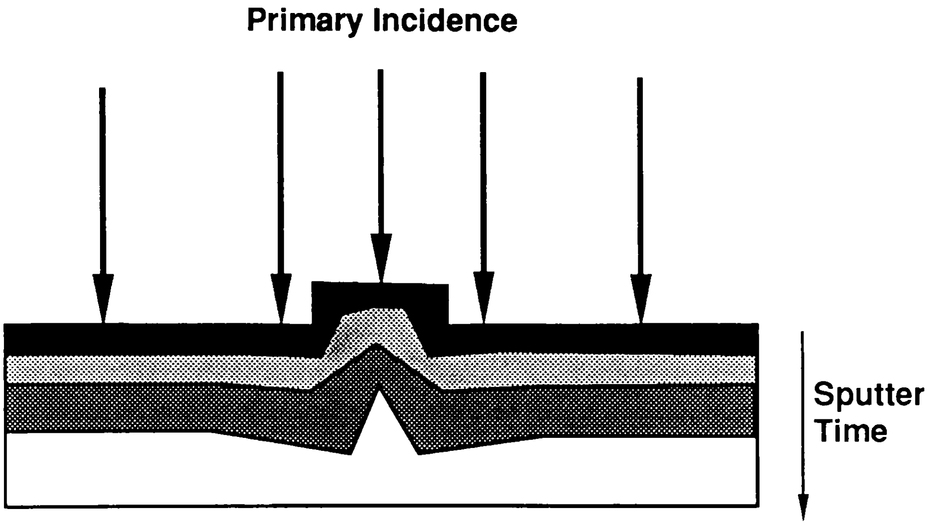
Primary Incidence
Sputter
Time

Figure 3.8 Development of cone features during sputter erosion as a consequence of initial surface roughness

been made with nitrogen primary ions where cone formation was again suppressed by an alteration in the chemical nature of the surface due to the presence of the nitrogen atoms [32]. Optimum resolution can therefore result from analysis of smooth amorphous targets. Interestingly, semiconductors tend to amorphise under ion bomdardment [105][36], reducing the likelihood of developing surface roughness.

The effects on measured resolution as a function of depth has been described in terms of a Sequential Layer Sputtering (**SLS**) [9] model which explains fundamentally, the development of surface roughness on the monolayer scale. This model assumes all other factors contributing to the development of surface roughening and depth resolution can be neglected

If one assumes that sputtered material originates from only the surface monolayer of atoms, then due to the random nature of the sputtering process, a fraction of the second layer will be exposed after primary beam incidence. At such points on the surface, the second layer then effectively becomes the surface monolayer. Under the same random process, a fraction of this second layer will be sputtered to reveal a new surface and so on (Figure 3.9).

The fraction of the exposed layer is a function of time and is known as the Free Fractional Surface. The distribution of the free fractional surface as a function of depth can be expressed in a good approximation by a Gaussian function if n, the number of layers involved, is relatively large [33]:

$$\Theta(z_i(t)) = \left(\frac{a}{2\pi \bar{z}}\right)^{1/2} \exp\left[-\frac{(z_i - \bar{z})^2}{2a\,\bar{z}}\right] \qquad (3.23)$$

where $\Theta(z_i(t))$ is the free fractional surface of the *i*th atomic layer, *a* is the monolayer thickness, and $\bar{z}$ the average sputtered depth [33].

Since the standard deviation of this function is

$$\sigma = (a\bar{z})^{1/2} \qquad (3.24)$$

the dependence of the depth resolution as a function of sputtered depth can now be derived from the resolution definition $\Delta z = 2\sigma$ as

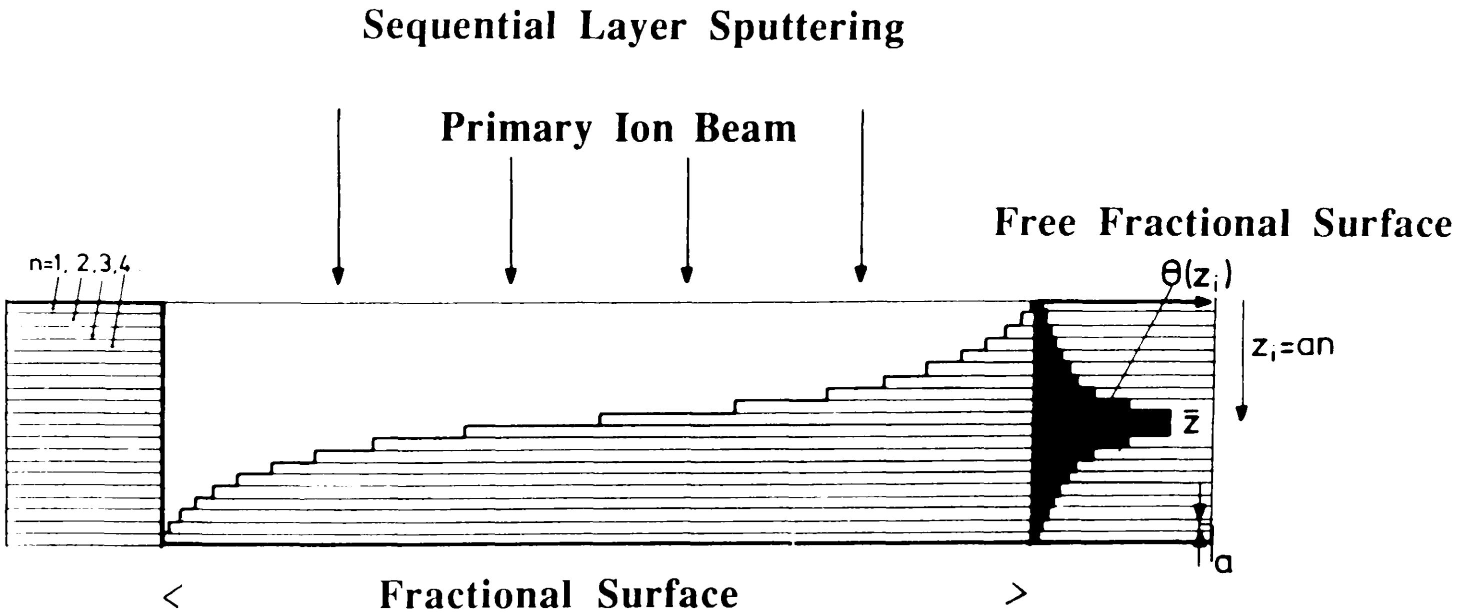
Sequential Layer Sputtering
Primary Ion Beam
Free Fractional Surface
n=1, 2,3,4
Θ(z_i)
z_i=an
z̄
a
< Fractional Surface >

Figure 3.9 Distribution of fractional free surface $\Theta(z_i)$ at depths z_i.[5]

$$\Delta z = 2(a\bar{z})^{1/2} \tag{3.25}$$

or the relative depth resolution

$$\frac{\Delta z}{z} = 2\left(\frac{a}{\bar{z}}\right)^{1/2} \tag{3.26}$$

Other assumptions made are that the sputter rate is constant throughout the sample and that all other sputtering effects such as ion induced effects at high primary energy [68], can be neglected.

Comparison with experimental results [33][34][38][37] have indicated the validity of the above model.

The above effects tend to be cumulative, and therefore at very large depths below the surface, the degree of mixing may be such that an alternative method of depth analysis, which does not rely on sputter erosion, may be more beneficial.

Dynamic Range

The dynamic range of a profile is defined as the maximum ratio of the measured concentration for a particular element I_{max} / I_{min}, I_{min} being the continuous background concentration (Figure 3.10).[9][67]

As with depth resolution, there are many factors affecting the dynamic range in profiling. Being mostly instumental in nature their effect can be minimised by the correct choice of experimental parameters and instrumental design.

Crater-Edge Effects.

With a static primary beam incident for long periods of time, the focussed spot may tend to drift slightly from its nominal position due to thermal or charging effects within the ion gun assembly. As a result, material outwith the desired analysis area contributes to the background of ions. This effect is of particular significance in the profiling of sharp concentration gradients resulting in a loss of resolution as well as dynamic range (Figure 3.11)[36][67].

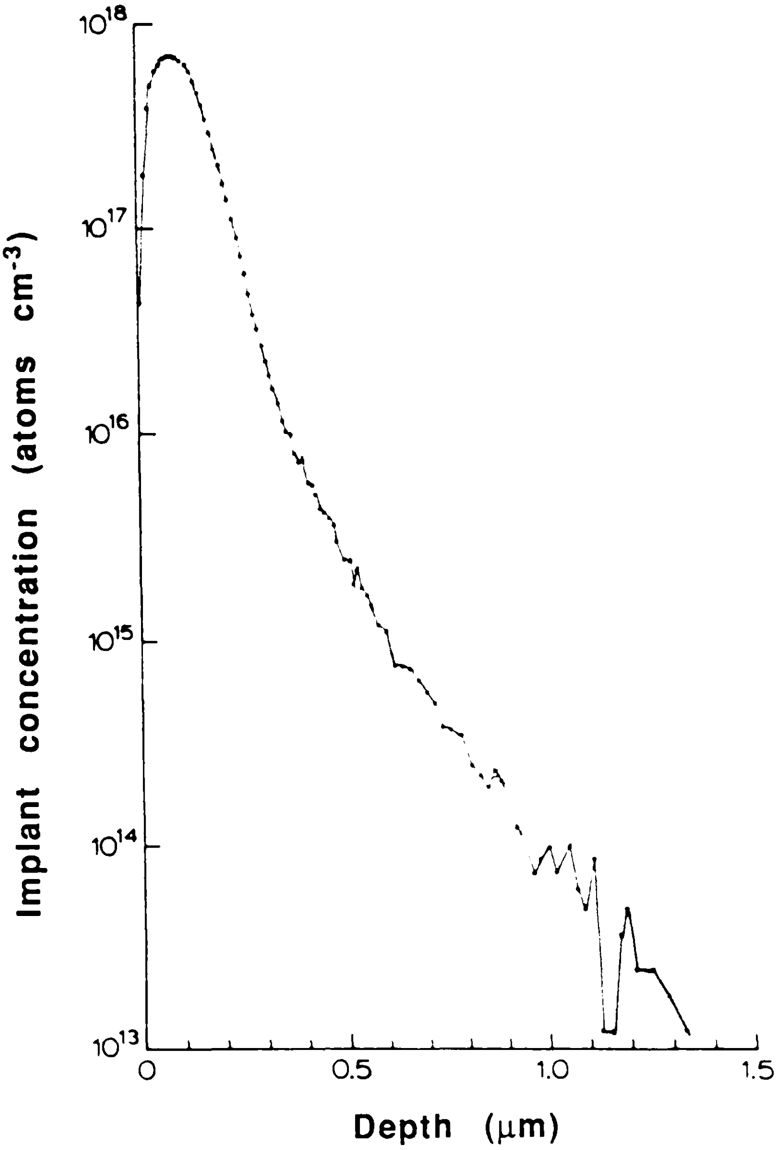

Figure 3.10 Typical SIMS implant profile showing a dynamic range of 5 orders of magnitude

Figure 3.11 Crater edge effects in sputter profiling

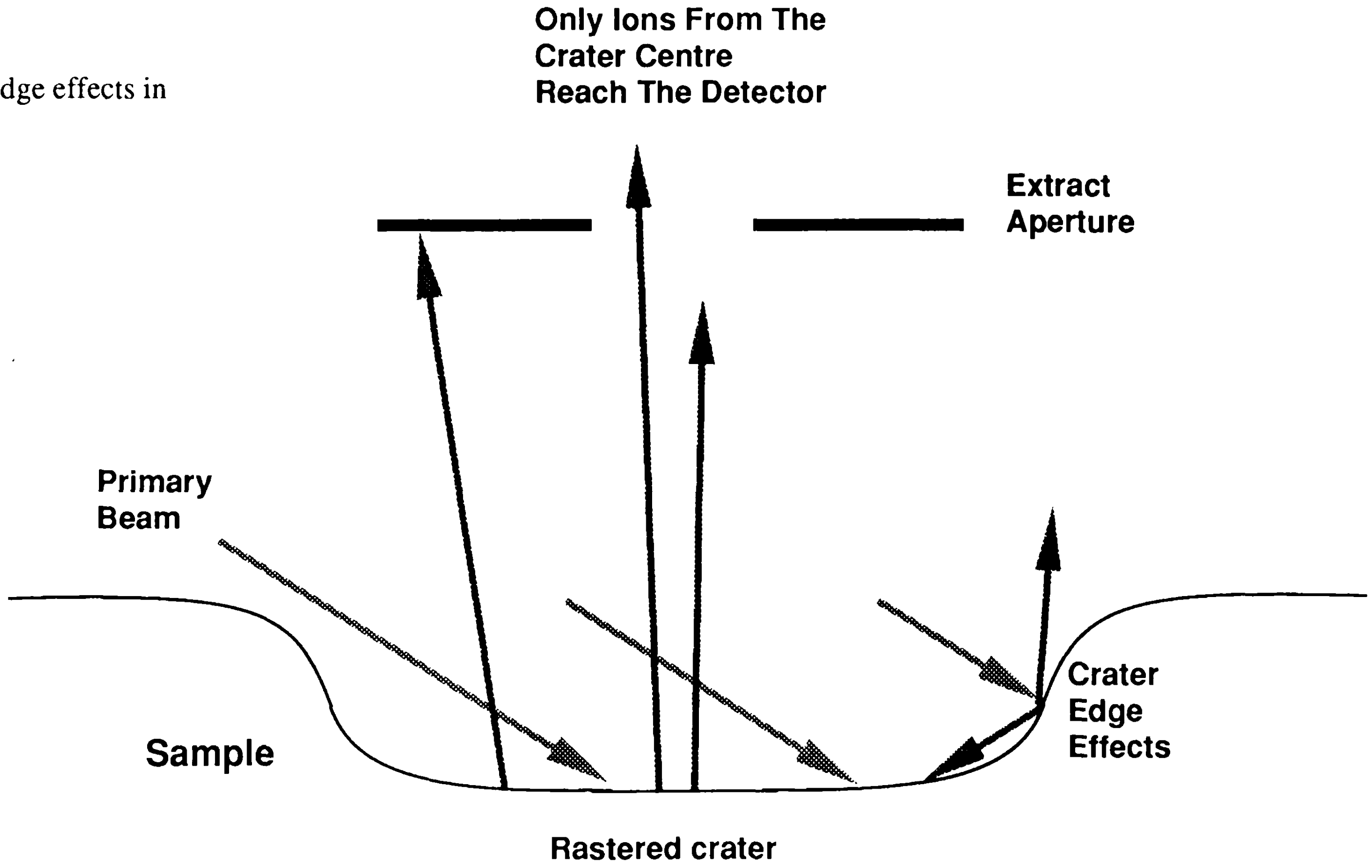
Only Ions From The
Crater Centre
Reach The Detector
Extract
Aperture
Primary
Beam
Sample
Crater
Edge
Effects
Rastered crater

Similar problems also arise due to the non-uniformity of the primary beam current. The radial current distribution of the primary beam is usually assumed to be Gaussian in form and the sputtered crater effectively reflects this in its shape. The implication of this is that material sputtered by the tails of the distribution, originate from layers closer to the surface (Figure 3.7).

Both of these effects can be reduced by increasing the sputtered crater via rastering of the primary beam over an area several times that of the focused beam spot. Analysis can then be performed on material originating from the flat central portion of the crater, by a restricted acceptance angle to the spectrometer, or electronic gating. Alternatively, it has been demonstrated, [104], that the measured profile may be analytically corrected for such edge-effects by using a standard interface to define the primary ion beam parameters.

Another serious crater-edge effect is the contribution due to the unfocussed neutral component of the primary beam [67], formed due to inefficient differential pumping of the ion gun, and alsodue to charge exchange processes within the gun assembly. This problem can usually be solved by placing deflection plates at the exit aperture of the ion gun and deflecting the ion beam onto the target, the neutral beam being undeviated (Figure 3.12).

Redeposition.

A different source of anomalous background is due to redeposition [98][67][35] onto the surface of previously sputtered material. These may be low energy neutrals, unaffected by the extraction field, which remain in the sample vicinity and are eventually re-adsorbed. Another so-called "memory" effect arises when material deposited locally to the sample and from ion optics is resputtered by high energy secondary particles and deposited onto the sample (Figure 3.13).

Residual Gas.

A major source of contamination is due to the adsorption rate of molecules from the ambient gas within the analysis chamber, onto the sample surface. This source of contamination may be neglected if the sputter rate and the residual pressure satisfy the relation [33][116][36]:

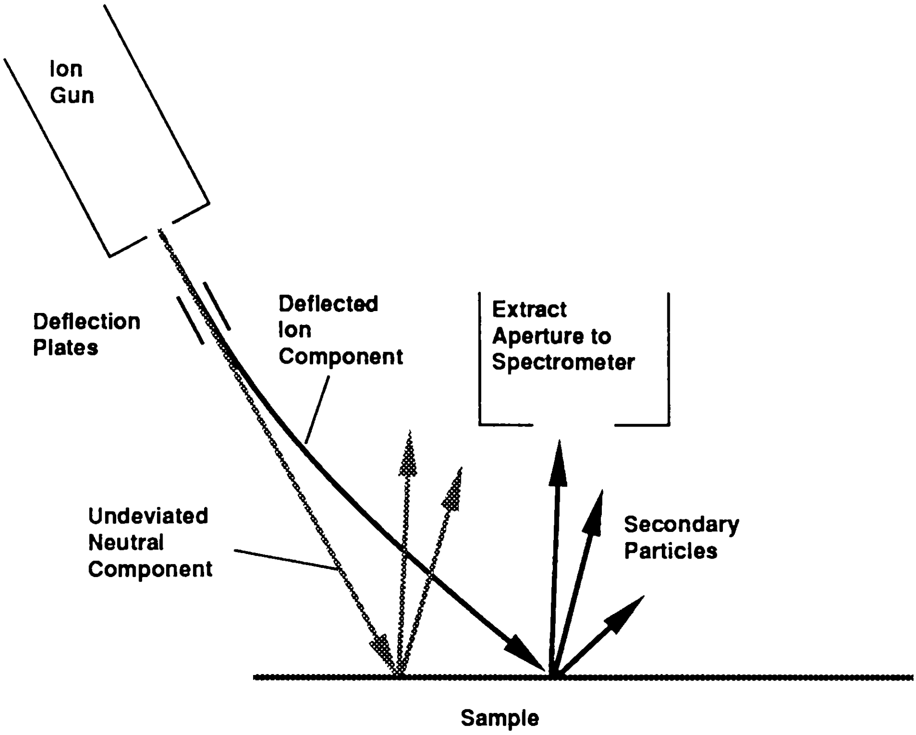
Ion
Gun
Deflection
Plates
Deflected
Ion
Component
Extract
Aperture to
Spectrometer
Undeviated
Neutral
Component
Secondary
Particles
Sample

Figure 3.12 Experimental correction for primary beam neutral component

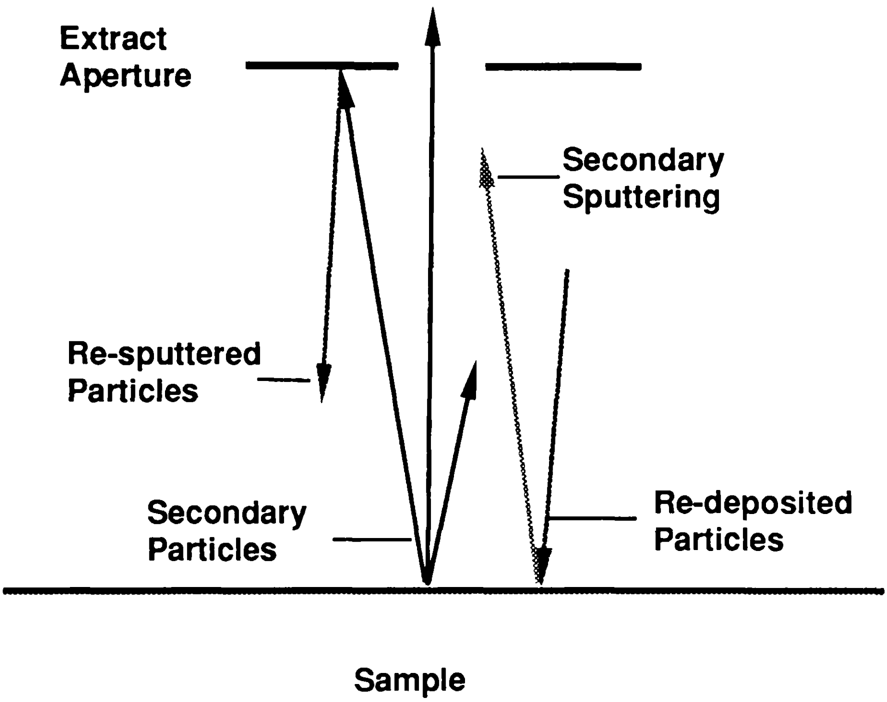
Extract
Aperture
Secondary
Sputtering
Re-sputtered
Particles
Secondary
Particles
Re-deposited
Particles
Sample

Figure 3.13 Redepostion (memory) effects in sputter analysis

$$j_P[\mu A / cm^2] / p_B[torr] \geq 10^8 \tag{3.27}$$

However, the increase in sputter rate may be detrimental to the depth resolution, hence UHV (<10-9 torr) conditions are preferable in order to retain the erosion rate at a desirable level and the effects of surface adsorption to a minimum.

Other contamination may arise from impurities in the primary beam, arising from contamination of the source region or the source material, being deposited onto and into the solid. For time of flight operation in particular, problems may arise when using a source element comprised of numerous isotopes, which in pulsed operation would result in multiple primary pulses, thus causing a broadening of the temporal distribution of secondary particles and a loss in mass resolution. Experimentally these problems can be dealt with by thorough outgassing of the source and incorporating mass filtering into the ion gun assembly.

Time of Flight Operation

In SIMS depth profiling, ion etching is performed continuously with ion currents accumulated over a defined counting time for each element as the mass range of the analyser is scanned. Each scan then corresponds to a point on the depth scale. The primary beam is normally rastered to improve sputtering uniformity, and gated electronically to ensure the detected secondary ions originate from the crater centre.

Depth analysis via AES is carried out by directing the electron beam at the centre of the crater during ion erosion. The peaks in the Auger energy spectrum can then be monitored as a function of time.

Because TOF analyses all masses simultaneously on each analysis cycle, under dc operation the detected signal will simply be a dc level which yields no mass information, hence a different procedure must be adopted for depth profiling, which involves pulsed ion production.

For TOF SIMS, this involves a pulsing (or blanking) of the primary ion beam with the ions impinging on the centre of a crater which has been etched by the gun operating in dc mode.

If laser post-ionisation is involved, a pulsed laser ensures time of flight separation of the ionised species. In this case, the gun may operate in either mode with the SIMS ions contributing to the ion background (unless removed by some separate means). In continuous mode the laser is fired to coincide with the rastering beam passing over the central portion of the crater, in order to reduce crater-edge effects. However, with respect to a line of sight detector, the continuous incidence of secondary ions can lead to serious contamination of the device, and hence a reduction in performance and useful lifetime.

This problem can be alleviated by pulsing the primary beam, during data acquisition. Optimum temporal and spatial overlap of the laser pulse with the secondary particles ensures maximum sensitivity. Due to this switching of gun modes, extra care must be taken, particularly with very thin layers, to ensure the etched depth between data points is less then the smallest structure to be resolved.

If the ion pulse length is very short, the damage to the crater floor is minimised, and dynamic range can be improved by accumulation of data over a number of pulses.

Comparison of Performance in Depth Analysis.

In depth analysis, the performance of any technique relying on ion erosion is determined by the factors described above. Such is the case with SIMS, AES and methods involving post-ionisation such as RIMS.

The following comparison will be confined to SIMS and AES, both widely adopted depth profiling techniques relying on sputter erosion, but different in the respect of the information carrying particle, and their relative performances with respect to sensitivity and quantification.

If it were the case that the information derived from the various techniques was identical then the same could be said of their relative performances. However, optimum performance of the individual processes depends on necessary conditions, rather than the most desirable.

In comparison with SIMS, the useful information in AES is not derived from the sputtered material, therefore a reduction in the sputter rate should not influence the overall sensitivity. This may be achieved either by a reduction in the primary source intensity or by lowering the primary ion energy which, more importantly, results in a drop in the degree of atomic mixing. Such variation in experimental conditions may contribute to an improvement in the overall depth resolution, although the fundamental limiting factor to AES is the information depth of the Auger electrons.

The degree of information derived from SIMS analysis depends on the total primary ion flux, hence a reduction in the ion energy, without a variation in other parameters, such as the source gas pressure and ionisation efficiency, reduces the information available. Also being prone to surface contamination, the sputter rate must be maintained at a suitable level.

Typical primary ion energies used in SIMS (~5 keV), result in ion ranges within the target of the order of 100 Å which would have the effect, in the case of AES analysis, of a contribution to the degradation in depth resolution more significant than the contribution due to the information depth of the Auger electrons. High depth resolution AES therefore employs ion energies ≤ 1 keV for layer erosion in order that the contribution from the ion-solid interaction is of minor importance. As already mentioned, SIMS operated at such low energy would most likely experience an increased component of surface contamination.

A further effect to be considered when using beams of such low energy, is the relative effect on the ion trajectories of the extraction potentials present. Obviously the preferred high voltages for high ion extraction efficiency will be unsuitable, again reducing the overall sensitivity in SIMS. Extraction of electrons on the other hand, being of much lower mass can still be maintained with lower potentials on the electrodes.

In general, the attainable depth resolution is decided by the required sensitivity. Both SIMS and AES are capable of a resolution down to the nanometre range, while SIMS itself, under the most ideal experimental conditions (extremely low residual gas pressure and primary beam energy), and a reduction in the dynamic range may exhibit a slight improvement.

In applying methods of post-ionisation to depth profiling, the optimum resolution is limited by the same fundamental physical and instrumental artefacts encountered in SIMS. However, if the method of ionisation of the neutral material is highly efficient, there should be a resulting increase in the dynamic range over that obtainable via SIMS. Ful-filling this requirement is RIS with the added benefits of atomic selectivity, and without the matrix problems of SIMS.

Chapter 4.

Instrumentation.

Introduction

Much of the early work in applying RIS to spectroscopy and trace analysis, and indeed many of the present investigations, centred on the analysis of gas phase samples. Experimental arrangements involved the use of thermal ovens for the generation of atomic beams intercepted by the lasers. Other experiments have utilised the high vapour pressures of some materials, e.g. Caesium and Rubidium [58], in proportional counter studies.

For analysis of solid samples with particular application to structural determination, generally more complex apparatus is required due to the necessity for sample vapourisation, and the presence of surface contamination. Also, the requirements for stability and reproducibility of experimental conditions over prolonged analysis times impose further restrictions on the equipment used.

The following sections, describe in detail the major components of the apparatus used, many of which had to be designed and built by the author to meet the particular requirements of the experiments performed. Other elements, such as the laser system are commercially available and required little in the way of development.

Mass Spectrometer

The decision to use a time of flight (TOF) mass spectrometer was a consequence of the complementary modes of operation of TOF and of the pulsed lasers normally used in RIS, with the added advantage of the simplicity and cheapness of construction, with its performance not reliant on low tolerance manufacturing, but rather a careful choice of operational parameters [119], and the high ion transmission efficiencies attainable. TOF also allows a complete mass spectrum per pulse as opposed to rf or magnetic based systems which require tuning of the parameters to a particular mass.

The principle of the Time Of Flight is essentially quite simple. Ions generated at the sample surface are imparted with approximately equal energies by an accelerating electric field, which ejects them into a field free region where the ions are separated in time according to their mass (m) and charge (q), and subsequently detected by an ion detector. The time of flight t of a particular ion of mass m can be determined from a simple energy conservation consideration and is given by the expression:

$$t = \sqrt{\frac{md^2}{2qV}} \qquad (4.1)$$

where V is the accelerating potential and d the distance travelled by the ions.

The main disadvantage of TOF lies in its limited mass resolution, i.e. its ability to separate different masses, which in the case of a simple linear flight path, of length at most a few metres, is at best ~50 to 100.

Mass resolution $m/\Delta m = t/(2\Delta t)$ is defined as the mass at which the spread of the temporal distribution of particles arriving at the detector is equal to the difference in flight time of consecutive masses. Often, the resolution is defined relative to a particular mass as simply the ratio of the flight time to the peak width. Alternatively, the absolute resolution may be calculated for the system from the measured temporal separation of known masses. However, the specified resolution is dependent on the choice of measured width.

In the case of mass peaks of similar intensity a reasonable choice of width would be that of Full Width at Half Maximum (FWHM), in which case the resolution could be expressed as (see AppendixA):

$$R = m = \frac{n^2}{4\left(\sqrt{m_2} - \sqrt{m_1}\right)^2} \qquad (4.2)$$

where m_1 and m_2 are the known masses and n is the number of measured widths separating the two.

However, a system with a mass resolution defined in such a manner may be ineffective when attempting to resolve a low intensity mass peak obscured by the tails in the distributions of those of neighbouring mass. For this reason the resolution is commonly defined relative to the measured width at 10% maximum.

The expression for the absolute resolution may be retained with the value n replaced by that corresponding to the revised width definition.

In the spectrometer sample region, the generated ions have finite initial spatial, temporal and energy distributions, which are the major factors contributing to the limitation of the ultimate mass resolution.

The spatial contribution arises from the variation in time of flight (corresponding to a variation in path length) for ions produced at different points in the sample region.

When applied to laser post-ionisation of material ablated from a surface, the initial spatial distribution is defined by the volume of overlap between the sputtered particles and the interacting laser, together with the angular acceptance of ions by the extract electrodes. Under such circumstances, the temporal distribution is not a serious problem since for short laser pulses of the order of a few nanosecond s in duration, the relatively slow particles are effectively frozen within the interaction volume, and therefore formation of all ions is effectively simultaneous.

Particles sputtered from a surface are generally considered to follow a cosine distribution in their propagation from the sample surface. The variation in the velocity component, normal to the surface and along the spectrometer axis determines the energy resolution of the system. Further broadening of the energy spread may result from collisional and electrostatic effects within the ablated plume.

In order to minimise the aforementioned effects, suitable experimental parameters must be adopted.

Once again, with respect to laser post-ionisation, the simplest method of reducing the effect of the initial spatial distribution is to reduce the beam diameter of the ionising laser by suitable focusing. Unfortunately, this tends to reduce the number of ions available for analysis, and hence a suitable balance must be reached between improved mass resolving power and maximum sensitivity. Alternatively, the angular acceptance of the ion optical assembly may be reduced with the disadvantage of lower spectrometer transmission.

The energy resolution is limited by the initial energy spread of the atoms, prior to ionisation, relative to the accelerating potential. The normal solution is therefore to increase the accelerating voltage such that the initial energy distribution is negligible compared to the average kinetic energy of the ions. This also serves to improve the transmission efficiency of the spectrometer. Unfortunately, the existence of such high fields in the interaction region has an undesirable effect on processes involving ion ablation, namely deflection of the primary beam. This leads to a need to use primary ions of a much greater energy which may have a detrimental effect on the analysis.

In conclusion, the various pros and cons of spectrometer operation must be weighed up in order to determine the optimum parameters applicable to a particular experiment.

The spectrometer used comprised a total flight path of approximately 1.2 m from sample to detector. The accelerating potential was variable over a large range, although typically between 200 and 1000 volts, and was applied directly to the sample stub. Ion extraction and collimation was accomplished by a series of electrodes positioned close to the sample surface. The ion detector was a Thorn EMI 9642/3 18 dynode electron multiplier biased ~ -3 kV for positive ion detection, and was mounted on axis with the ion optics.

Vacuum System

In order to restrict mass background effects, from such origins as secondary ion emission of surface adsorbed residual gas molecules in the chamber, whether at the sample surface or at the detector, analysis must be carried out under Ultra High Vacuum (UHV) conditions. To this end, a vacuum system was designed and built 'in-house' capable of producing conditions below 10^{-9} mbar.

The analysis chamber was of standard tubular construction with the necessary ports for laser entry and time of flight as well as sample loading, perpendicular to the cylinder axis (Figure 4.1). The top flange comprised a port for the sample manipulator and the necessary electrical feedthroughs for the accelerating potential and the ion optical assembly. The lower flange comprised the main pumping port and the angled ion gun port. A secondary chamber was added at a later stage to house the additional equipment required for improved UHV operation (Figure 4.2). Due to the limited number of available ports, viewing of the interior was restricted to the laser windows.

To maintain the integrity of the vacuum for long periods of time, an airlock was incorporated to facilitate rapid sample introduction and removal. This entry chamber

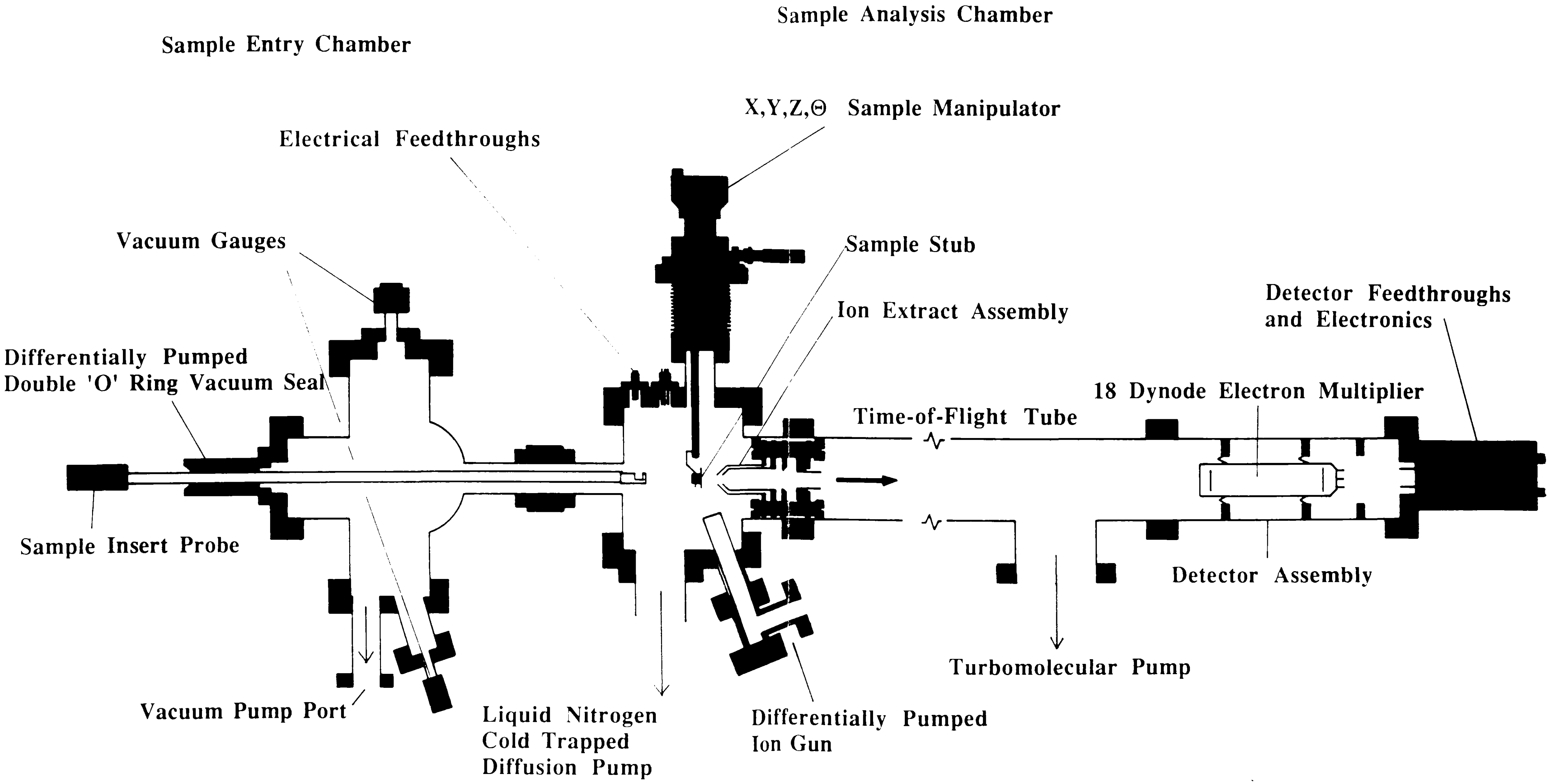
Sample Analysis Chamber
Sample Entry Chamber
X,Y,Z,Θ Sample Manipulator
Electrical Feedthroughs
Vacuum Gauges
Sample Stub
Ion Extract Assembly
Detector Feedthroughs
and Electronics
Differentially Pumped
Double 'O' Ring Vacuum Seal
18 Dynode Electron Multiplier
Time-of-Flight Tube
Sample Insert Probe
Detector Assembly
Turbomolecular Pump
Vacuum Pump Port
Liquid Nitrogen
Cold Trapped
Diffusion Pump
Differentially Pumped
Ion Gun

Figure 4.1 Side Elevation

Laser Mass Spectrometer

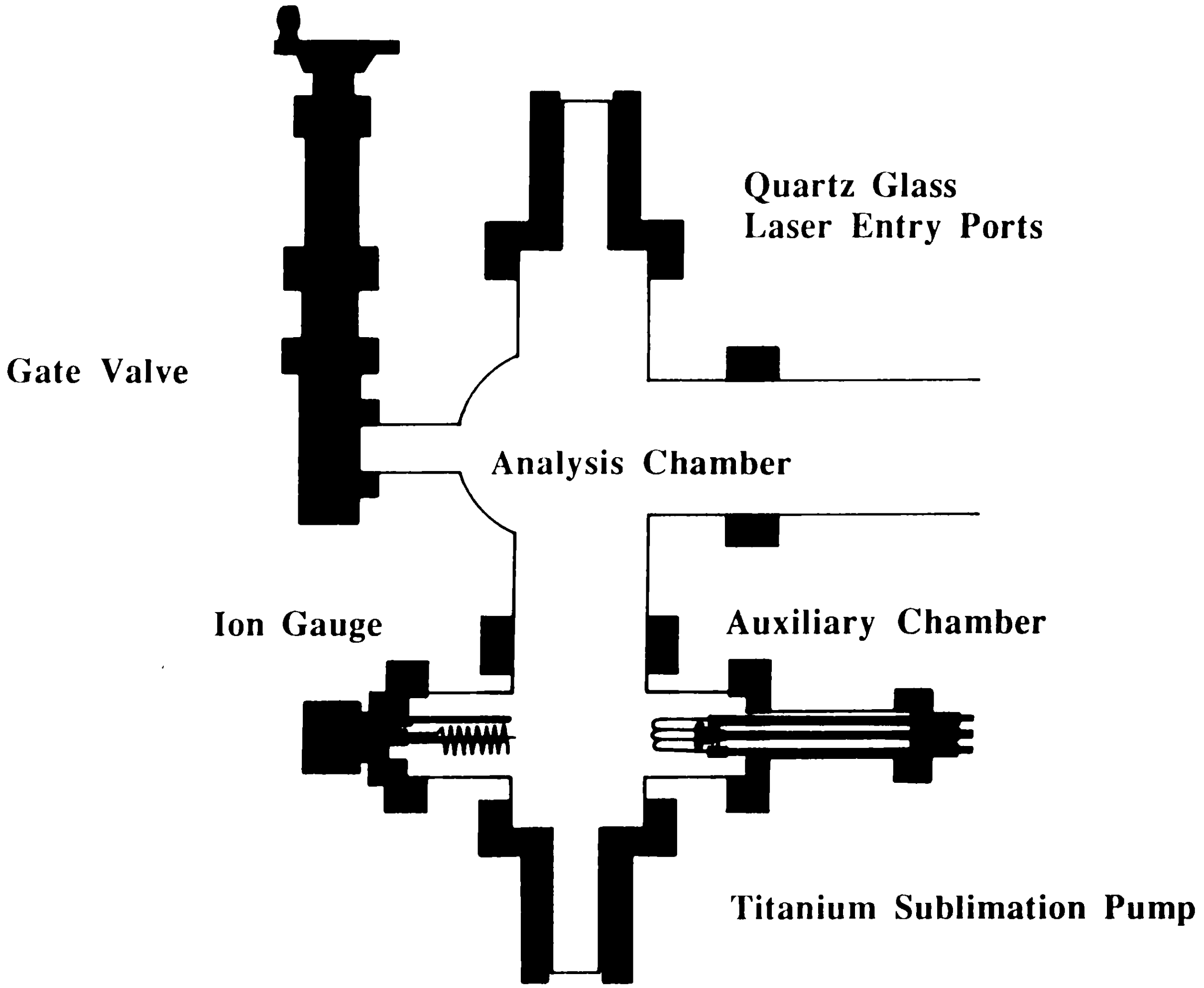
Quartz Glass
Laser Entry Ports
Gate Valve
Analysis Chamber
Ion Gauge
Auxiliary Chamber
Titanium Sublimation Pump

Figure 4.2 Plan view, showing the analysis chamber only, of the laser mass spectrometer.

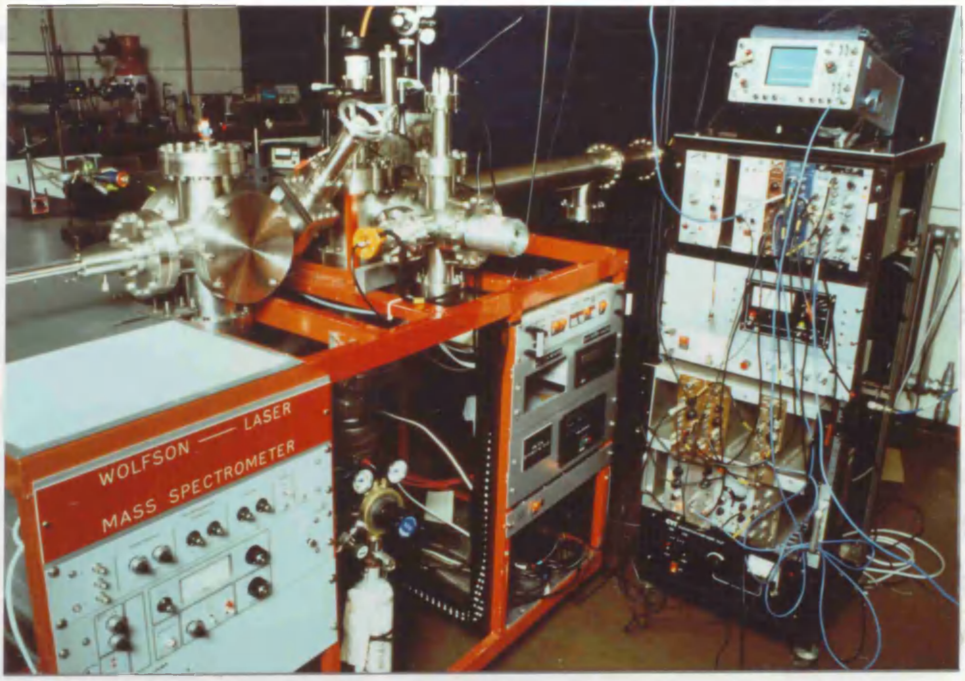
WOLFSON —— LASER
MASS SPECTROMETER

Figure 4.3 The photographs show the laboratory arrangement of the spectrometer, complete with electronics.

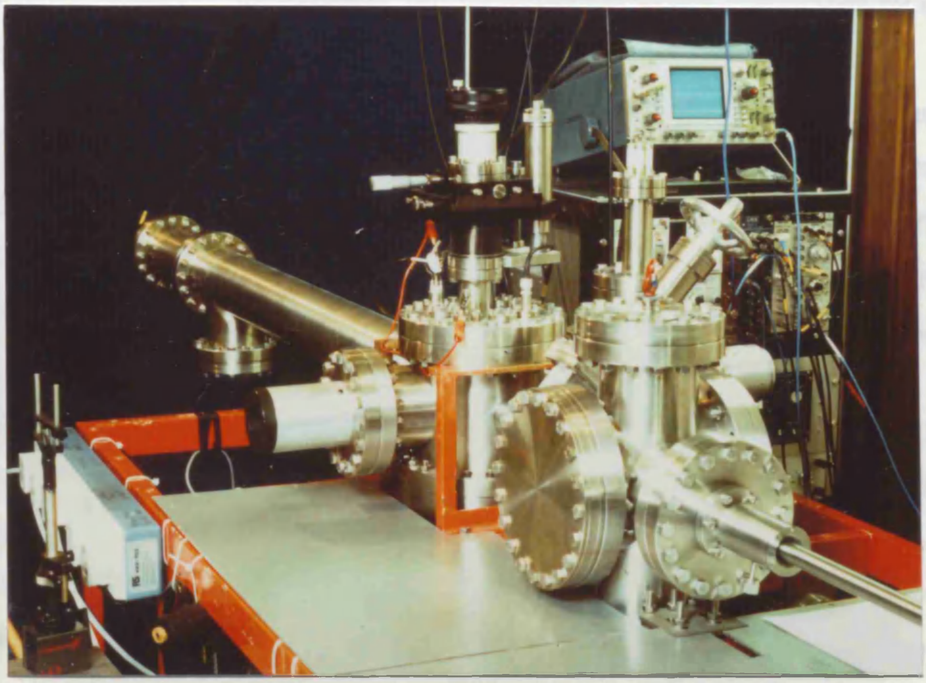

was of a similar construction the analysis chamber and was connected via a 'viton' sealed, manually operated gate valve. Samples were loaded through a viton sealed door.

To improve the ease of use of the system, particularly during the sample loading and transfer procedures, and to prevent any problems occurring due to undesir able changes in backing pressure, the various pumps could be isolated effectively from the each other and the chambers by solenoid operated vacuum valves controlled from a central switch panel.

All UHV surfaces were of high quality stainless steel. All flanges were of the standard UHV compatible 'Conflat' type. The main chambers were also routinely baked to ~ 150^0 C externally to enhance the removal of water and molecules of high sticking coefficient, by evaporation from the interior walls. (Figure 4.3 shows two photographs of the apparatus)

Pumping was affected by an oil diffusion pump (Edwards Diffstak 63/150M 135 litres per second), mounted below the main analysis chamber. This was preceded by a liquid nitrogen cold trap to restrict the backflow of oil vapour from the pump and to enhance the removal of moisture via condensation on the cold internal surfaces. In order that the liquid nitrogen level was maintained at all times above 50 percent maximum, an automatic transfer system was required (Figure 4.4). Nitrogen gas was used to pressurise the liquid nitrogen reservoir to 5 psi above atmosphere. This was sufficient to force liquid flow through a narrow thermally insulated feed line to the trap. Gas flow to the reservoir was governed by a solenoid valve, controlled by a programmable electronic timer.

Due to the restricting apertures of the ion optical assembly, the flight tube was differentially pumped by a turbomolecular pump (Balzers TPU 050 50 litres per second). For improved UHV conditions, a supplementary titanium sublimation pump (CVT) was included in the main chamber extension. The entry lock was evacuated by a second turbo pump, yielding pressures of typically 10^{-7} to 10^{-6} mbar. In all cases, backing was provided by rotary pumps.

Pressure in the analysis chamber was monitored by a Leybold Ionivac IM 210 ion gauge, with a pressure range of 10^{-2} to 10^{-10} mbar. For the entry lock, a pirani gauge and a penning gauge were adequate (both Edwards).

Sample transfer was achieved using a sliding probe inserted in a differentially pumped double 'o' ring seal (VSW). The seal was evacuated by an independent rotary

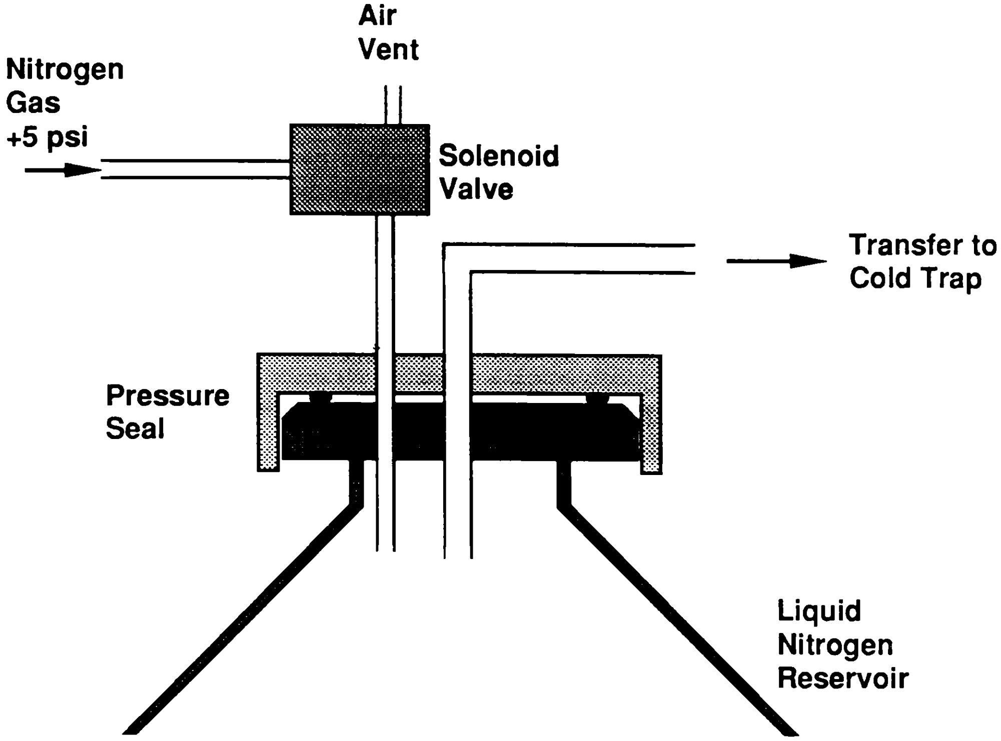
Air
Vent
Nitrogen
Gas
+5 psi
Solenoid
Valve
Transfer to
Cold Trap
Pressure
Seal
Liquid
Nitrogen
Reservoir

Figure 4.4 Liquid nitrogen reservoir and transfer system to cold trap

pump. During transfer the seal was capable of supporting a pressure differential of the order of 10^{-8} mbar to atmosphere.

The stainless steel sample stubs were held in identical spring loaded forks (Figure 4.5) on the transfer probe and on a sample manipulator (VSW) offering tri-axial positioning plus rotation. The sample fork was electrically insulated from the manipulator to allow use of the stub as the accelerating electrode.

The detector assembly was of a ring type construction and was mounted on the end flange of the flight tube for ease of removal and detector replacement. The multiplier itself was held between the rings on leaf springs to reduce the risk of shock damage to the detector or its glass casing. All electrical conections were made to the same end flange.

Laser entry and exit was permitted via 35mm diameter planar quartz glass windows perpendicular to the spectrometer axis.

Ion Optics.

The ion extraction system was designed to be simple in construction with the minimum of optical elements to limit the number of instrumental variables. At the same time there was desire for versatility in the design if the need arose for additional and/or more sophisticated elements to be incorporated, or the possibility of transfer to an alternative analysis chamber. For these reasons a modular approach was adopted.

The basis of the optical mount is simply a pair of stainless steel rings of variable separation which were machined to fit snugly within the flight tube. These rings then support all the optical elements of a similar ring construction. Suitable electrical insulation is provided by ceramic spacers (Figure 4.6).

The assembly comprises two concentric conical electrodes for field shaping and extraction with a further ring electrode to improve collimation. The secondary ions are then steered onto the detector window by a set of XY deflector plates (Figure 4.7).

Under a static extraction field, there is no distinction made between ions created by different means unless their production is temporally and spatially separable. As an example, under the action of an ablating primary ion beam, secondary ions are liberated by the sputtering mechanism and/or may also be generated by post-ionisation of the sputtered neutral particles at a different position and at a later time.

For a pulsed primary ion beam, the ablated material propagates outward from

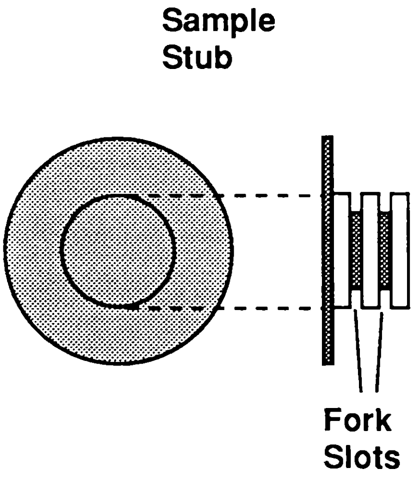
Sample
Stub
Fork
Slots

Figure 4.5 Scale diagrams of the sample stub and the sample forks. The forks are translated perpendicular to each other and are each accomodated in a slot in the stub.

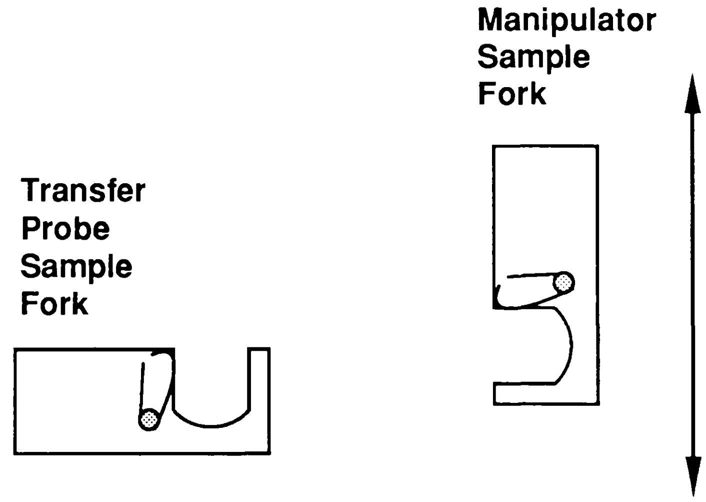
Manipulator
Sample
Fork
Transfer
Probe
Sample
Fork

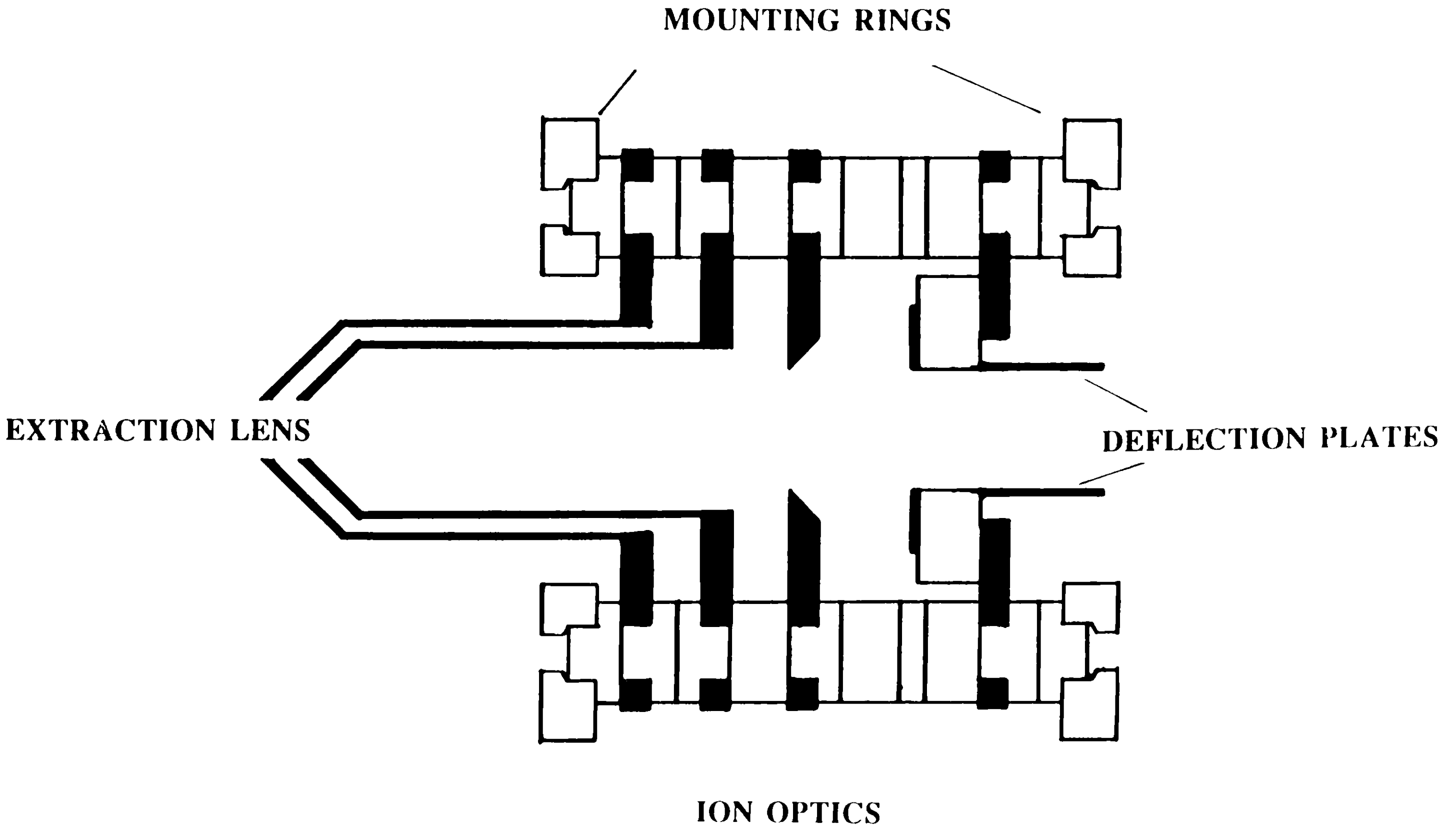
MOUNTING RINGS
EXTRACTION LENS
DEFLECTION PLATES
ION OPTICS

Figure 4.6 ion extract assembly for time of flight mass spectrometer

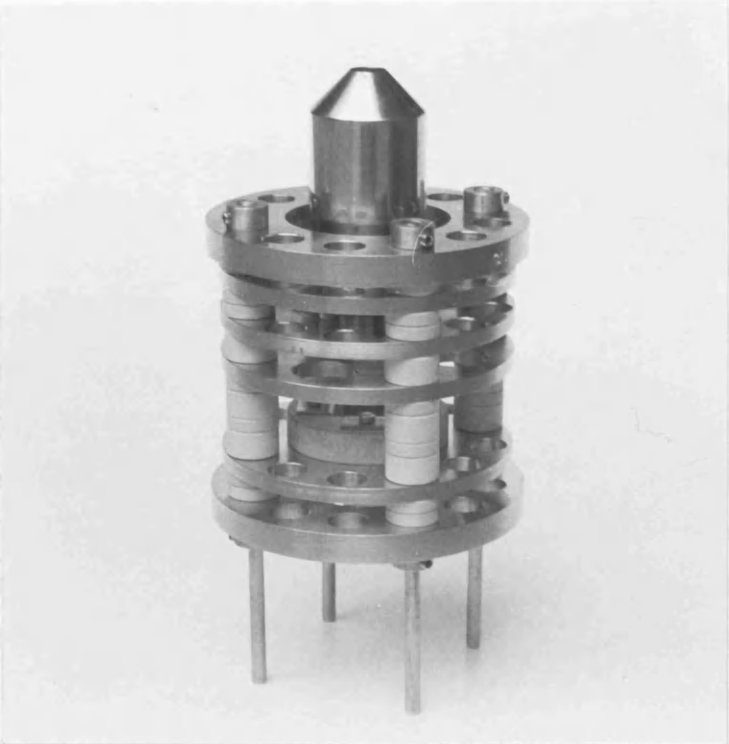

Figure 4.7 Two views of the ion extract assembly: note the incorporation of extra holes to permit improved pumping efficiency.

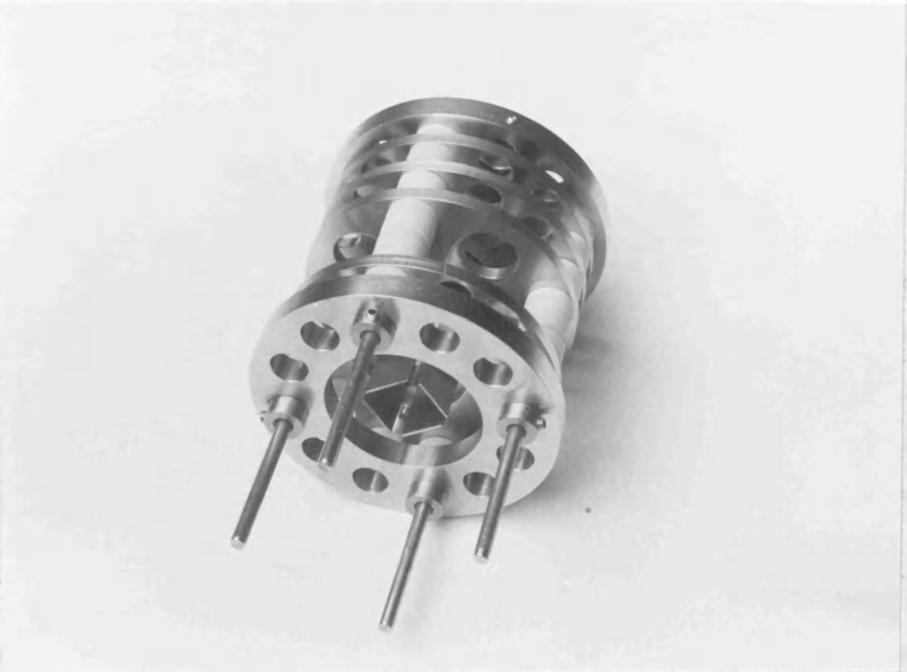

the surface in a wavefront with a time spread defined by the pulse duration and the kinetic energy distribution of the secondary particles. The ion component is immediately influenced by the local fields and accelerated from the proximity of the sample. The remaining neutral component may then be post-ionised at later time.

The ability to resolve the individual ionic components at the detector imposes several major requirements on the ion gun performance, the experimental geometry and the timing sequence of various pulsed mechanisms.

Since the secondary particle density is highest at the sample it is desirable to perform the post-ionisation (e.g. by laser) as close to the sample surface as is permitted without interacting with the sample lattice itself. Also for maximum sensitivity, the ionising pulse should overlap the peak in the secondary particle pulse density. If the pulse length is sufficiently short, the faster secondary ions (under the influence of an external field) and the neutral component will be separated in space and subsequently resolved at the detector. If this condition cannot be satisfied it may be necessary to sacrifice sensitivity for the sake of resolution by delaying the ionising pulse to coincide with the edge of the particle pulse.

However, if the primary ion pulse length is long in comparison to the transit time of the particles across the interaction region, the degree of overlap of the ion and neutral components will always be significant, resulting in a secondary ion superposition on the laser induced signal.

The primary ion gun used throughout these experiments was incapable of producing ion pulses of duration less than about 3 μs. This is considerably longer than the transit times of the particles between the sample and the first electrode which are typically 0.2 μs for the neutral particles and perhaps a factor of ten shorter for the ions.

Methods of secondary ion removal involve the use of high voltage fast pulsed deflection systems, to divert the path of the secondary ions from the acceptance window of the extraction system prior to post-ionisation of the remaining neutrals, or incorporate energy filtering into the mass spectrometer arrangement [52]. This only adds complexity to the procedure due to the necessary inclusion of additional electronics for pulse generation and timing.

It would therefore be of benefit if an alternative method of secondary ion suppression could be devised which operated under static field conditions and was reliant only on the physical shape of the electrodes and the electrostatic geometry. Such an approach has indeed been devised, and has been adopted with some success. This will be discussed in a subsequent chapter.

Sample Vapo risation.

In order for resonant ionisation to be performed, the sample must be in the vapour phase. For solid samples this is usually achieved by ion bombardment (ion sputtering) or by the action of an ablating laser. The main method employed during the course of these experiments was that of ion sputtering. The physical principles of both ion and laser sputtering will be explained in detail at a later stage.

Sputtering was performed throughout by a focused beam of Krypton ions. The ion gun (Kratos Macrobeam)(Figure 4.8) was capable of ion production up to 5 eV in beam currents of at most 20 μA. The geometry of the vacuum system is such that the ion gun axis is at an angle of approximately 67^0 to the spectrometer axis, and therefore the sample normal. However, under typical extract field conditions, this is not the case with regard to the primary ion beam. The spot size was approximately 1mm at normal incidence, and is therefore essentially elliptical in normal use. A raster facility was available for sample surface etching which operates by superimposing triangular waveforms on the ion gun X-Y positioning plates. The gun also required to be differentially pumped in order to reduce the flow of non-ionised gas into the analysis chamber, in this case by a turbomolecular pump (Balzers TPU 050).

The ion source is of the Extractor Source type, which is basically a modification of the hot-cathode ionisation gauge. In normal continuous operation, the atoms of the source gas are bombarded by a continuous stream of electrons. These originate at a circular filament which surrounds the cylindrical grid into which the source gas flows (Figure 4.9). The electrons are accelerated by a relatively positive potential on the source grid. They are then sufficiently energetic to strip weakly bound outer electrons from the atoms comprising the source gas, within the plane of the cathode. Multiple passes of the electrons through the source grid are possible due to the repelling action of the source repeller or can which is at the same potential as the cathode. The positive ions thus created, are then extracted from the source region by an extraction electrode, collimated and focused by a double 'Einzel' lens and collimating aperture within the gun column. Using this type of source, the ion current produced can be continuously

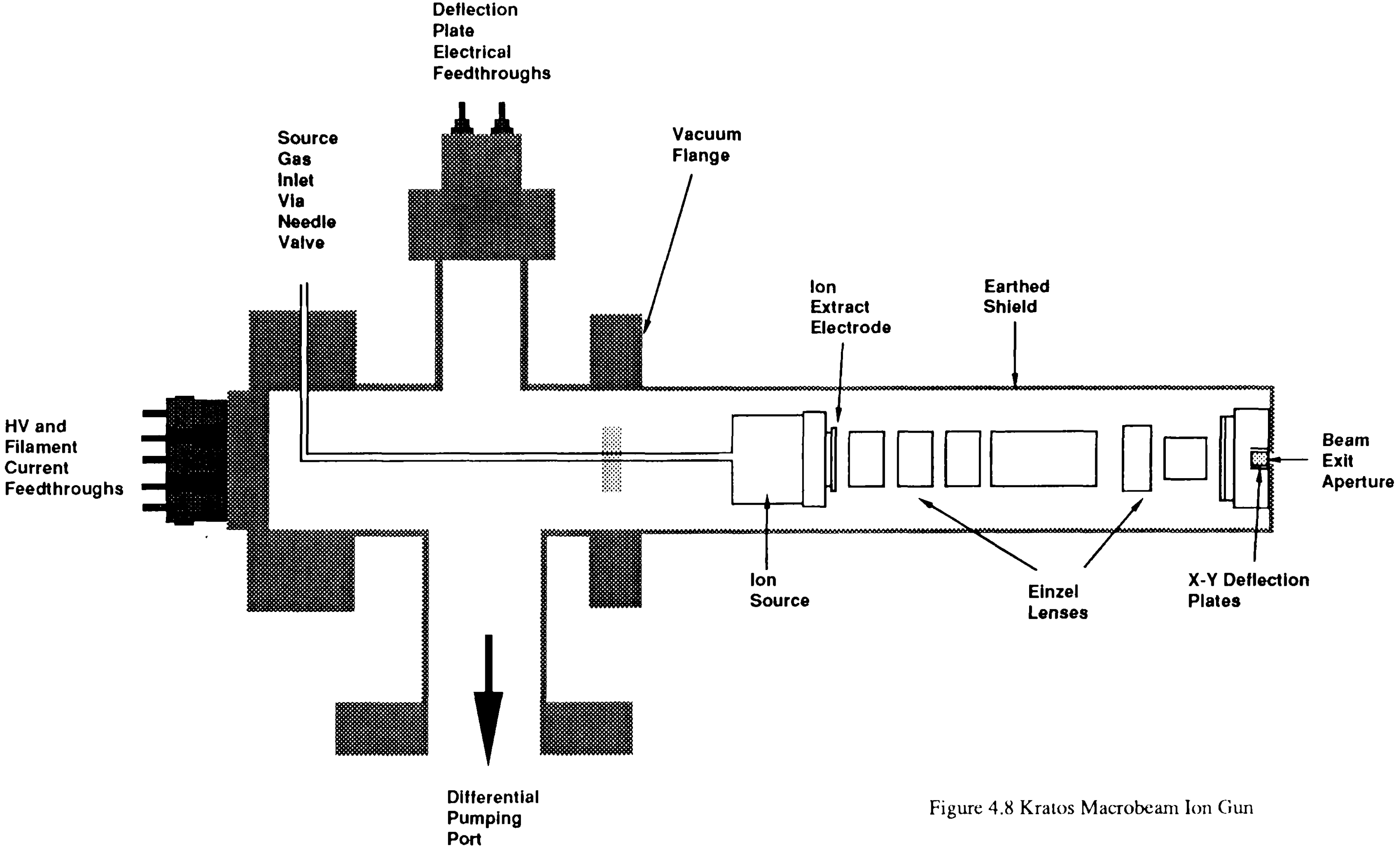
Deflection Plate Electrical Feedthroughs
Source Gas Inlet Via Needle Valve
Vacuum Flange
Ion Extract Electrode
Earthed Shield
HV and Filament Current Feedthroughs
Beam Exit Aperture
Ion Source
Einzel Lenses
X-Y Deflection Plates
Differential Pumping Port

Figure 4.8 Kratos Macrobeam Ion Gun

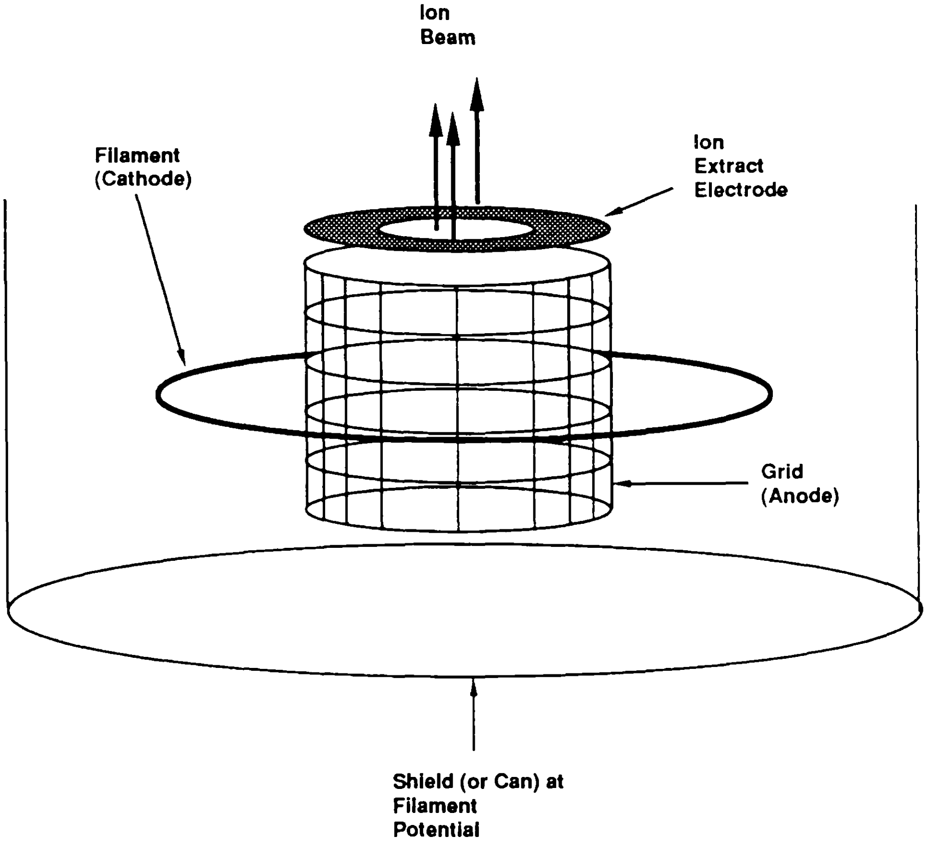
Ion
Beam
Filament
(Cathode)
Ion
Extract
Electrode
Grid
(Anode)
Shield (or Can) at
Filament
Potential

Figure 4.9 Magnified view of the ion source within the gun assembly. Ions created at the filament are accelerated towards the grid by a positive potential. Ionisation is achieved via electron impact.

varied over many orders of magnitude by suitable variation in the source gas pressure and/or the cathode emission current.

Although the gun was designed for continuous operation, it was adapted to offer the alternative of a limited pulsed mode for time of flight operation. If the source grid potential is held negative with respect to the filament, the flow of electrons is halted. If then a large positive potential is applied to the grid, this potential barrier is removed for the period of the pulse resulting in the creation of ions in a narrowly defined temporal distribution. The electronics (Figure 4.10) produce a positive pulse ~300 volts and 300 ns wide. Ion pulses created by this method were a few microseconds in duration due to the spatial extent of the ion source and collisional and electrostatic effects in the column. The advantage of running in this mode is that the contribution to the background pressure and ion detection from secondary neutrals and ions is noticeably reduced as well as consumption of the sample surface layers. Operating in this mode, however, resulted in significantly lower beam currents (a factor of ten or more)(Figure 4.11) for particular gun parameters.

The ion beam profile was investigated with the use of a test target consisting of a pair of parallel nickel wires fixed 2mm apart, electrically insulated from the surrounding areas and mounted on a single axis translation stage within the vacuun system (Figure 4.12). The ion gun was then normally incident, onto the target at a distance of 2.5cm, inducing a current flow in the wires which was subsequently measured by a digital nano-ammeter (Keithley 106). With the ion beam static (i.e. no raster), the target was translated perpendicular to the ion stream. Due to the small dimension of the wires (~0.1 mm) relative to the specified beam diameter, at any time only a small fraction of the total number of ions within the beam were incident on the target wires and hence the variation in measured current with the target translation, was a representation of the true radial distribution of ions within the beam, with a resolution defined by the wire dimension.

As can be seen (Figure 4.13) the wires are clearly resolved. The current distribution is close to symmetric with the expected separation of 2mm which is an indication of the accuracy of this experimental procedure.

The manufacturers specification is for a Gaussian beam profile. However, the measured profile is broader in the wings than a typical Gaussian distribution. This dispersion may be a consequence of energy loss in the wings from collisions with the edges of the ion gun exit aperture. Such an energy loss results in the ions becoming

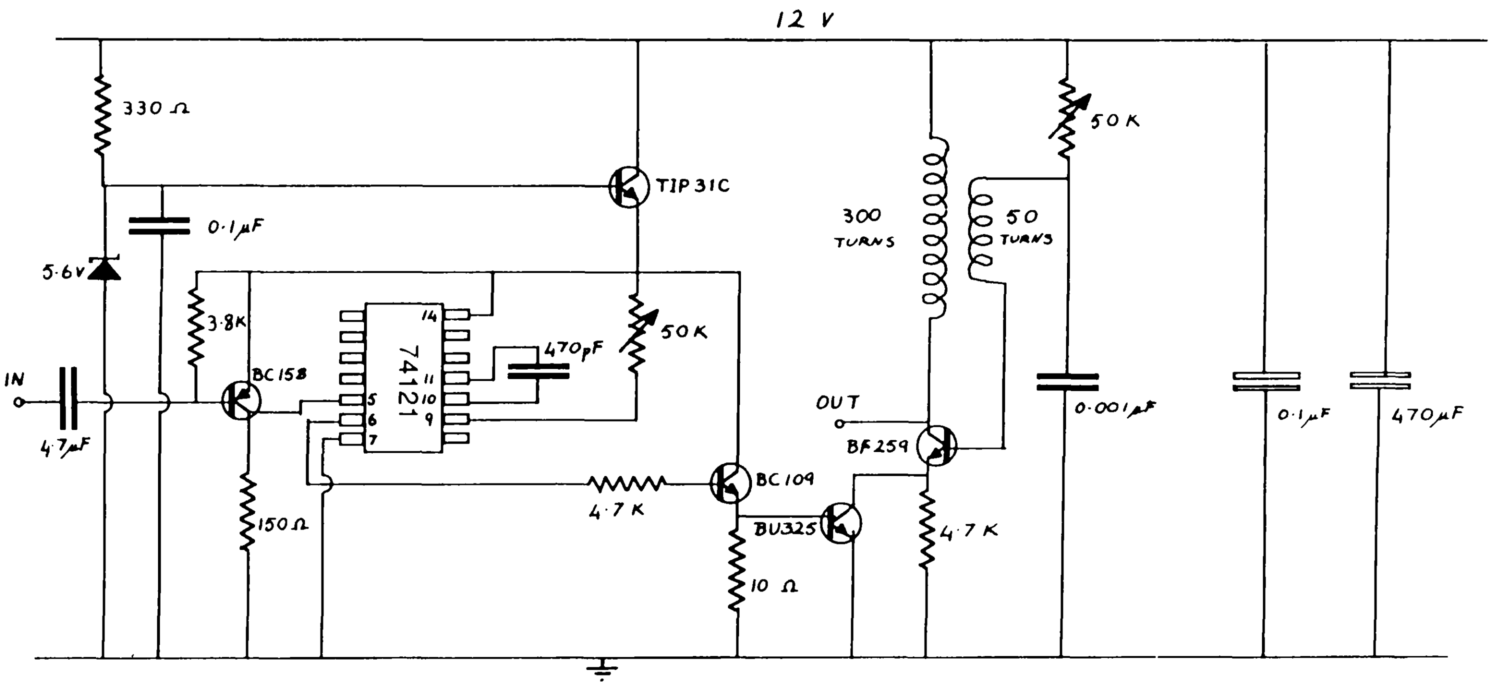
12 V
330 Ω
TIP 31C
0·1μF
5·6V
3·8K
14
74121
11
10
9
5
6
7
470pF
50K
IN
4·7μF
BC158
150Ω
4·7K
BC109
BU325
10 Ω
300 TURNS
50 TURNS
50K
OUT
BF259
4·7K
0·001μF
0·1μF
470μF

Figure 4.10 Schematic of the ion gun pulsing electronics. The circuit generates a pulse os width 300 ns and 300 V, which is applied to the extract grid.

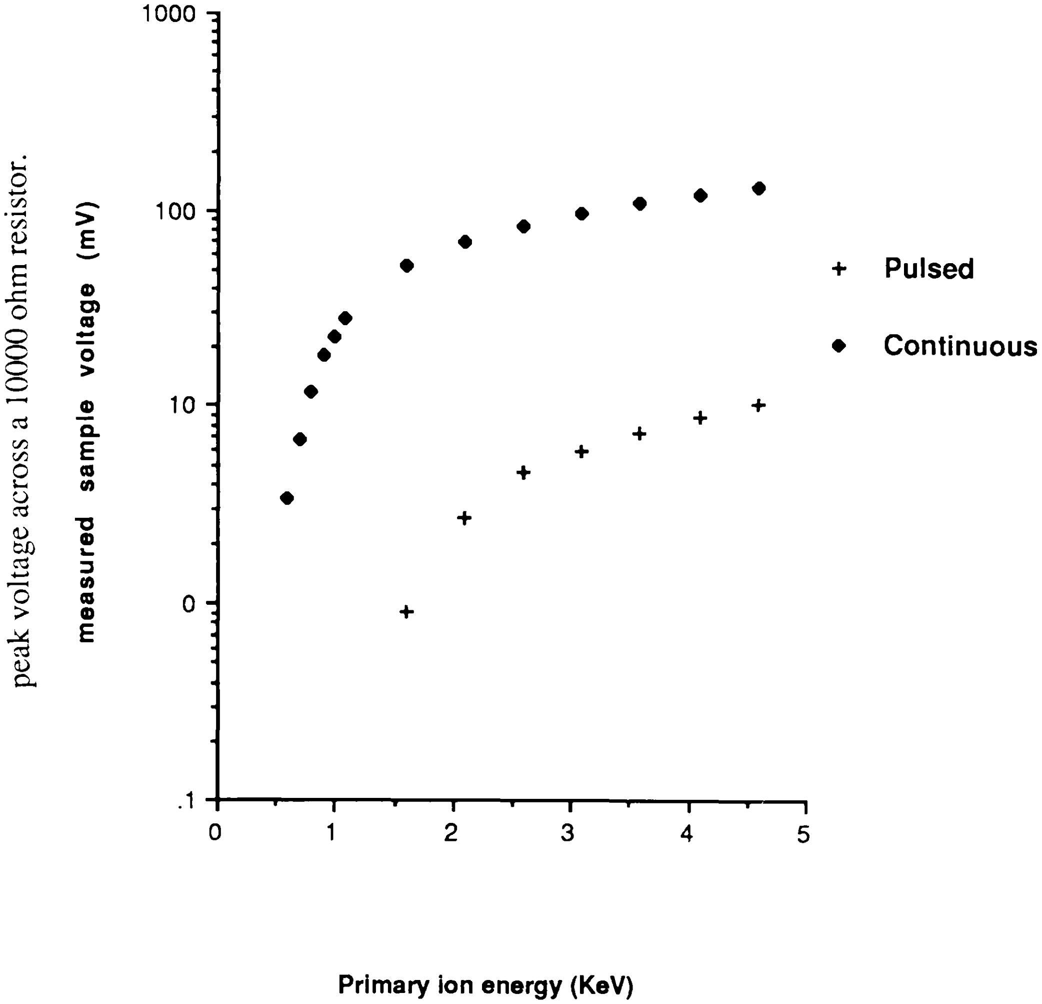

Figure 4.11 comparison of ion beam currents available in pulsed and continuous modes

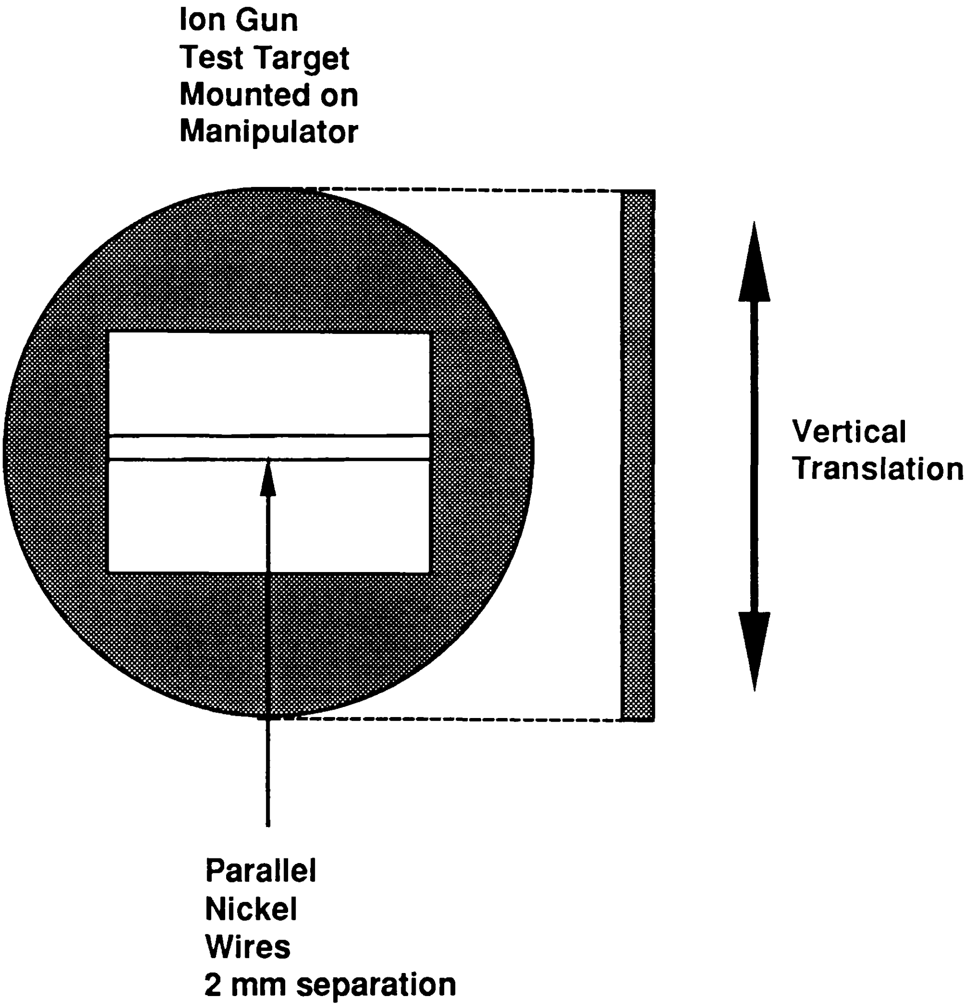
Ion Gun
Test Target
Mounted on
Manipulator
Vertical
Translation
Parallel
Nickel
Wires
2 mm separation

Figure 4.12 Ion beam test target

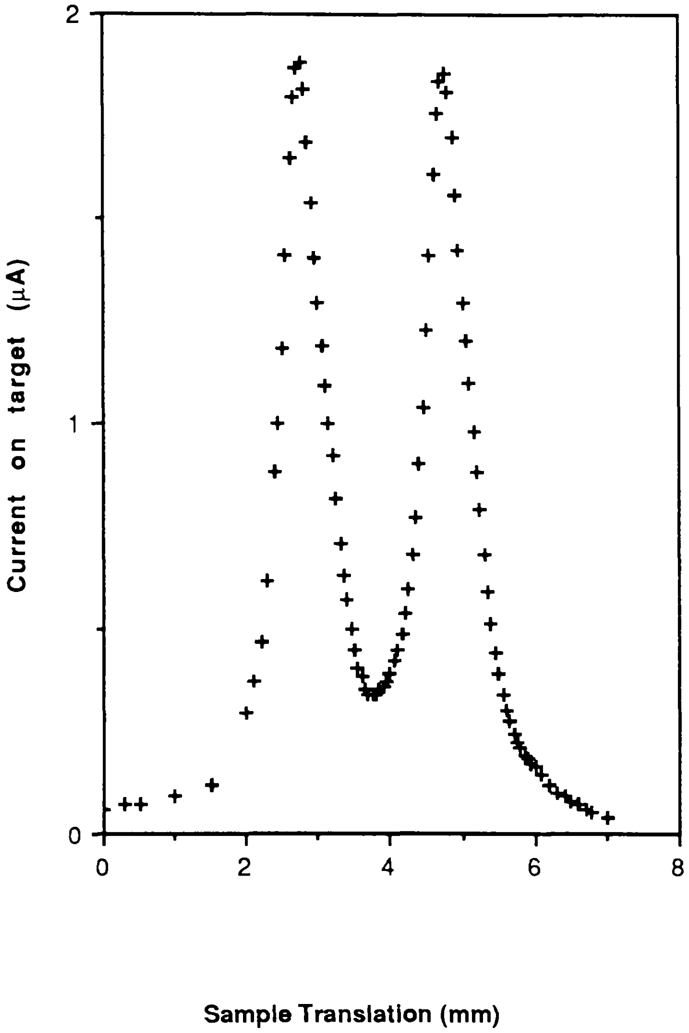

Figure 4.13 Current measured on the test sample as a function of sample translation normal to beam direction

more prone to deviation from their regular path due to electrostatic repulsion of these ions with others within the beam (space charge effects)

Laser ablation as a mechanism for sample vaporisation was also possible, although this approach was limited by the system geometry, which allowed little more than glancing incidence of the laser onto the sample, without a rotation of the stub. Such sample movement also affects the extraction field and the acceptance of the optics. An experiment utilising laser ablation will be described in Chapter 8.

Glasgow RIMS Instrument.

For the sake of completeness it is necessary to include some of details of the 'Glasgow RIMS Instrument', designed and built in conjunction with Cambridge Mass Spectrometers. It is mentioned here as the instrument was briefly used as a comparative tool in the laser ablation analysis performed on a GaAs sample, which will be described in Chapter 5. Further details concerning the instrument, not presented below, can be obtained in the reference literature[101][71][102].

As with the instrument detailed above, this instrument also employs a time-of-flight spectrometer, although of a more sophisticated nature. An 'ion reflector' is incorporated at the end of the 1.5 metre flight tube, which, as its name suggest, reflects the 'packet' of ions through approximately 180^0, back along the flight tube to the detector. This has the effect of compressing the ion 'packet' by compensating for their initial spread in kinetic energy after generation at the sample. As a result of the reflection, the total flight path is effectively doubled to 3 metres. To assist with the overall transmission efficiency of the spectrometer, a guide wire, biased a few volts negatively, is incorporated along the entire flight path, to the detector which is a double channel plate device (Figure 4.14).

The spherical analysis chamber was designed to allow for flexibility in use, comprising various radially mounted ports of various sizes in order to incorporate most forms of standard analytical instruments, as well as the versatile sample manipulator, and a sample entry lock. As with the previous instrument, laser admission is via quartz glass ports perpendicular to the spectrometer axis. A further laser port was incorporated to allow incidence at 45^0 to the sample, for purposes of ablation.

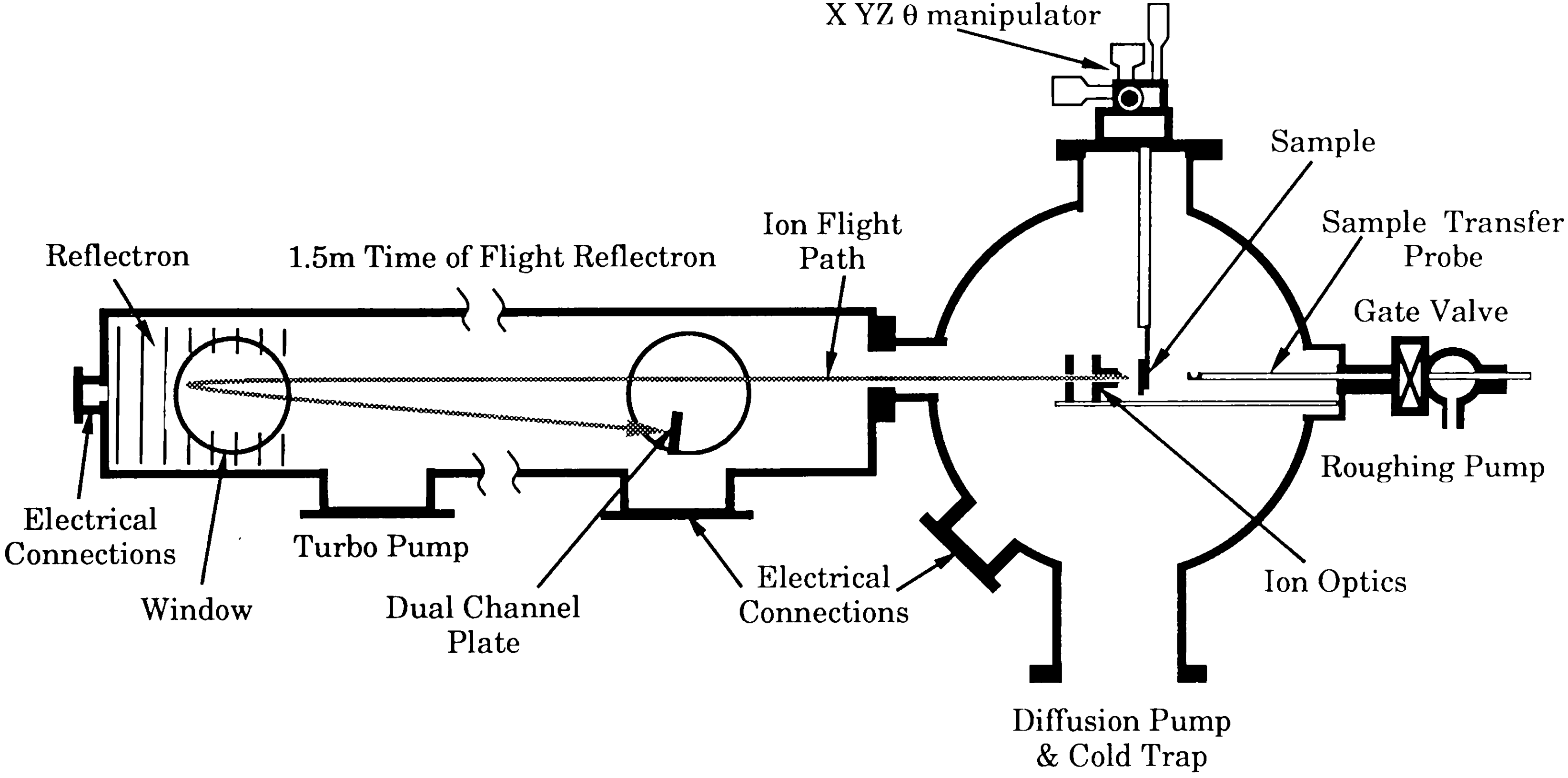
X YZ θ manipulator
Sample
Sample Transfer Probe
Gate Valve
Reflectron
1.5m Time of Flight Reflectron
Ion Flight Path
Roughing Pump
Electrical Connections
Turbo Pump
Window
Dual Channel Plate
Electrical Connections
Electrical Connections
Ion Optics
Diffusion Pump & Cold Trap

Figure 4.14 Side elevation of the Glasgow RIMS instrument, as used in the laser ablation studies to be described in Chapter 5.

The laser system comprises a Spectron Nd:YAG, with facilities for frequency doubling, trebling and quadrupling, pumping two tunable Spectron dye laser sytems, although this work required only the use of the quadrupled Nd:YAG output at 266 nm.

Data Acquisition.

During the course of experiments, two different data acquisition systems were used. For depth profiling and wavelength dependent measurements in which cases only one mass at any one time was being investigated, a peak sensing Analogue to Digital Converter (ADC) was sufficient, while for time of flight spectra, where there is a large time spread of detected ions, more sophisticated electronics had to be employed.

The electronic arrangement shown, (Figure 4.16), produces a gate of variable width and delay, initiated by a trigger pulse at time zero for the mass spectrometer (i.e photo-diode laser trigger or ion gun pulser trigger). This gate then acted as a strobe for the analogue to digital conversion of the amplified detector output at the desired mass specified by the position of the gate.

The peak sensing ADC was an Ortec AD 811 with 11 bit resolution and an input range of 0 to 2 volts.

Acquisition was controlled by an LSI 11 computer with monitoring of events on a computer display and simultaneous storage to floppy disk. Data was then transferred to an IBM mainframe for analysis.

Time-of-Flight spectra were recorded via a LeCroy 2261 transient recorder. The 2261 stores events in a charge coupled array of 640 elements, or bins, each of width 10ns. Therefore on each analysis cycle (laser pulse), a time-of-flight window of 6.4 μs could be recorded. The charge in each bin is then digitised via an 11 bit ADC and transferred to an IBM PC/AT for storage and analysis. Mass data could be accumulated over a number of shots, specifiable by the operator.

Triggering of the 2261 was performed by a pulse from the same electronics as described above with the addition of a digital delay generator (SRS DG535) used to specify the start time for storage relative to the time zero (i.e mass window analysed).

System Triggering.

In order that the pulse to pulse temporal stability of the laser is optimised, the triggering of the excimer laser must be accomplished by two fast voltage pulses. The first initiates the charging to high voltage, the second ~25 ms later then fires the electrical discharge. If the ion gun is also running in pulsed mode, it must be triggered prior to the firing of the laser. Finally, a trigger must be supplied to the data aquisition system corresponding to time zero for the TOF.

All triggering was initiated by an external voltage pulser, Ortec 485, via various delay generators (Figure 4.15). The laser trigger-pulse separation was variable for optimum charging time and stability, controlled by GG200 gate generators A and C. Also, the delay between firing of the ion gun and the laser is also continuously variable for maximum temporal overlap of the secondary particles with the incoming laser photons using another GG200 gate generator B.

Fig.4.16 illustrates the electronic arrangement required by the data aquisition system. The timing sequence is as follows:

The computer signifies its readiness to accept data by delivering a pulse via the output register. This signal is then used to create a waiting state by producing a gate of effectively infinite width, which is sent to the input of a dual input coincidence unit.

The trigger from the spectrometer, corresponding to the laser firing or the ion gun trigger pulse, is fed into the same coincident channel.

The resulting coincident pulse is then used to initiate the production of a further gate, this time of variable width and delay corresponding to the arrival time of the mass of interest which becomes the ADC strobe.

The coincident signal also resets the electronics in anticipation of a further ready signal from the computer.

In most cases the ion signal was fed directly into a Lecroy VV100BTB pre-amplifier. When necessary, further amplification was performed by LRS 133b and 134 fast amplifiers. The amplified signal was then inverted in an Ortec 433A sum/invert.

Laser System.

Of major importance to the technique of RIS is the ability to ionise atoms of the

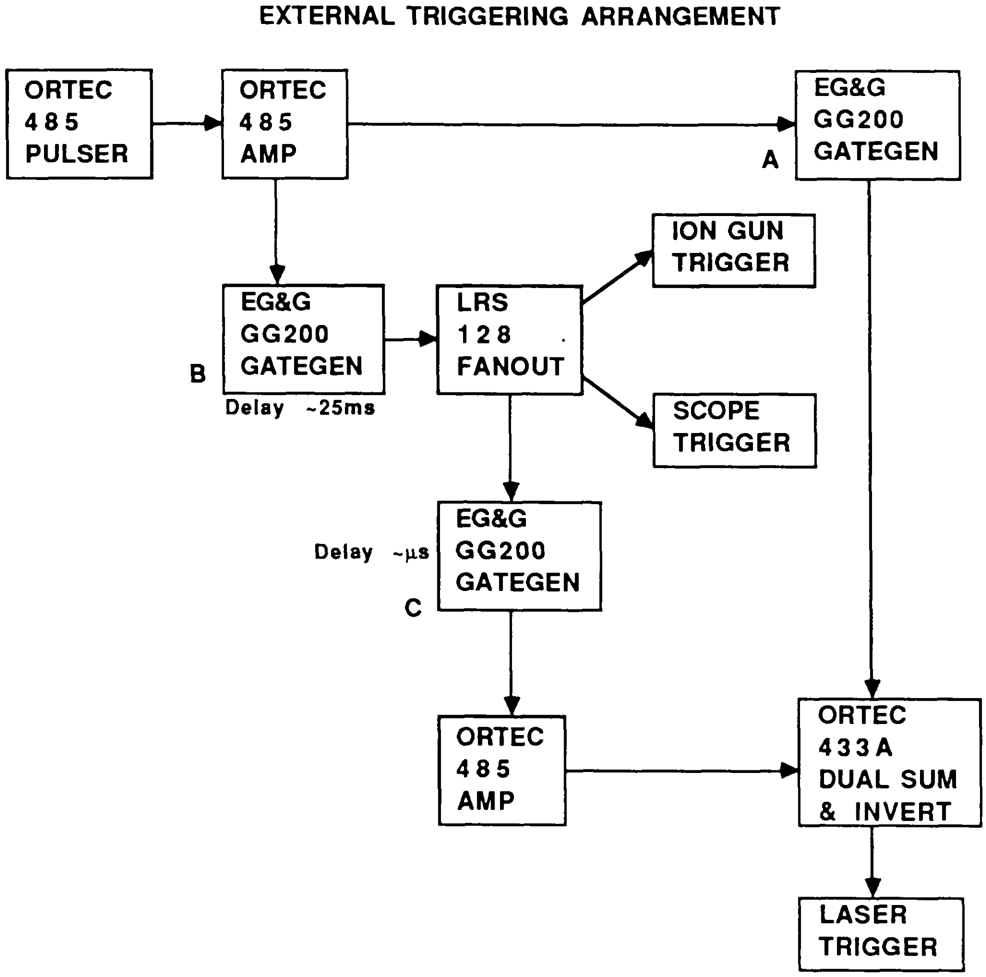
EXTERNAL TRIGGERING ARRANGEMENT
ORTEC 485 PULSER
ORTEC 485 AMP
EG&G GG200 GATEGEN
A
ION GUN TRIGGER
EG&G GG200 GATEGEN
B
Delay ~25ms
LRS 128 FANOUT
SCOPE TRIGGER
EG&G GG200 GATEGEN
Delay ~μs
C
ORTEC 485 AMP
ORTEC 433A DUAL SUM & INVERT
LASER TRIGGER

Figure 4.15 Triggering electronics arrangement for the laser, ion gun and data acquisition, controlled from an external pulsing source.

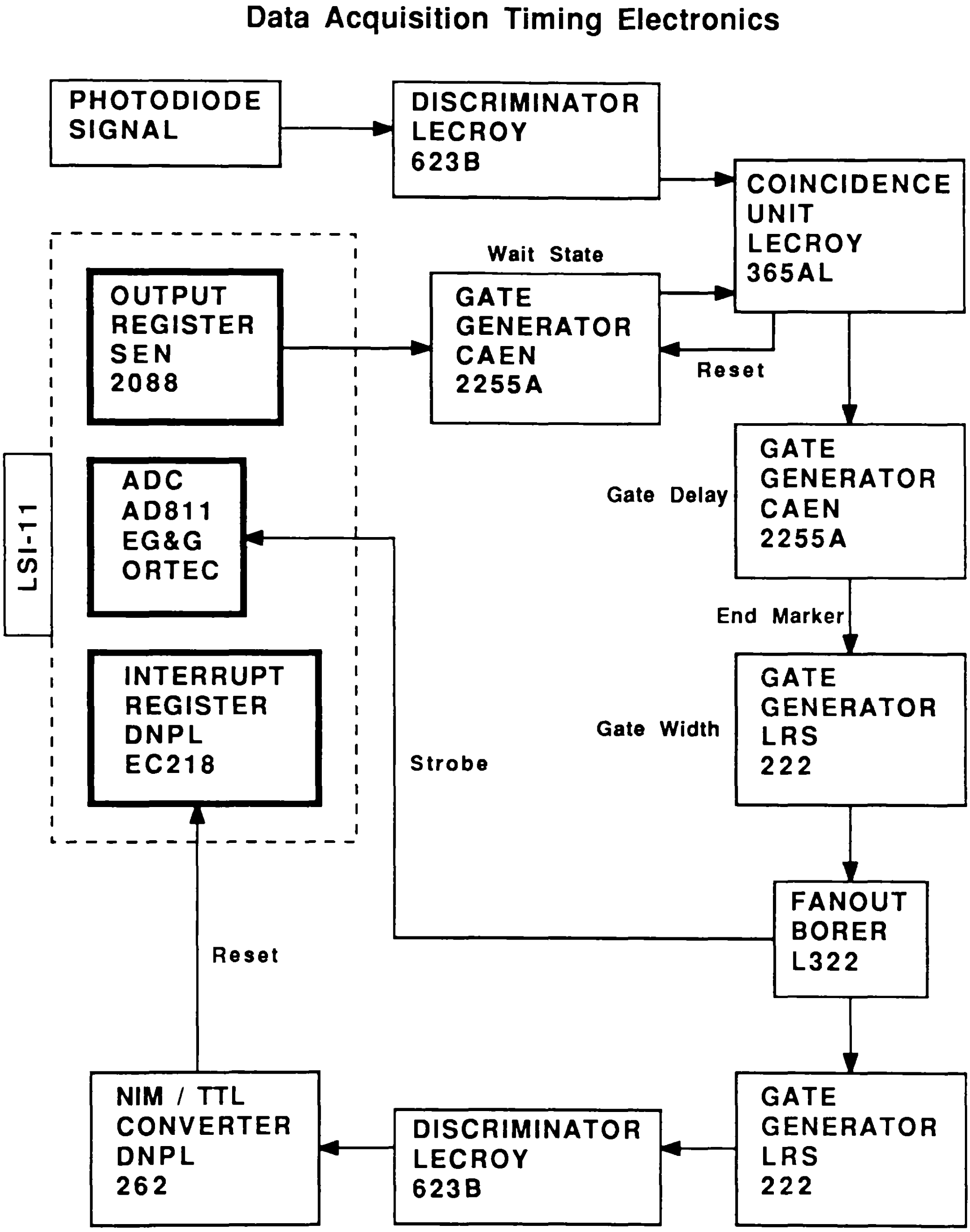
Data Acquisition Timing Electronics
PHOTODIODE SIGNAL
DISCRIMINATOR LECROY 623B
COINCIDENCE UNIT LECROY 365AL
Wait State
GATE GENERATOR CAEN 2255A
Reset
OUTPUT REGISTER SEN 2088
LSI-11
ADC AD811 EG&G ORTEC
GATE GENERATOR CAEN 2255A
Gate Delay
End Marker
INTERRUPT REGISTER DNPL EC218
Gate Width
GATE GENERATOR LRS 222
Strobe
FANOUT BORER L322
Reset
NIM / TTL CONVERTER DNPL 262
DISCRIMINATOR LECROY 623B
GATE GENERATOR LRS 222

Figure 4.16 Data acquisition electronics for production of variable width and delay gate for the ADC.

selected element with 100% efficiency. To achieve this, very high photon fluxes are required, variable over as large a range of wavelengths as is possible.

These requirements are met with modern pulsed dye lasers which offer tunability over a range from about 300 to 1500 nm. With the addition of frequency doubling, the lower range may be further extended. Dye lasers are capable of producing up to 10's of millijoules in pulses of less than 10ns. This is of course dependent on the pump source characteristics and the lasing efficiency of the dye used.

In the experiments to be described, the pump source for the single dye laser (Lumonics EPD 330), was an Xenon Chloride Excimer Laser (Lumonics TE-860-3). Frequency doubling was also available on the output from the dye. Beam manipulation was performed with quartz glass optics for improved UV transmission.

Excimer Laser.

Excimer (Excited Dimer) Lasers are inert gas halide molecular lasers which rely on the unbound nature of the ground state of the molecule, dissociation occuring in less than a picosecond. Therefore , population inversion can easily be attained via the formation of a relatively long lifetime bound state of the molecule [81]. Excited molecules are usually formed in an electric dicharge. For the XeCl molecule, lasing action occurs at 308 nm.

The laser used was capable of output energies of up to 80 mJ in a 7-8 ns pulse, in a divergent beam suitable for dye laser pumping.

Dye Laser.

Dye lasers are broadly tunable systems which rely on the fluorescent properties of organic dyes. Their mode of operation relies on optical pumping from the lower singlet states to higher singlet states of the dye molecules. Relaxation of the upper state followed by radiative decay to the lower state then occurs over a broad wavelength band.

In the Lumonics system, the dye, dissolved in a suitable solvent, is circulated through two intracavity cells, an oscillator and an amplifier, where it is pumped, transversely, by the excimer beam focused into the cells by cylindrical lenses. Tuning of the beam is then accomplished by a grazing incidence reflection grating at one end of the oscillator cavity (Figure 4.17). This reduces the lasing action to a narrow band of the gain profile of the dye. The grating angle was servo driven under the control of a Lumonics EPD-60 compuscan system. This allowed precise wavelength scans over varying ranges at varying scan rates. To further reduce the linewidth, a beam expander can be introduced into the oscillator cavity.

Frequency Doubling.

In many of the ionisation schemes devised for the elements, the transition energies required for excitation are beyond the range of available dyes. In such circumstances it becomes necessary to adopt second harmonic generation of higher wavelength lasers if one does not wish to resort to the use of multiphoton excitation with its lower transition probability. (See Appendix B.)

The doubling crystal used throughout was Potassium Dihydrogen Phosphate (KDP) which allows frequency doubling over the range 260 to 330 nm with efficiencies of better than 10%.

An important aspect of doubling dye laser output is the need to preserve doubling efficiency when scanning the dye laser over large wavelength ranges. It is necessary to maintain the angle of incidence of the fundamental laser relative to the crystal at all times. To achieve this, the crystal was mounted on an Inrad 5-12 auto tracking system (Figure 4.18). The automatic mechanism operates by filtering a small portion of the doubled light onto two photo-diodes which feedback signals to the servo controller to adjust the orientation of the crystal and the primary laser for a maximum signal.

Laser Power Measurement.

For measurement of the absolute energy in each laser pulse, a model ED-200 Gentec Pyroelectric Joulemeter was employed. Once an absolute scale had been established, the Gentec was replaced with the more sensitive, more responsive Molectron J3-05, requiring only a fraction of the total pulse energy to form an accurate relative scale. In each case the joulemeter integrates each pulse resulting in a peak voltage signal proportional to the total pulse energy (calibration : 0.87 volts /mJ).

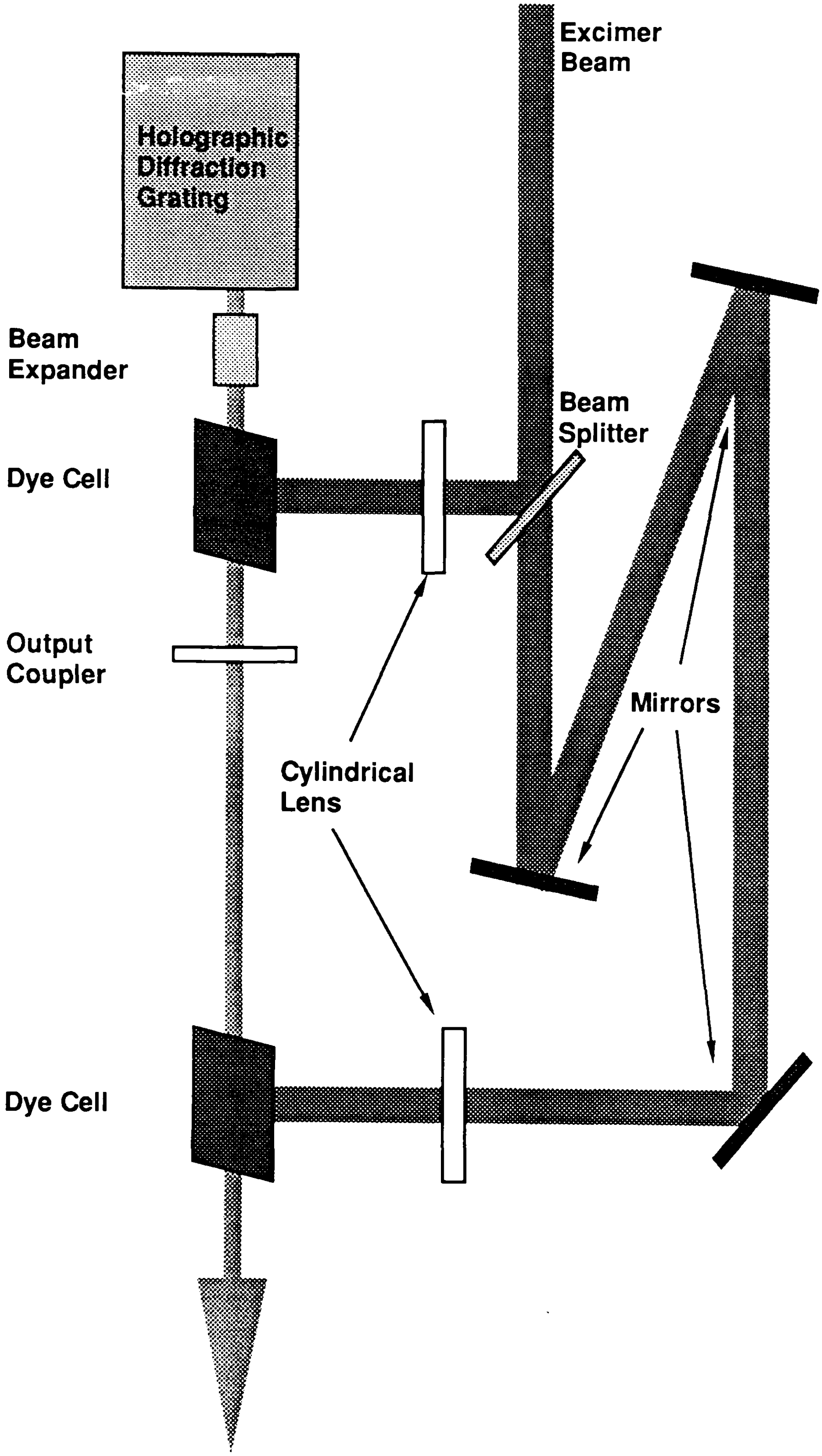
Excimer Beam
Holographic Diffraction Grating
Beam Expander
Beam Splitter
Dye Cell
Output Coupler
Mirrors
Cylindrical Lens
Dye Cell

Figure 4.17 Schematic of the optical arrangement of the excimer pumped, Lumonics EPD 330 dye laser.

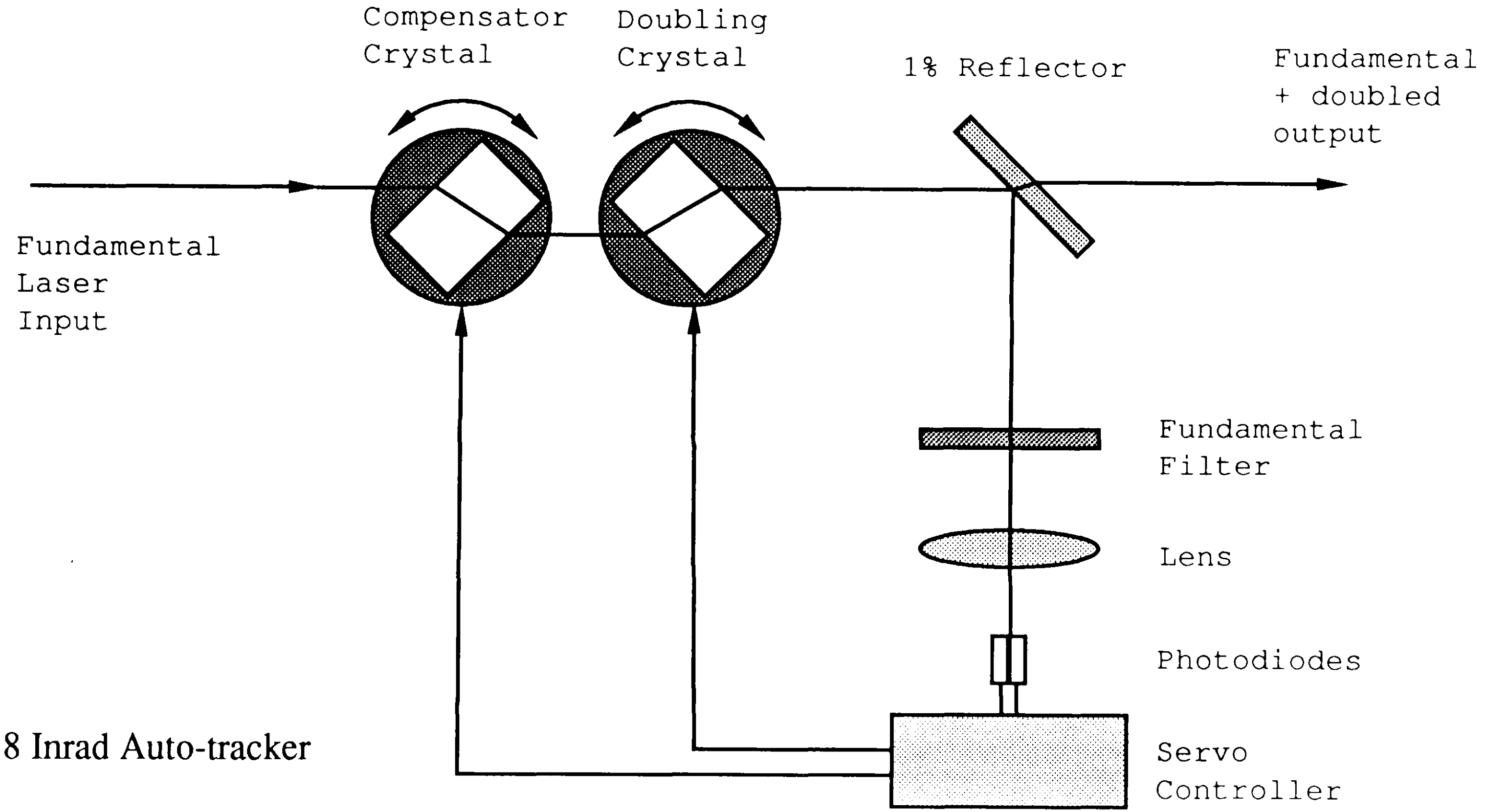
Compensator
Crystal
Doubling
Crystal
1% Reflector
Fundamental
+ doubled
output
Fundamental
Laser
Input
Fundamental
Filter
Lens
Photodiodes
Servo
Controller

Figure 4.18 Inrad Auto-tracker

Optical Attenuator.

In experiments to be detailed in following chapters, it was necessary to have a means of continuously varying the total laser power incident on the interaction region. This was achieved by utilising a manually operated variable attenuator.

The device consisted of a system of four quartz glass plates arranged in two pairs on rotatable mountings (Figure 4.19). During manual operation these plates are rotated relative to each other in order to vary, in a controlled manner, the angle of incidence of the laser beam on the surfaces, and thereby the degree of attenuation of the beam.

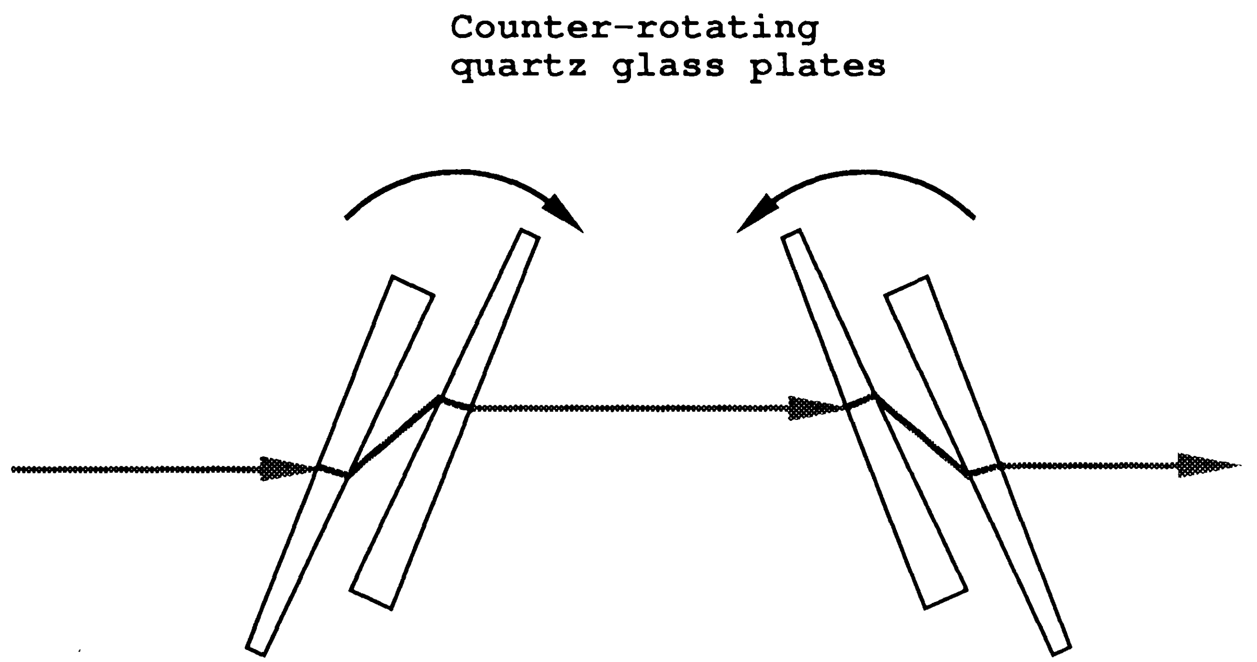
Counter-rotating
quartz glass plates

Figure 4.19 Optical attenuator

Chapter 5

Resonant Ionisation of Gallium and Aluminium in a TOF Mass Spectrometer.

Introduction.

This chapter is primarily concerned with a study of the resonantly enhanced ion formation of Gallium and Aluminium in the time-of-flight mass spectrometer. These group III elements are commonly employed in the production of III-V semiconductor material, and it was therefore deemed worthwhile that preliminary testing of the system, should involve these elements with regard to future profiling experiments.

Experimental Arrangement.

For a detailed description of all the apparatus used, namely the mass spectrometer, the laser system and the data acquisition, the reader is referred to Chapter 4.

The sample involved in the Gallium study was a 1 cm^2 section of MBE grown GaAs (100) semiconductor substrate, fixed to the stainless steel sample stub with conductive epoxy, while for Aluminium, the sample was a section of 99.99% Aluminium foil of thickness 0.025 mm, with direct metal to metal contact with the stub. In both cases, the sample surface was oriented with its surface normal colinear with the spectrometer axis. The laser was focused using a 50 cm focal length quartz lens.

Results and Discussion.

Gallium SIMS

The first series of experiments carried out involved the system operating in a time-of-flight SIMS mode with the primary ion gun pulsed by the method described in Chapter 4, and incident on the GaAs sample. The primary ion source material was research grade krypton gas. A typical TOF mass spectrum obtained from this sample is shown in Figure 5.1.

Due to the comparatively long pulse length of the primary ions, the mass resolution is severely restricted, to such an extent that the spectrometer is unable to resolve the secondary arsenic ion component as well as the two isotopes of gallium.

To give an indication of the mass range observed, the masses corresponding to the predominant peaks were calculated relative to that of peak 6 which was attributed to a combination of the unresolved Ga and As secondary ions with an average mass of 72.32 amu (Table 5.1). The possible origins of observed background peaks in SIMS may be attributed to surface contamination from oxygen adsorbed onto the sample during its exposure to air, forming oxides in the sputtering process, residual gas molecules adsorbed within the vacuum chamber which are a source for various combinations of compound molecules and fragments on sputtering, as well as molecular Ga and As species. There is also the possibility of a peak occurring from backscattering of the primary krypton ions. Also, as a titanium sublimation pump was used during the pump down period, it is possible that a surface layer of Ti was formed on the sample which may be responsible for the observed peak number four (Titanium having a predominant isotope at mass 47.95 amu).

In an attempt to reduce the contribution of the contaminants to the overall amount of sputtered material, the sample could be sputter cleaned by operating the ion gun in continuous beam mode, offering a much higher sputtering rate (see Chapter 4 for comparison of pulsed and DC currents), and rastering the beam spot over the sample surface.

On returning to pulsed operation after five minutes of sputter cleaning, the reduction in surface contaminants is evident (Figure 5.2), as well as a significant enhancement of the Ga/As peak, which is to be expected due to the increased exposure of GaAs as the surface layer presented to the primary ion beam. However, it was

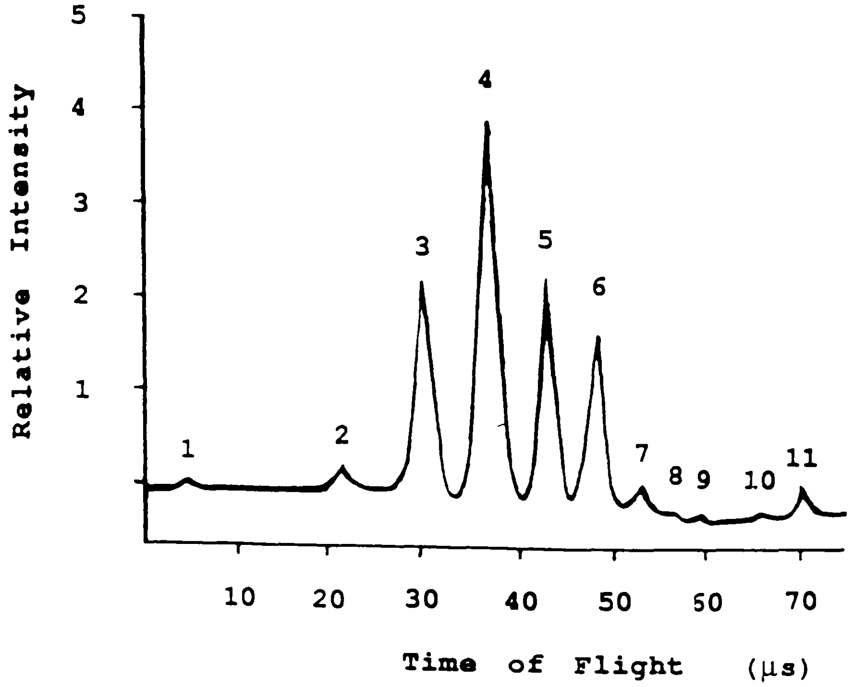

Figure 5.1 SIMS-TOF spectrum from a GaAs substrate obtained from photographs of an oscilloscope trace. Vertical scale forthis, and subsequent figures, corresponds to screen scale divisions.

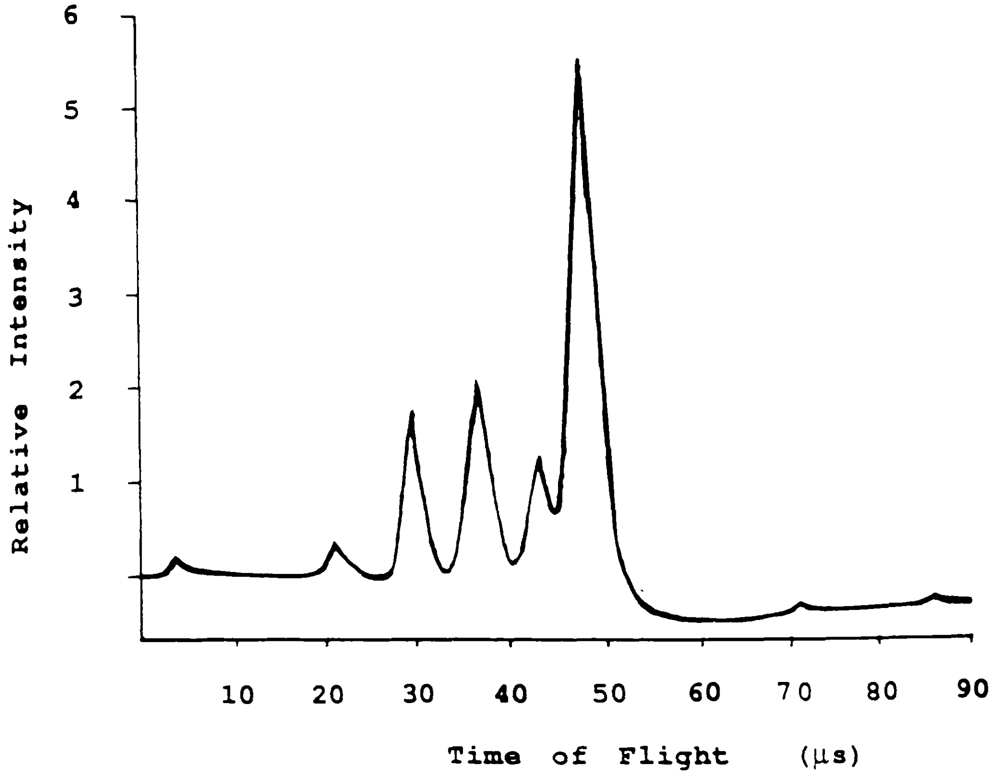

Figure 5.2 SIMS-TOF spectrum from the same GaAs substrate after a 5 minute period of sputter cleaning of the surface.

Table 5.1 Calculated masses for the peaks in the spectrum shown in Figure 5.1.

Peak No.	Calculated Mass (amu)
1	0.7
2	15.2
3	28.2
4	44.9
5	60
6	72.3
7	89.7
8	98.4
9	157.5
10	236.2
11	540.7

noted that the background peaks increased markedly with time, at a visible rate (Figure 5.3), due to what can only be further surface adsorption from the residual gas. This results from the reduction in the effective sputter rate when swiching to pulsed operation, compared with the continuous primary current incidence, and a failure to fulfill the requirement of Equation 3.27.

Sputter cleaning was repeated, this time for a prolonged period of thirty minutes, and as can be seen in Figure 5.4, the reduction in the background peaks is more evident. However, once again, there is an immediate redevelopment of these peaks, which eventually attains the degree established in the previous case (Figure 5.3) only 5 minutes after the removal of the DC ion beam, implying the eventual attainment of an equilibrium condition between sputter removal and surface adsorption (Figure 5.5).

The typical base pressures achieved during the course of these preliminary experiments ranged from 1 to 5 x 10^{-7} mbar with partial pressures of krypton gas ranging from 2 to 8 x 10^{-6} mbar during ion gun operation. The reason for the apparently poor vacuum conditions attainable, even after prolonged pump down periods, was attributed to a small leak. At a later stage this problem was realised and rectified with a subsequent improvement in the quality of vacuum of, eventually, better than two orders of magnitude.

As can be seen from the next series of spectra (Figure 5.6 is the spectrum before cleaning, Figure 5.7 the result of 10 minutes exposure to the DC ion beam, and Figure 5.8 35 minutes later), even a reduction in the residual gas pressure by a factor of four, results in a reduction in the rate of re-adsorption. The relative intensities of the peaks eventually attain steady values, Figure 5.8, differing from those they possessed prior to cleaning, Figure 5.6, implication of apparent equilibrium between the adsorption and sputter removal rates for the pulsed system, which compares favourably with that observed at the higher pressure (cf. Figure 5.5), although in this case the time required to achieve such levels is significantly longer.

With an improvement of an order of magnitude in the vacuum quality, the rate of re-adsortion is significantly reduced to an extent that over the same observational period as for the previous spectra, the background peaks fail to gain the same degree of intensity as under poorer vacuum conditions.

A further surface study of this sample, this time under the influence of an ablating laser at 266 nm (quadrupled Nd: YAG, < 1mJ, moderately focused to a spot

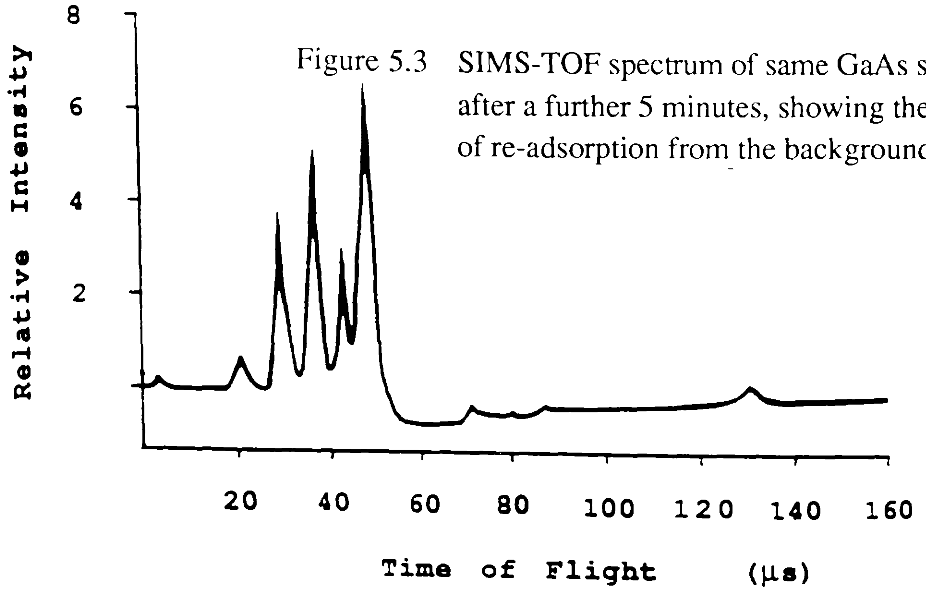

Figure 5.3 SIMS-TOF spectrum of same GaAs sample after a further 5 minutes, showing the results of re-adsorption from the background gas.

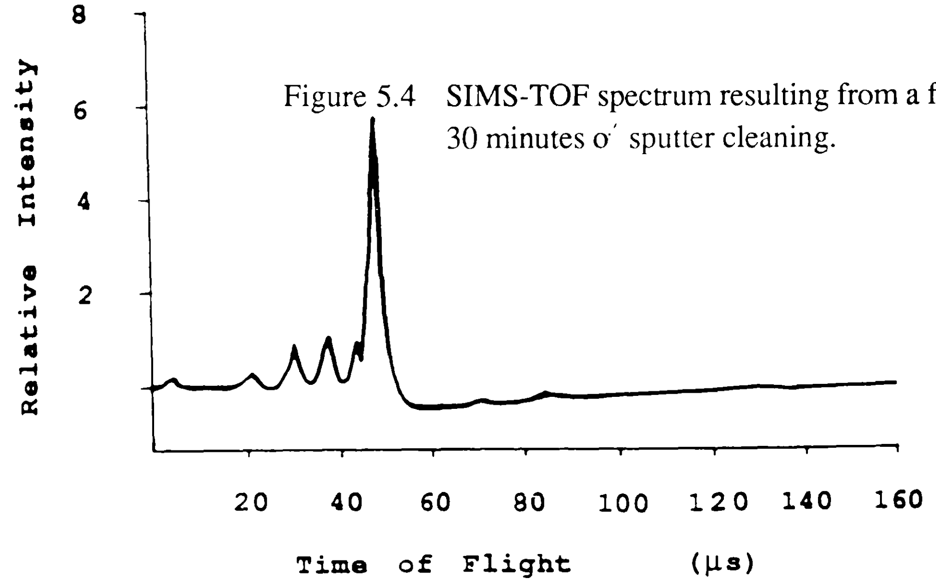

Figure 5.4 SIMS-TOF spectrum resulting from a further 30 minutes of sputter cleaning.

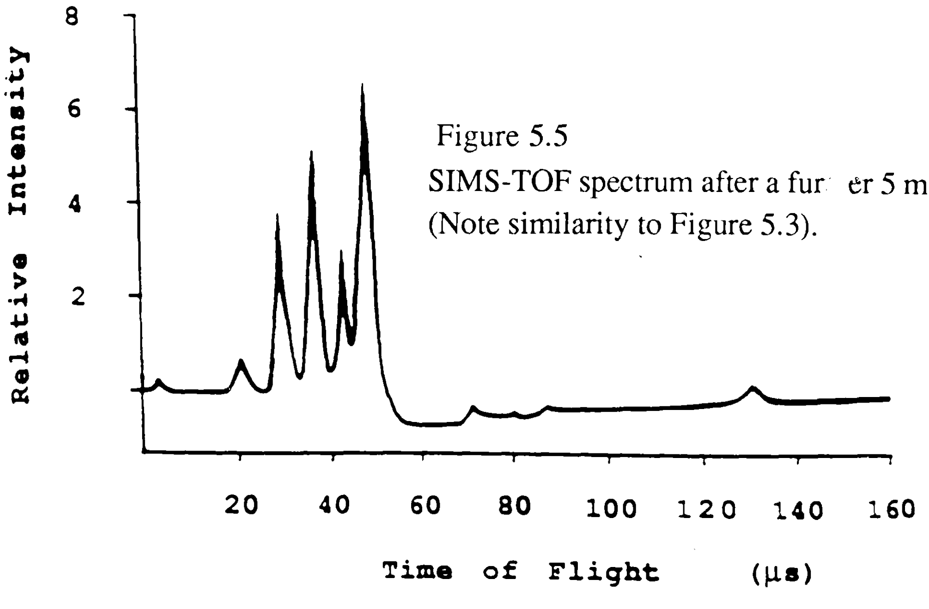

Figure 5.5
SIMS-TOF spectrum after a further 5 minutes (Note similarity to Figure 5.3).

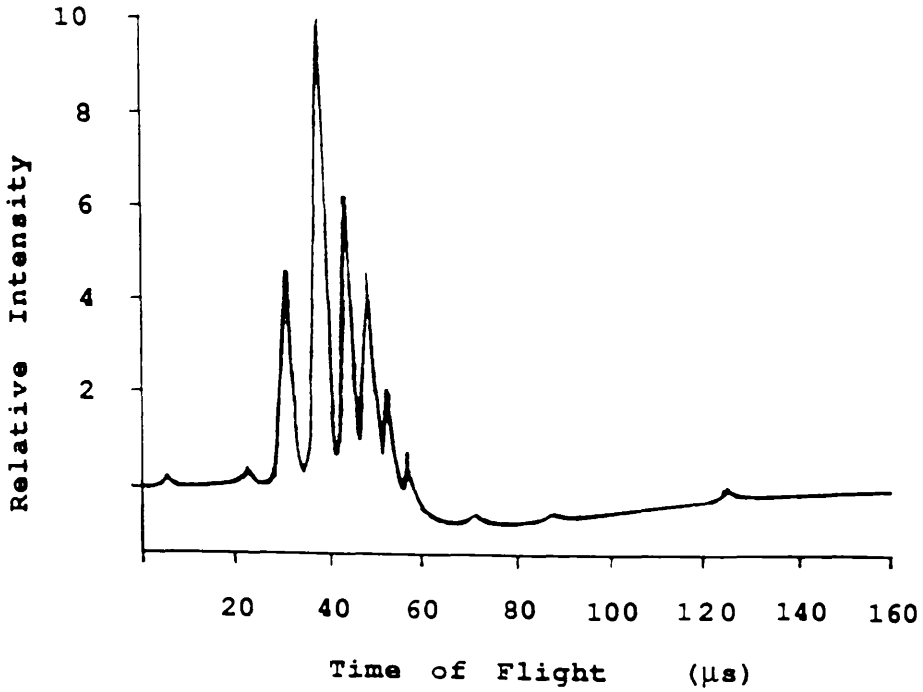

Figure 5.6 SIMS-TOF spectrum from GaAs after a reduction in the base pressure.

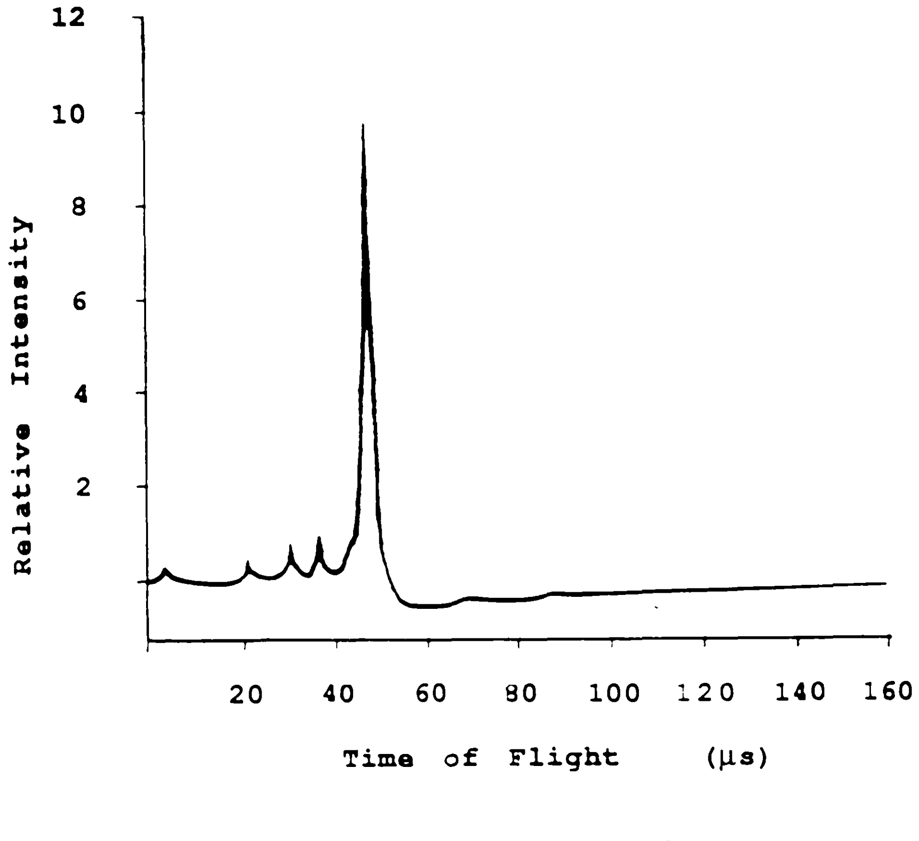

Figure 5.7 SIMS-TOF spectrum resulting after 10 minutes sputter cleaning.

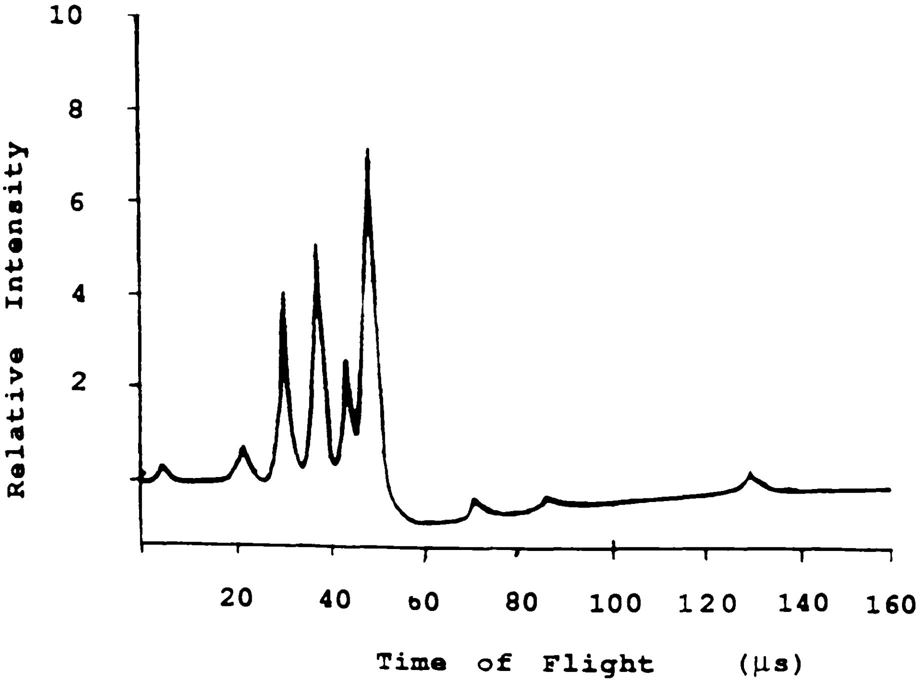

Figure 5.8 SIMS-TOF spectrum ing from further re-adsorption 35 minutes.

of ~1 mm diameter), reveals in addition to the bulk constituents, the presence of prominent peaks corresponding to Na and K, Figure 5.9 (a)&(b), as well as numerous molecular species, most notably As_2, As_3 and As_4 (refer to Table 5.2), only the latter of which has a relative intensity less than monatomic As, in agreement with observations of Danielzik [15]. These spectra result from a single laser event.

After cleaning the surface with a higher intensity (~10 mJ) of laser radiation for several hundred laser shots, the spectrum had changed markedly with significant reductions in the molecular Ga species, and most noticeably the oxides of Ga by an order of magnitude, Figure 5.10 (a)&(b). As expected from a cleaner surface the relative intensities of the Ga peaks increase, while the intensities of the the various As molecules remain essentially unchanged, indicating the potential problems which exist in accurate quantification of secondary ions formed in this manner. Such quantitative problems were highlighted in experiments on GaAs, by laser ablation at 266 nm, by Sheuler and Odom [90], who found that in order to liberate appreciable numbers of As ions from the sample, excessively high power densities were required, due partly to the higher ionisation potential of As (9.81 eV) relative to Ga (6 eV), which resulted in severe damage to the sample, effectively eliminated its prospects for quantitative thin film analysis.

It was at first suspected that the occurrence of Na and K in the laser ablation mass spectrum indicated the presence of those same elements in the SIMS spectrum, which would correspond to two of the lower mass secondary ion peaks observed. This would imply that, due to an inability to match any of the calculated masses reasonably to Na and K, the assumptions made regarding the calculation of the masses, namely the contributing elements to peak 6, Gallium and Arsenic, led to unreasonably high mass values. However the relative intensities of Na and K in laser ablation did not compare to the peaks formed in ion sputtering, and were affected to a lesser degree, relative to the SIMS analysis, on cleaning of the surface. Also, the other prominent background SIMS peaks redeveloped rapidly after cleaning, via adsorption from the background gas, which suggested that the elements Na and K were not responsible, and instead, are most probably due to organics and oxides.

These observations also serve to highlight some of the important differences which may arise between ion sputtering and laser ablation, namely that photon bombardment is much more efficient in the removal of surface adsorbed species from the sample, occurring in probably the first few incident pulses, and appears to be less

Table 5.2.

Peak No.	Calculated Mass (amu)	Most Probable Mass (amu)	Probable Species
1	22.95	23	^{23}Na
2	39.03	39	^{39}K
3	40.99	41	^{41}K
4	69.00	69	^{69}Ga
5	71.01	71	^{71}Ga
6	74.98	75	^{75}As
7	138.04	138	$2^{69}Ga$
8	140.11	140	$^{69}Ga^{71}Ga$
9	142.09	142	$2^{71}Ga$
10	144.09	144	$^{69}Ga^{75}As$
11	145.71	146	$^{71}Ga^{75}As$
12	150.02	150	$2^{75}As$
13	153.98	154	$2^{69}Ga+^{16}O$ (Ga_2O)
14	155.96	156	$^{69}Ga^{71}Ga+^{16}O$
15	158.00	158	$2^{71}Ga+^{16}O$
16	225.18	225	$3^{75}As$
17	300.27	300	$4^{75}As$

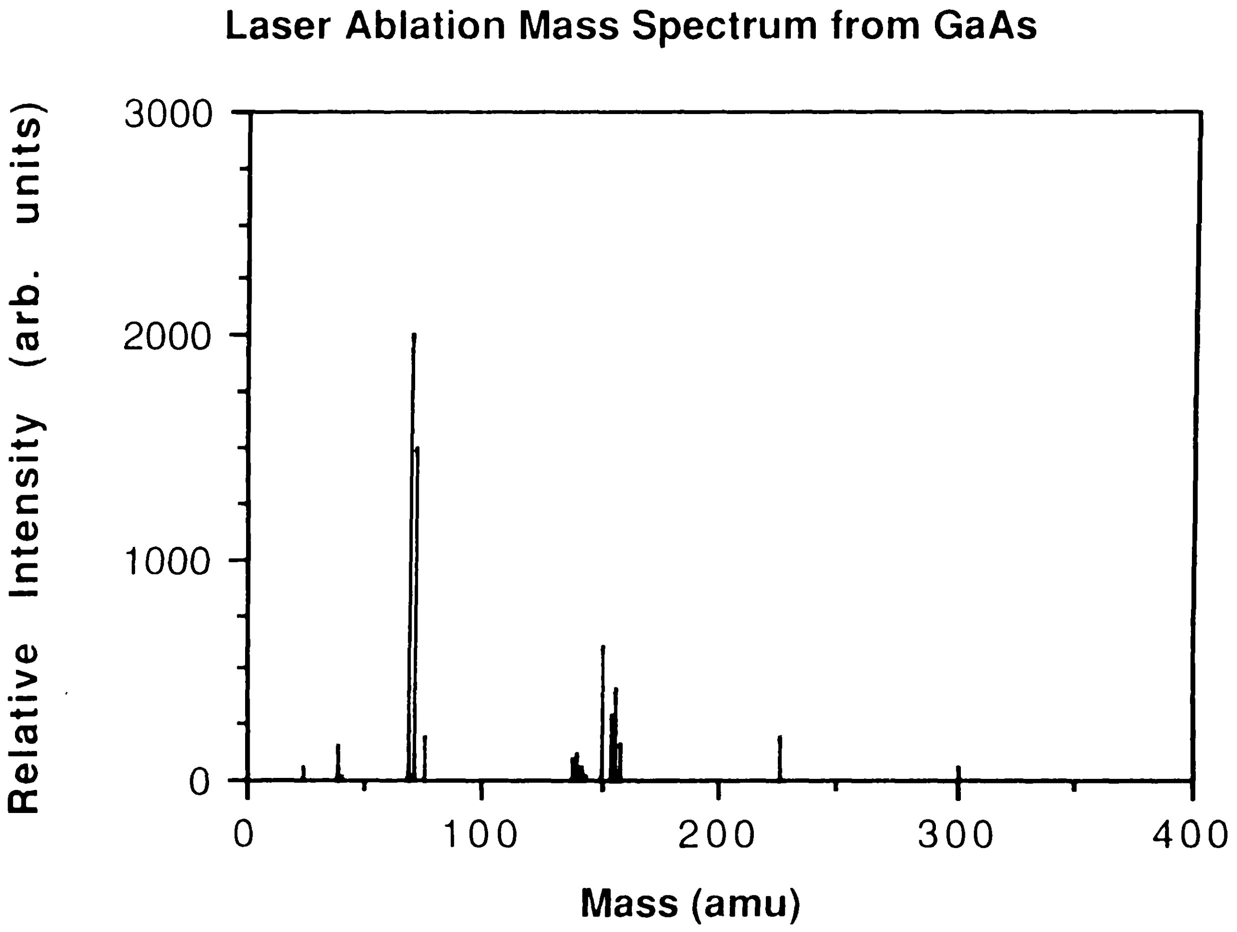

Figure 5.9(a) Mass spectrum resulting from the action of an ablating laser at 266 nm, derived from time-of-flight signal intensities on an oscilloscope, from the GaAs substrate.

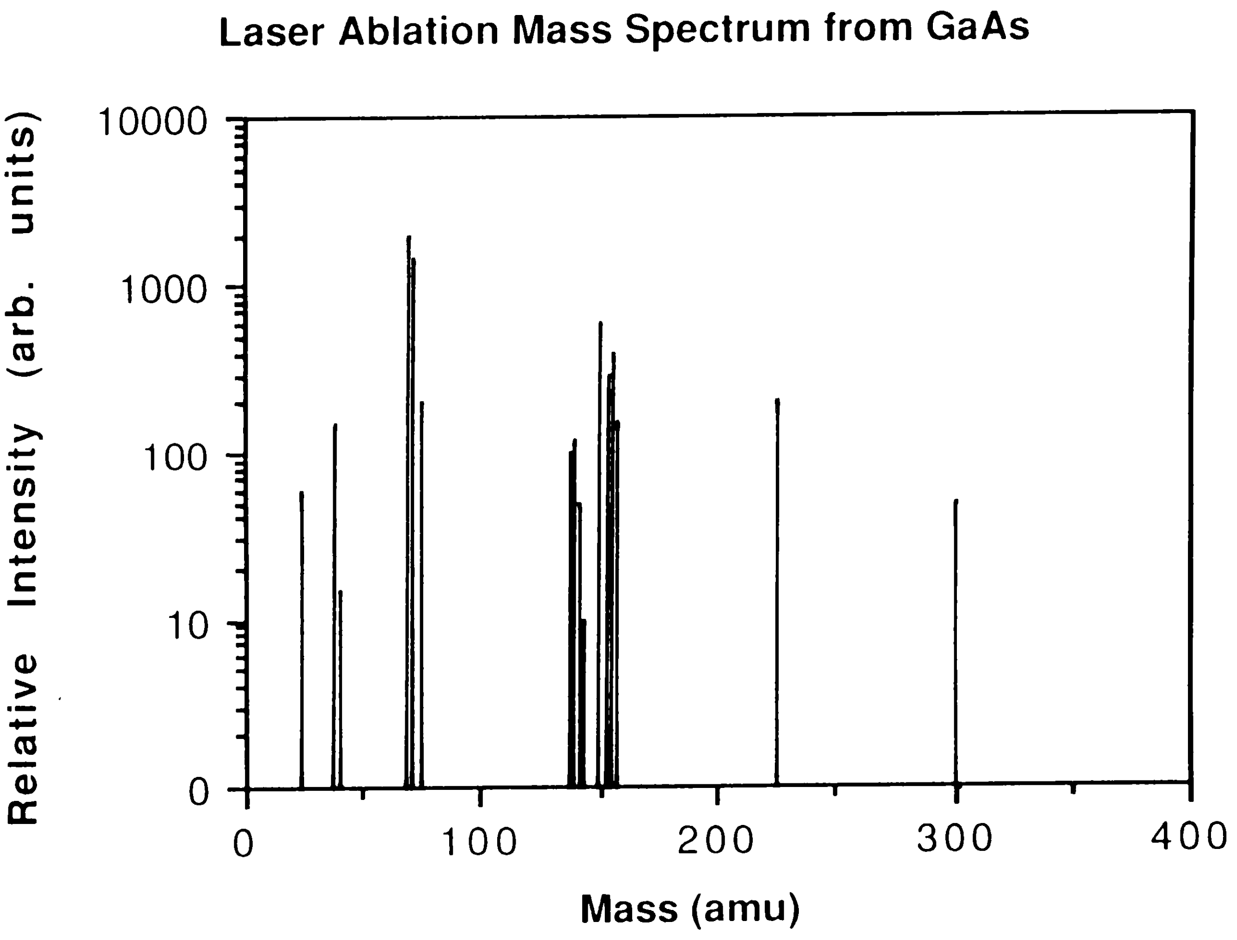

Figure 5.9(b) Log plot of the mass spectrum shown in Figure 5.9(a).

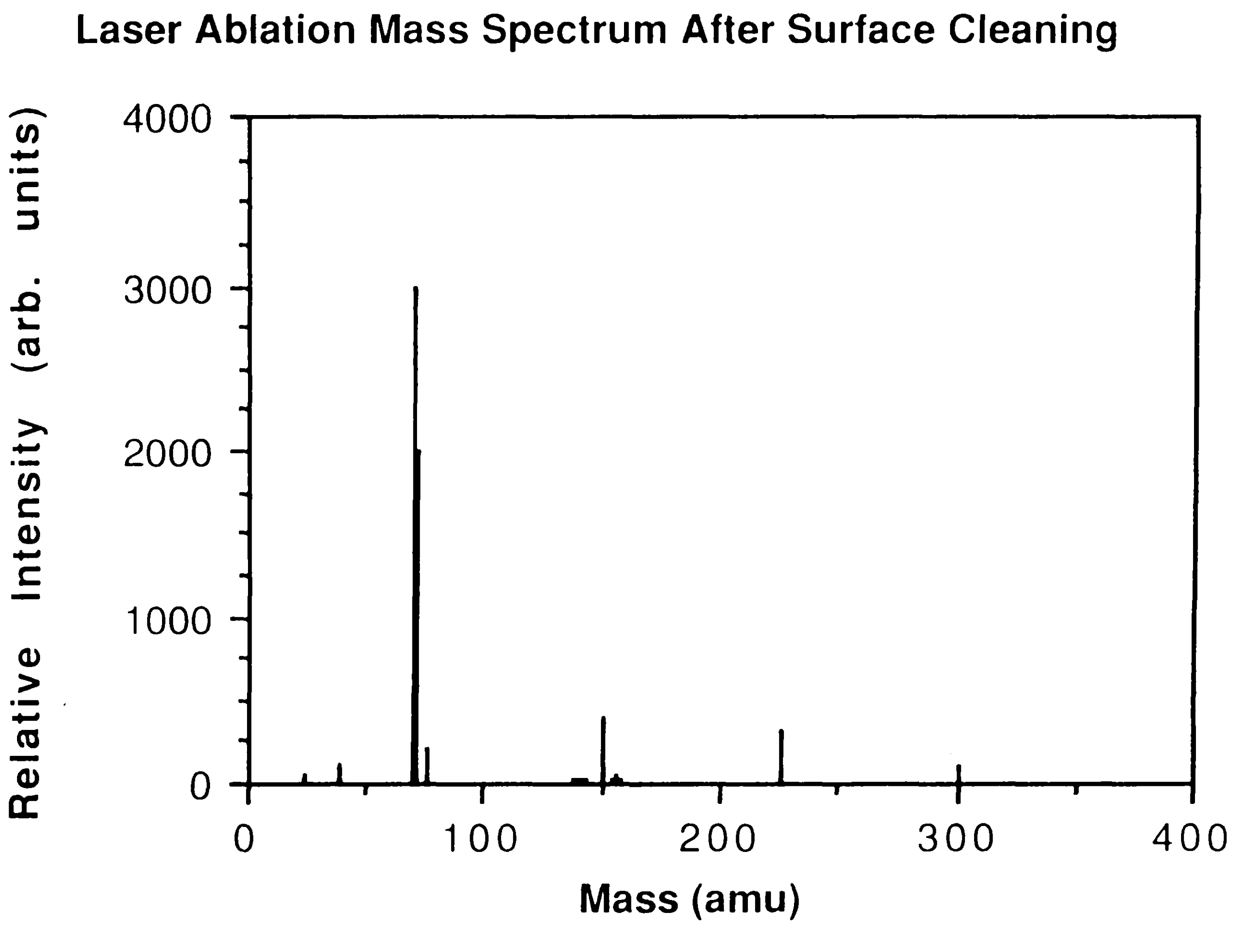

Figure 5.10(a) Mass spectrum resulting from the action of an ablating laser at 266 nm from the GaAs substrate after surface cleaning with higher intensity laser radiation.

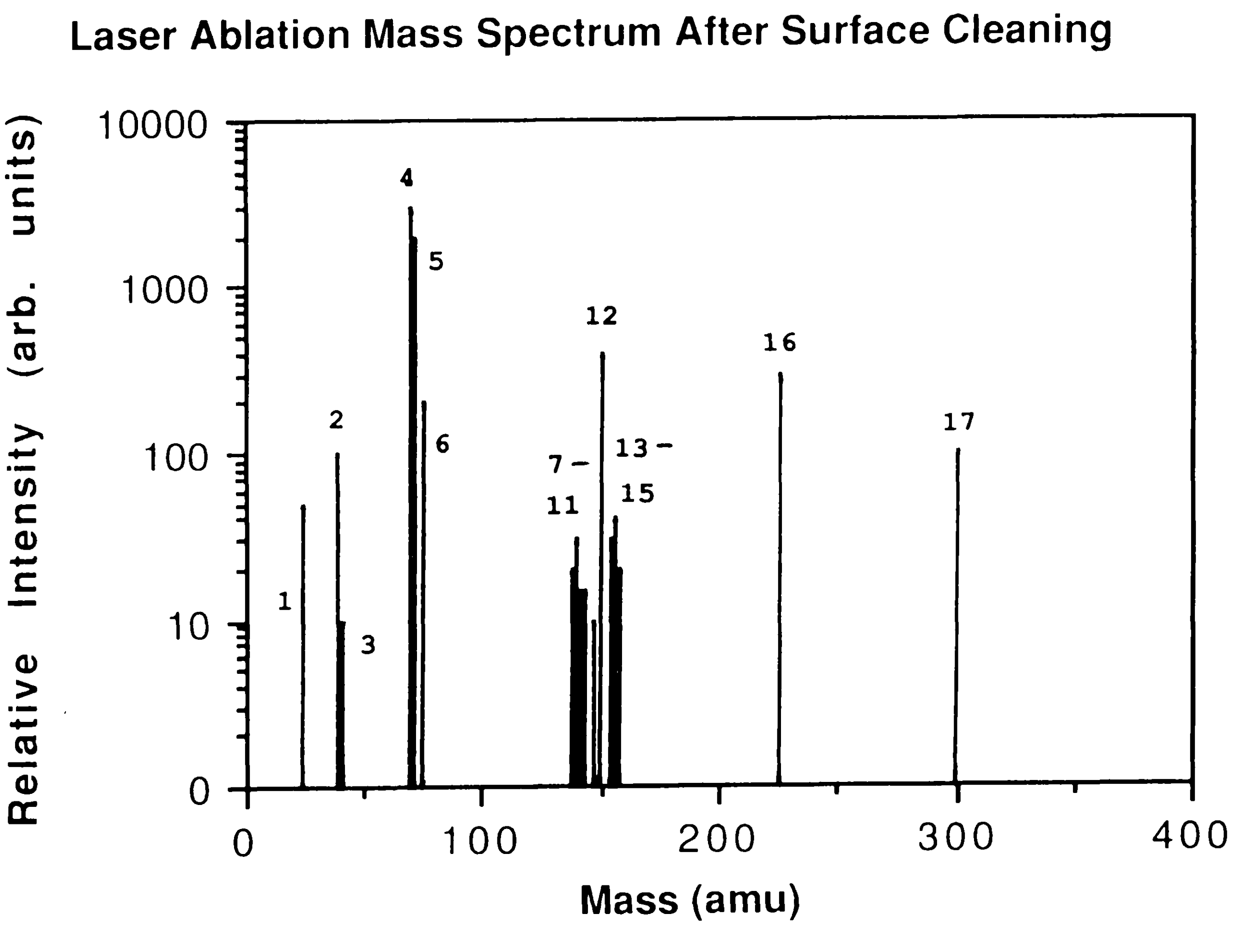

Figure 5.10(b) Log plot for the mass spectrum shown in figure 5.10(a).

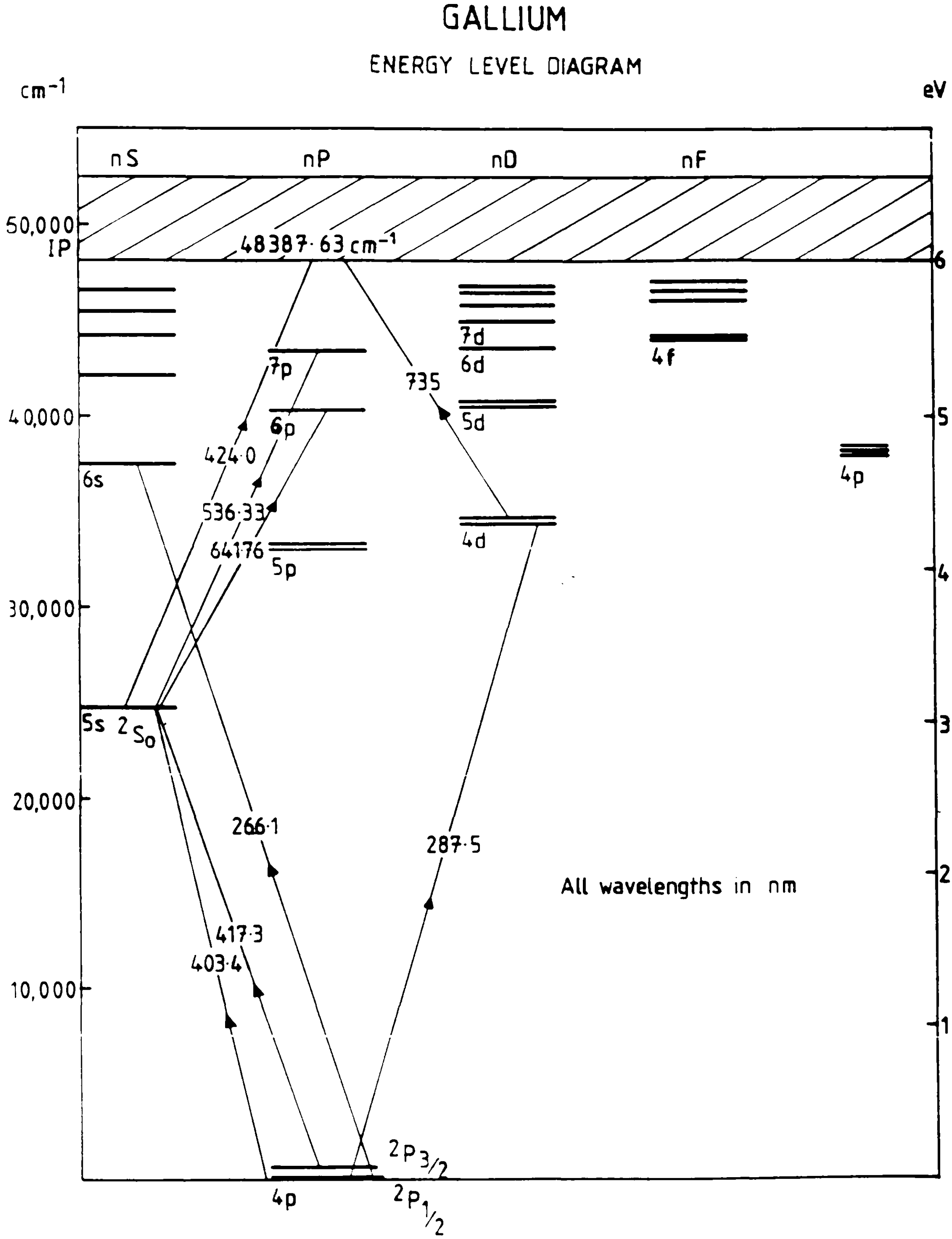
GALLIUM
ENERGY LEVEL DIAGRAM
cm⁻¹
eV
nS
nP
nD
nF
50,000
IP
48387·63 cm⁻¹
40,000
30,000
20,000
10,000
6
5
4
3
2
1
6s
5s
2 S0
7p
6p
5p
4p
7d
6d
5d
4d
4f
4p
424·0
536·33
641·76
735
266·1
287·5
417·3
403·4
2P3/2
2P1/2
All wavelengths in nm

Figure 5.11

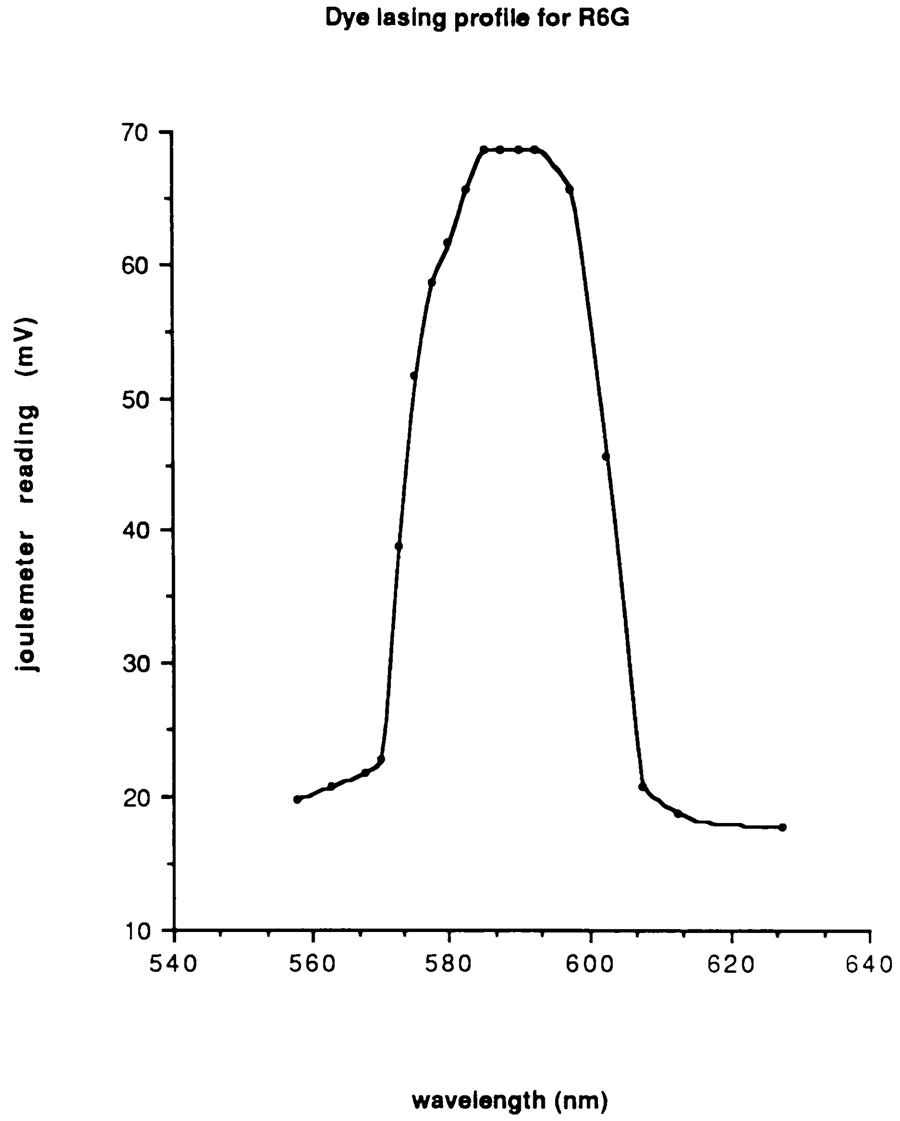

Figure 5.12 Graph of joulemeter signal versus wavelength for the dye laser output. Dye used was Rhodamine 6G.

prone to re-absorption, possibly as a result of elevated surface temperatures. In the case of the more surface selective collisional ion sputtering, liberated material is more likely to originate from the first few monolayers of the sample, with which adsorbed species are generally associated.

With further improvement to the vacuum quality, down to the 10^{-9} mbar range, the rate of re-adsorption had diminished to a degree that after sputter cleaning, pulsed ion gun operation was possible over prolonged analysis periods without significant re-development of the surface contaminant levels.

Gallium RIMS.

The analysis now proceeds to the next stage, involving the introduction of the resonant laser excitation step.

The excitation scheme adopted for Gallium was that of a single photon excitation from the 4p $^2P_{1/2}$ ground state to the 4d $^2D_{3/2}$ excited state (separation 34781.67cm^{-1} [74]), via the absorption of a photon of wavelength 287.508 nm. Both the 4p ground state and the 4d excited state are in fact doublets with relative level splittings of 826.24 and 6.25 cm^{-1} respectively, Figure 5.11. However, excitation to the $4d_{5/2}$ from the $4p_{1/2}$ is forbidden (See Chapter 2), and must be achieved from the $4p_{3/2}$ upper ground state. The excitation wavelengths from the upper ground state of Ga to the split, excited 4p state are 294.503 and 294.45 nm.

The source of the excitation wavelength was the frequency doubled component of a red laser at ~575 nm, generated in a KDP crystal. The dye used was Rhodamine 6G (or Rhodamine 590) (Exciton) in a solution of ethanol. Ionisation from the excited state can be achieved via the absorption of a photon from the red laser at twice the exciting wavelength. This arrangement is perhaps not the most desirable, as the resonant wavelength at ~575 nm does not correspond to the peak/plateau of the tuning curve of the dye as can be observed from Figure 5.12, and hence the full power available cannot be efficiently applied on resonance. Also, wavelength dependent measurements become less accurate due to the variation in lasing efficiency and hence in available laser power at both wavelengths, the red fundamental and its frequency doubled component. However, on the positive side, the lasing efficiency of the dye is remarkably good (up to 20%) in comparison with alternative dyes for this wavelength, and was not particularly prone to variations in the concentration of the solution.

Figure 5.13 shows the first resonantly induced ion signal for Ga observed with this apparatus, superimposed on the pulsed secondary ion signal. At this stage the laser was unfocused, with an asymmetric beam profile approximately 5mm across, and was directed close to and parallel to the sample surface. The accelerating potential was relatively low at +200 volts, and was applied directly to the sample stub. As a result, the two Gallium isotopes were unresolved due to the wide initial spatial distribution and the relatively large energy spread of the resonant ions with respect to their average kinetic energy.

With the aid of moderate focusing of the laser and adjustment of the extract electrode potentials, the effect of the spatial distribution on the mass resolving power was reduced considerably, thereby allowing a degree of resolution of the two isotopes.

The effect of the initial energy spread of the resonant ions was alleviated to an extent by increasing the accelerating potential and thereby reducing the relative energy spread of the ions. Increasing the potential also serves to improve the ion extraction efficiency by increasing the axial velocity (i.e. along the spectrometer axis) of the ions relative of their radial velocity, thereby reducing the dispersion of the particles, and hence bringing more ions within the acceptance angle of the ion optics and the influence of their associated fields. However, in situations such as this experiment which utilise a primary beam of charged particles incident at quite severe angles to the normal, there is a limit to the extraction field strength which can be applied, governed by the deflecting effect of the sample electrode surface, which in the case of low energy primaries may produce a significant surface reflected ion component, as well as a reduction in the current density on the sample, which will ultimately result in a drop in the total secondary particle yield and a loss in both spatial and mass resolving power. In the present case a sample potential of +600 volts was adopted which was found to be the minimum voltage which would allow reasonable resolving of the Ga isotopes.

With the laser rather more tightly focussed (~1mm across), in order to give a maximum in ion intensity and optimum resolution of the Ga isotopes, and with SIMS ions sufficiently suppressed (by the method described in Chapter 4, and demonstrated in Chapter 7), a single event mass spectrum, Figure 5.14, was obtained with the isotopes well resolved. This signal was then transferred to the transient recorder based acquisition system (Chapter 4), for subsequent data accumulation and storage, over a

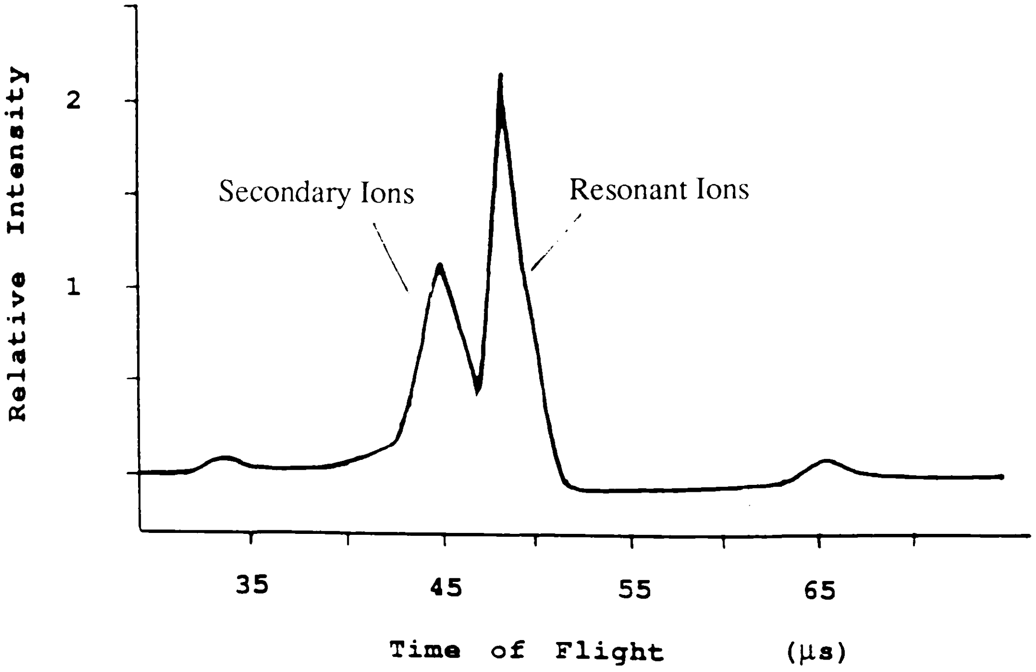

Figure 5.13 Simultaneous SIMS / RIMS-TOF spectrum obtained from the GaAs substrate with the laser tuned to the resonant transition for Ga.

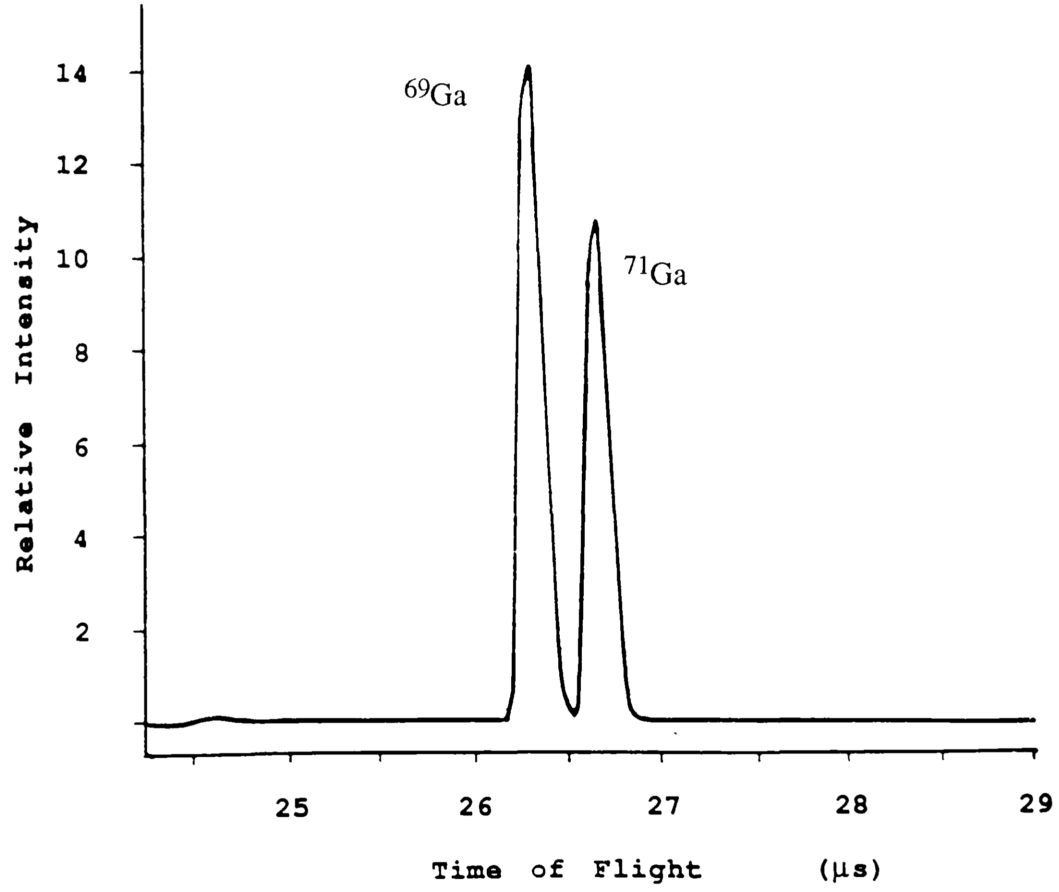

Figure 5.14 Ga resonant ion TOF spectrum with improved mass resolution.

user designated number of events. Figure 5.15 shows the mass spectrum obtained after one thousand laser shots. Due to a build up of noise in the signal line, an inbuilt software discriminator was implemented, which unfortunately had the effect of removing the lower portion of the Ga resonant signal, and consequently, the isotopic ratios are not accurately represented in this case.

With SIMS suppression again in effect, a wavelength dependent analysis of the intensities of both Ga isotopes was performed in the region of the Ga resonance. Figure 5.16 shows the peak intensity versus wavelength dependence for single event spectra with isotopic ratio comparing well with the known natural abundance ratio, and the FWHM of the peaks (~0.125 nm) also in reasonable correspondence. This implies the laser bandwidth was great enough to cover the hyperfine structure of the isotope shifts.

A similar wavelength dependent analysis was performed with the aid of the transient recorder. Figure 5.17 shows a series of spectra, displaying the resonant behaviour of Ga, each for one hundred events. From this same data, a peak height versus wavelength graph was plotted (Figure 5.18) for the ^{69}Ga peak, displaying a FWHM in reasonable agreement with that for the single event.

Aluminium SIMS.

The subject for analysis was now switched to Aluminium. Once again the initial work involved simply a pulsed SIMS time-of-flight study of the sample surface yielding a mass spectrum of the form of Figure 5.19. As was the case with the previous sample, several prominent peaks are clearly in evidence, while others are barely discernible.

From the observed intensity of the third peak and an approximate calculation of its mass from the flight time (Equation 4.1), it could reasonably be attributed to Aluminium secondary ions and was therefore assigned a mass of 27 amu. The relative masses of the other peaks could then be calculated from their flight times relative to that of Aluminium. Table 5.3 gives the masses of the various SIMS peaks calculated in this manner.

In comparing the masses in Table 5.3 with those from Table 5.1 for GaAs, we see a fair correspondence between peaks 1, 2, 4 and 5 for both tables as well as between peak 7 in Table 5.3 with peak 9 in Table 5.1.

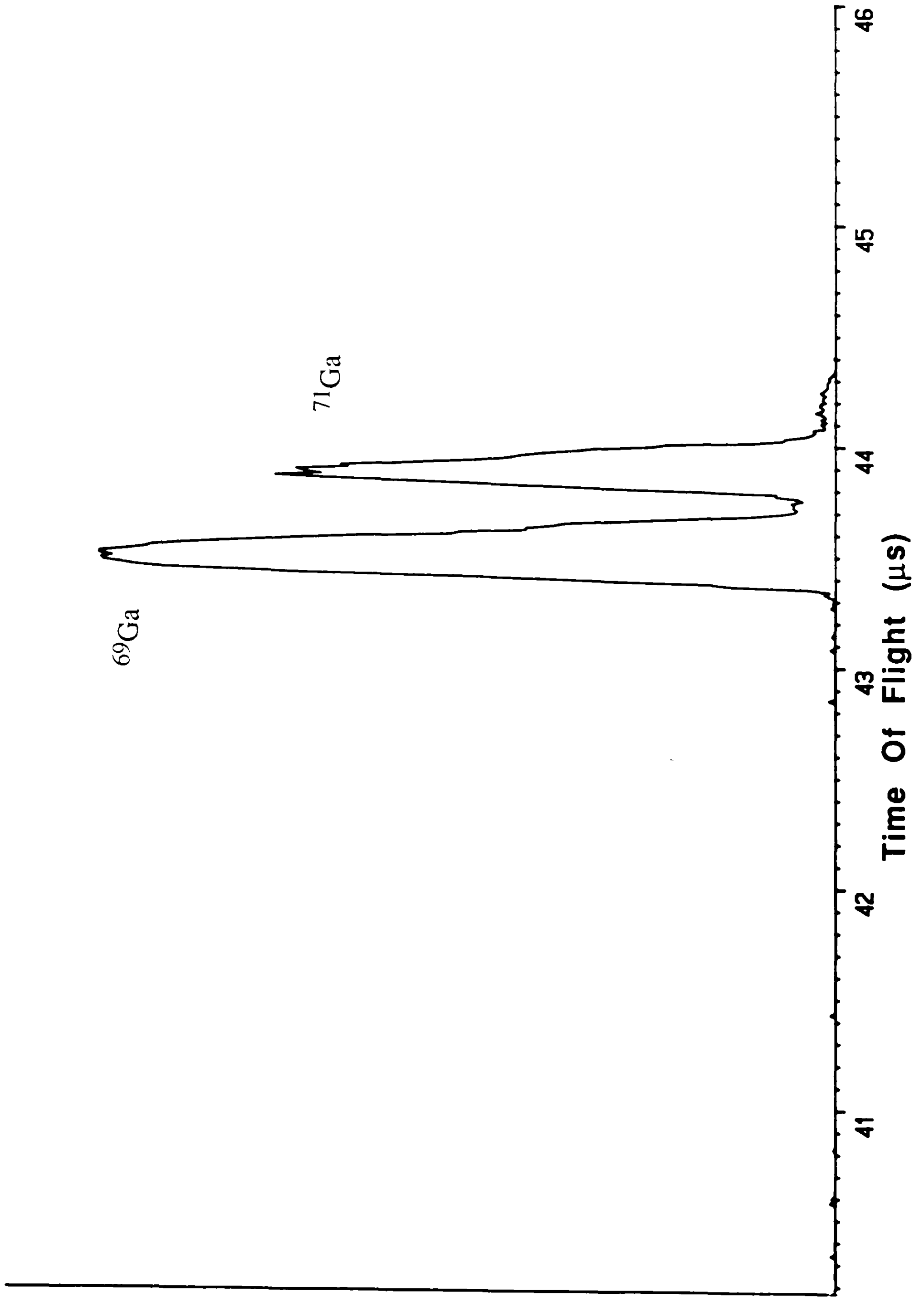

Figure 5.15 Ga RIMS-TOF spectrum as recorded by the transient recorder based acquisition system (refer to Chapter 4).

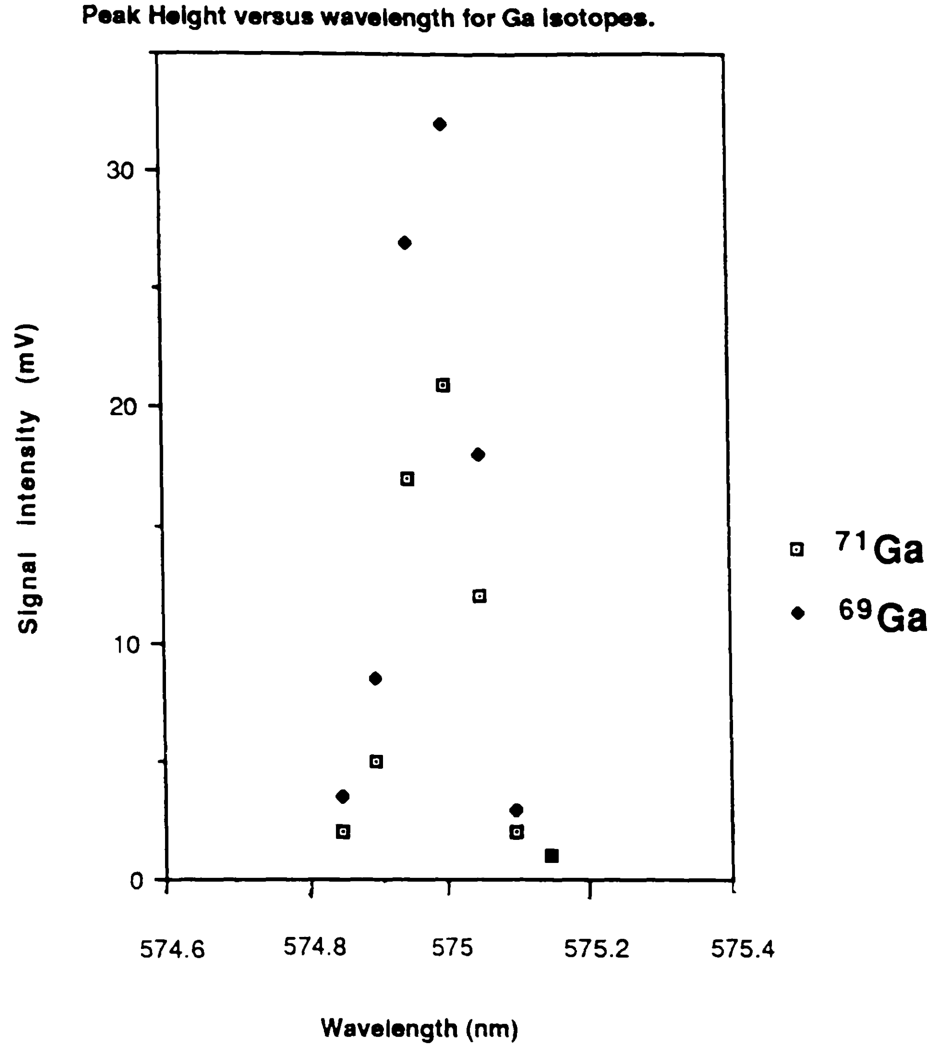

Figure 5.16 Graph of peak height, as measured on an oscilloscope trace, versus wavelength around resonance for both Ga isotopes.

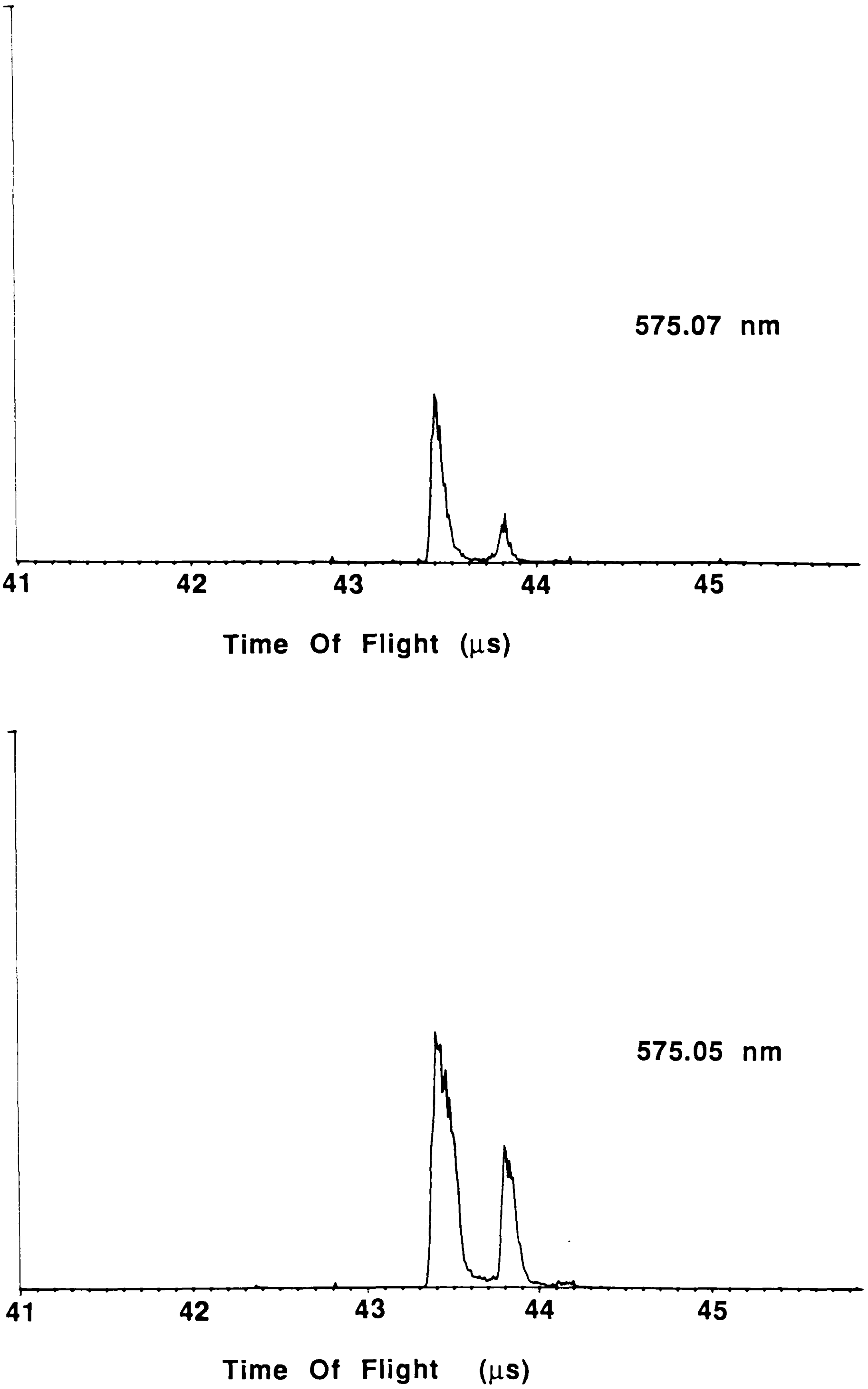

Figure 5.17 The following series of mass spectra show the variation in total ion intensity as a function of wavelength for the Ga isotopes. The spect . were recorded by the transient recorder for 100 laser shots.

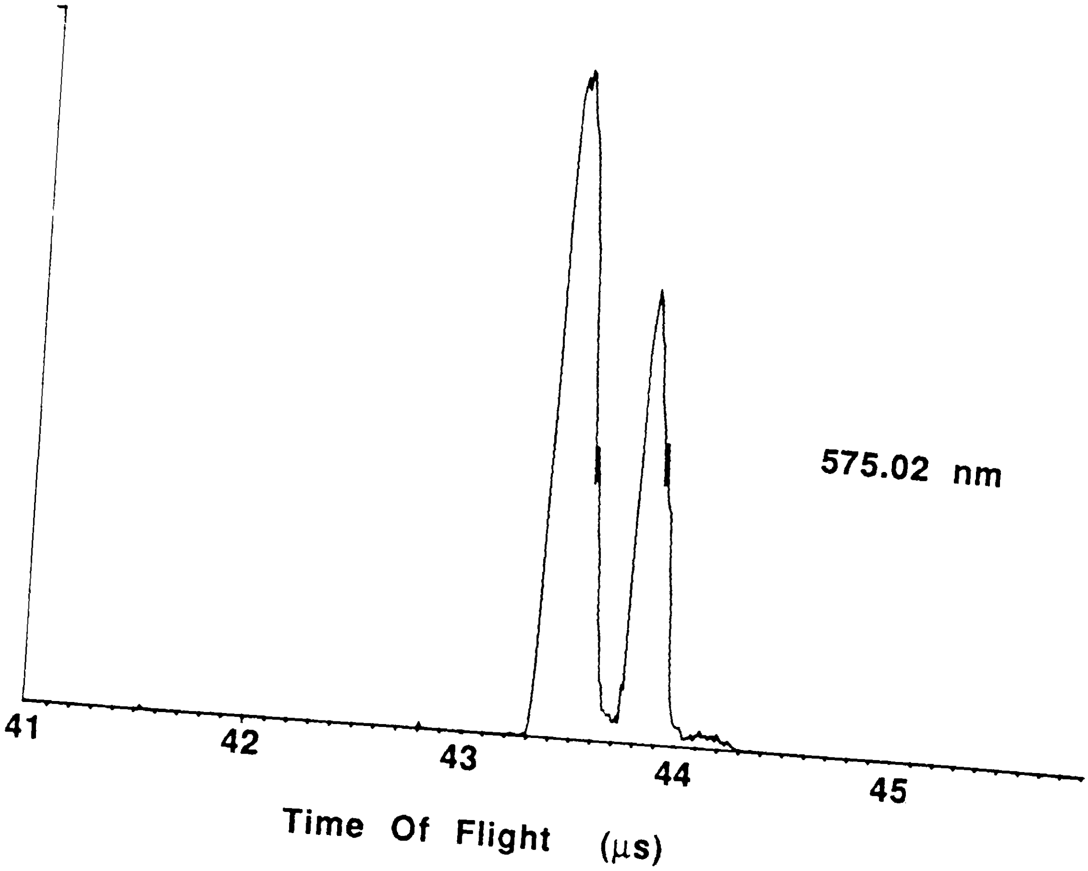
575.02 nm
41
42
43
44
45
Time Of Flight (μs)

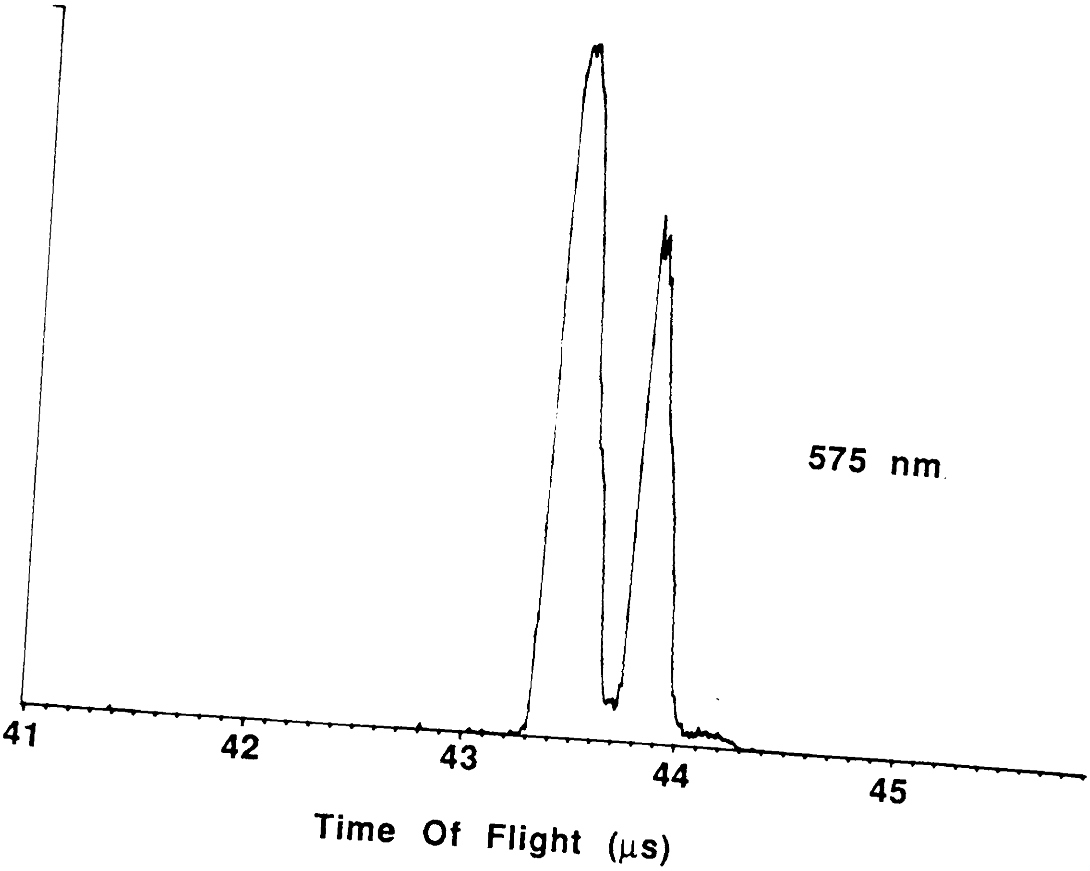
575 nm
41
42
43
44
45
Time Of Flight (μs)

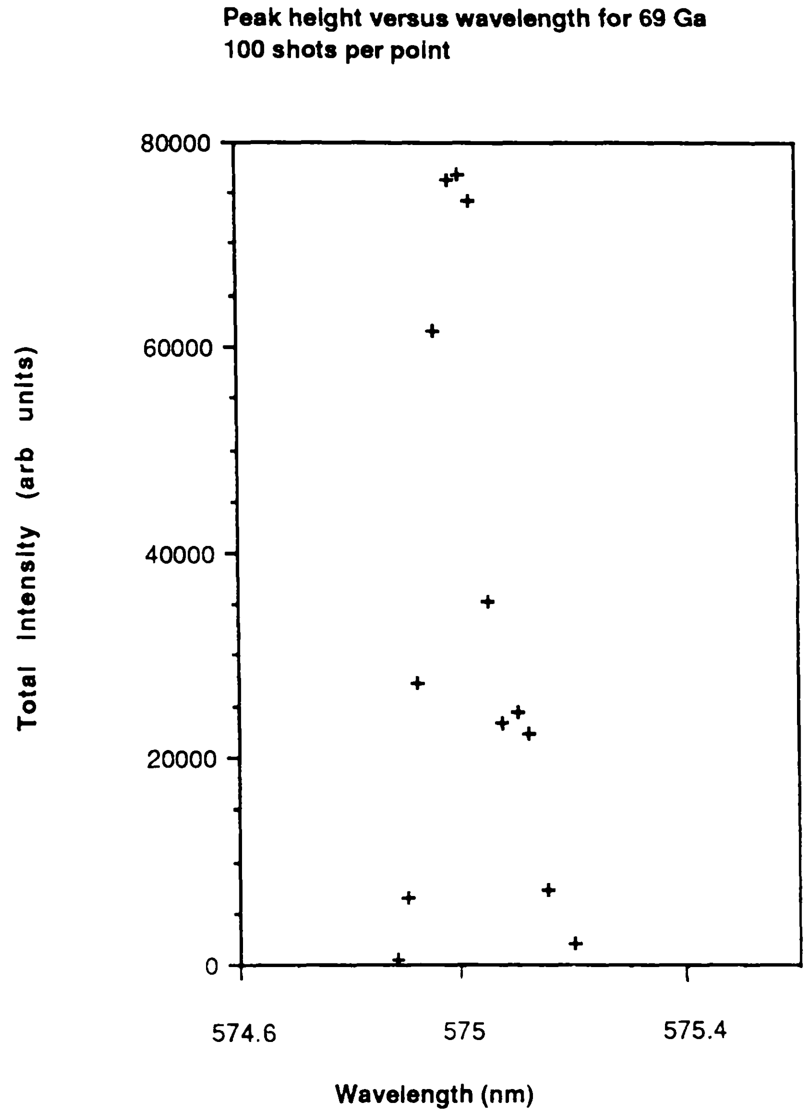

Figure 5.18 Graph of total ion intensity versus wavelength for the ^{69}Ga isotope, as shown in Figure 5.17.

After sputter cleaning, the major background peaks had diminished considerably to reveal a triplet of previously obscured masses, Figure 5.20, of roughly equal intensities. These were subsequently calculated to be 39.2, 41.5 and 43.2 amu. Note that the flight times in this case differ due to a change in the accelerating potential.

A possible candidate for mass 39.2 is ^{39}K which has already been observed as a surface contaminant on GaAs, and is by far the most abundant isotope of K at ~93%. Similar elemental candidates for the other two peaks cannot be found, which would tend to imply that these two masses, if not all three, result from organic or oxide contaminants as are the more predominant peaks.

After further cleaning, and with a base pressure now in the 10^{-9} mbar regime, the extraneous peaks had all but disappeared, and showed no significant signs of redevelopment under pulsed operation during the course of further experimentation.

Aluminium RIMS.

As with Ga, the resonant excitation of Aluminium proceeds through the absorption of a single UV photon from a *p* to a *d* state, in this case from the 3p ^{2}P ground state to the 3d ^{2}D excited state, Figure 5.21. Once again, both states have split levels corresponding to the J = 1/2 and 3/2 levels with separation 112.04 cm^{-1} for the *p* state, and J = 3/2 and 5/2 for the *d* state with a separation of only 1.34 cm^{-1}[74]. From the $3p_{1/2}$ state, excitation is only available to the $3d_{3/2}$ at a wavelength of 308.305 nm, while from the upper gound state, $3p_{3/2}$, excitation is possible to both the $3d_{3/2}$ and $3d_{5/2}$ with resonant wavelengths of 309.373 and 309.36 nm respectively.

The required UV photons are generated in the same KDP crystal as used for Ga, although in this case, the source laser originated from Rhodamine 610 (Exciton) dye, in ethanol solvent. The energy available from the red photons at twice the excitation wavelength is sufficient to promote an electron into the continuum. In this case the transition wavelengths sit comfortably within the plateau region of the dye.

Figure 5.22 shows the spectra obtained on passing the 'on resonance' laser close to the sample surface. The mass peaks observed correspond to the sputtered secondary ions and the resonantly ionised neutrals. The resonant transition involved in this case was that from the $3p_{1/2}$ to the 3d state. The delay between the primary ion pulse and the firing of the laser was varied for maximum intensity of the resonant

Table 5.3 Calculated masses for the peaks in the SIMS-TOF spectrum shown in Figure 5. 19 from Aluminium foil.

Peak No.	Calculated Mass (amu)
1	0.8
2	14.6
3	27
4	45.2
5	60.8
6	73.3
7	157.1

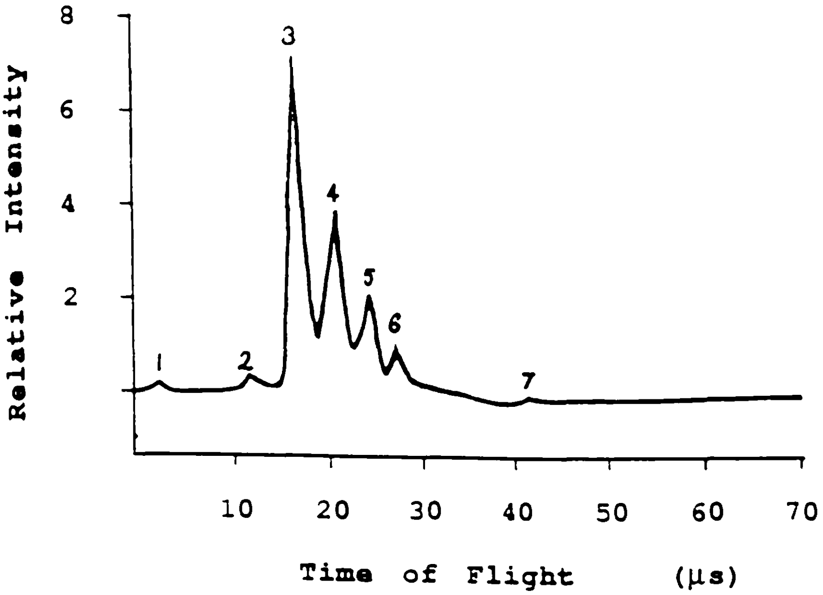

Figure 5.19 SIMS-TOF spectrum (as obtained from an oscilloscope trace) from aluminium foil.

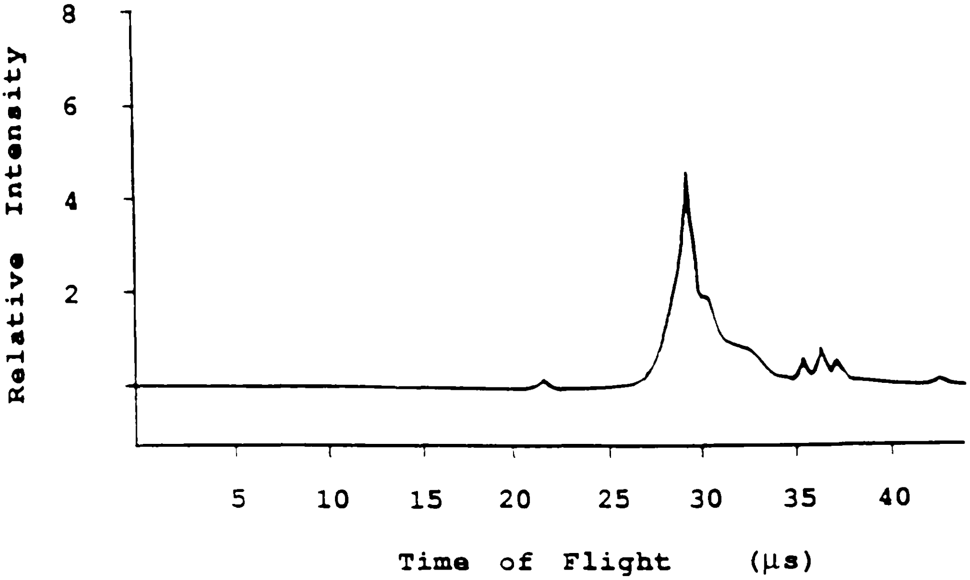

Figure 5.20 SIMS-TOF spectrum from the same Al foil sample after sputter cleaning of the surface for several minutes.

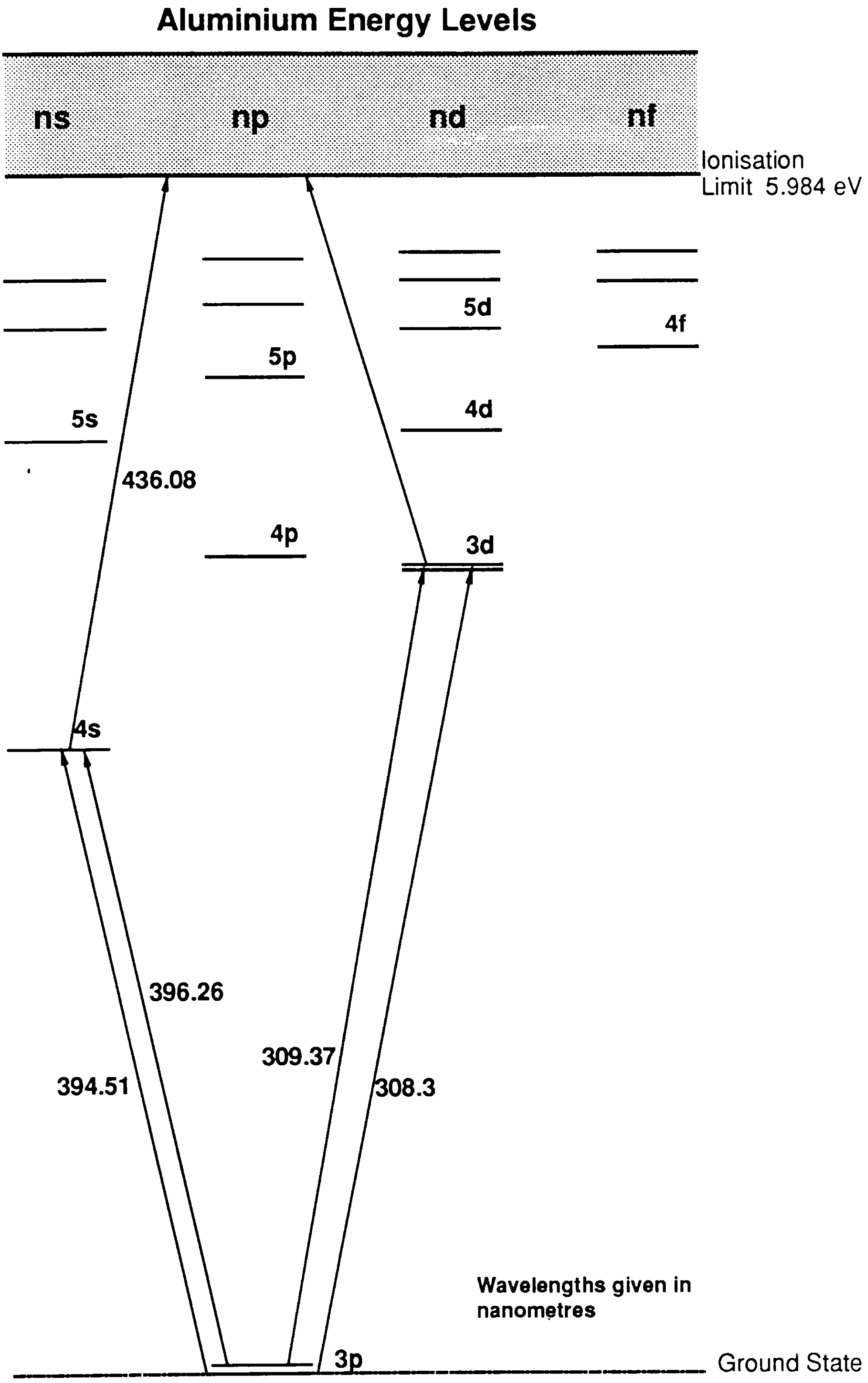
Aluminium Energy Levels
ns
np
nd
nf
Ionisation
Limit 5.984 eV
5d
4f
5p
5s
4d
436.08
4p
3d
4s
396.26
309.37
394.51
308.3
Wavelengths given in
nanometres
3p
Ground State

Figure 5.21

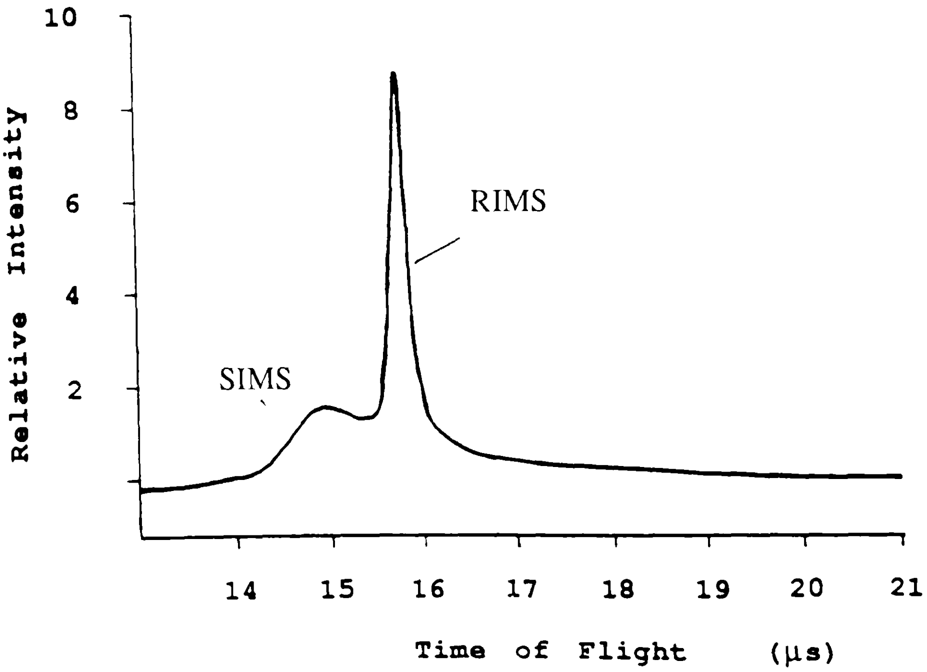

Figure 5.22 Combined SIMS / RIMS-TOF spectrum of Al from Al foil sample.

peak.

With the ion gun maintained in the pulsed mode, the ADC gate delay was adjusted to coincide with the resonant peak arriving at the input. Under computer control, the wavelength of the red laser was scanned over 6 nm, corresponding to 3 nm in the doubled UV, in a range extending over the resonant transitions from both the $3p_{1/2}$ and $3p_{3/2}$ ground states. This is shown in Figure 5.23, where there is a substantial enhancement at the resonant wavelengths. The permanent background level again corresponds to the portion of the secon .y ion pulse, which is laser independent, below the resonant signal.

Of particular note is the relative intensity of the peaks which implies a similar ionisation probability from both ground states in Aluminium. In thermal equilibrium, the population of atomic energy states is given by the Boltzmann distribution, and therefore, the relative population of two states N_2 and N_1 with respective statistical weights g_2 and g_1, is:

$$\frac{N_2}{N_1} = \frac{g_2}{g_1} e^{(-\Delta E / k_B T)} \tag{5.1}$$

where ΔE is the separation in energy between the two states, T is the temperature, and k_B is Boltzmann's constant. For a two level system where all atoms are in the lower state $N_1 = N_0$ at T=0, it can be shown that the fractional population in the upper state at a temperature T can be expressed by:

$$N_2 = \frac{N_0}{\left[1 + \frac{g_1}{g_2} e^{\Delta E / k_B T}\right]} \tag{5.2}$$

For the Aluminium 3p ground state, the energy separation is 112.04 cm^{-1} and statistical weights equal to the level degeneracies 2J+1 are 1 and 2 respectively for the $3p_{1/2}$ and $3p_{3/2}$, which suggests a population in the J = 3/2 state of as high as 53.9 %, at room temperature of 300 K. With the additional consideration of a possible transition from the J = 3/2 to both 3d excited states in single photon excitation, a transition probability from the upper ground state comparable with that from the lower state is not unreasonable, assuming of course the absorption cross-sections from the

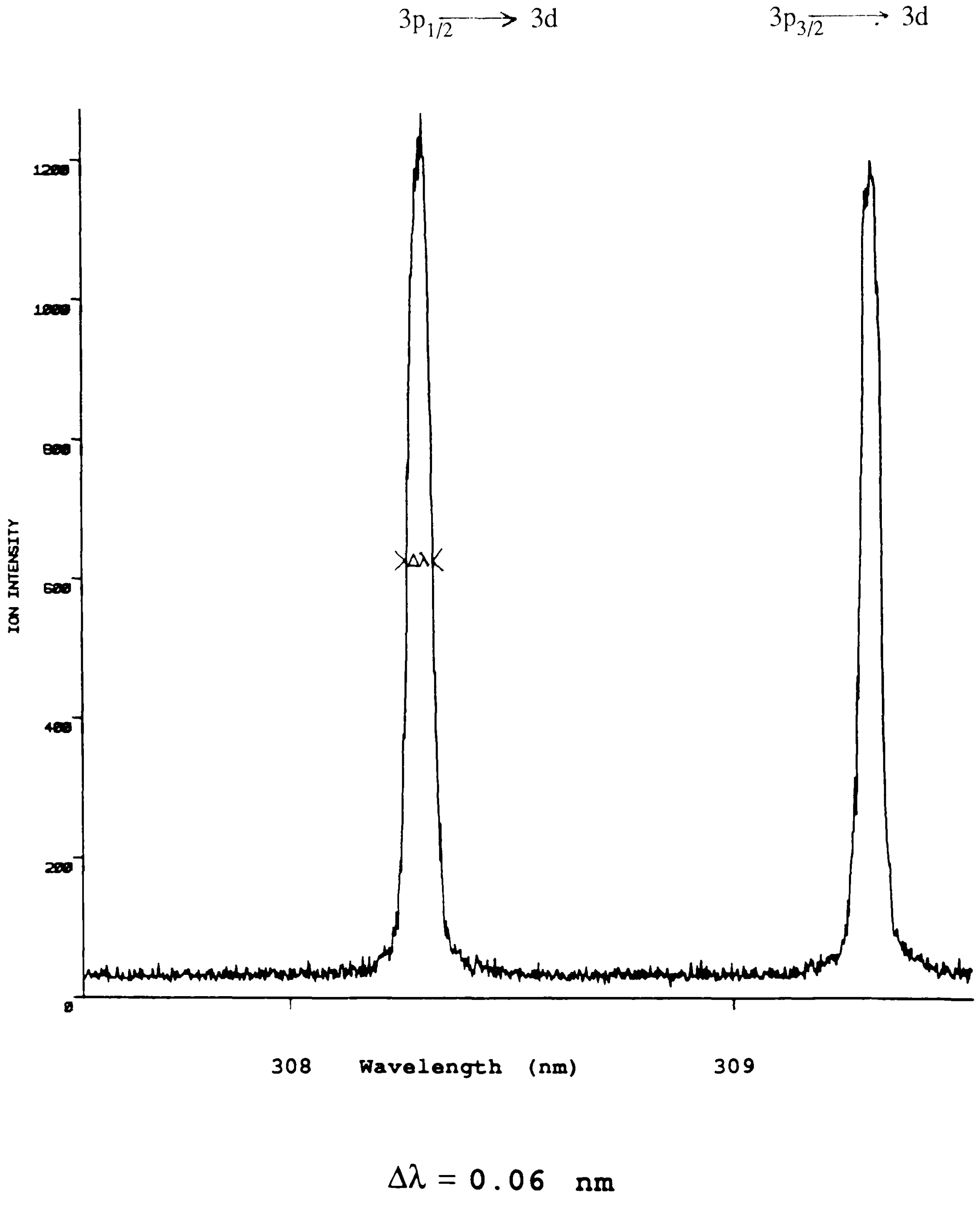

Figure 5.23 Aluminium ion yield as a function of laser wavelength showing the enhancements corresponding to resonant excitation from the split ground state. The ADC was gated to detect Al only. (Note the vertical scale is in arbitrary units)

two states are similarly comparable.

The measured transition widths are typically 0.06 nm for the excitation wavelength compared with a specified linewidth for the laser of ~0.03 nm.

For a reflection grating (of the Littrow type, as used in the dye laser), the resolving power is directly proportional to the number of lines illuminated, hence in a typical laser cavity, the laser linewidth is determined by the beam diameter within the oscillator. In order, therefore, to reduce the dye laser linewidth, an 'inline' prism beam expander was introduced into the cavity, directly in front of the grating, which serves to increase the vertical dimension of the beam by approximately a factor of ten, and reduce the divergence to ensure a more parallel beam, incident on the grating.

The effect of incorporating the beam expander is clearly evident in the wavelength dependences of Figure 5.24, displaying a decrease of typically a factor of three in the measured transitions. Also, as the theory presented above suggested, a higher transition probability from the upper ground state is indeed obtainable.

The implication of an observable difference in transition width between both situations (i.e with and without beam expander), is that there must be a significant contribution to the width of the transition in Figure 5.23 from the laser linewidth.

A typical decrease in the transition linewidth with the beam expander in place is, as already mentioned a factor of 3, which is less than the expected (specified) factor of ten, implying in this case, that a degree of broadening at least comparable with the laser linewidth, is occurring due to some other mechanism.

In the interaction of radiation with atoms in the gaseous phase, two types of transition broadening effects occur, namely homogeneous and inhomogeneous broadening.

Homogeneous broadening occurs in situations where each atom involved in the interaction is indistinguishable from every other (and hence no particular frequency can be associated with a particular atom), and is characterised by a Lorentzian lineshape. Two major sources of homogeneous broadening are collisional and power (saturation) broadening (see Appendix C). Power broadening in its simplest terms can be described by enhancement in the induced transition rates as the radiation intensity increases. This effectively reduces the lifetime of the states, thereby increasing the linewidth (by the uncertainty principle). Since the transition probability to an excited state is inversely related to the lifetime of the state, saturation effects can also result in a reduction in the ionisation probability, to the detriment of the analysis procedure.

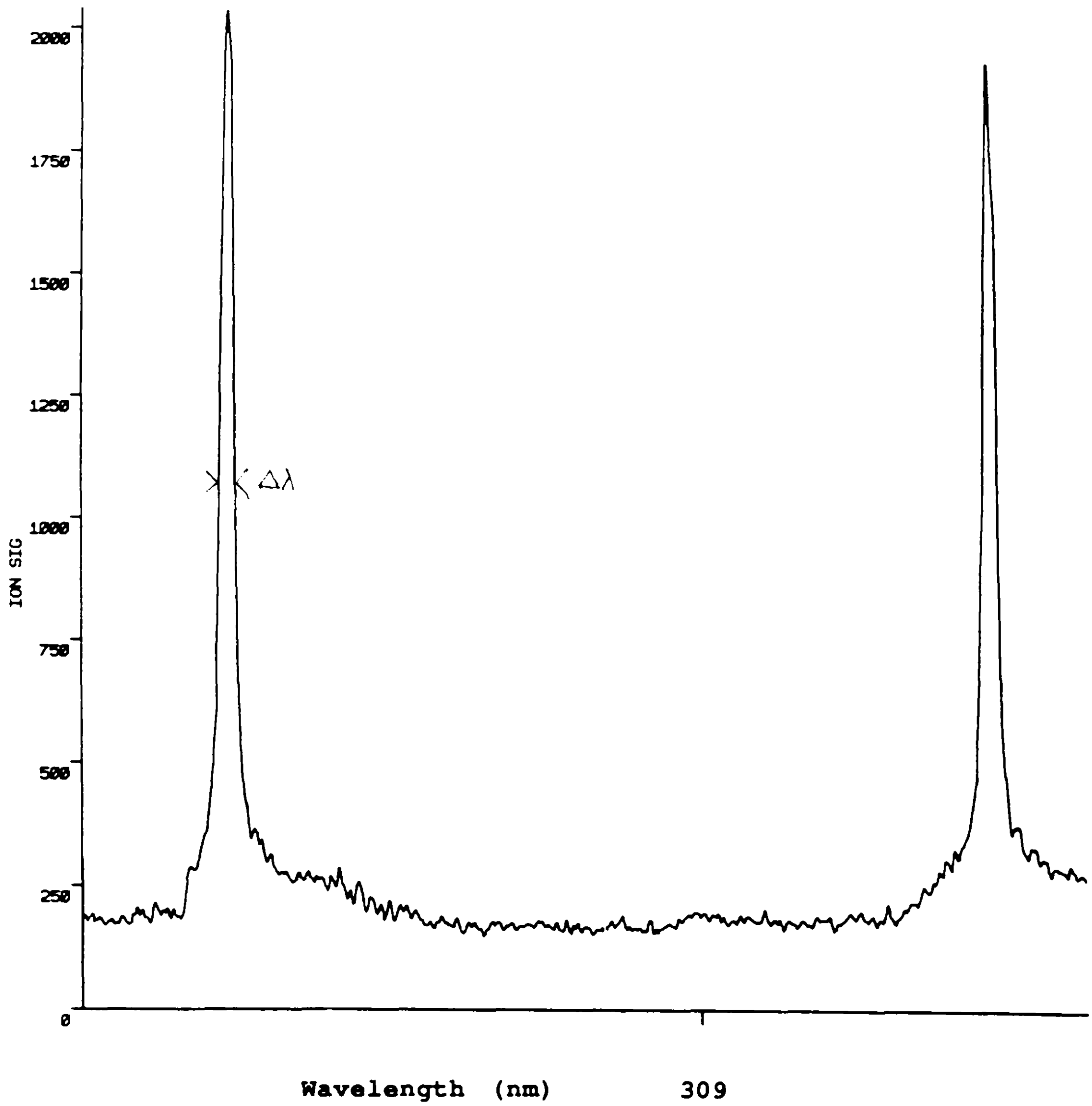

Δλ = 0.02 nm

Figure 5.24 Wavelength spectrum of Al ion yield showing the the effect on the interaction linewidth of reducing the laser linewidth.

In situations where the different atoms absorb at different frequencies, described by some parameter distribution, the broadening is termed inhomogeneous, and in this case, is generally characterised by a Gaussian line profile.

A prime example of such broadening is Doppler broadening (see Appendix C), in which case, the absorption frequency is dependent on the velocity of the individual atoms. In the case of ion sputtering, the temperature of the gas is typically low, evidence of which can be derived from the relative intensities of the measured transitions (Figure 5.23). Assuming, therefore, a temperature comparable with room temperature, ~300 K, the contribution to the transition widths from the distribution in velocities of the atomic components from Equation (C.10), is ~7×10^{-13} m (7×10^{-4} nm). which is small in comparison to the widths observed, thereby inferring that Doppler broadening is not a dominant factor here. Even if the effective temperature on sputtering is much higher than assumed here, perhaps an order of magnitude, the contribution to the broadening is only increased by a factor of about 3 relative to that at room temperature, still too small to be responsible.

The following discussion is concerned with further resonant ionisation analysis performed on the Aluminium sample, with the ion gun operating throughout in continuous mode.

The first series of wavelength spectra, Figure 5.25, illustrate the evolution of the resonant absorption lineshapes, as the energy of the incident primary ions is increased from 1.5 to 3 KeV. This has the effect of increasing the ion current in the manner implied by the graph of Figure 5.26, and thereby the number density of sputtered particles within the interaction volume of the post-ionising laser. This in turn enhances the resonant ion production. The effect can be observed in the initial, essentially linear portions of the curves of Figures 5.27 and 5.28 for peak height and peak area as a function of ion energy (current). At higher primary currents (~2.25 eV) however, the detected ion signal at line centre reaches a maximum value and remains essentially constant over the remainder of the range. Similarly, the variation in the total peak area, at around the same ion energy, displays a considerable reduction in the rate of increase, towards a constant level at higher energies. The implication here is that the ion detection efficiency of the spectrometer has reached an apparent saturation

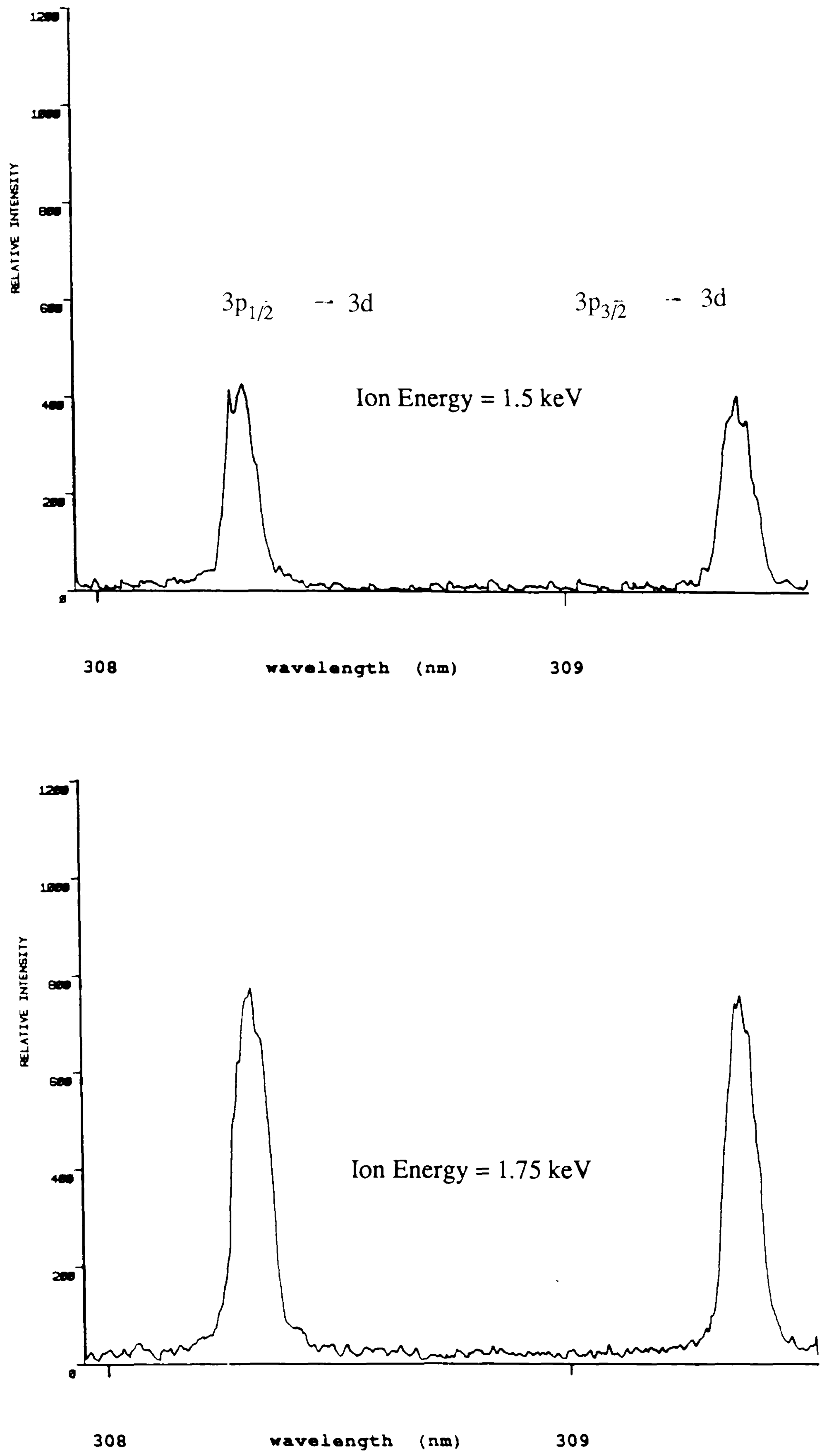

Figure 5.25 The following series of spectra show the relative effects on the Al ion yield and interaction linewidths of increasing the primary sputter ion energy.

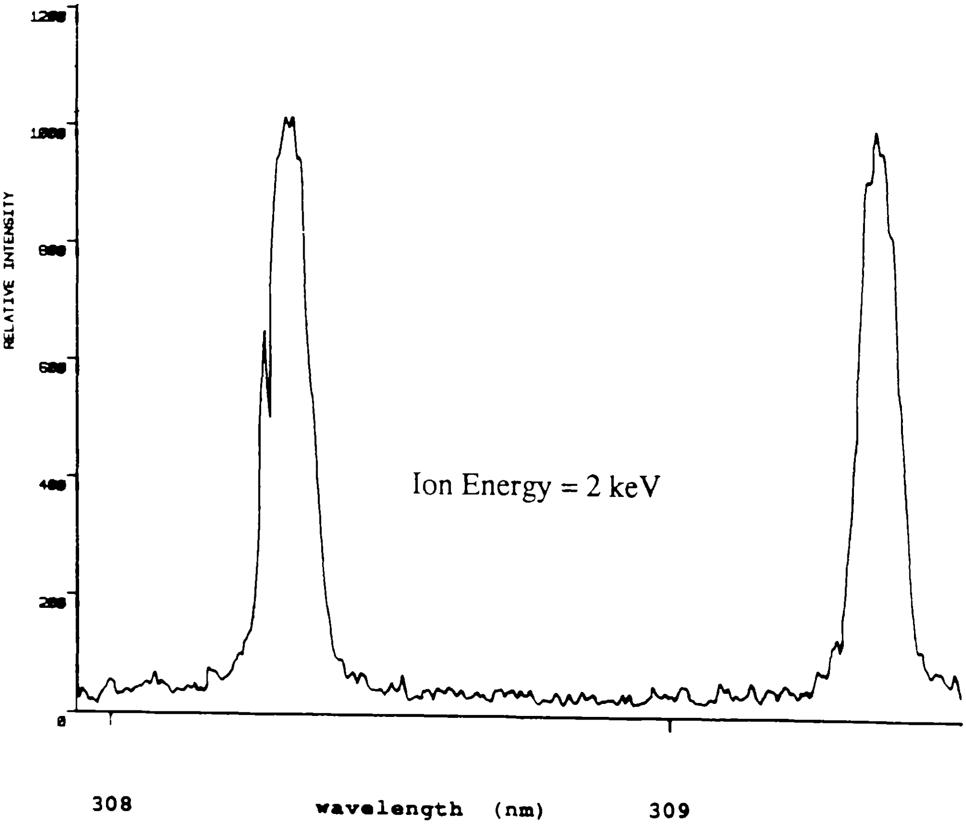
1200
1000
800
600
400
200
0
RELATIVE INTENSITY
Ion Energy = 2 keV
308
wavelength (nm)
309

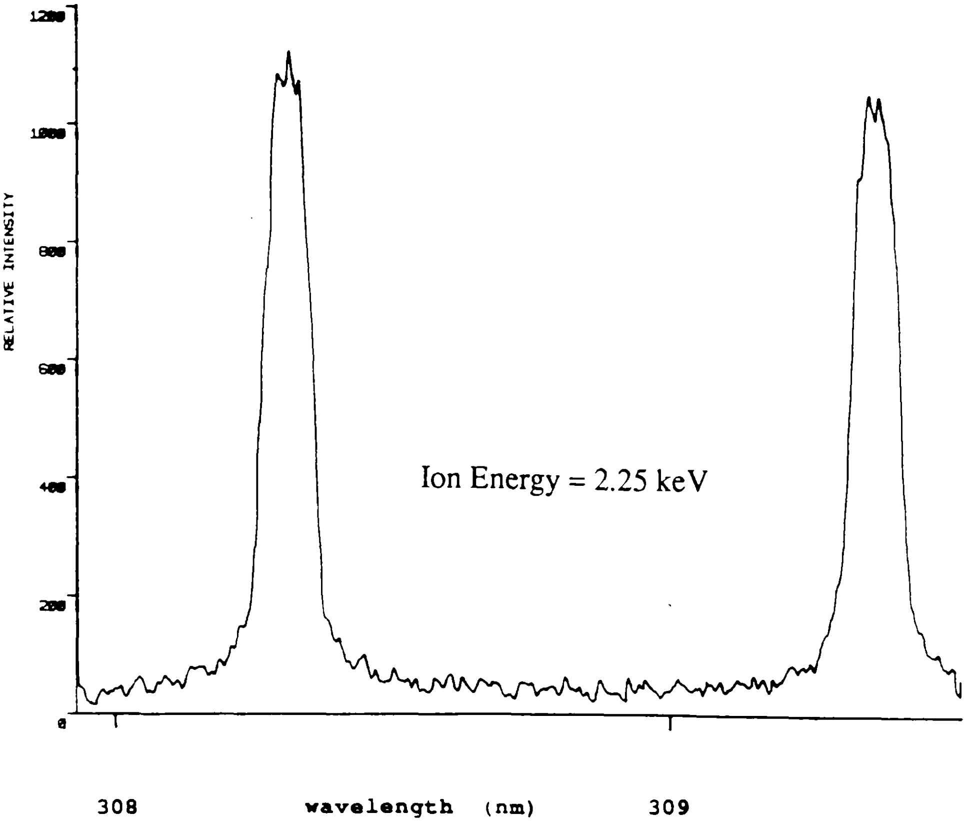
1200
1000
800
600
400
200
0
RELATIVE INTENSITY
Ion Energy = 2.25 keV
308
wavelength (nm)
309

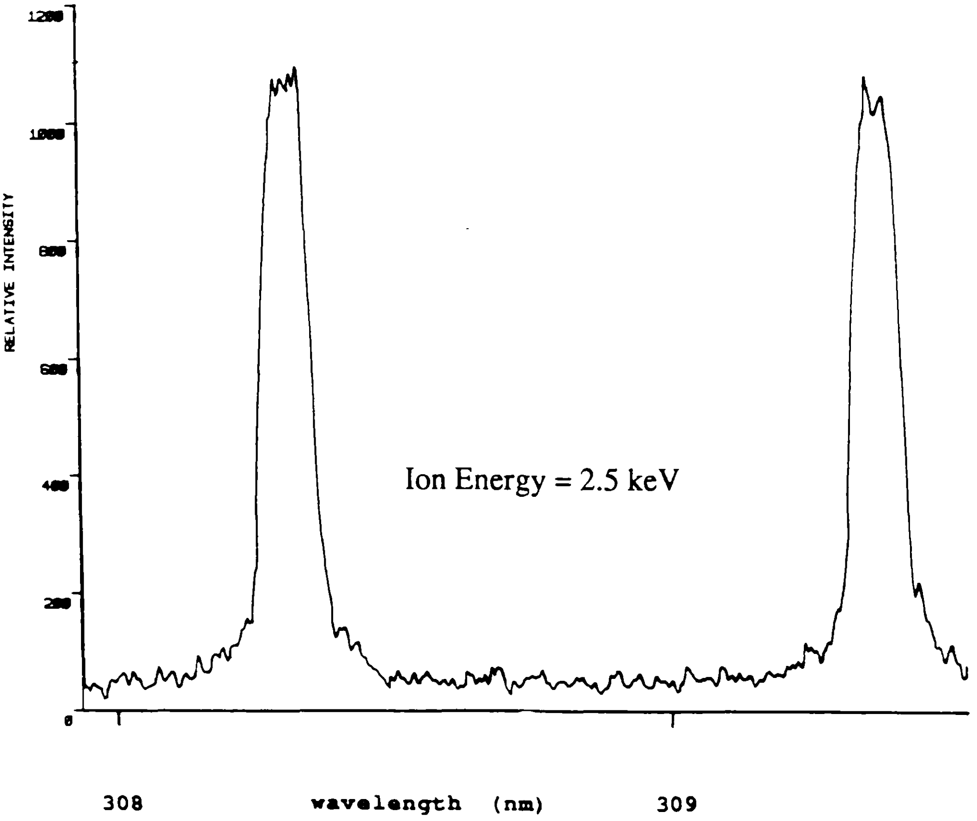

1200
1000
800
600
400
200
0
RELATIVE INTENSITY
Ion Energy = 2.5 keV
308
wavelength (nm)
309

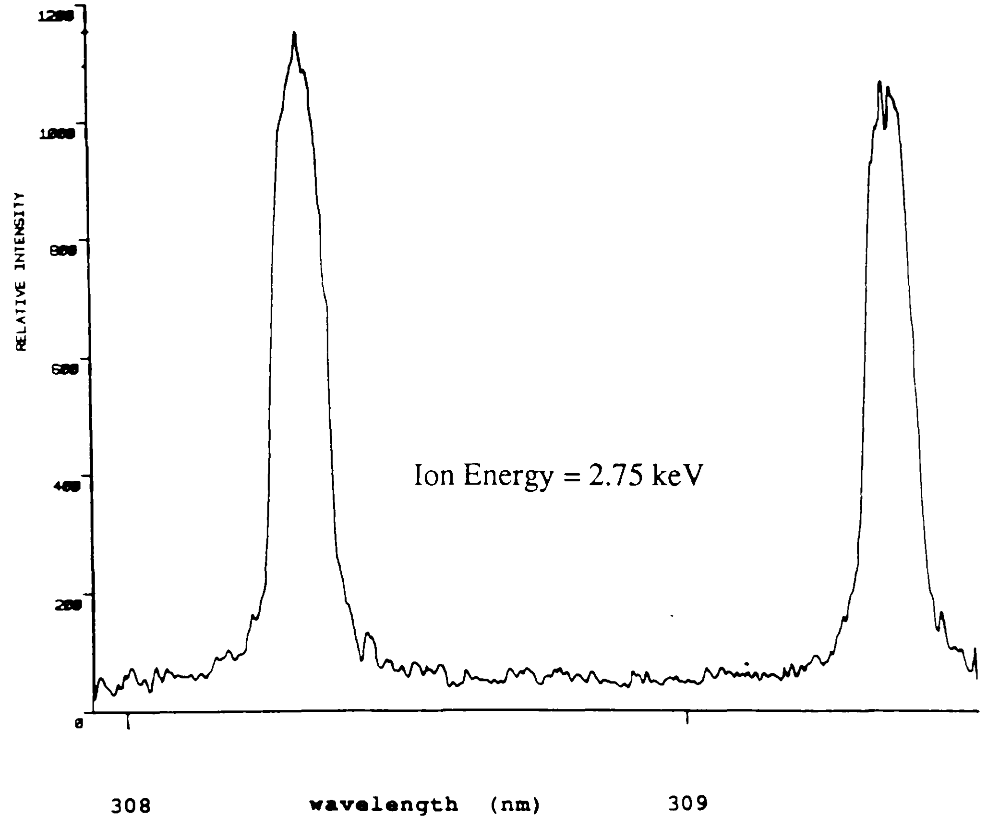

1200
1000
800
600
400
200
0
RELATIVE INTENSITY
Ion Energy = 2.75 keV
308
wavelength (nm)
309

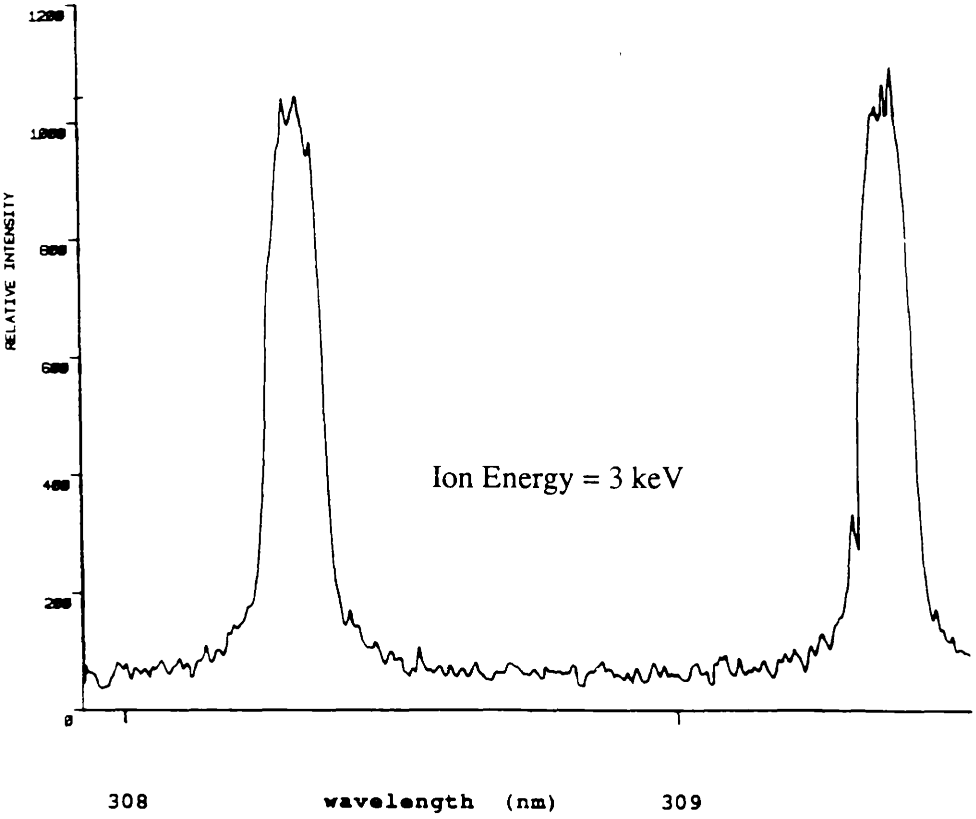
1200
1000
800
600
400
200
0
RELATIVE INTENSITY
Ion Energy = 3 keV
308
wavelength (nm)
309

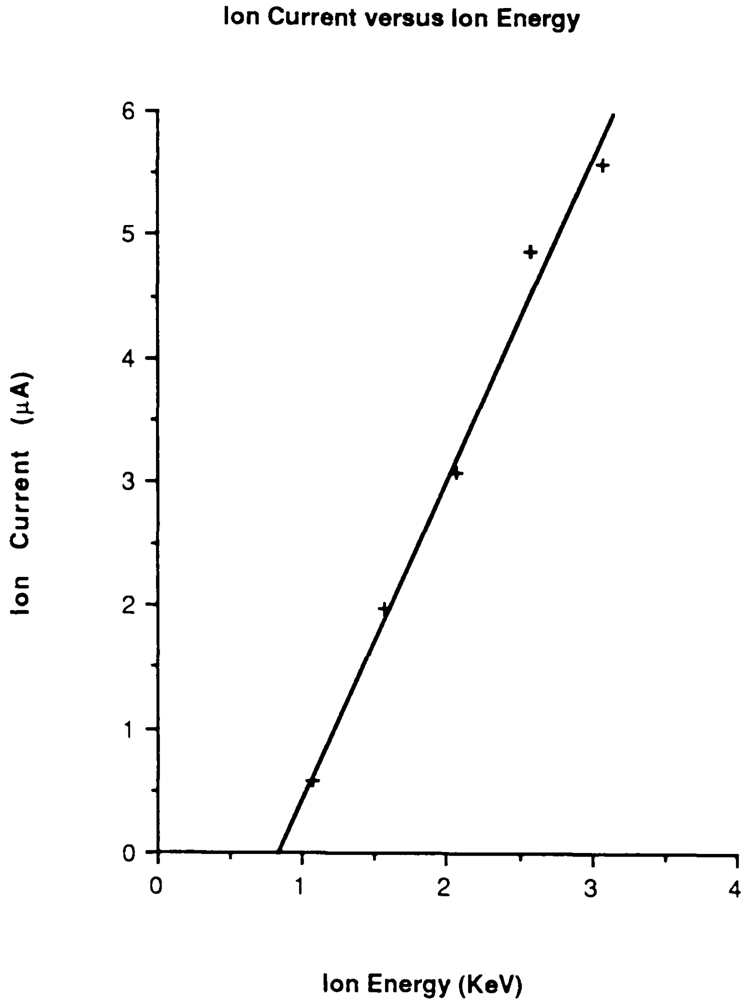

Figure 5.26 Dependence of ion current with ion energy

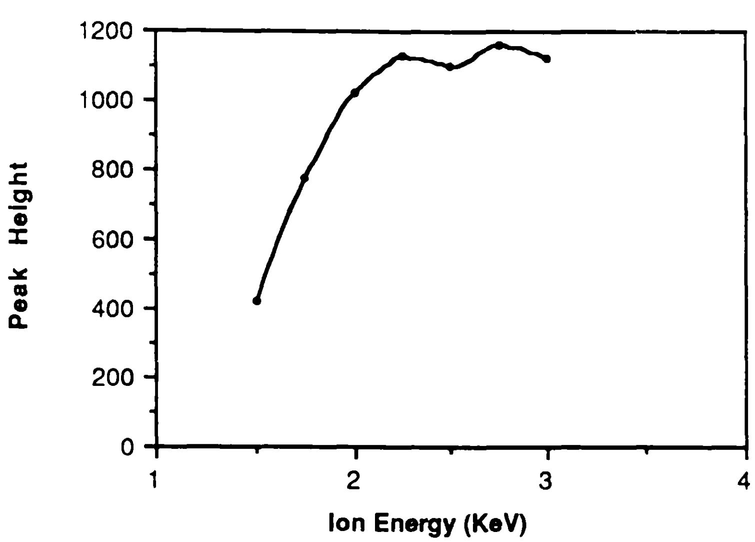

Figure 5.27 Al intensity as a function of primary ion energy (current) for the laser tuned to the first resonance transition shown in Figure 5.25.

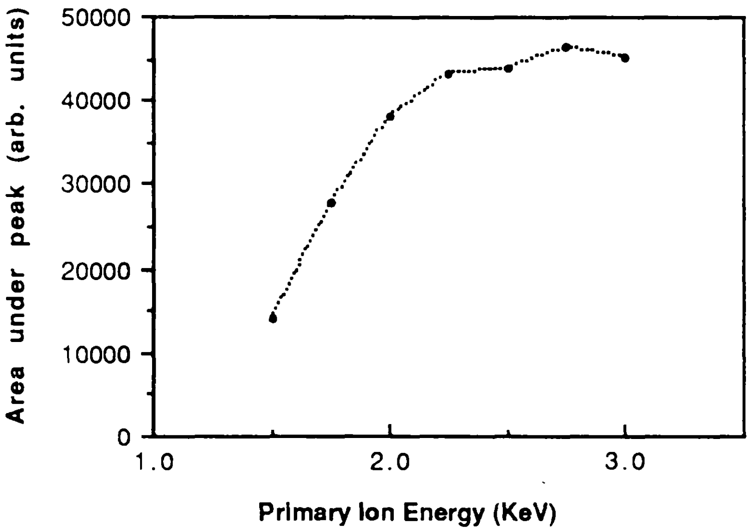

Figure 5.28 Resonant peak area, for the first transition shown in Figure 5.25, as a function of primary ion energy (current).

condition, due to space charge effects in either the ion detector or in the region of ion formation. Since the electron multiplier potential was adjusted for a signal maximum, corresponding to the maximum in primary ion energy, at a minimum voltage, space charge limitations within the dynode assembly due to its geometry and internal fields, over the charge density range encountered, should be minimised, and consequently, the likely situation occurring is one of saturation of the ion throughput of the ion extract optics, for positive charge, due to the repulsive effect of the associated field of the laser formed positive ion plasma, and alteration of the electrode potentials resulting from surface charging. Charging problems have indeed been observed as dips in the output potentials of the current limited power supplies.

With respect to the broadening of the transitions, one might expect this effect to result from collisional processes within the particle cloud, as the particle density increases (see Appendix C), however the required particle density (calculated from Equation (C.12)),which corresponds to the broadening observed in this instance is extremely high, typically very much greater than the number density of particles at atmospheric pressure ~3x10^{25} particles per unit volume. For an erosion rate of ~1.5 x 10^{-6} mm s^{-1}, from Equation 3.17, and the concentration of Al atoms, 6 x 10^{-19} mm^{-3} [53], the number of particles sputtered per second is the product of the two quantities, and is ~9 x 10^{13} (assumptions made include a spot size of 1mm^{2}, a current of 3μA, and a sputter yield of 5), which corresponds to a contribution to the number density of particles in the vicinity of the ion spot and the laser beam of ~9 x 10^{22} per unit volume, significantly less than at one atmosphere pressure.

Thus, in the case considered, the measured broadening is attributed to an increase in the relative height of the wings of the profile with respect to the saturated height at line centre, and not to a broadening of the interaction linewidth.

The slower rise in Figure 5.28 (for the area v current) after the peak height is saturated can be attributed to this gradual wing broadening.

All wavelength spectra were obtained under the maximum in laser intensity which was approximately 3mJ per pulse. The laser beam was focused using the 50 cm focal length lens at a distance of 45 cm from the spectrometer axis. Due to the divergence of the laser ~1 mrad, the beam was focused most effectively at a distance of approximately 65 cm from the lens, and at the sample the spot size area was between 1.5 and 2 mm^{2}. This implies a total maximum power density in the laser volume at the sample of ~2.5 x 10^{11} W/m^{2}, of which ~10% is at the UV wavelength.

A precise relation between the broadening and the ion energy (current), cannot be accurately determined, as the measured half height widths do not correspond to the true widths at half maxima in ion production.

The next series of figures, 5.29 show the effect on the Aluminium resonant transitions resulting from a variation in the total intensity of the post-ionising laser. As in the previous case, the peak height of the transitions appears to achieve a saturation level due to what is believed to be space charge limitations in the ion extract region. The most notable change is in the peak widths, which display a marked broadening with increasing laser intensity, implying a degree of power broadening present. Inserting the previously calculated value of ~$2.5\text{x}10^{10}$ W/m^2 for I, the intensity or power density of the laser at the resonant transition wavelength of 308.3 nm, in Equation (C.44) in Appendix C, a value of ~44 for the saturation parameter is obtained assuming the laser halfwidth is 0.025 nm, the minimum measured width in this case, which implies a broadening by a factor of approximately 6.7. This is rather an overestimate, but indicates that there is sufficient laser power available to be responsible for the broadening as opposed to other mechanisms.

Since the resonant excitation scheme adopted relies on the absorption of two photons, at different wavelengths, and different absorption probabilities, a relation between the measured intensity for the combined laser and the ion signal provides little in the way of useful information concerning the transition rates and the ionisation efficiency, unless the ion signal is found to be linearly related to the intensity, which would imply a saturation of the resonant excitation step, or the ionisation step can be shown to be completely saturated.

Graphs of the peak intensity and peak area as a function of the total laser power are shown in Figure 5.30 and 5.31 respectively. A graph of the measured FWHM for the first transition versus the laser intensity is shown in Figure 5.32.

In this case, the peak area dependence on laser power does not appear to exhibit the same saturation behaviour, at least over the range available. This can be attributed to the effect of power broadening of the resonant excitation lineshape in addition to the to the apparent broadening resulting from space charge saturation. Over the range of power available, the overall effect of the variation in laser intensity was to broaden the transitions by a factor of ~2, while in the case of the ion energy dependence, the apparent broadening was a factor of ~1.4.

Power broadening is also apparent in the ion energy dependent experiment,

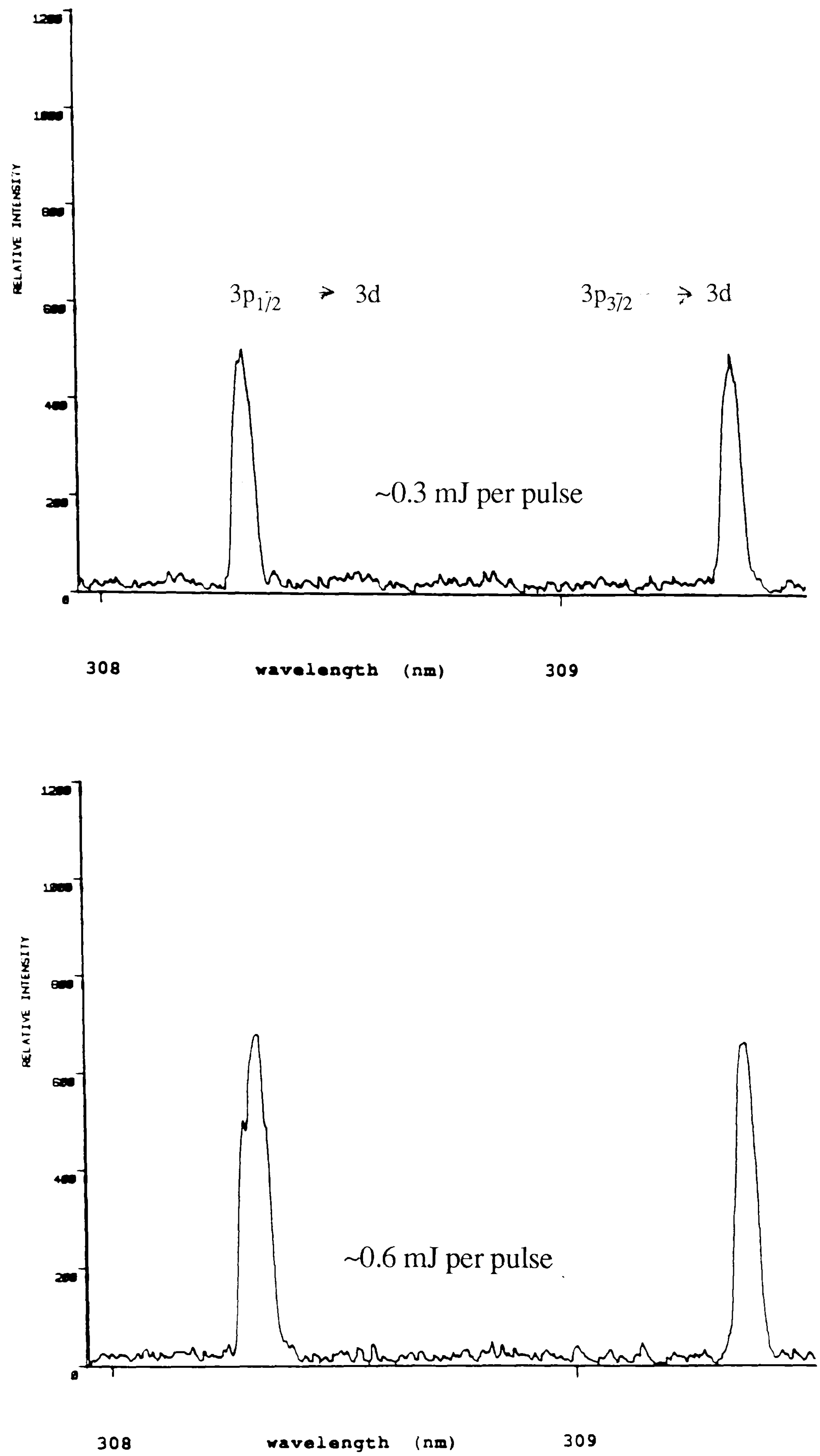

Figure 5.29 The following series of spectra show the effect of increasing the laser pulse energy on the relative Al ion yield and interaction linewidths. Throughout, the primary ion energy was maintained at 3 keV.

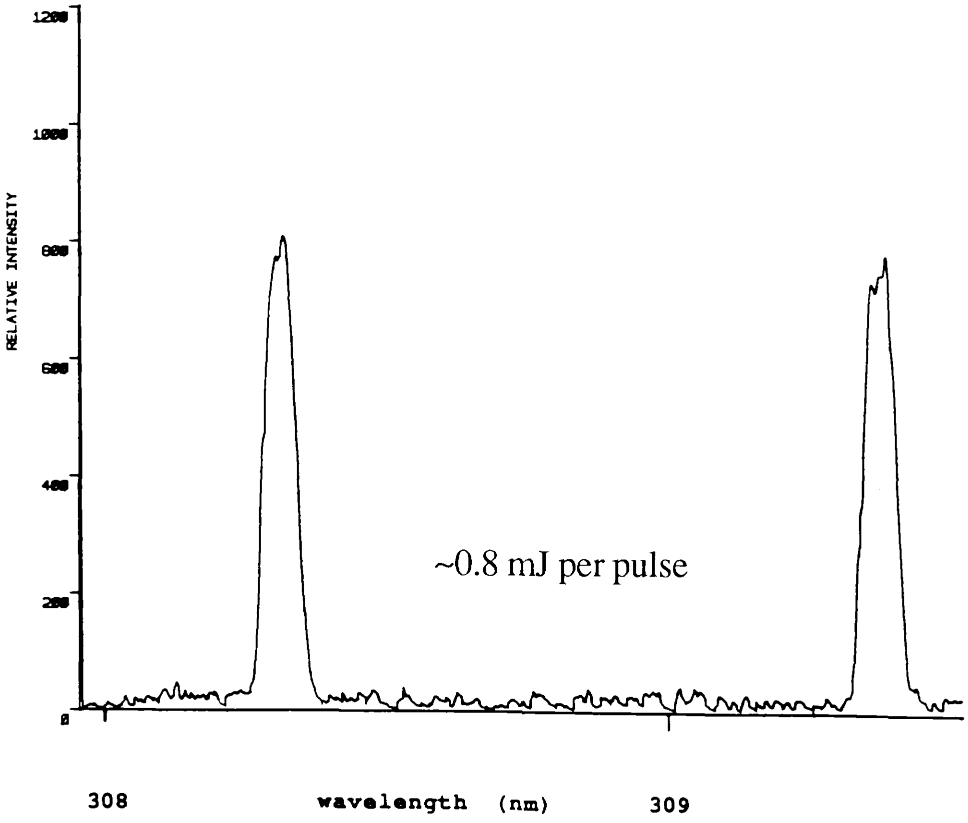
1200
1000
800
600
400
200
0
RELATIVE INTENSITY
~0.8 mJ per pulse
308
wavelength (nm)
309

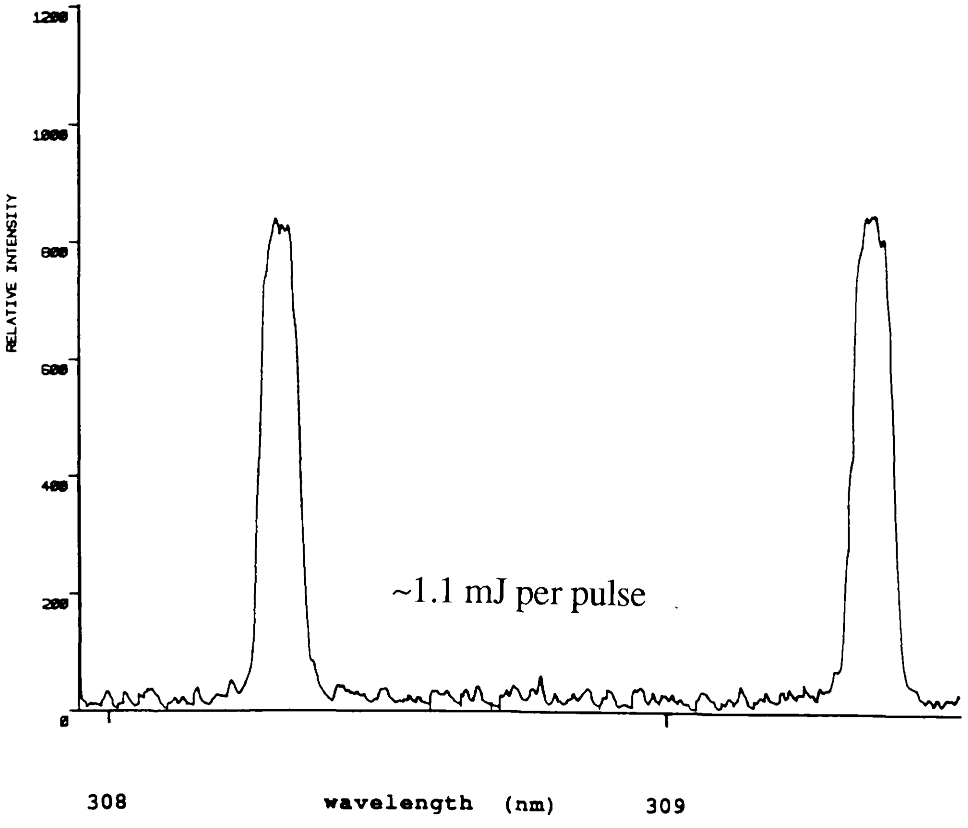
1200
1000
800
600
400
200
0
RELATIVE INTENSITY
~1.1 mJ per pulse
308
wavelength (nm)
309

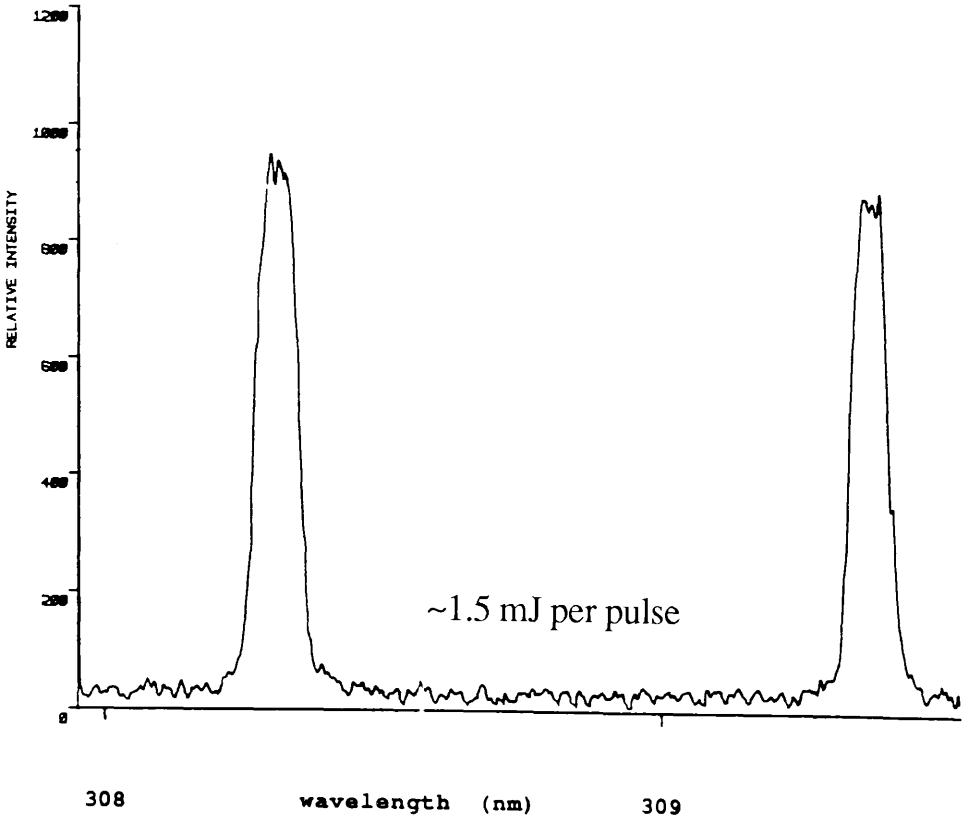
1200
1000
800
600
400
200
0
RELATIVE INTENSITY
~1.5 mJ per pulse
308
wavelength (nm)
309

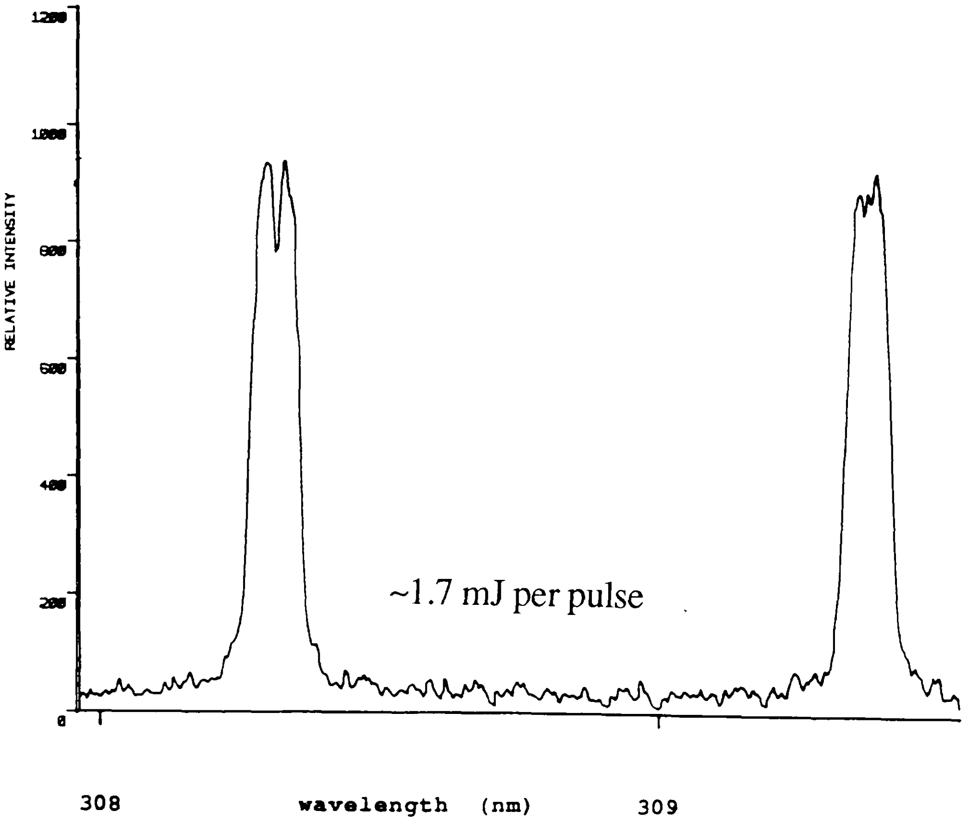
1200
1000
800
600
400
200
0
RELATIVE INTENSITY
~1.7 mJ per pulse
308
wavelength (nm)
309

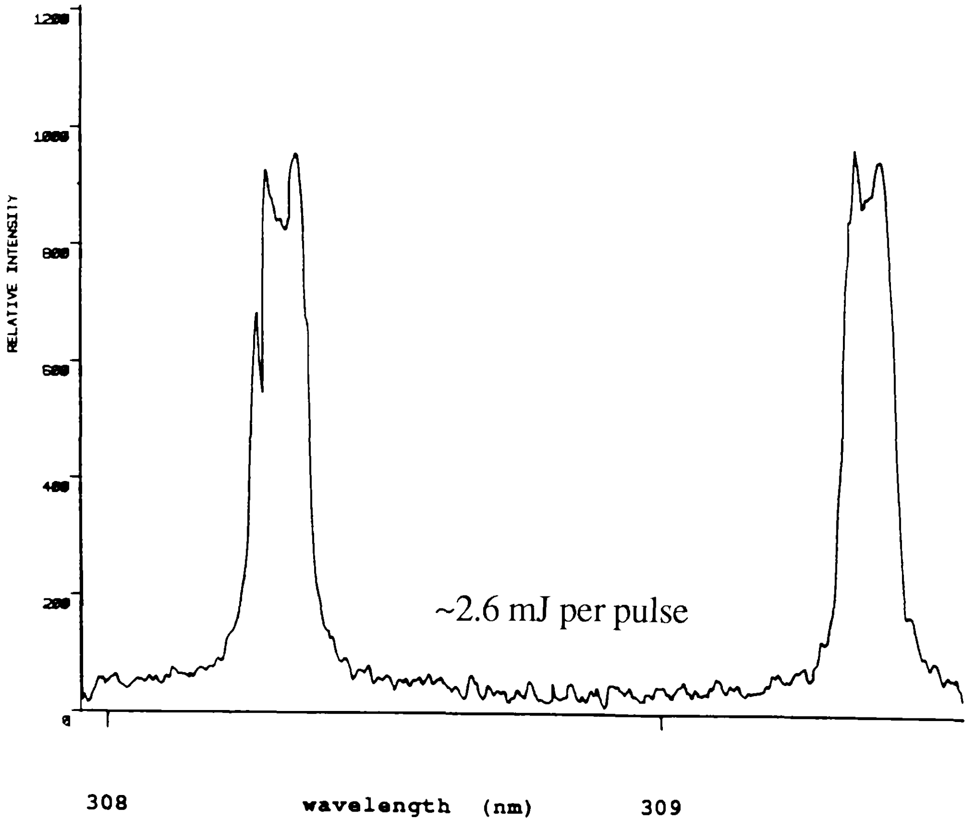
1200
1000
800
600
400
200
0
RELATIVE INTENSITY
~2.6 mJ per pulse
308
wavelength (nm)
309

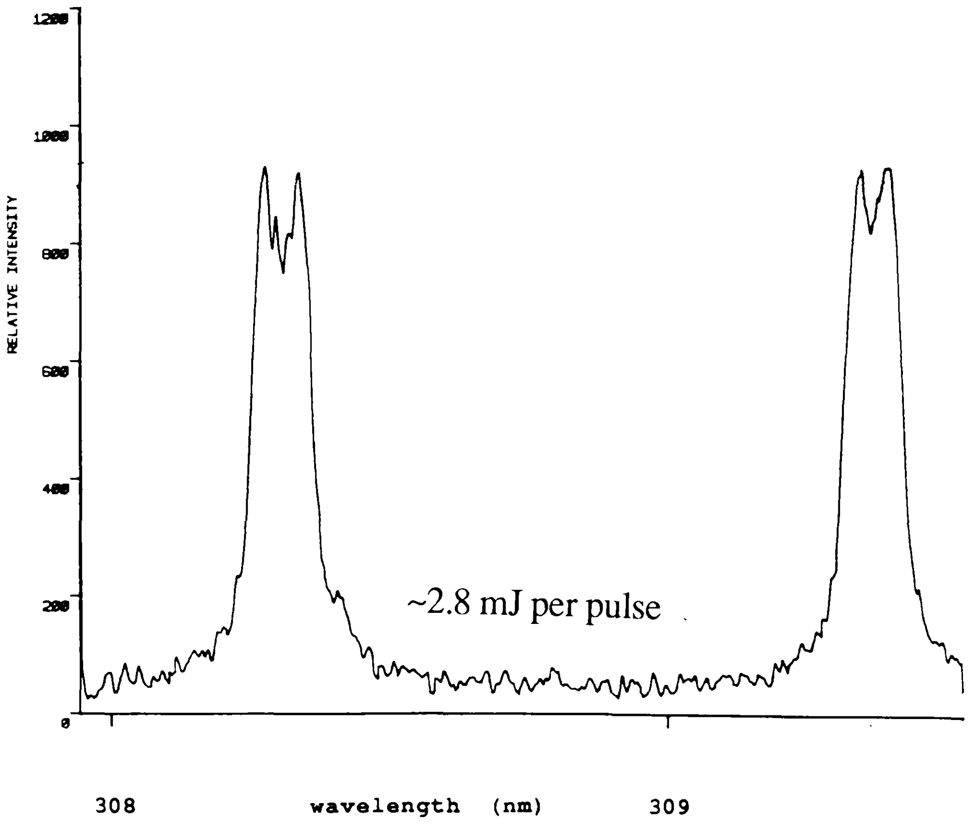
1200
1000
800
600
400
200
0
RELATIVE INTENSITY
~2.8 mJ per pulse
308
wavelength (nm)
309

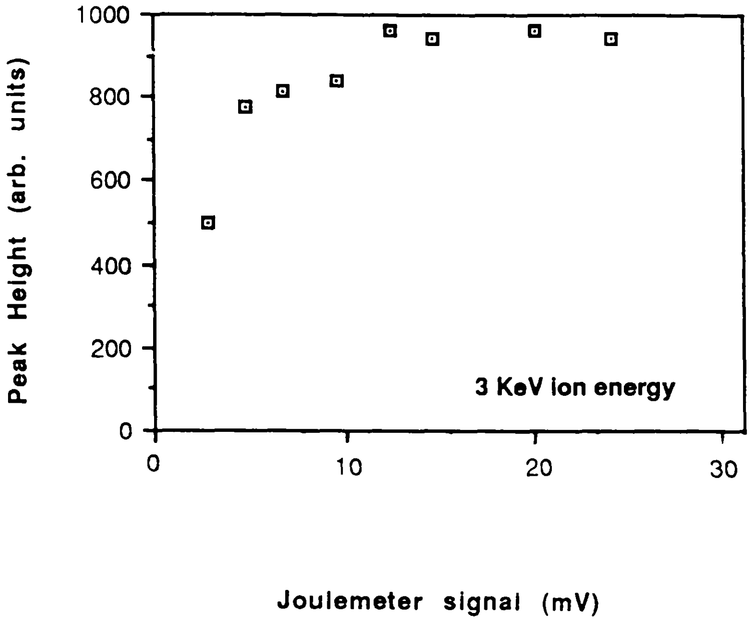

Figure 5.30 Al signal intensity as a function of joulemeter signal for the first transition shown in Figure 5.29.

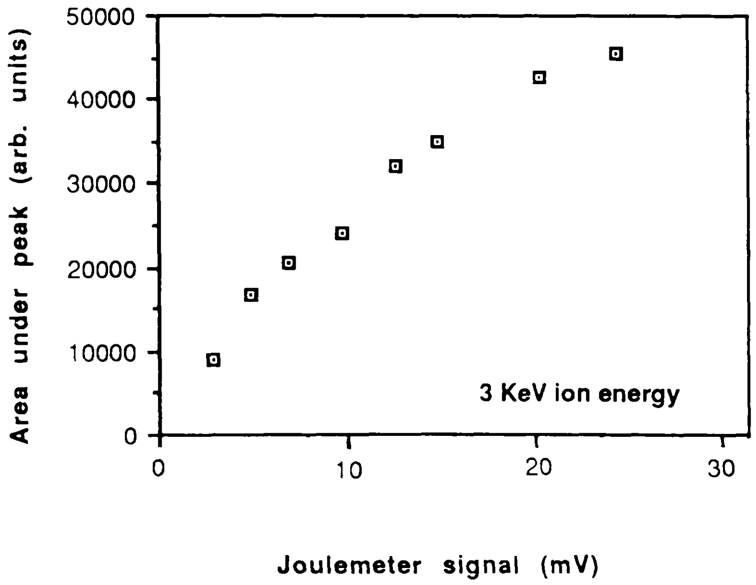

Figure 5.31 Resonant peak area for the first transition shown in Figure 5.29, as a function of joulemeter signal.

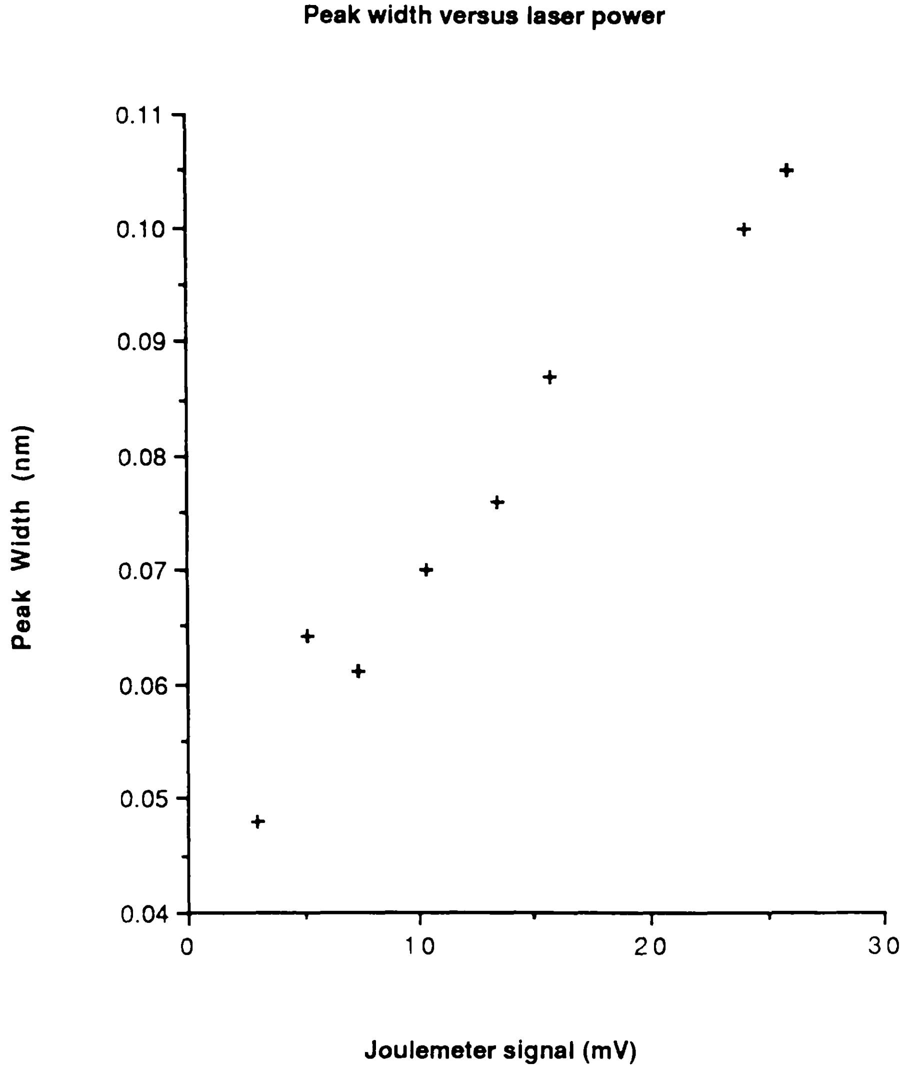

Figure 5.32 Resonant peak width for the first transition shown in Figure 5.29, as a function of jouleme ter signal.

where the width at the lowest ion energy of 1.5 eV at maximum laser intensity is greater than the width measured at the lowest laser intensity level for the higher ion energy of 3 eV by a factor 1.5, even though the peak heights in both cases are comparable, and far from the saturation level.

An interesting feature of this series of measurements is the apparent splitting of the absorption lines under conditions of simultaneously high laser intensity and high primary ion energy (current). The possibility of this splitting being attributed to a form of field effect, such as the Stark effect, resulting from the intense electric field associated with the laser, was discounted when no measurable shift in the position of, or increase in separation of, the two main ground state transition wavelengths was observed. In fact a more likely explanation is that the dip in the lineshape results again from space charge, in this case from a reduction in the transmission efficiency of the spectrometer around the line centre. This effect arises when the density of resonantly formed ions at these centre line wavelengths far exceeds the saturation value to an extent that space charge reduces the positive ion throughput of the optics rather than just saturate it.

Chapter 6

Application of RIMS to Depth Profiling in III-V Semiconductors.

Introduction.

The preliminary experiments, detailed in the previous chapter, have clearly demonstrated the effectiveness of resonant ionisation with regard to enhancement of the detection efficiency for Aluminium and Gallium. This chapter will deal with the specific application of RIMS to depth characterisation of semiconductor material.

Experimental Arrangement.

There were two samples involved in this study, both comprised of epitaxially grown layers of GaAs and AlGaAs, on a GaAs substrate.

The first sample, hereafter referred to as sample A, comprised a single layer of $Al_xGa_{1-x}As$ (x = 0.3), of thickness 1.3 µm. The samples were square sections, cleaved from the wafer, of side 1cm and 3 mm.

The other, sample B, was more complex in structure comprising two layers of AlGaAs sandwiching a layer of GaAs. The surface AlGaAs (x = 0.4) layer was of thickness 100 nm, the GaAs sandwich layer of thickness 300 nm, and the second AlGaAs layer (x = 0.5), also 300 nm thick. At a depth of a further 500 nm, was a multi-layer structure of alternate GaAs and AlGaAs (x = 0.5).

In order to reduce the effects of thermal instabilities within the laser cavity and similarly within the frequency doubling crystal, the laser was allowed a 'warm up' period in order to stabilise its output characteristics. Stable operation also required the laser be in operation, at a pulse repitition rate of 5 pulses per second, for the duration of the analysis.

Due to the limited computer disk storage space, the total acquisition time required to be restricted otherwise continuous acquisition for a period of hours would result very quickly in overflow of capacity . This was achieved by incorporating a switch inline from the trigger pulse to the ADC strobe which allowed a degree of manual control of the data acquisition rate.

The residual gas pressure within the system was typically 4 x 10^{-9} mbar. For ion gun operation, the chamber was filled with Krypton gas to a partial pressure of 4 x 10^{-7} mbar.

The implication of the enhanced detection efficiency available using RIMS, is the possibility of reducing the primary ion current, via a possible reduction in the primary ion energy, thereby providing a 'softer' approach to depth analysis than has otherwise been possible without the inevitable losses in sensitivity arising from lower primary and therefore secondary ion current. For this reason, a decision was made to conduct the experiment at as low a primary energy as would allow a reasonably detectable signal intensity, but not sufficiently low so as to result in any substantial deviation of the ion beam by electrostatic deflection by the positively biased sample stub. An appropriate choice, in this instance was an energy of 2 kV, sufficient to produce a current of several μA at the sample.

The procedure adopted for performing profile analysis involved the ion gun operating throughout the experiment in continuous beam mode. The beam spot was raster scanned over the sample for a defined period of time in order to remove a uniform layer of material. The raster waveform was then removed from the beam steering plates resulting in the beam being held stationary at the centre of the crater, with the laser aligned for maximum overlap close to the surface. During this period the acquisition system was triggered, recording a value for the resonant ion peak intensity. In order to minimise the damage to the the crater centre resulting from the higher effective current density of the stationary beam spot, the acquisition time must remain small by comparison with the period for erosion. Typically the erosion time was a few minutes in comparison with an acquisition time of a few seconds, the ion intensity being an average over a number of laser shots.

Control of the primary beam raster facility was performed manually via the controls supplied.

Results and Discussion.

For Sample A, Figure 6.1 shows the variation of the resonant Aluminium signal acquired over the duration of the experiment, a total of 420 minutes, for an incident ion energy of 2 KeV and a current, as measured at the stub, of 1.5 μA.

The profile has two distinct portions, a slow negative gradient corresponding to the AlGaAs layer, followed by the more rapid reduction in intensity at the boundary between the AlGaAs and the substrate.

The reason for the gradual slope of what should be a constant aluminium concentration through the layer is more evident if one investigates the variation in laser intensity over the same period of time. As Figure 6.2 shows, the laser intensity decreases steadily over the duration of the experiment by an overall factor of 2. The total energy in the laser pulse at the commencement of the experiment was ~1.6 mJ, insufficient for saturation. Normalisation of the ion signal by the laser intensity is not normally applicable in this situation, Aluminium requiring different photon energies for the two absorption steps. However, if it is assumed that the resonant excitation step is saturated, the ion signal can be linearly normalised with respect to the simultaneous laser intensity to obtain a profile of the form of Figure 6.3. The levelling of the initial portion of the profile would imply, that over at least this portion of the profile, that the assumption regarding the resonant step is valid, and there is a degree of proportionality between the ionisation rate and the laser power.

As the sample had already undergone a degree of sputter erosion prior to the profile analysis, in order to optimise the spectrometer transmission of the resonant ions and to tune the laser wavelength on resonance, the initial surface layer is not defined and therefore, it is not posssible to determine the resolution at the boundary with respect to the known thickness of the original AlGaAs layer.

The experiment was repeated on a second section of the same material. This time the square section was of side 3 mm, and was mounted, along with a similarly proportioned section of aluminium foil.

The purpose of including the foil was to act as a source on sputtering, of Al atoms in order to allow accurate tuning of the laser onto the resonant absorption line, positioning of the laser for maximum spatial overlap, and maximising of extraction efficiency of the spectrometer, without unnecessary damage and erosion of the study

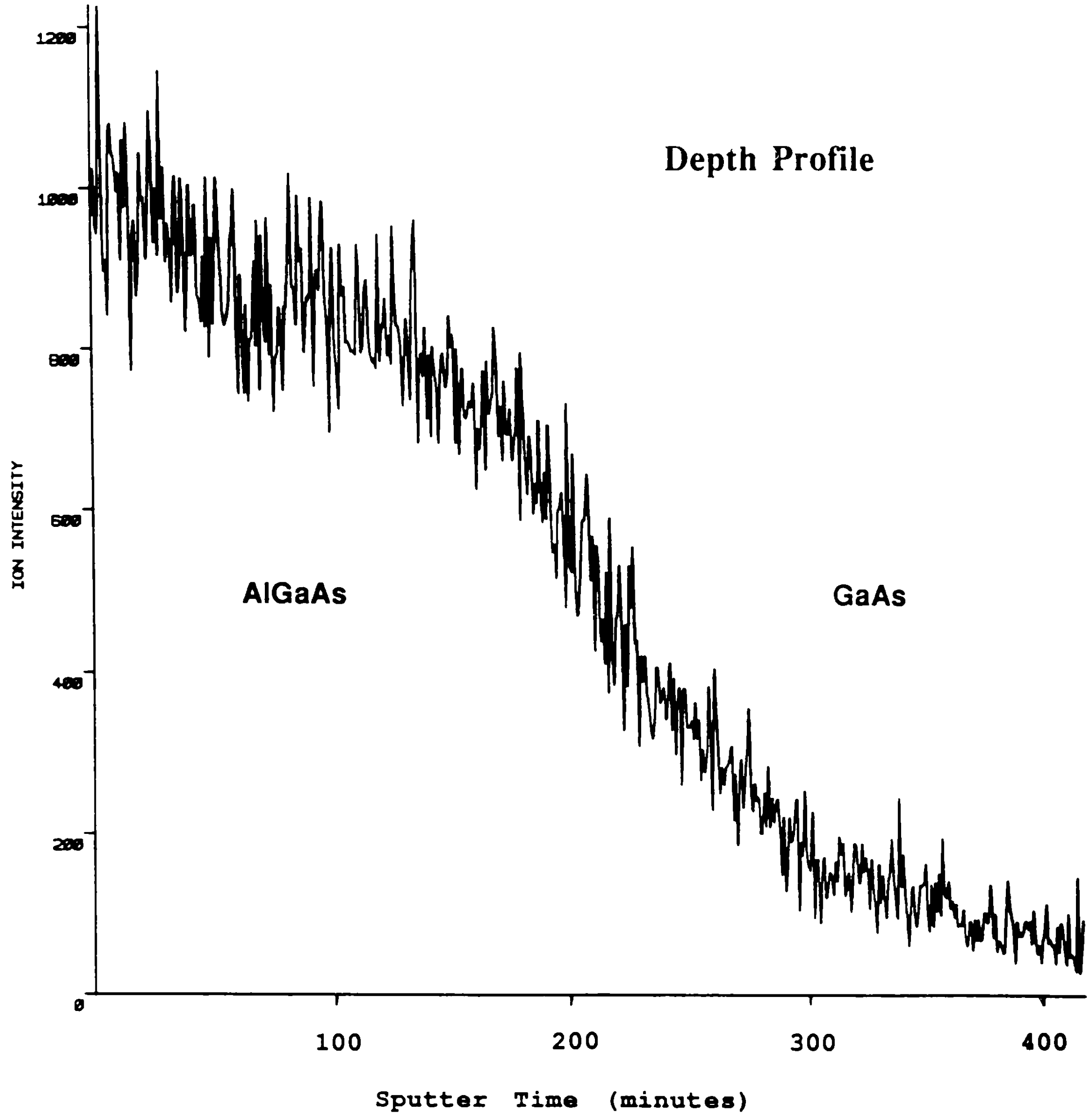

Figure 6.1 RIMS depth profile of Aluminium concentration at an AlGaAs/GaAs boundary. Ion energy 2 keV

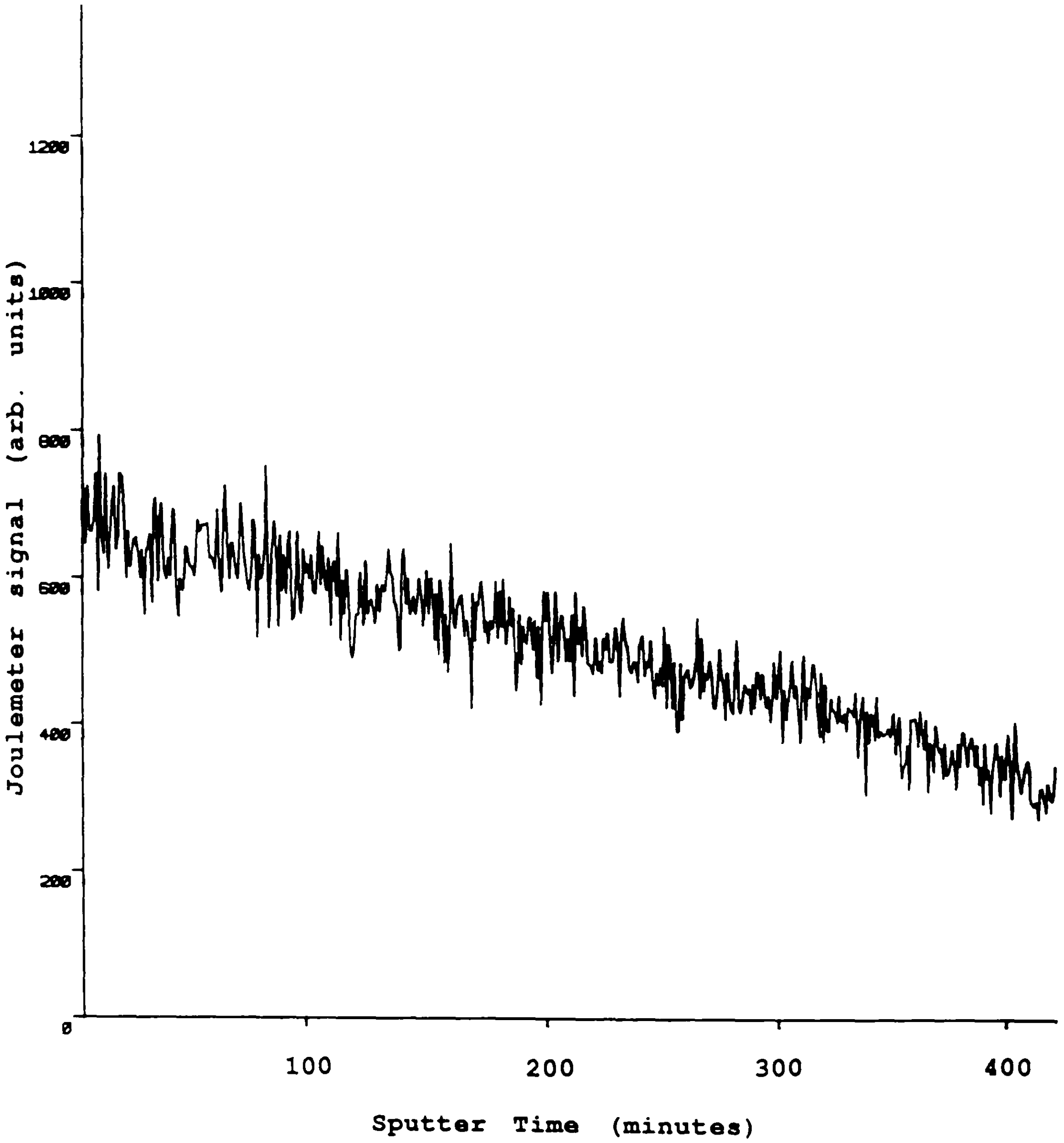

Figure 6.2 Relative laser intensity as a function of erosion time for the analysis of Figure 6.1.

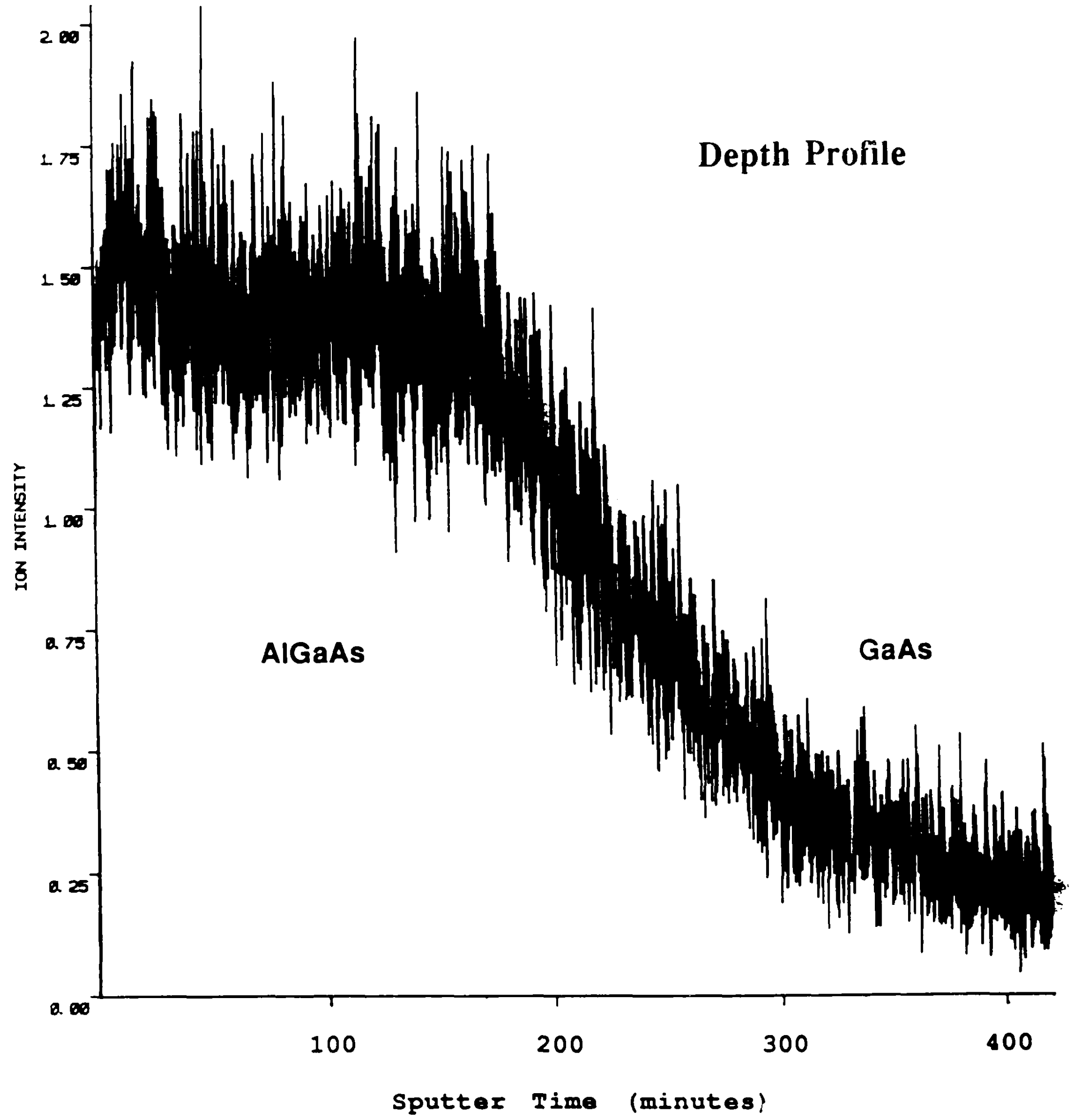

Figure 6.3 RIMS profile of Figure 6.1 linearly normalised to laser intensity. (i.e. Ion signal / Joulemeter signal)

sample prior to commencement of the depth analysis. Once these procedures had been carried out, the semiconductor sample could be translated into position, with little or no need for further adjustment of the experimental parameters.

Figure 6.4 shows the depth profile obtained. The two most notable features of the profile in this case are the apparent regions of higher Aluminium concentration at the surface and near the GaAs/AlGaAs boundary. The enhancement at the surface can be explained by aluminium, sputtered from the aluminium foil at an earlier stage, being redeposited as a layer onto the sample stub and onto the semiconductor sample. This surface Aluminium deposit is then eroded away to leave the constant Aluminium concentration associated with the AlGaAs layer.

At the boundary layer, a possible explanation for the enhancement is, that due to the lighter mass of aluminium compared to the other bulk constituents, the aluminium recoil particles have a greater range within the material and hence tend to accumulate with depth particularly at a boundary between two materials where there may be a discontinuity in density and/or erosion rate. Alternatively, the effect may be, as are so many in depth analysis, of a procedural or instrumental nature.

Sample B was mounted in a similar fashion with an identical section of Al foil. Both samples were square of side 3 mm. The experimental parameters were also similar to the above conditions, namely a primary energy of 2 kV, a sample bias of +300 V, though in this case a partial pressure of 6.8 x 10^{-7} mbar. As with the previous case, the current measured at the sample stub was 3 ± 0.1 μA. The total analysis time in this instance was ~950 minutes. A period of 2 minutes was allowed for depth erosion between acquisition times.

Figure 6.5 shows the depth profile obtained after a period of 180 minutes. In comparison with Figure 6.6 the main features of the concentration profile are evident. Comparison of the peak concentrations of the AlGaAs layers indicates a ratio of 4/5 in reasonable agreement with the expected value from their fractional Al concentrations. Also visible, though poorly resolved, is the multiple layer structure.

With the ion gun operating at the relatively low energy of 2 kV adopted here, it is unlikely that atomic mixing effects are the limiting factors to the depth resolving power of these experiments, since the range of atomic mixing, at this relatively low energy, extends over only a few tens of Angstroms. Also, other methods of depth

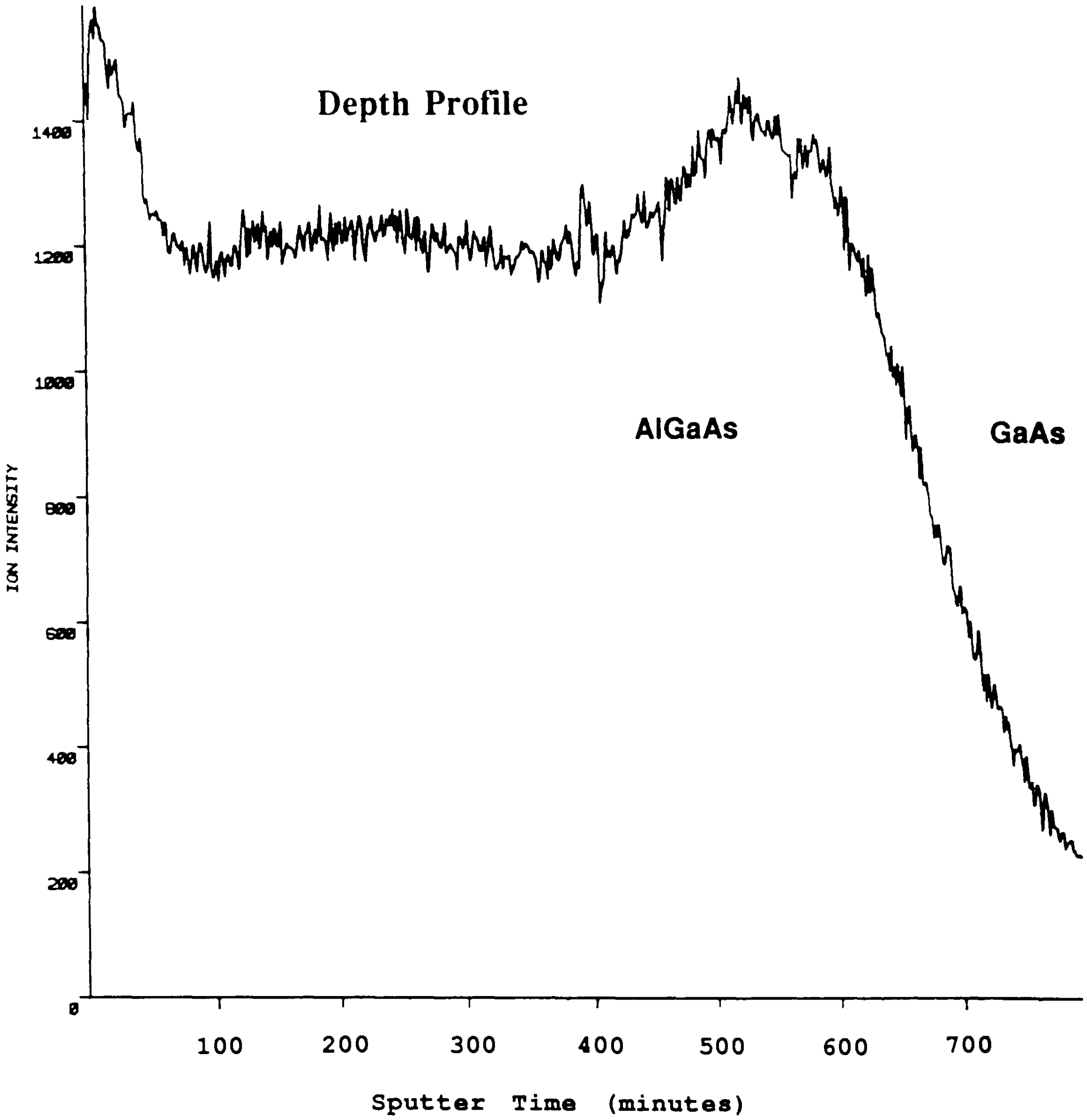

Figure 6.4 Aluminium RIMS depth profile through an AlG As/GaAs interface (Sample A).

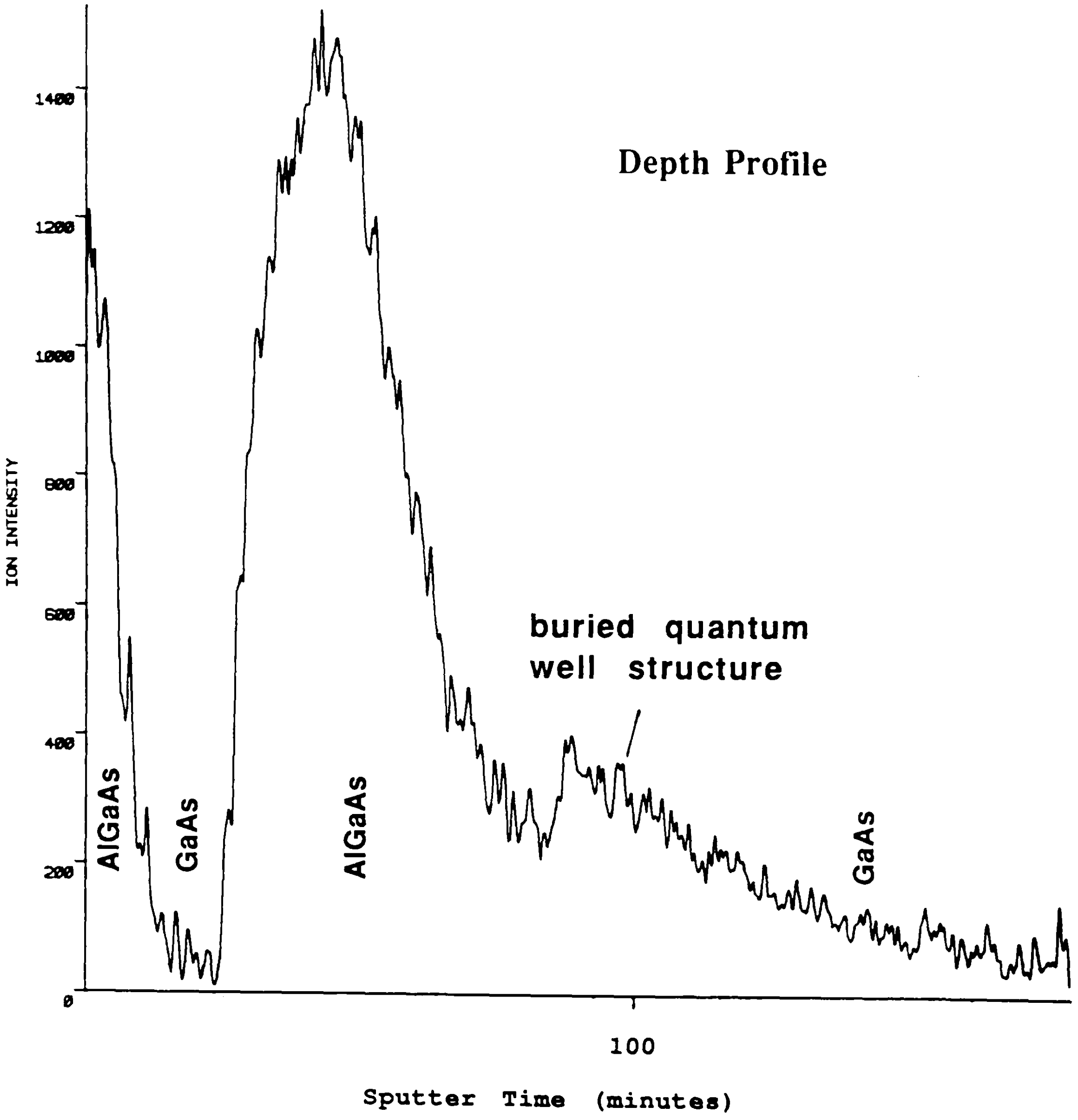

Figure 6.5 Aluminium RIMS profile through sample B layered structure

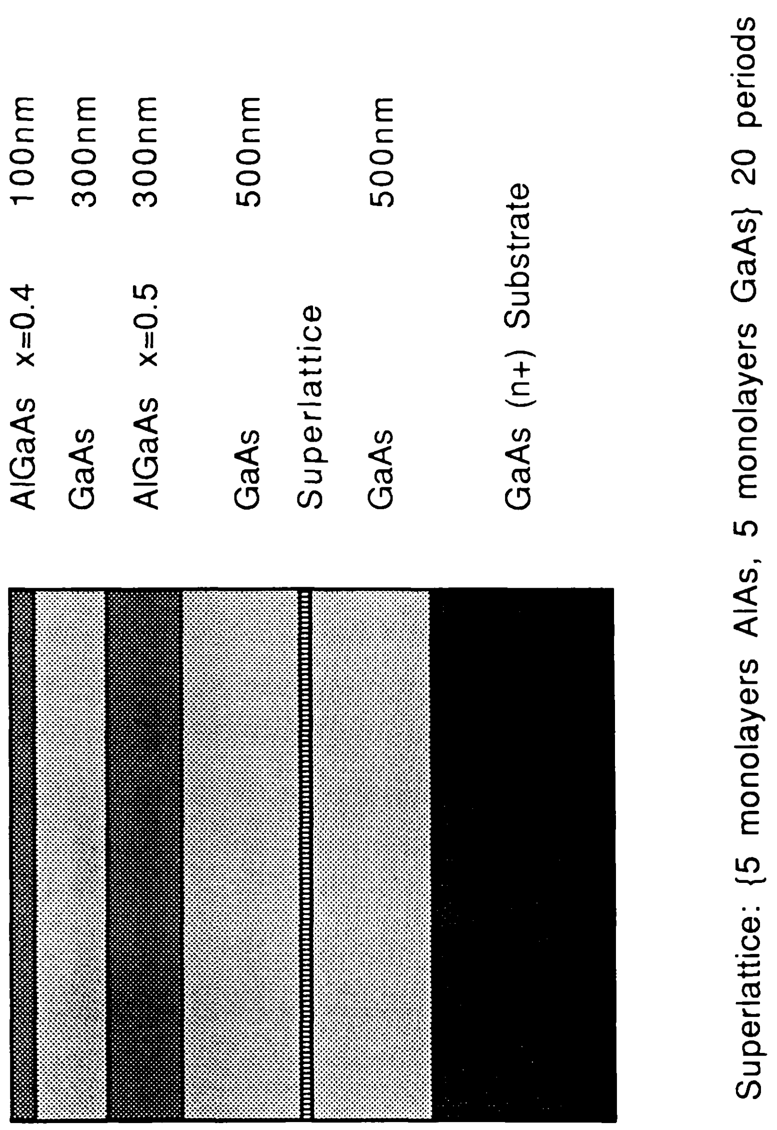
AlGaAs x=0.4 100nm
GaAs 300nm
AlGaAs x=0.5 300nm
GaAs 500nm
Superlattice
GaAs 500nm
GaAs (n+) Substrate
Superlattice: {5 monolayers AlAs, 5 monolayers GaAs} 20 periods

Figure 6.6 Structure of test sample B

analysis relying on sputter erosion typically employ energies in excess of a few thousand volts and display far better resolving ability than here. It is therefore more likely that the resolution limit is imposed by other, instrumental, effects. These can result from crater geometry, secondary sputtering from electrodes and the background partial pressure of Aluminium in the analysis region. However, the most likely cause, is the non-uniformity of the sputtering of the sample due to the extreme obliquity of the incident primary beam which results in material originating from various depths through the sample. This effect can be assisted by the spatial acceptance of the secondary ion optics being comparable with or larger than the dimensions of the spot.

As has already been indicated (Chapter 3), the conditions for maximum sputter yield include a primary beam incidence of around 60 to 70 degrees relative to the sample normal. Beyond this angle, the sputter rate falls off much more rapidly. In the experiments outlined above, one major problem may be that the minimum incident angle, as defined by the system geometry, is $\sim 67^0$ which is already near the peak in sputter yield, though more likely beyond it. Under normal operating conditions where there are voltages present, in particular the sample bias, the ion beam may be sufficiently deviated for the primary incidence to be significantly greater than optimum thereby resulting in a reduction in sputter yield. Also, due to the rapid fall off in yield, small variations in the angle during beam rastering, may result in more significant variations in yield.

Atomic mixing tends to be a constant of the analysis parameters, i.e. mass and energy of the primaries. In situations where the sputter depth is very much greater than the range of particles within the material (~10's of nanometres), atomic mixing would be expected to make a constant contribution to the broadening of a profile rather than a depth dependent contribution as observed in these analyses.

Another contribution to the observed broadening may be made by the neutral component of the ion beam. Since the ion gun electrode assembly consists of a linear column, the ion and neutral components cannot be separated as in more sophisticated devices which incorporate non-line-of-sight source to sample arrangements. The neutral component is also unfocused and hence contributes additional non-uniformity of erosion and thereby a depth dependent resolution function.

The cause of the significantly different sputter times and therefore sputter rates during the experiments on both samples can be explained by the different areas covered by the rastering beam and hence the differing effective current densities during erosion.

From Equation 3.4 the sputter yield Y for GaAs due to 2kV primary ion normal incidence is ~16.5/U_s, where U_s is the sublimation energy for GaAs and has a value of 3.3 eV, leading to a value for Y of 5 particles per incident ion. For the multilayer sample, the boundary between the GaAs sandwich layer and the second AlGaAs layer occurs at a depth of 400 nm. The time for sputtering to this depth was approximately 30 minutes, implying an erosion rate, in this instance, of 0.8 μm/hour. Inserting this value into Equation 3.15, along with the calculated value for the sputter yield returns a value of 31 μA/cm^2 for the current density J, which corresponds to the incident ion current of 3μA on an area ~ 10 mm^2. The raster voltage applied to the deflecting plates was 50% maximum.

With respect to sample A, the 50% Al level in the AlGaAs/GaAs boundary occurs at a time of ~670 minutes. This corresponds to an erosion rate of ~0.12 μm/hour for the transition occuring at a depth of 1.3 μm.

Again, making the relevant substitutions into Equation 3.15, the area influenced by the primary beam is ~60 mm^2, for a slightly lower sputter yield for AlGaAs of 4.5, calculable from Equation 3.4 and assuming equivalent surface binding potential as for GaAs. In this case the raster voltage was at a maximum which would imply an increase in off axis beam deflection by a factor of 2 and hence in area covered by the beam by a factor of 4 in comparison with the factor of 6 reduction in current density calculated above. This discrepancy is not unreasonable considering the actual experiments were performed at oblique incidence and therefore more pronounced variations in the sputter yield may be responsible.

Further non-uniformity of the erosion process arises from the static condition of the beam during acquisition periods which effectively augments the ion dose in the central portion of the crater. The solution here would be to pulse the beam during this period, as suggested by Parks et al [83], unfortunately, the ion gun does not lend itself to the rapid switching of modes, i.e. between pulsed and continuous, the major problem being one of high voltage transients, which have undesirable effects on the more delicate components of the ion source, and as transient feedback along the voltage supply lines have had occasion to damage or destroy electronic components within the control unit. Also, the time required for the gun source parameters, most notably the filament current, to stabilise after switching modes is not conducive to the rapidity and flexibility of operation desired.

As well as proportionately reducing the sputter erosion rate, the increasing of the raster area should have the effect of improving the depth resolution by improving the uniformity of the sampled portion of the crater. This can be observed on comparing the depth resolution obtained during analysis of sample B with that for sample A. For sample A the resolution of the boundary (defined in Chapter 3) is ~270 nm while for sample B, the resolution at a depth of 700 nm corresponding to the boundary between the second AlGaAs layer and the 500 nm GaAs layer, has already deteriorated to ~400 nm. Furthermore, the embedded multi-layer structure of alternate GaAs/AlGaAs, appears only as a minor peak in the falling edge of the Al concentration of the 300 nm AlGaAs embedded layer, at the expected depth of 1200 nm, measured relative to the well resolved boundary at 400 nm.

Conclusion.

The main purpose of the experiments outlined above has been to assess the possibility for the specialised application of Resonance Ionisation Mass Spectrometry to depth analysis of III-V semiconductors, and from the results acquired, it could be said that the work has been moderately successful in that reasonable correlation between concentrations of Aluminium in known structural formations of layered GaAs/AlGaAs and the measured Aluminium profile has been possible.

The major problem encountered has been the effect of utilising relatively unsophisticated hardware, in what is essentially an instrumentally dependent process. This has led to serious limitations to both the depth resolution and the dynamic range of the analysis.

Recent experiments which have involved the use of far more sophisticated hardware, have provided standards of RIMS profile analysis already comparable with the much implemented, related technique of SIMS. Such experiments have however been few in number, and there still remain aspects of this application of RIMS which can be improved upon before it can be considered as a companion to, or replacement for existing processes.

The applicability of RIS to high resolution depth profiling has been demonstrated by Parks et al [84][85][86], Young et al [125] and Downey and Hozack [19][20][21].

The technique, at this early stage in development of the application, has been shown to be capable of a depth resolution of some 4 - 5 nm in semiconductor multi-layer sructures [36], with the possibility of enhancements via further reductions in the primary beam energy and improvements in experimental procedures. Figure 6.7 shows a RIMS depth profile of a GaAs/AlGaAs multi-layer sample [86] displaying in this case a resolution ~15 nm. Figure 6.8 shows the profile of a Be 'delta' (i.e. narrow) doped layer displaying a FWHM of appproximately 5nm [21] at a buried depth of ~100 nm.

A comparison of RIMS with SIMS under identical experimental conditions of primary ion and current has been carried out, with a reduction in the matrix effects associated with SIMS observed, together with improved signal to noise via a reduction in the number of background ions created in the selective ionisation process [20]. Figure 6.9 shows the profiles obtained by both methods of a Be doped GaAs/AlGaAs multilayer sample. Due to the variation in the sputter yield through the various layers the Be signal is normalised with respect to the sputtered As intensity. As can be seen, there are severe matrix effects associated with the SIMS profile, while that via RIMS more closely represents the simulated implantation profile [20].

Two different procedures have been adopted for RIMS profiling, firstly that of Parks et al., a layer removal by a DC ion beam rastered over the surface, followed by pulsed time-of-flight analysis by RIMS of material sputtered from the crater centre. In comparison, the experiments of Downey involved a constantly DC, rastering ion gun, as with SIMS, with triggering of the laser gated to coincide with the ion beam passing across the crater centre and the effective focus of the extract lens The detector and acquisition system is similarly gated electronically.

Both methods have their advantages and disadvantges in the degree of electronic sophistication required for control, however, the method of Parks is not prone to the continuum of secondary ions present during erosion and analysis, which have a finite probability of being detected, and thereby contributing to a loss in performance.

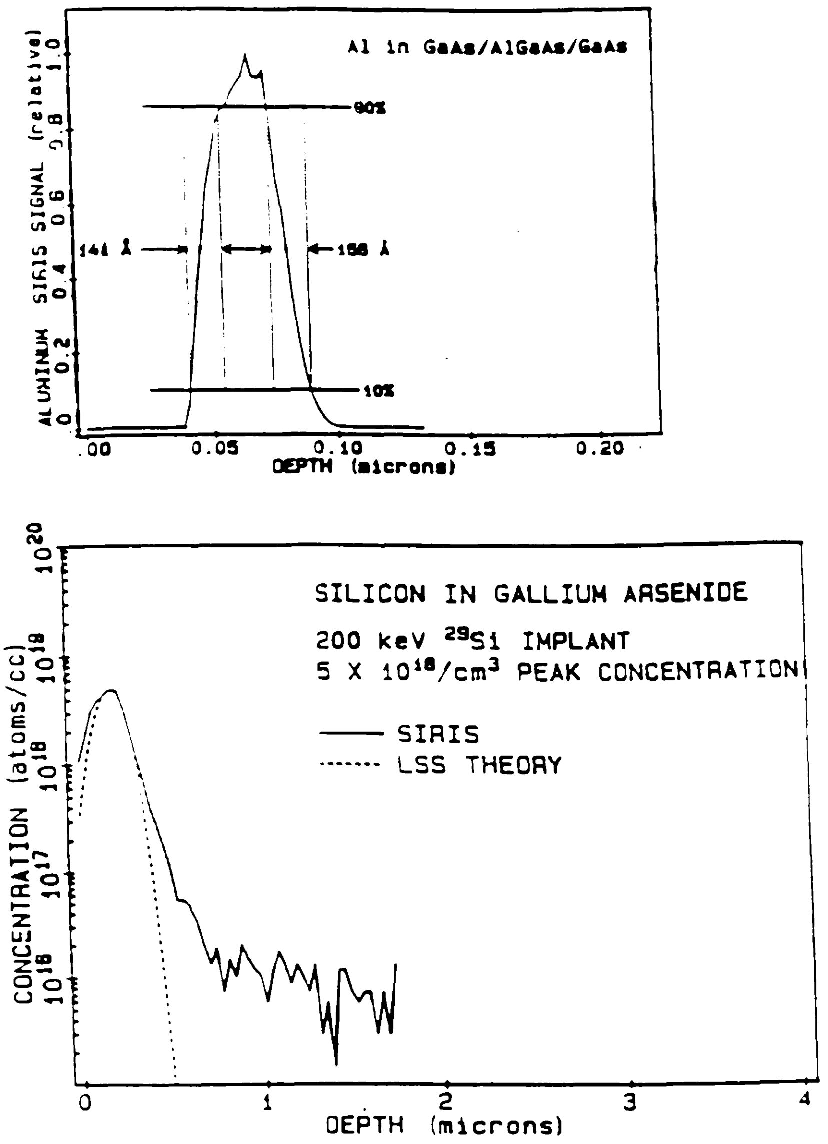

Figure 6.7 Examples of RIMS depth profiling in III-V materials. [86]

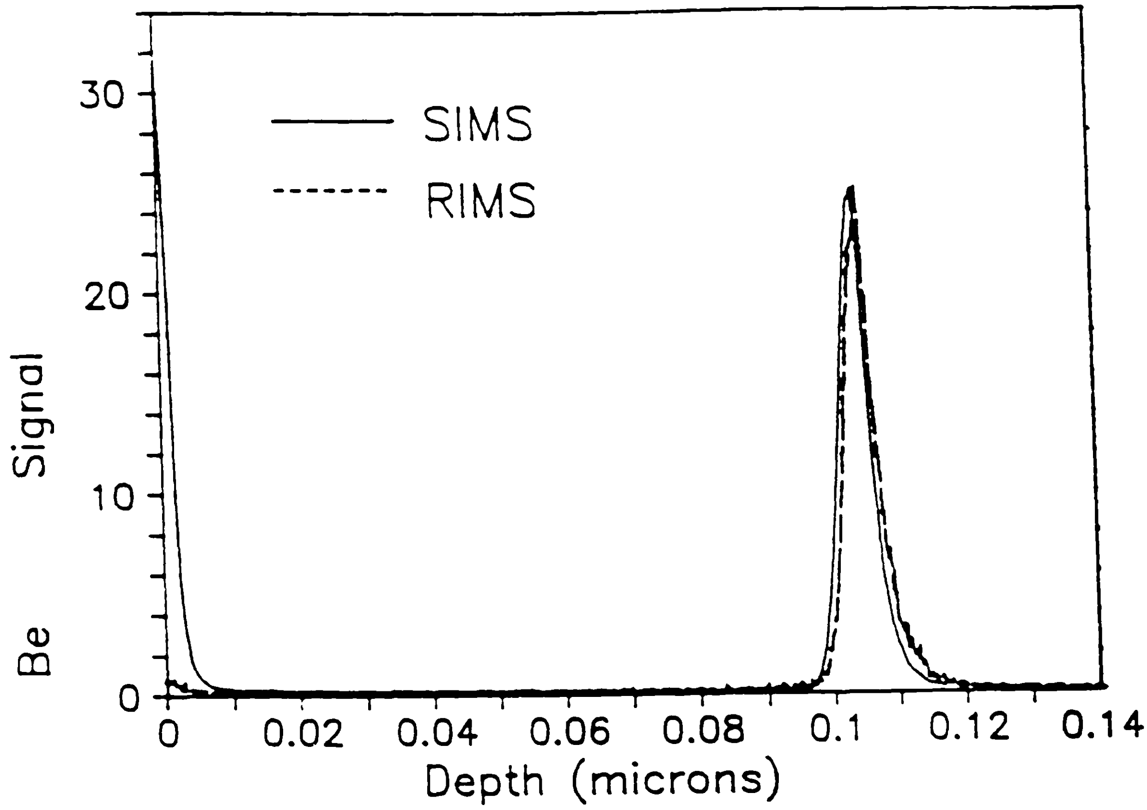

Figure 6.8 Comparison of depth resolution obtainable via RIMS and SIMS. [21]

Figure 6.9 Comparison of matrix effects in depth profiling by RIMS and SIMS [20]

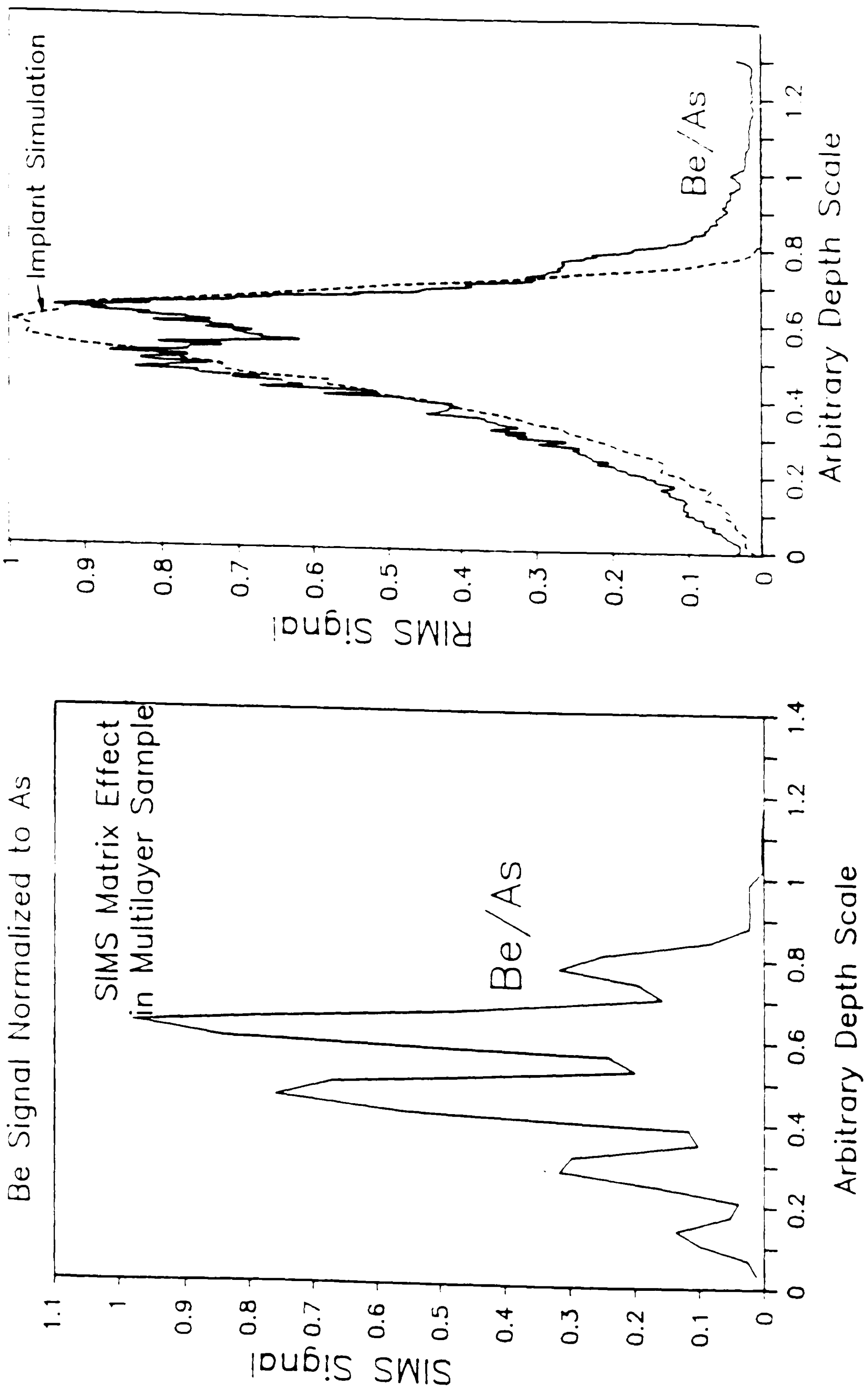

Chapter 7

Secondary Ion (SIMS) Suppression During Resonant Ion Detection.

Introduction.

This chapter will describe a proposed method to deal with the permanent secondary ion background present during ion sputtering, which interferes with detection of resonant ions. The method relies on static field conditions and the electrode geometry, and not on the use of time discriminating voltage pulsing.

Physical Basis.

In order that positive ions are extracted efficiently from the interaction region to the spectrometer, a positive bias is normally applied to the sample as a repulsive accelerating potential. If the polarity of the sample bias is reversed or the potential reduced, such that its potential becomes negative with respect to the first electrode, both primary and secondary ions are preferentially attracted to the sample surface. The remaining neutral particles are, however, still free to expand into the volume as normal. So far, this prevents any ions, apart from the perhaps the most energetic, from being extracted and detected, however any ion, including those formed in a laser volume, will be similarly affected, and hence an independent method must be found for extraction of this particular ionic component.

As the first and second conical electrodes are closely spaced (refer to Chapter 4 for details), application of a large negative potential to the second electrode may result in significant leakage of the field due to the second, through the aperture of the first. A sufficiently strong field may then be present to exert enough influence on a locally produced ion, to extract it from the interaction volume. In fact, through careful choice of the relative potentials on the electrodes and the sample, the field leakage may penetrate a significant fraction of the sample electrode separation. This effect is enhanced by the physical geometry of the electrodes which shape the equipotentials to form a better defined field focus.

Effectively, what is formed is a field reversal within the interaction volume. Depending on the position of the ions relative to this reversal, or saddle, point in the field, they may be accelerated either towards the sample or to the mass spectrometer.

As a result, if laser post-ionisation is performed in a well defined volume beyond the reversal point, the ions will be efficiently extracted with the minimum of secondary ion background.

In order to model the effects of various experimental parameters on the performance of the ion optics a computer simulation was performed. The software package used was **SIMION** (SIMulated ION) **3.1** running on a Compaq 386/25 PC, which allowed both equipotentials and ion trajectories to be calculated for this rotationally symmetric situation. The program was originally developed by D.C. McGilvery at Latrobe University, Department of Physics and Chemistry, Bundoora Victoria, Australia in 1977, and this revised version was developed at Idaho National Engineering Laboratory by D. A. Dahl and J.E. Delmore in 1987.

A simulation of the equipotentials formed by the electrodes in the particular situation described above and implemented below, is shown in Figure 7.1, together with the calculated trajectories of positively charged ions originating at various points in the interaction region (Figure 7.2), and with a range of initial directions relative to the spectrometer axis. Since the peak in the kinetic energy distribution of sputtered particles is typically a few electron volts, and the distribution falls away as $1/E^2$ (Chapter 3), few particles will be emitted with an energy exceeding a few tens of electron volts. The ion energies used in this case were all 100eV for singly charged ions of mass 70 amu. As can be seen, the relatively high (~+500 V) potential on the first electrode with respect to the sample, is extremely effective in restricting the motion of these sputtered secondary ions, while ions created, in this case by resonant post-ionisation, at a position beyond the reversal point in the field, experience the leakage field generated by the second, highly negative potential, and are propelled into the time-of-flight region.

Implementation.

The experiment was carried out during the GaAs investigation, and all equipment and experimental geometry was as detailed in that earlier study.

Figure 7.1 SIMION simulation of equipotentials for inversion optics.

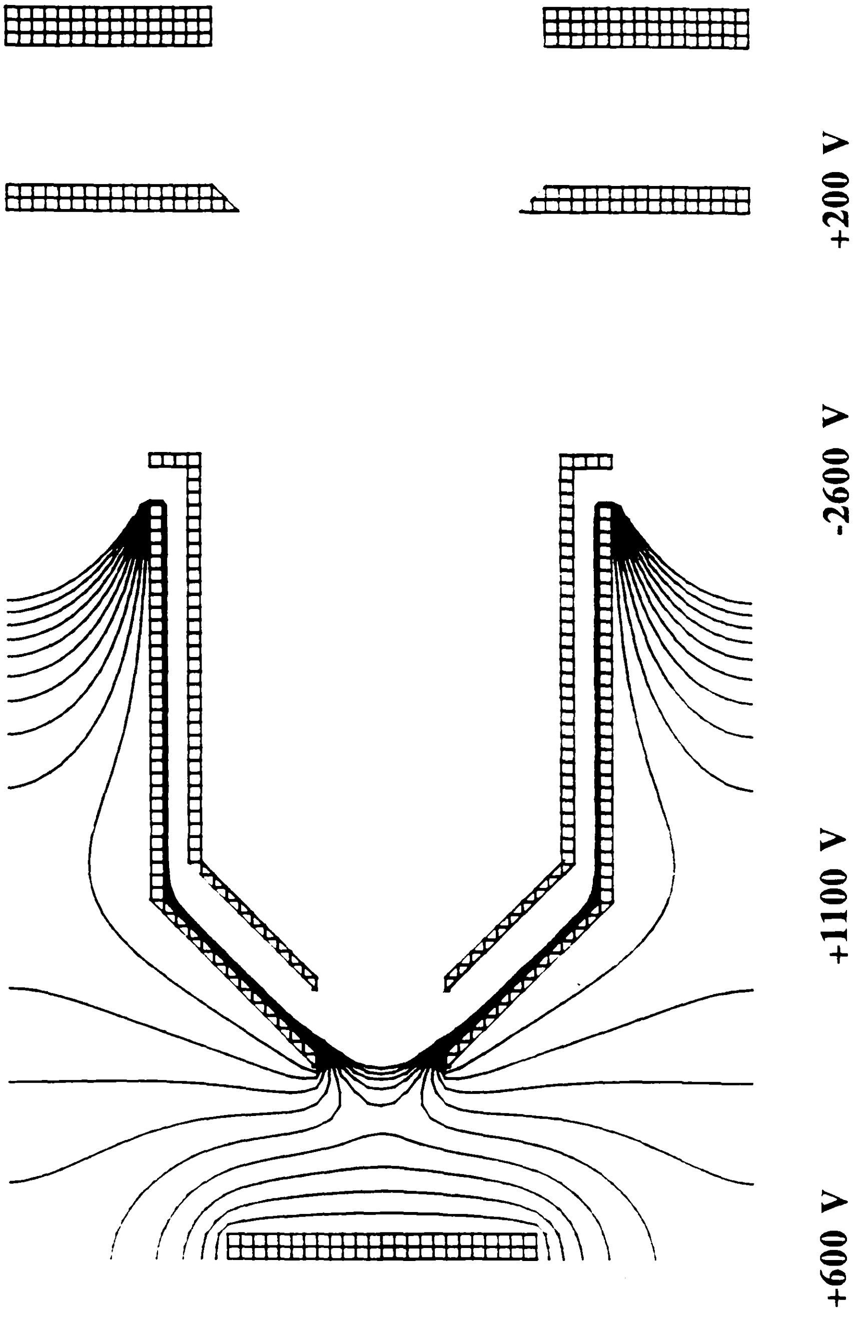
+200 V
-2600 V
+1100 V
+600 V

Figure 7.2. SIMION simulation of ion trajectories.

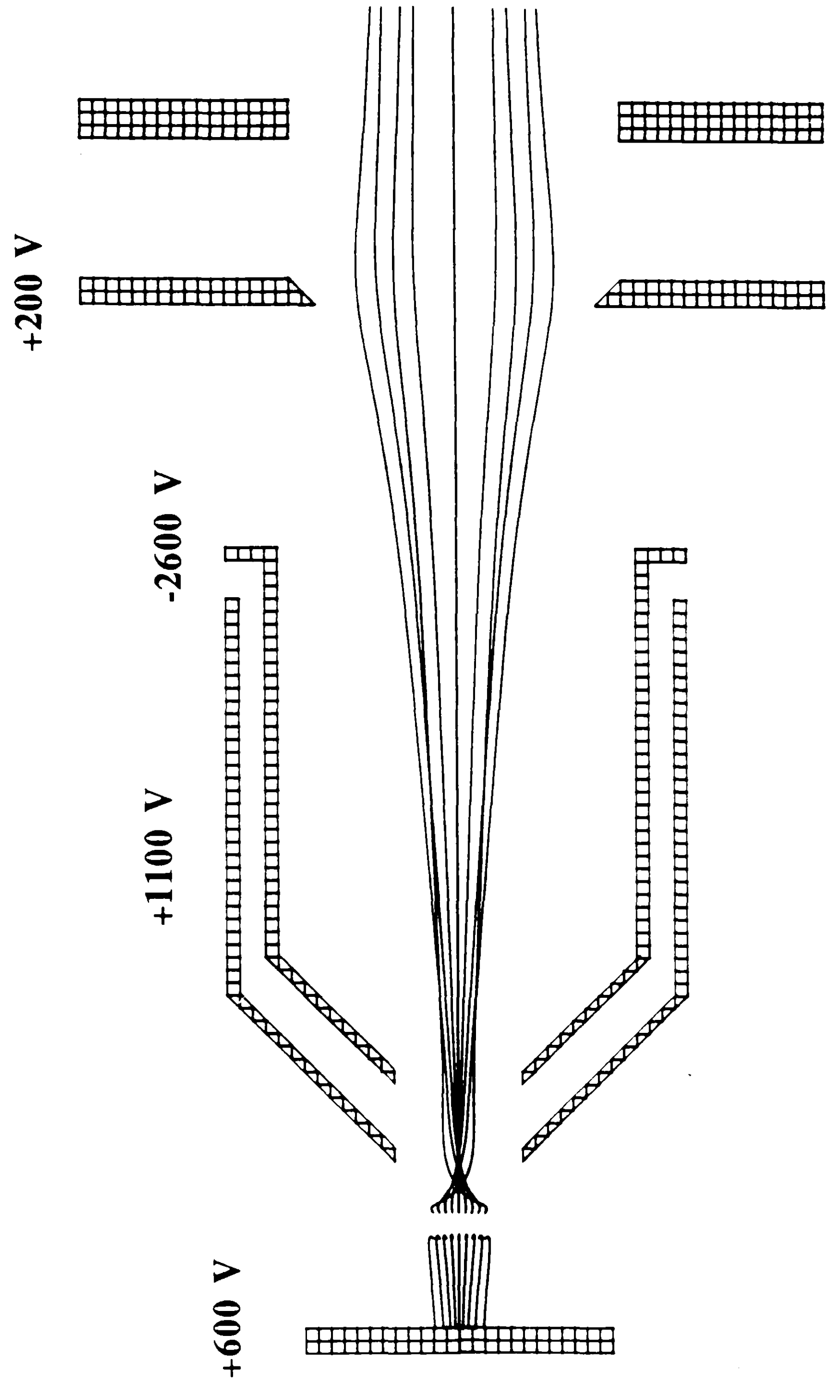
+200 V
-2600 V
+1100 V
+600 V

During the course of the investigation, four experimental parameters were varied. These were the laser beam position with respect to the sample surface and the aperture of the extract electrodes, the potentials applied to the two conical electrodes, and the delay between the firing of the laser pulse relative to the primary ion pulse. At all times, the potential on the sample stub was at a constant +600 volts.

Initially, with the focused laser passing close to (~1mm) the sample surface the electrode potentials were adjusted to optimise the resonant peak intensities and the mass resolution (conical electrode potentials were +600 and -2100 Volts respectively). Under these conditions, a TOF spectrum of the form of Figure 7.3 was obtained.

The laser was then translated across the interaction region (i.e the 12 mm gap separating the sample and the aperture of the first electrode), intersecting and perpendicular to the spectrometer axis, to a position approximately 3mm from the aperture of the first electrode, while simultaneously, the laser firing delay was altered to maintain maximum temporal overlap of the sputtered atom and photon pulses. The potential on the first electrode could then be adjusted for maximum extraction efficiency for the resonant ions. At this stage, with a relative first electrode to sample potential difference of +400 volts, there is a substantial reduction in the level of SIMS ions extracted in comparison with the relatively unaffected resonant peak intensities, Figure 7.4.

On positioning the laser to approximately 2 mm from the electrode, and adjusting all other parameters to maximise the resonant intensity, a spectrum as shown in Figure 7.5 is acquired. The secondary ion background has now all but disappeared, while the intensity and the resolution of the Gallium resonant peaks remains essentially unaltered.

Consequently, it has been demonstrated that, in the situation where the primary ion pulse duration is longer than the average transit time of the secondary particles across the region of laser interaction, it is possible to detect and monitor the resonant laser induced ion signal, without interference from the secondary ions directly liberated during sputtering. This is possible under static extraction field conditions, in a simple linear time-of-flight mass spectrometer, without significant degradation of performance. Furthermore, the technique is not restricted to pulsed operation and therefore applicable to situations utilising continuous wave lasers and/or continuous sputter removal of material.

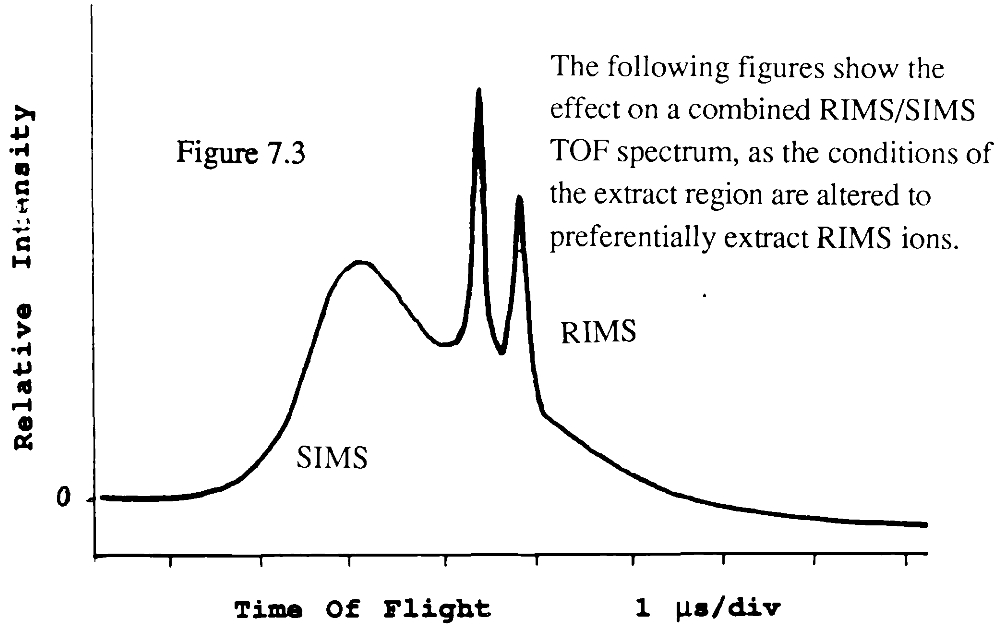

Figure 7.3

The following figures show the effect on a combined RIMS/SIMS TOF spectrum, as the conditions of the extract region are altered to preferentially extract RIMS ions.

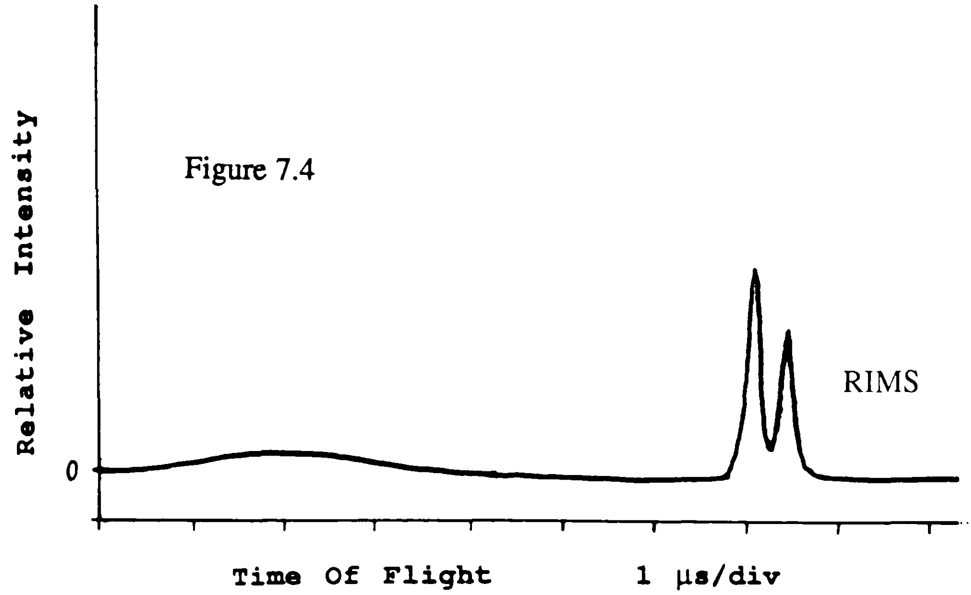

Figure 7.4

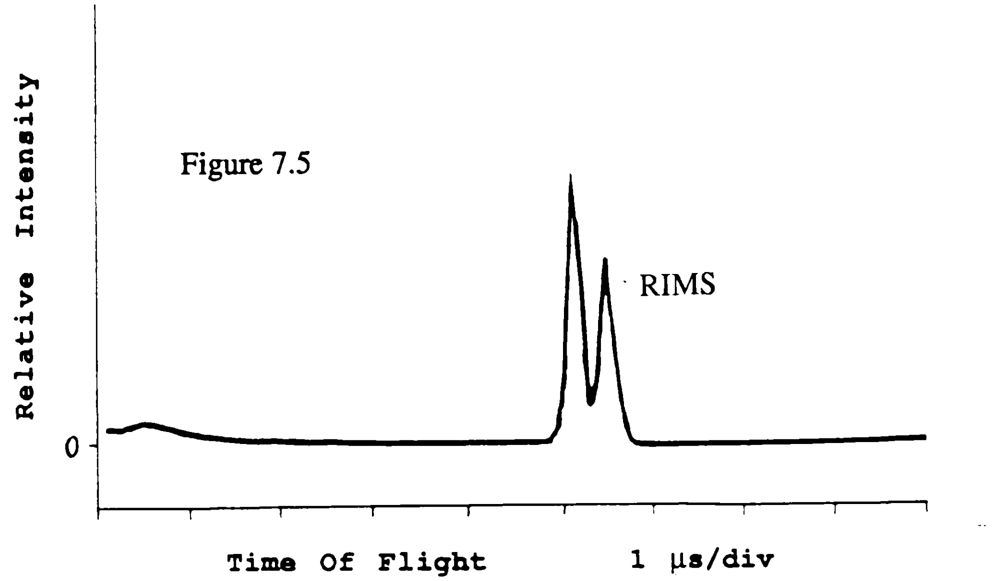

Figure 7.5

Chapter 8

Resonant Laser Ablation

(RLA)

Introduction.

The use of high powered lasers in the ablation of target samples for analytical applications has been of considerable interest since the technology became readily available. Typically, analysis is performed on the ions liberated directly in the laser-surface interaction as in LIMA, already mentioned in chapter 1, or alternatively, on the ablated neutrals via laser post-ionisation [90][6]. Due to the greater number of neutrals produced, typically 10^2 to 10^5, relative to the number of ions [90][21][70], post-ionisation is of greater interest to trace analysis.

The disadvantages of post-ionisation lie in the increased complexity of the equipment required, namely the need for separate post-ionising lasers in addition to the surface probe beam of either a laser or primary ions, and in the requirement for high geometrical and temporal overlap of a short laser pulse with the expanding ablation plume, itself likely to be generated by pulsed means.

It has been suggested [110], that the ion yield and the elemental selectivity in ablation may be significantly increased if the ablating laser is tuned to match resonant transitions of the element of interest in the target, thus eliminating the need for a separate post-ionising laser. Enhanced signals have indeed been observed in the analysis of Cd, Cu and Mo in a transmission LAMMA 500 instrument [110].

The samples used in the Cd and Cu studies were metal-doped polymers (e.g. araldite, albumin) with varying metal atom concentrations, whereas for the analysis of Mo, a steel alloy standard was used. All resonant transitions were in the UV region at 228.8 nm for Cd, 324.75 and 327.39 nm for Cu, and 311.21 and 313.26 nm for Mo. Ionisation proceeded via absorption of a second photon of the same wavelengh for each element except in the case of Cu which required additional energy from collisional mechanisms to achieve ionisation from high lying states. Photon fluences used were in the range 10^9 - 10^{11} W cm^{-2}. Enhancements were typically five-fold over the non-resonant signals, although a fifty fold improvement was observed for Cu in a particular epoxy resin, indicating the existence of severe matrix effects. Also, the widths of the resonances observed were particularly broad (0.4-0.7 nm.).

Similar observations of resonant enhancement have been made in separate laser ablation studies of Sodium and Copper [82]. The samples were polished sections of $Na_{0.7}WO_3$ and Cu. Experiments were carried out under vacuum conditions (10^{-4} torr) and also Helium buffer gas. In order to correct for any possible matrix effects and the pulse to pulse variation of the laser intensity, measurements were made to monitor the acoustic shock wave produced by the laser induced plasma expanding in the He buffer gas. It has been demonstrated [12], that in the range of 50 torr of He, the measured acoustic signal is linearly related to the amount of material vaporised.

For the case of Na, the laser was tuned to the D line at 589 nm at which an enhancement factor of over 70 was observed. For ionisation to proceed at this wavelength, three photons of the same energy are required, and hence at the low laser pulse energy used (<10μJ), the probability for ionisation by direct multiphoton interaction is very low. It was shown that the laser induced ion intensity was linearly dependent on the laser power, however the acoustic measurements also indicated a linear dependence of the amount of material ablated on the laser power, which implies a saturation of the resonant transition followed by collisional ionisation of the subsequently excited atoms within the relatively dense plasma. The situation is similar with Cu which requires a further three photons to reach the ionisation limit following resonant excitation at 578 nm.

As with the experiments of Verdun et al [110], the transition widths were relatively wide, in this case 2.2 and 1.4 nm for Na and Cu respectively under vacuum, and were broadened considerably to as much as 6 or 7 nm as the He buffer gas pressure was increased to 1 atmosphere.

The extent of this broadening is attributed to either collisional effects in the plasma formed at the surface, under the influence of intense laser powers, or increased confinement of the plasma under the high buffer gas pressure.

This chapter will describe an investigation of this so called Resonant Laser Ablation (RLA) in the analysis of Al and Ga in a semiconductor sample.

Laser Ablation.

The process of liberation of material from a solid surface, under photon bombardment, is known by various names [89], though most commonly laser ablation or desorption. The term ablation normally refers to the situation when the laser flux is greater than ~10^8 W/cm^2, while desorption applies to the use of fluxes less than ~10^8 W/cm^2. Indeed it has been recently shown in ablation studies [102], that significant measurable mass removal is initiated at a threshold of between 1 and 3 x 10^8 W/cm^2, with no evidence of cratering at lower powers, even after thousands of laser shots. These results are in agreement with the conclusions of Vertes et al.[111][112]. At the lower range in power the desorption is governed mainly by the effect of sample heating.

There exists a need to describe laser ablation in an accurate, quantitative manner as has been the case in recent years with ion sputtering [93]. Unfortunately, the physical processes involved in laser ablation are as yet poorly understood, and cannot be completely described by a sole mechanism, but rather a combination of complicated processes explaining the energy distribution of ablated particles and the formation of large clusters and droplets in some specific cases [50]. Studies have shown that the prominent mechanism occurring also tends to vary with sample composition and structure. Other factors such as the wavelength and power dependencies of the sputtering mechanisms occurring, are just as poorly understood and have been the subjects of much investigative work [89][50].

The most widely held view is that ablation occurs due to a rapid, or prompt, thermal vaporisation of the material within the beam spot [10]. Investigations however, have indicated [89][50][49], that this view of sputtering may only be correctly applied to situations where the surface temperature exceeds that necessary for vaporisation of the material to occur, possibly higher than the melting or boiling points of the material, and therefore in many cases it does not apply. The idea of a thermal process comes about from investigations of the velocity distribution of ablated atoms which can be shown to be essentially Maxwellian [11][6].

Alternatively, laser ablation has been shown to occur by the process of exfoliation, which is a macroscopic flaking of the sample surface due to thermal induced shocks within the material [89][49] and is characterised by irregular erosion patterns on the sample surface.

Another method, that of hydrodynamical ablation [50][113], refers to material removal as a consequence of transient melting which occurs when the temperature is too low for vaporisation to occur but is sufficient for the melting to proceed. Material is normally emitted in the form of droplets which are formed by the melting and subsequent thermal expansion of surface features by the laser. The melting is characterised by non-periodic surface wave patterns, while droplet formation is usually evident under close investigation of the surface after ablation.

Electronic sputtering is believed to be the major participant in neutral ejection from semiconductor and dielectric material [47][77][78]. The most likely model considered for this form of sputtering is that of the generation of a high density electron-hole (e-h) plasma [44][108][109][77][78]. An e-h pair is formed by laser induced electronic excitation across the band-gap of the semiconductor which may subsequently induce a weakening of the tetrahedral bonds. The crystal then experiences a phase transition and becomes fluid. It has been suggested [47], that phonon associated recombination occurs at the surface with the emission of a subsequently energised atom. Electronic sputtering is characterised by a high degree of sputter uniformity as well as extremely rapid erosion rates [89][49].

Whatever the mechanism, laser ablation/desorption liberates many more particles in a single laser pulse than does a typical ion pulse.

A quantity known as the mass ablation coefficient has been determined experimentally, in analysis of thin polystyrene films, and is expressed by the relation

$$\dot{m}(\mathrm{kg/s\,cm^2}) \sim 110\left[\frac{\phi_a(\mathrm{W/cm^2})}{10^{14}}\right]^{1/3} \lambda_{\mu m}^{-4/3} \qquad (8.1)$$

where ϕ_a is the incident photon flux at an ablating wavelength λ [24]. The experiments were restricted to high power densities in the 10^{14} W/cm^2 regime, well above typical LIMA power levels. Investigations to determine whether the relation is appropriate when power densities are reduced by many orders of magnitude, are currently a source of much interest.

Experimental Arrangement.

The spectrometer arrangement was as before, with the exception of a lower operating pressure ~ 1×10^{-9} mbar, due to elimination of the partial pressure of Krypton present during ion gun operation.

The semiconductor sample used in the first experiment was a $1 cm^2$ section, comprising a 1.3μm layer of $Al_{1-x}Ga_xAs$ (x = 0.3) deposited by molecular beam epitaxy onto a GaAs substrate.

Laser output again consisted of the red fundamental from the excimer pumped Rhodamine 610 dye, and its frequency doubled component, after passing through a KDP crystal. Pulse energies of 1mJ in the red and about 100μJ in the blue were available.

The laser was moderately focused using a 50 cm focal length quartz lens to a beam spot of about 1mm diameter, and was directed at grazing incidence to the sample surface. At this initial stage, the sample was positioned with its surface normal collinear with the spectrometer axis.

With a positive potential of 300 Volts on the sample stub, typical flight times for Al and Ga were approximately 27 μs and 43 μs respectively.

By appropriate positioning of the time gate, the wavelength dependences of Al, Ga and Na were obtained over the tuning range 615 to 620 nm in the red corresponding to 307.5 to 310 nm in the doubled UV.

In a second experiment, analysis was performed on the remainder of a sample which had undergone a depth analysis as described in Chapter 6 (sample B). In this case the laser dye was Rhodamine 590 (R6G), also doubled in the KDP crystal.

A positive potential of 1000 Volts on the sample stub reduced the flight time for Gallium to ~22 μs.

Results and Discussion.

The resonant ionisation scheme used for Aluminium was identical to that already investigated in Chapter 5, namely the absorption of a single blue photon from the 3p ground state to the 3d excited state, followed by ionisation via absorption of a photon from the red fundamental. The measured ion intensity as a function of wavelength is shown in Figure 8.1 .

The peaks corresponding to resonant excitation from the split ground state in Al at the wavelengths 308.305 and 309.367 nm, are clearly in evidence, with an observed enhancement of better than two orders of magnitude. The measured widths at half maximum of the resonances are less than 0.05 nm with respect to the fundamental red laser, and are correspondingly smaller for the UV excitation wavelength. The doublet separation of the excited state was too small to be resolved in this experiment.

Off resonant signals may be attributed to multiphoton ionisation of sample surface impurities of equal mass to aluminium, as well as spurious non-resonant ionisation of Al, due to fluctuations in the power density on the sample as the wavelength varies. This results from movement of the incident beam due to misalignment of the optical components.

As Gallium does not have a single photon transition within the lasing range of R610 a different excitation scheme had to be adopted for resonant ionisation of Ga. This involved the absorption of two red photons by the 4p ground state doublet to excite the 5p doublet with parity conserved [74]. The energy supplied by a further red photon is then sufficient to promote the excited electron into the continuum. Within the tuning range adopted only one transition was available, that linking the $J = 3/2$ level of the ground state with the excited state. The wavelength dependence of the ^{69}Ga ion intensity is shown in Figure 8.2, and again a strong enhancement is observed at the resonant transition wavelength of 618.644 nm. As with Aluminium, the peak width, with respect to the red wavelength, is less than 0.05 nm.

Since Ga has two isotopes of mass 69 and 71 amu in the ratio 3 to 2, clearly resolved in the spectrometer, the behaviour of ^{71}Ga as a function of wavelength, was also investigated. Once again the resonance was clearly evident, Figure 8.3, with the signal on resonance in the correct ratio with respect to the ^{69}Ga data.

As a check of the non-spurious nature of the resonant effects observed in the ablation of Ga and Al, a wavelength dependence was carried out on Na which is present as a surface contaminant on the sample, and which has no resonant transitions in the wavelength range used. As can be seen, Figure 8.4, no resonances are observed

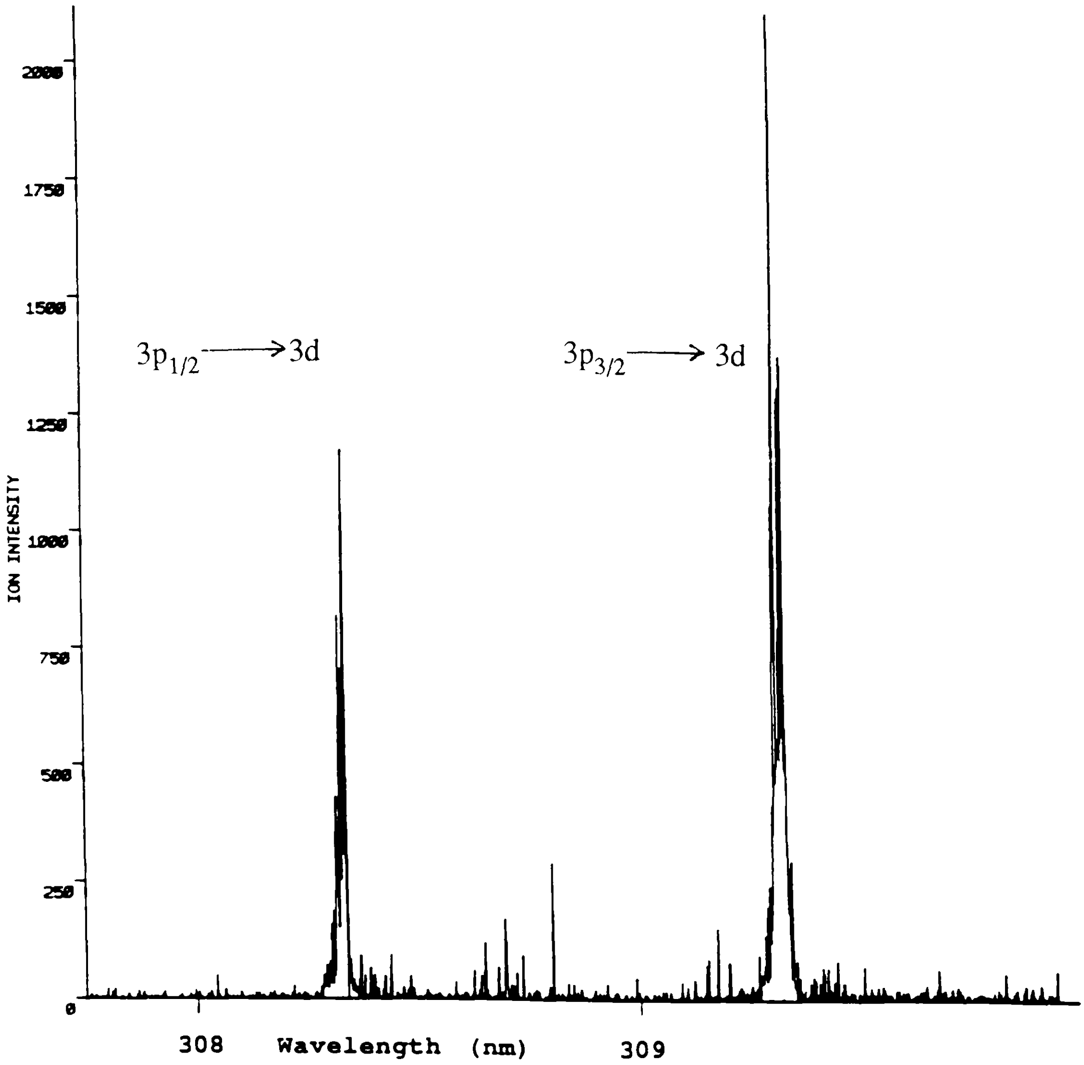

Figure 8.1 RLA wavelength spectrum from an AlGaAs sample, showing the enhancements in yield when the laser is tuned on resonance. Once again the twin peaks correspond to excitation from the split ground state of the Al atom. ADC gate delayed to coincide with Al arriving at the detector.

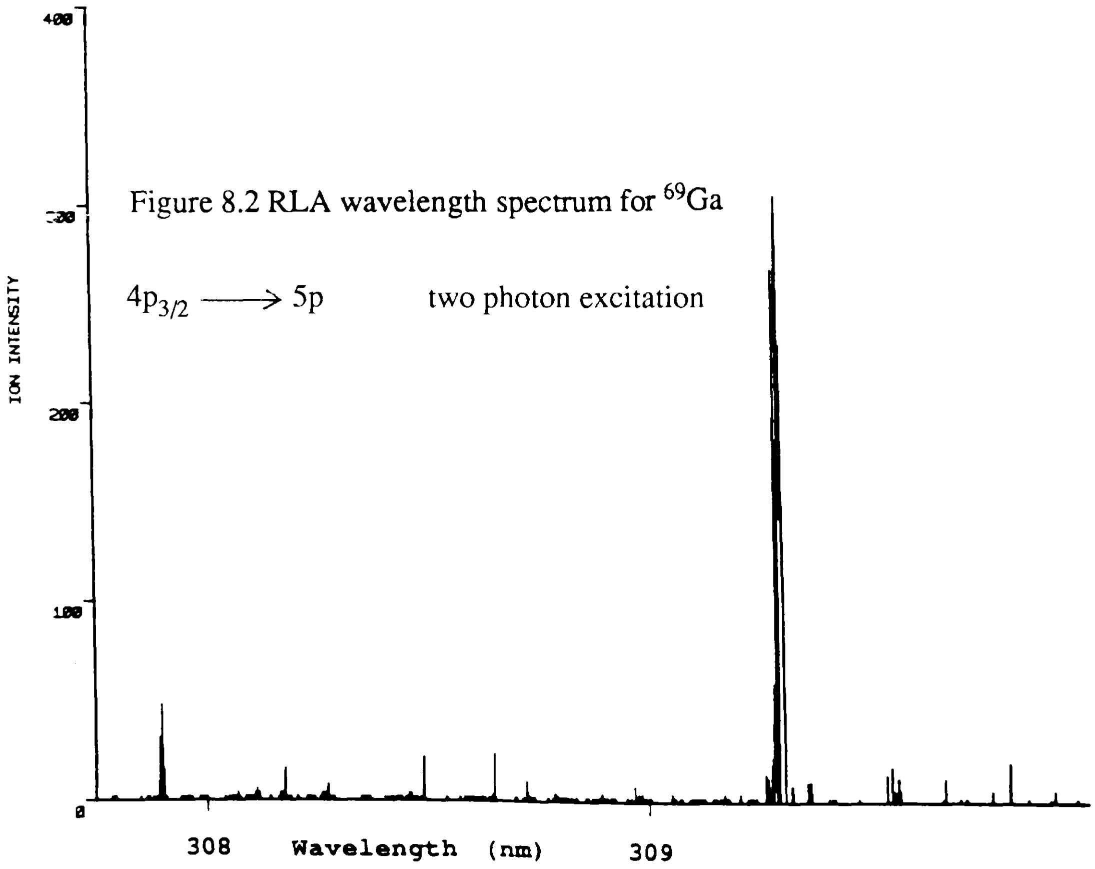

Figure 8.2 RLA wavelength spectrum for ^{69}Ga

$4p_{3/2} \longrightarrow 5p$ two photon excitation

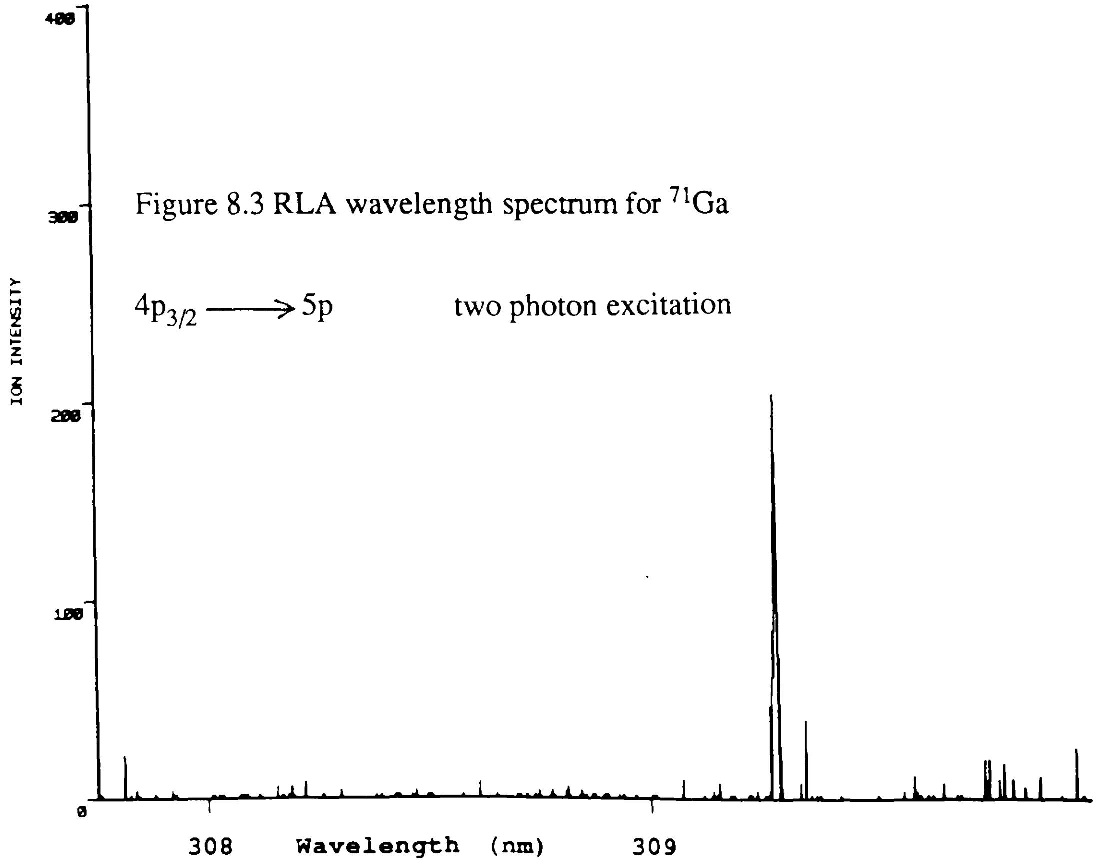

Figure 8.3 RLA wavelength spectrum for ^{71}Ga

$4p_{3/2} \longrightarrow 5p$ two photon excitation

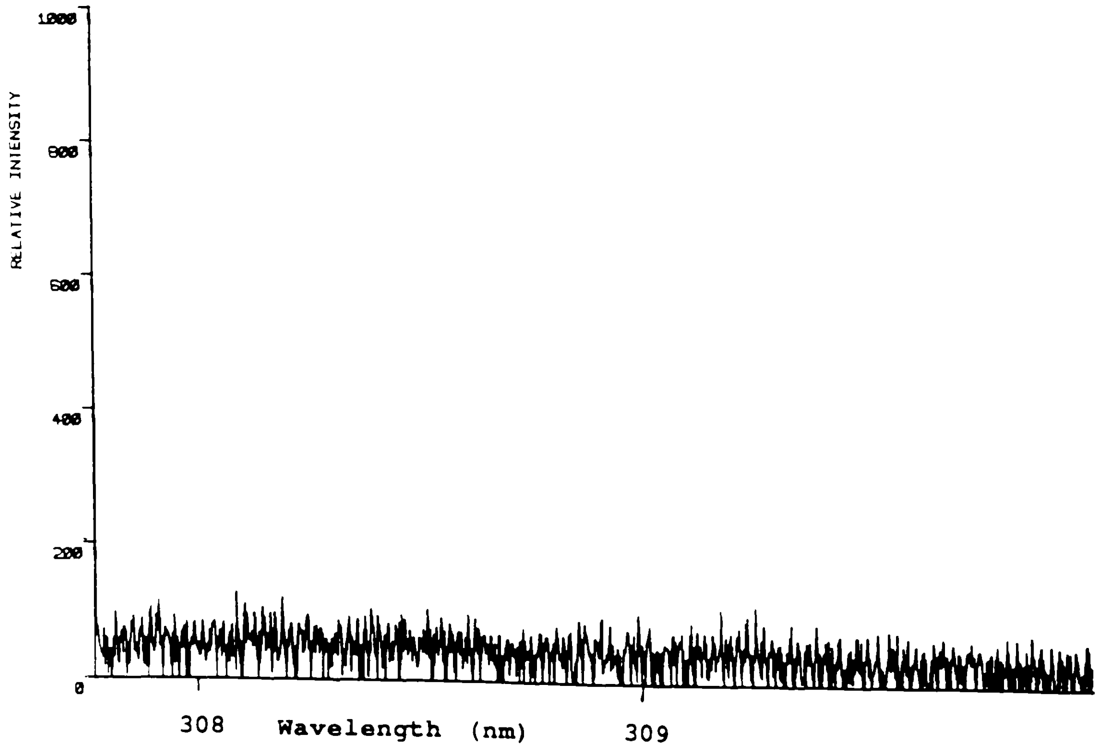

Figure 8.4 Laser ablation wavelength spectrum for Na over the same range as the previous spectra for Al and Ga showing no resonant behaviour. Na is present as a surface contaminant.

as expected, although the permanent non-resonant background is much higher than for either Al or Ga (in agreement with Chapter 5), due to the ease of desorption of the surface impurities, as a result of the lower surface binding energies for surface adsorbants.

In order to investigate whether this resonant effect occurred in a matrix different from the the smooth MBE grown layer of AlGaAs, a separate experiment was carried out on the ablation of a Calcium sample (A. P. Land [72]). The apparatus used was also different and has been described extensively elsewhere [71][101][102].

Resonant enhancement effects similar to those observed for Al and Ga were obtained.

Using a uranium hollow cathode lamp for precise calibration of the laser wavelength, to better than 0.04 nm, it was decided to investigate for any shift or broadening of the Ca resonant transitions compared to those for resonant post-ionisation of the sample ablated by a second laser. It was found that the position of the resonances matched exactly, with widths also comparable (Figure 8.5).

The implication of the observed narrow width is that the resonant phenomenon does not occur in the solid phase since the absorption band for a solid sample is several nanometres broad. Thus, one may infer that in the 'resonant ablation' process, the same conditions apply as regards the material state of the sample prior to ionisation, namely that a vapour phase has been formed. This is consistent with the acoustic wave measurements on Na ablation which indicate that the total amount of material vaporised on resonance is identical [82] with that vaporised well away from the resonant wavelength. This indicates a dissociation of the processes of ablation and resonant ionisation.

Effect of Angle of Incidence on RLA.

With the mass selection for the spectrometer again tuned to Al, a series of wavelength scans were obtained with the sample stub rotated up to a maximum angle of 25^0 around a vertical axis perpendicular to the laser direction, thereby varying the angle of incidence and the power density of the laser onto the target. Similar resonant enhancement effects were observed.

Due to the variation in extraction efficiency by alteration of the extract field lines

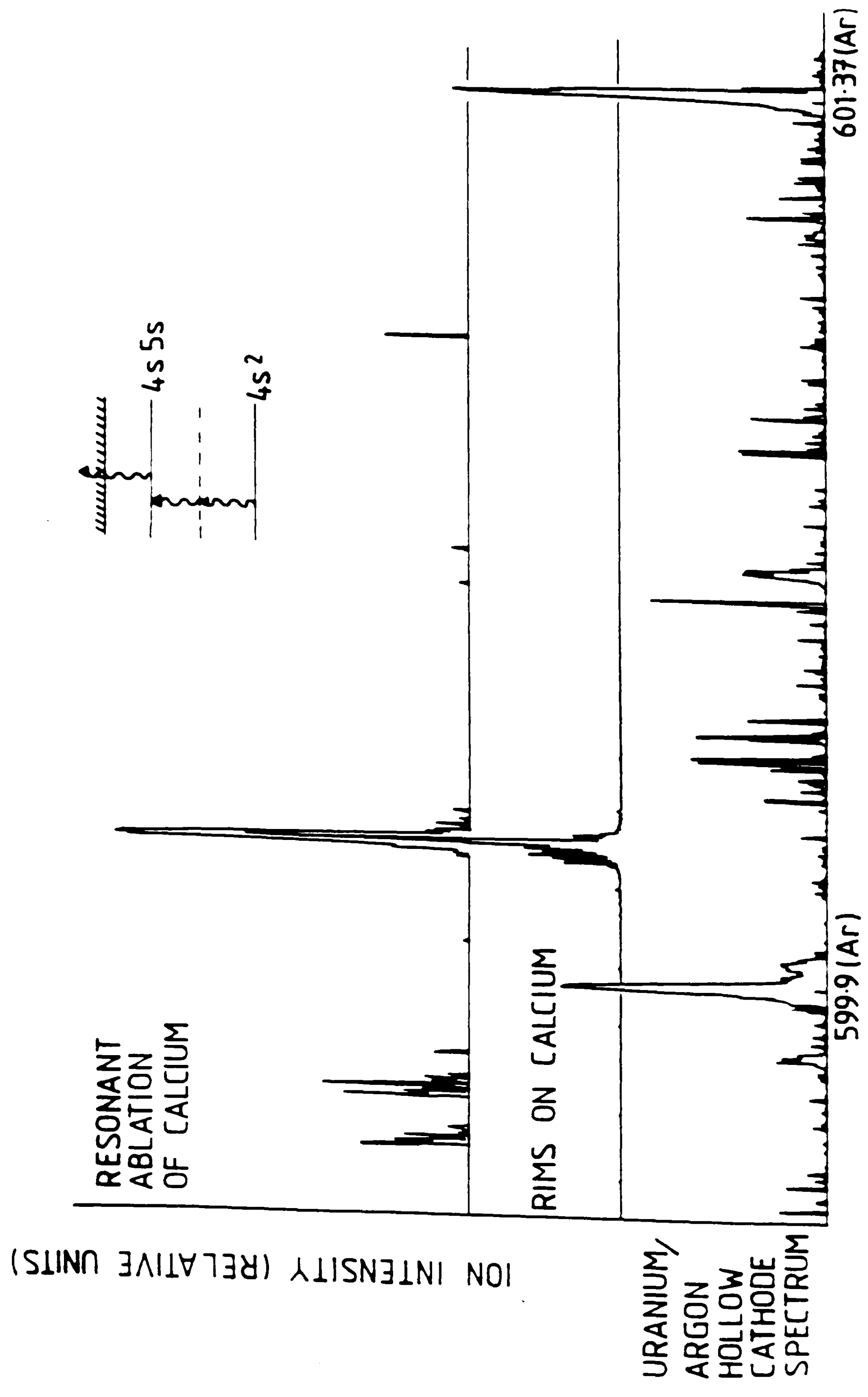

Figure 8.5 RLA wavelength spectrum for Ca

and the position of the beam on the sample, as well as the laser power density, the following experiment is in no way an attempt to describe quantitatively the variation of ion production as a function of incidence angle of the ablating laser or laser power density on the surface, but merely to indicate that the resonant effect is not restricted to grazing incidence studies and may be adopted in other more typical geometries. Further, more quantitative studies of the dependences on the aforementioned parameters are planned.

It should also be noted that the signal amplification factor may vary from plot to plot due to saturation of the ADC at particular incidence. The total laser pulse energy was ~200-300 μJ.

Figure 8.6 shows the considerable increase in ion yield obtained after a sample rotation of about 6^0. The signal amplification is identical to that for grazing incidence (Figure 8.1).

A further 4^0 rotation of the sample to 10^0 displays a further increase in the ion yield (Figure 8.7). In this orientation, the scan was repeated with a factor of ten reduction in the amplification resulting in the maximum in intensity being well below saturation of the ADC (Figure 8.8).

With the amplifier returned to the initial gain setting, the sample was rotated to 15^0 (Figure 8.9). Once again, with a lower amplification a non saturated signal could be observed (Figure 8.10). It is clear at this stage that the signal strength has begun to reduce, and as a result of a further 5^0 rotation, the signal drops by a factor of about five (Figure 8.11).

By 25^0, the measured intensity has dropped to a fraction of its original grazing incidence level, with events appearing to be of a more spurious nature (Figure 8.12).

As mentioned above, the reduction in ion signal most likely arises due to a drop in the extraction efficiency of the spectrometer rather than an effect of varying the incidence angle.

In general there is little effect on the interaction linewidth as measured at half maximum intensity, although the wings appear somewhat more pronounced possibly due to some form of homogeneous broadening mechanism.

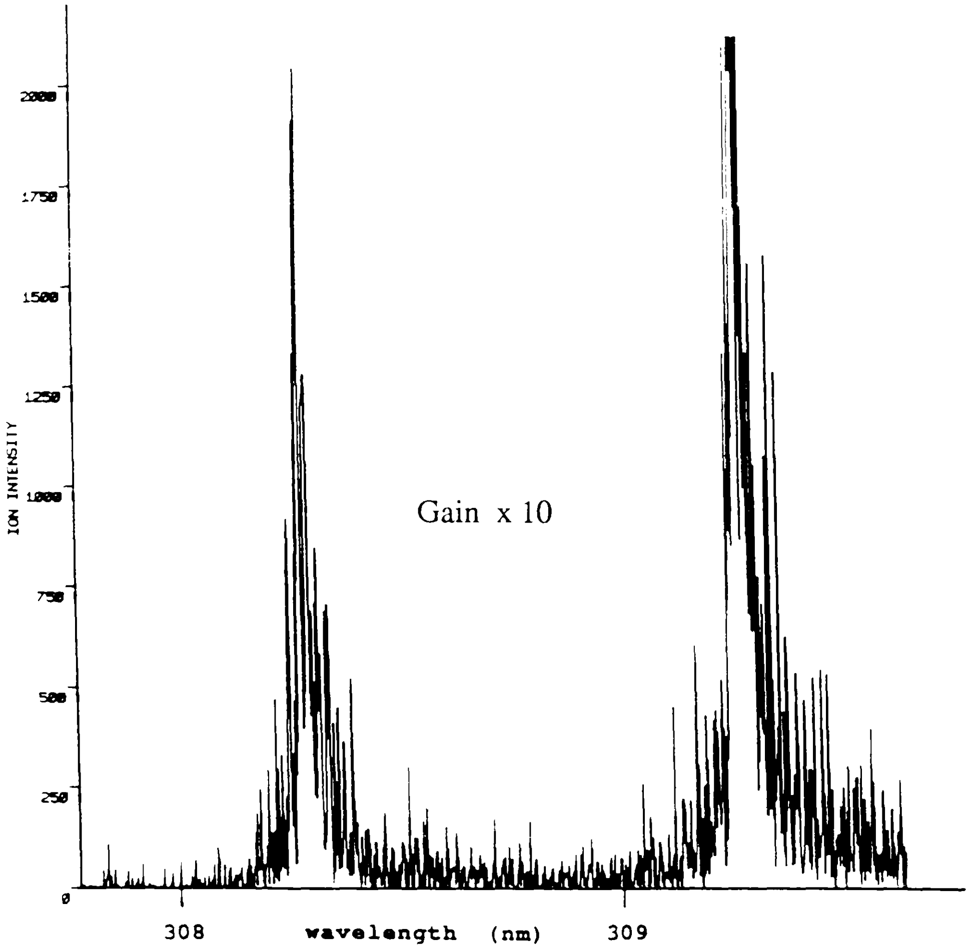

Figure 8.6 RLA wavelength spectrum for Al. Effect of a 6^0 rotation of the sample stub into the path of the laser beam, showing the enhancement in relative ion yield compared with that at grazing incidence Figure 8.1, for the same amplifier gain.

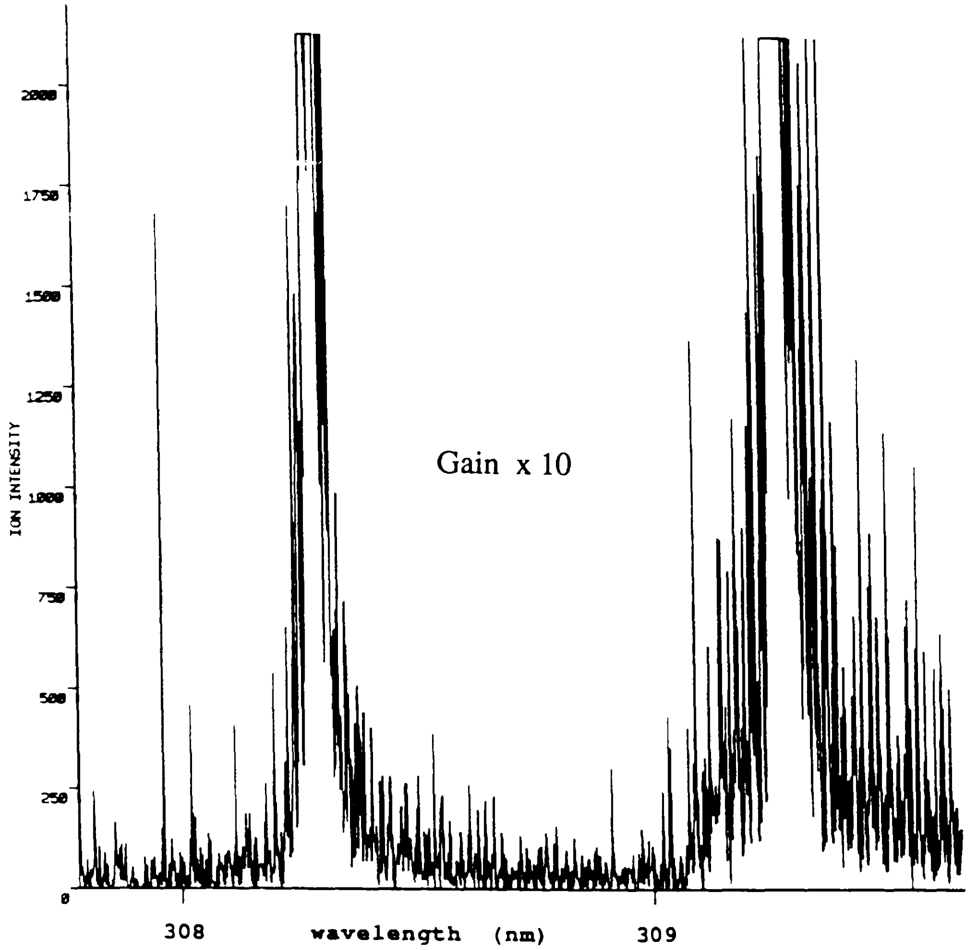

Figure 8.7 RLA wavelength spectrum for Al. Effect of a 10^0 rotation of the sample stub into the path of the laser beam, showing the enhancement in relative ion yield for the same amplifier gain as Figure 8.1.

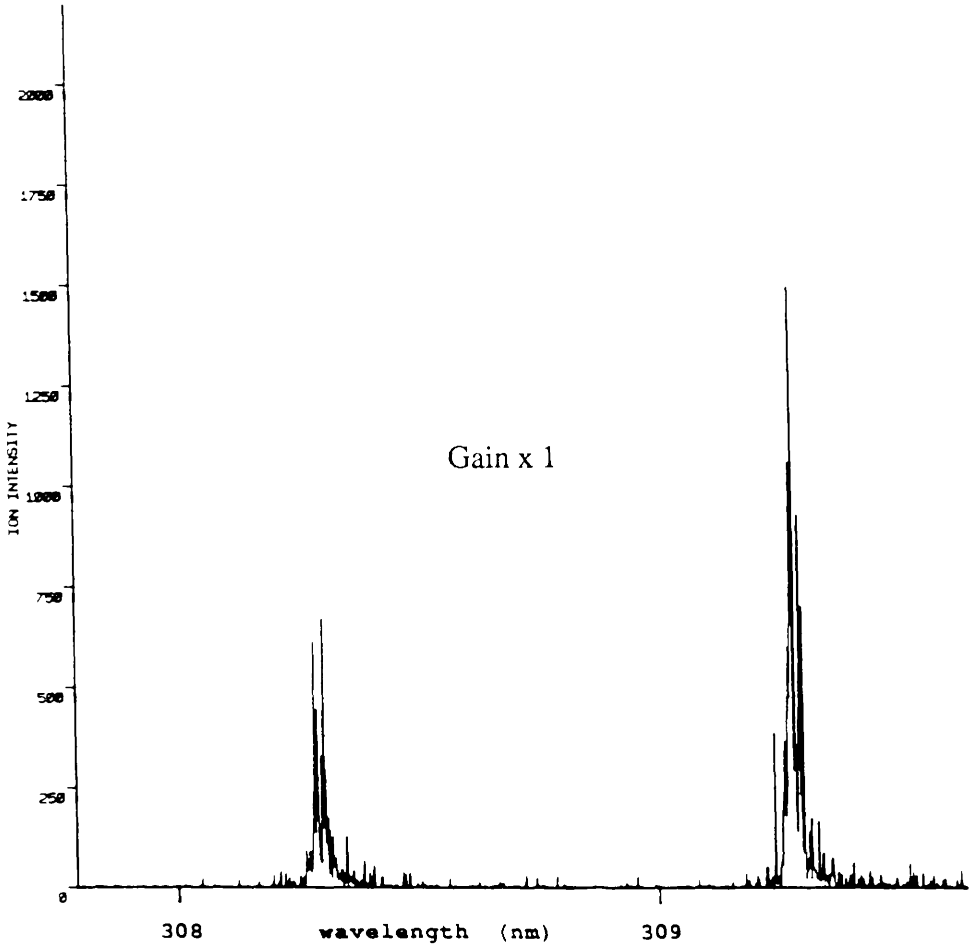

Figure 8.8 RLA wavelngth spectrum, as of Figure 8.7, with a reduction in the amplification by a factor of 10 in order to reduce the signal intensity below the saturation level of the ADC.

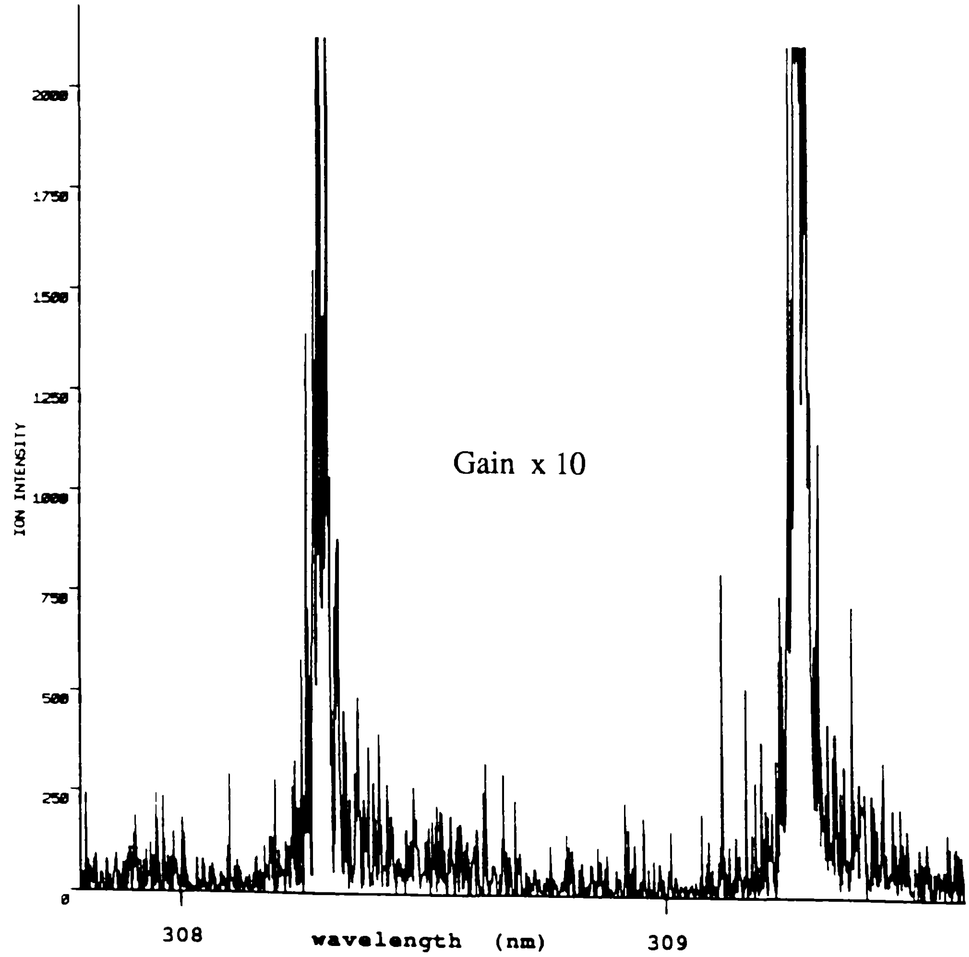

Figure 8.9 RLA wavelength spectrum for Al. Effect of a 15^0 rotation of the sample stub into the path of the laser beam, showing a drop in the relative ion yield compared to that for 10^0, for the same amplifier gain as Figure 8.1.

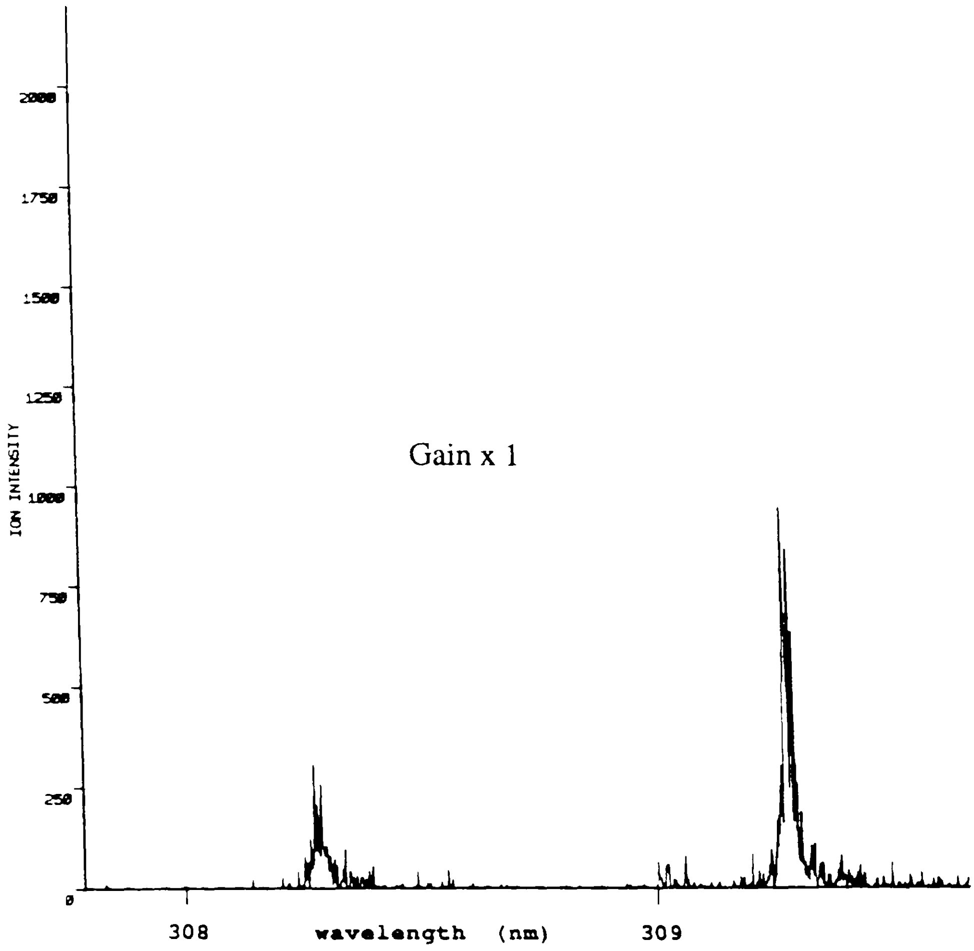

Figure 8.10 RLA wavelngth spectrum, as of Figure 8.9, with a reduction in the amplification by a factor of 10 in order to reduce the signal intensity below the saturation level of the ADC.

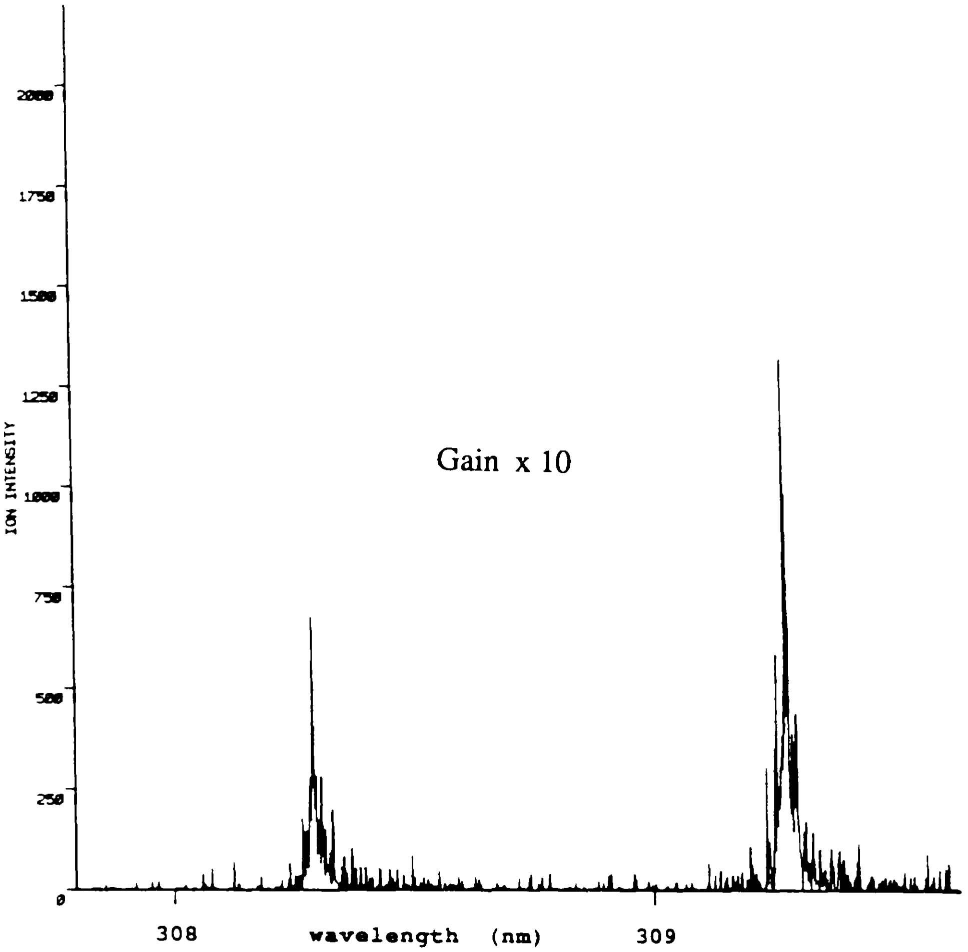

Figure 8.11 RLA wavelength spectrum for Al. Effect of a 20^0 rotation of the sample stub into the path of the laser beam, showing a further drop in the relative ion yield compared to that for 15^0. Same amplifier gain as Figure 8.1.

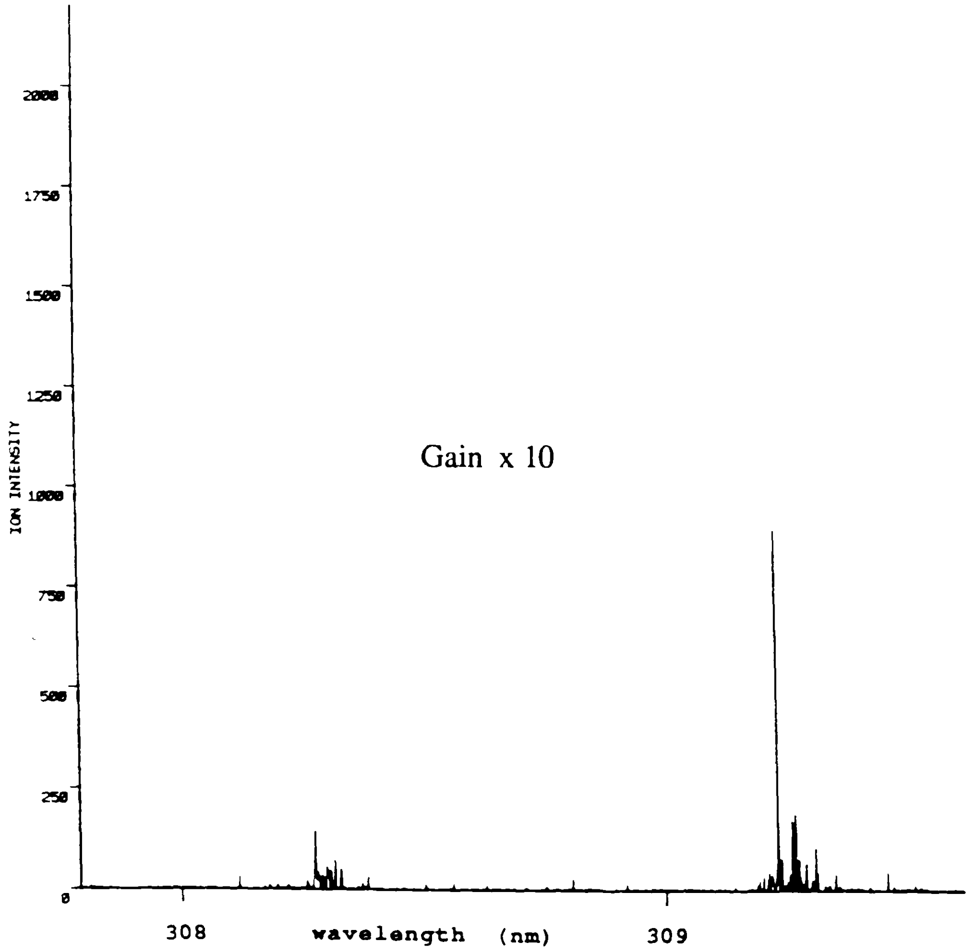

Figure 8.12 RLA wavelength spectrum for Al. Effect of a 25^0 rotation of the sample stub into the path of the laser beam, showing a dramatic reduction in the relative ion yield compared to that for smaller angles. Same amplifier gain as Figure 8.1.

Laser Power Density Effects in RLA.

In a separate experiment, involving the use of a different dye (R6G), ionisation of Ga was investigated via the adoption of an ionisation scheme similar to that used for Al above, namely excitation by absorption of a UV photon, with ionisation by a red photon at twice the wavelength. Excitation proceeds from the $4p^{1/2}$ ground state to the $4d^{3/2}$ excited state via absorption of a photon of wavelength 287.5 nm (frequency doubled 575 nm photons).

Figure 8.13 shows the ion signal as a function of the laser wavelength over a 2 nm range for the fundamental laser, corresponding to 1 nm for the excitation wavelength.

In comparison with the previous data, the width of the resonant peak is relatively wide ~0.075 nm, and also has a saturated appearance at a level corresponding to ~1 volt, which is well below the saturation level for both the ADC and the amplifying circuitry. Responsibility must therefore be placed on a saturation of the spectrometer detection efficiency, not unreasonably considering the higher extraction potential used.

The electron multiplier potential was reduced from its initial value of 2.5 kV to 2.2 kV prior to repeating the wavelength scan. Figure 8.14 shows the dependence obtained, displaying an overall reduction in the maximum intensity below the saturation level, as well as a decrease in the width of the lineshape to ~0.035 nm. This leads to the conclusion that an observed broadening can result from space charge effects within the electron multiplier, i.e. an instrumental effect, as opposed to other broadening mechanisms such as power and pressure broadening within the ablation region.

These spectra were produced whilst the laser was incident at grazing incidence to the sample. The total energy within the laser pulse, i.e. UV plus red, was ~175 μJ, focused at the sample to a spot of ~0.5 mm diameter, although the shallow incidence results in a rather elongated spot on the surface. Due to the substantial surface reflected component of the laser, the extent of the contribution from the total power to the interaction is not clear, thereby making any attempt to gauge the effects of varying the power, at present purely relative.

Figure 8.15, is a plot of the ion signal versus the joulemeter signal over the range of available laser pulse energy, up to a maximum of 175 μJ, for the laser

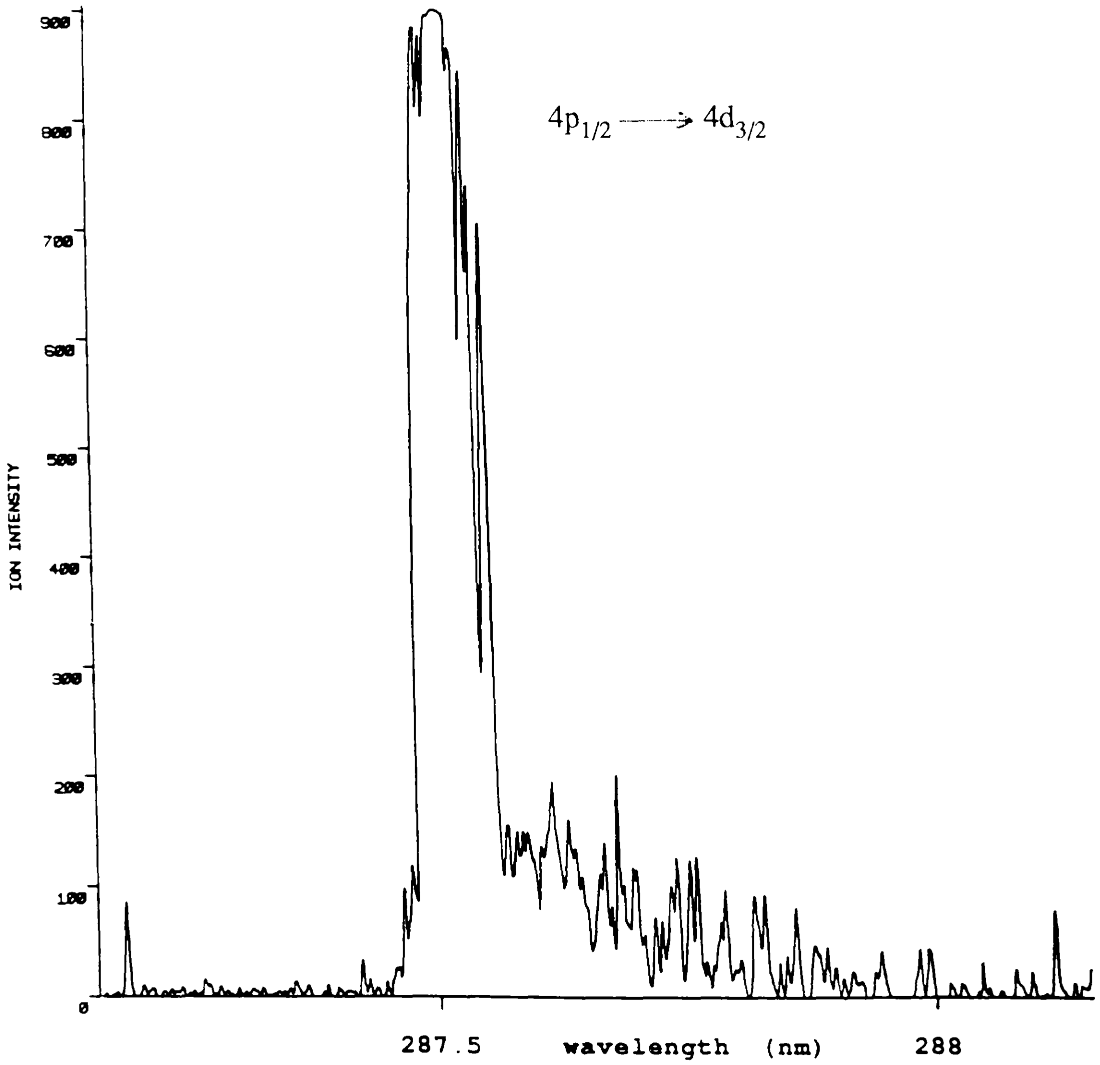

Figure 8.13 Wavelength spectrum for Ga showing saturation effects in spectrometer

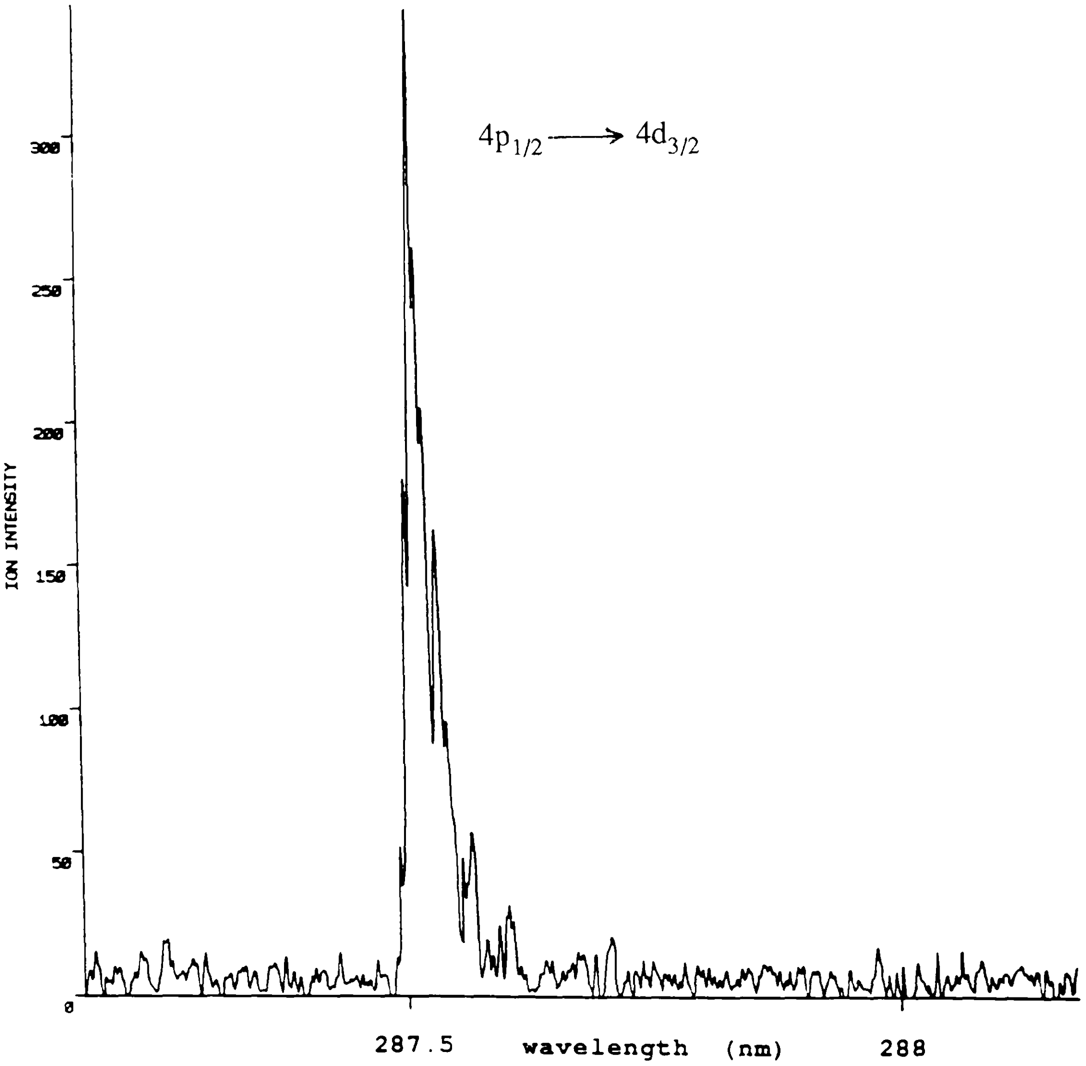

Figure 8.14 Effect on peak shape via a reduction in the detector potential

wavelength tuned on resonance. Clearly evident is a threshold value, followed by a rapid rise to the eventual onset of apparent saturation of the ionisation. Measurement of the gradient of the log-log plot (Figure 8.16), indicates a fourth to a fifth order power dependence of the ion signal for the initial portion of the curve, falling to a quadratic relationship then to an eventual zeroth order dependence as the laser power is increased.

In interpreting the overall ion production as a function of laser intensity, it must be realised that two coupled mechanisms are involved, namely, a dependence on the amount of particles liberated from the surface, and on the ionisation probability of the neutral particles by a two photon resonant process. Since the ion production increases initially, very quickly, the dominant mechanism must be the rate of ablation, suggesting that over the lower power range, the shape of the power dependent curve, reflects the dependence of the amount of Ga ablated.

In order that the ion signal follows the ablation, it is not necessary for the ionisation process to be saturated, only that the power dependence of material ablated is more rapid, while for the ion signal to reflect the ionisation rate, the rate of ablation must be constant. It is therefore conceivable, assuming a significant reduction in the liberation of neutral particles as the power is increased, that some combination of both mechanisms is occurring.

An investigation of the statistical variation of laser intensity at the maximum available revealed a deviation of 4.6% with respect to the mean value, which had the effect of inducing a fluctuation in the measured ion intensity of 9.7%, a factor of 2.1 larger, implying a quadratic dependence on ion formation. Since this portion of the power curve is relatively flat, i.e. the dependence on intensity is less than first order, the fluctuations correspond to the photon absorption rather than the ion formation on ablation, and therefore, the resonant ionisation process can be said to be far from saturated.

A similar power dependent examination was conducted at a wavelength 0.85 nm below the resonant excitation wavelength, and as Figure 8.17 indicates, for most of the range, including a portion beyond the resonant ablation threshold, the ion signal is indiscernible from random noise fluctuations. At higher powers, corresponding to the saturation region for the resonant case, the degree of ion signal statistics is sufficient to suggest the onset of a measurable degree of nonresonant, laser induced, secondary ion formation. In this case, however, the threshold does not appear to be as well

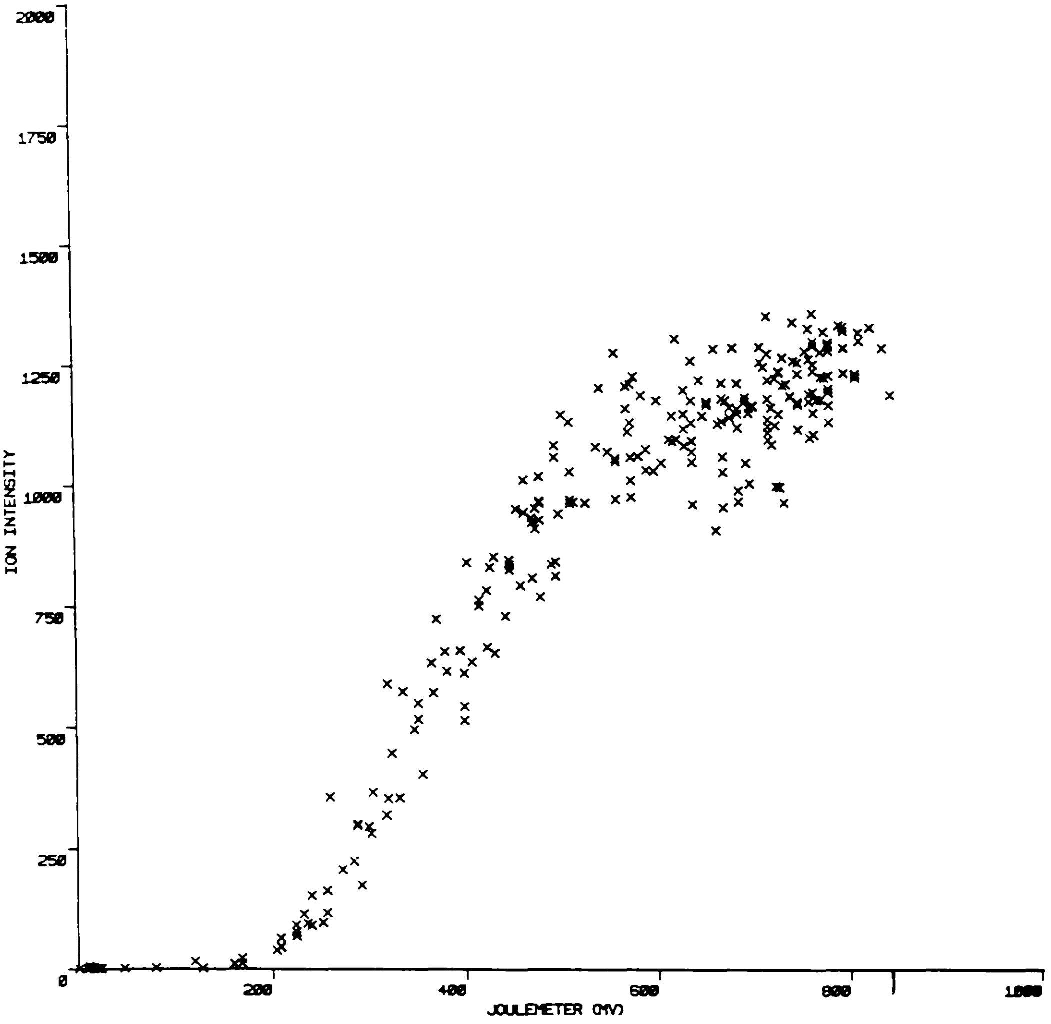

175 μJ

Figure 8.15 Resonant power dependence for Ga (max joulemeter =175μJ)

Resonant Transition $4p_{1/2} \longrightarrow 4d_{3/2}$ (287.5 nm)

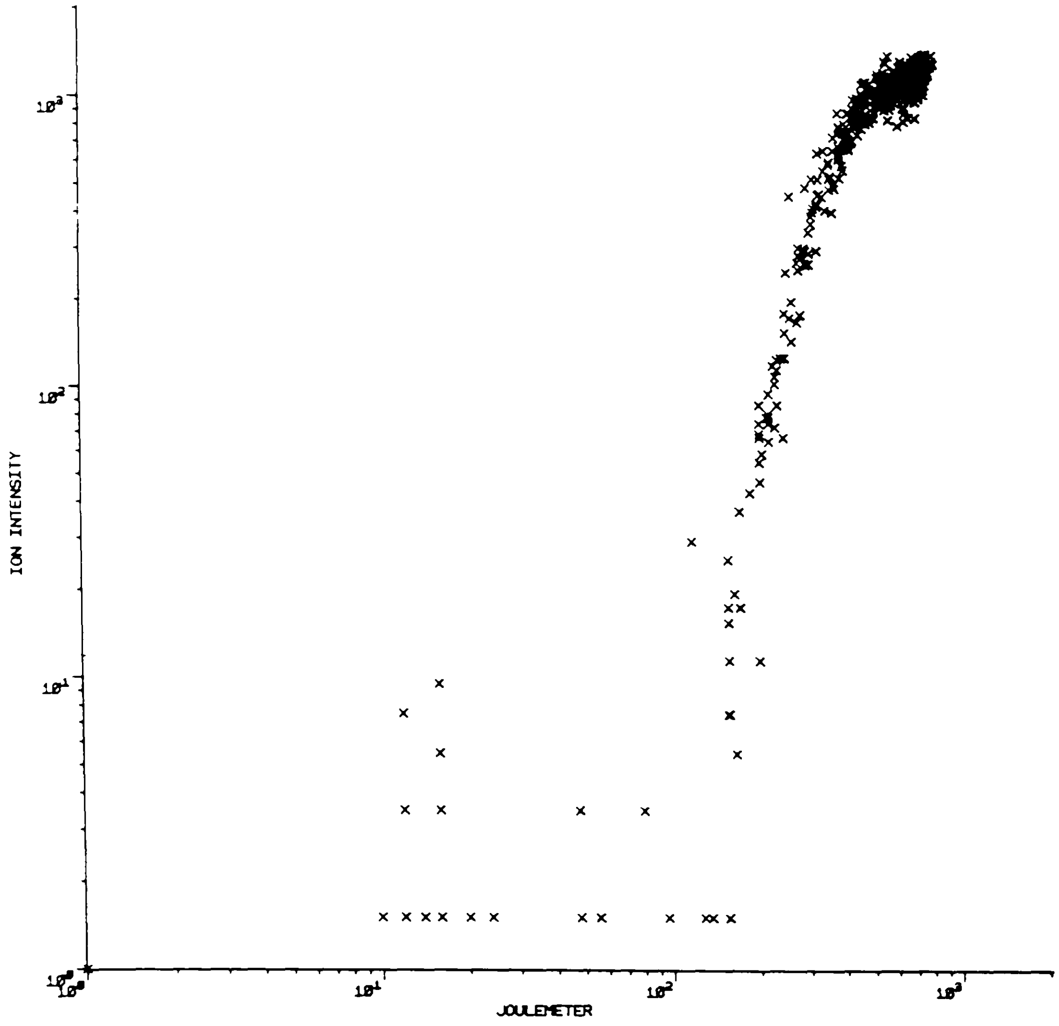

Figure 8.16 Log -log plot for the data of Figure 8.15
maximum joulemeter reading 175 μJ

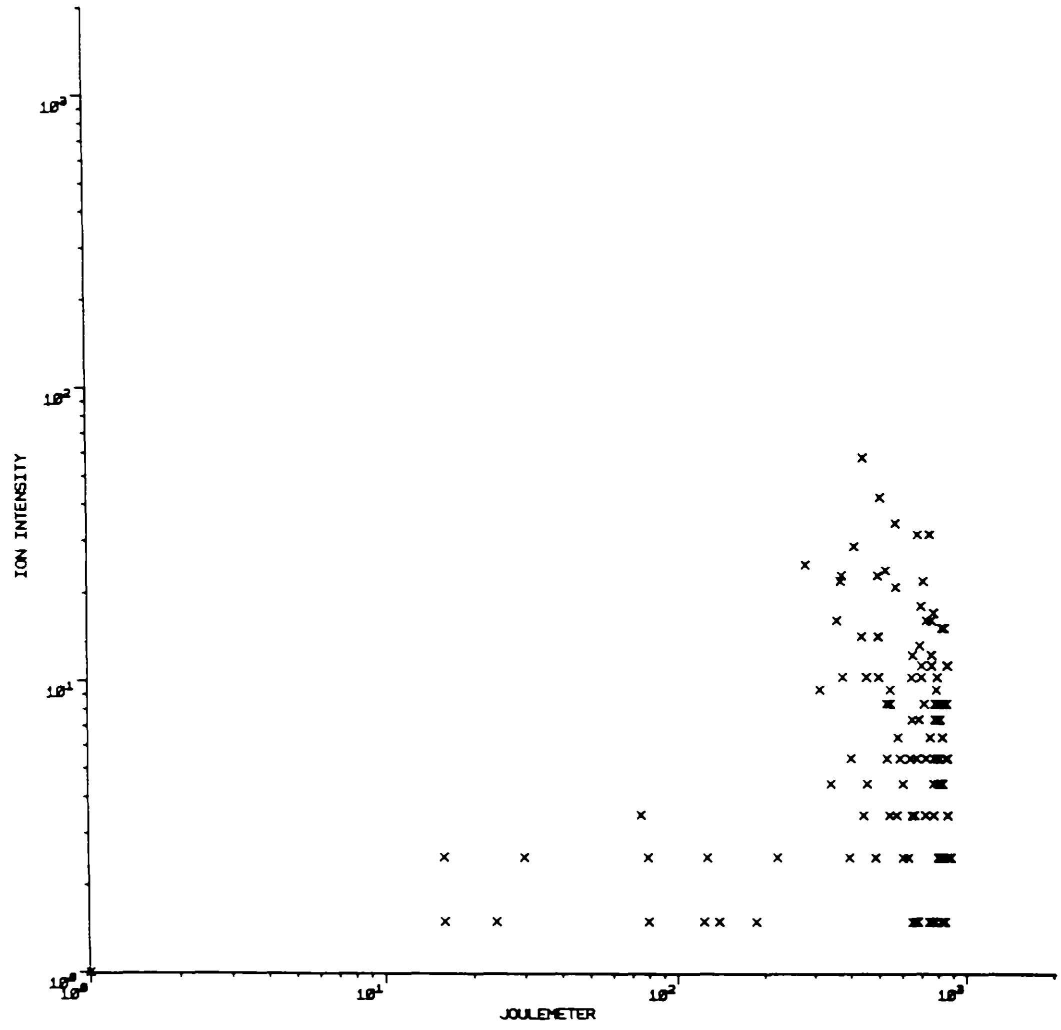

Figure 8.17 Non-resonant power dependence for Ga

maximum joulemeter reading 175 μJ (286.65 nm) defined and the shot to shot fluctuation is more pronounced.

The experiment was repeated, for both resonant and non-resonant wavelengths, over a greater range in laser intensity, up to ~1.1 mJ per pulse, or ~$4x10^6$ W/cm^2 for oblique incidence. In this case the off-resonant data was acquired at a wavelength 0.8 nm below resonance (or 1.6 nm in the red fundamental), though still sufficiently far from resonance (cf. measured linewidths), to produce no wavelength dependent enhancement.

Both sets of data are plotted simultaneously in the graph of Figure 8.18 for easier comparison. Once again, different threshold values for detectable ion formation are evident, however, in this case the larger range in available pulse energy allows determination of the non-resonant ion component as a function of intensity.

A log-log plot for this data, Figure 8.19, reveals the existence of three distinct rates of ion formation, on-resonance. The initial portion of the curve labelled A in the diagram, in agreement with the previous power dependence of Figure 8.16, has a fifth order rate of increase up to about 500 on the joulemeter scale, corresponding to ~0.4 mJ, after which the rate drops to a quadratic dependence, labelled B, which extends up to approximately the threshold for the non-resonant situation at a value of 900 (0.73 mJ). From this point onwards, labelled C, the rate increases once again to fifth or sixth order, similar to the dependence of the non-resonant secondary ion signal on intensity. It should be noted that at the higher laser power, corresponding to the final portion of the curve, there was considerable broadening of the time-of-flight distribution of ions, and since the ADC operates in a peak sensing manner, the absolute values aquired in this portion do not represent the rate of ion formation as accurately as at lower power where the temporal distribution is much narrower, and entirely within the acquisition window of the ADC. Therefore the slope of part C should in fact be steeper than observed.

The following discussion is an attempt to describe qualitatively and systematically the mechanisms involved in this interaction which contribute to the measured ion intensity over the entire range in laser pulse energy, however the explanation is purely speculative and further evidence may come to light in future analysis which may refute these ideas.

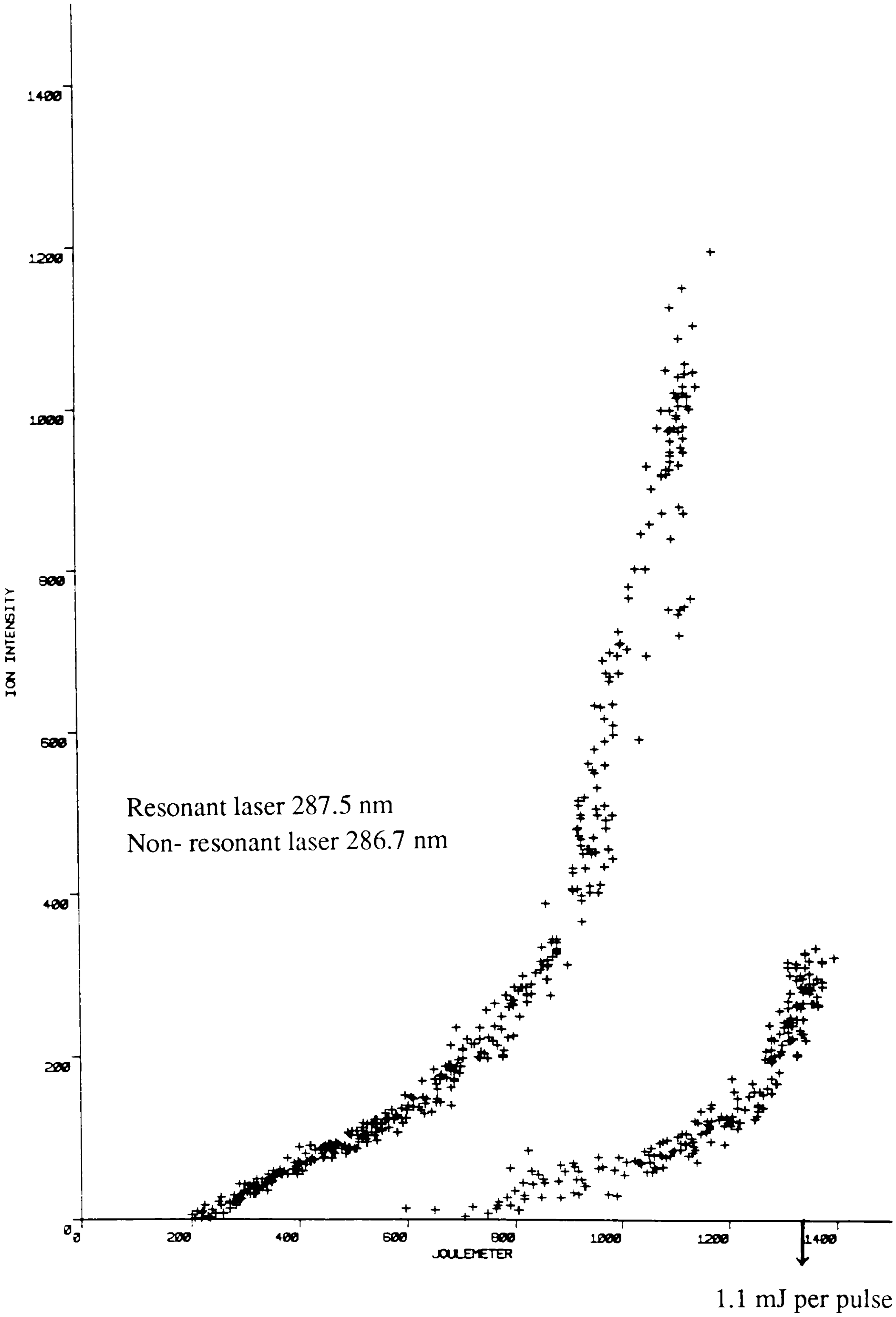

Figure 8.18 Power dependences for Ga, resonant and non-resonant cases

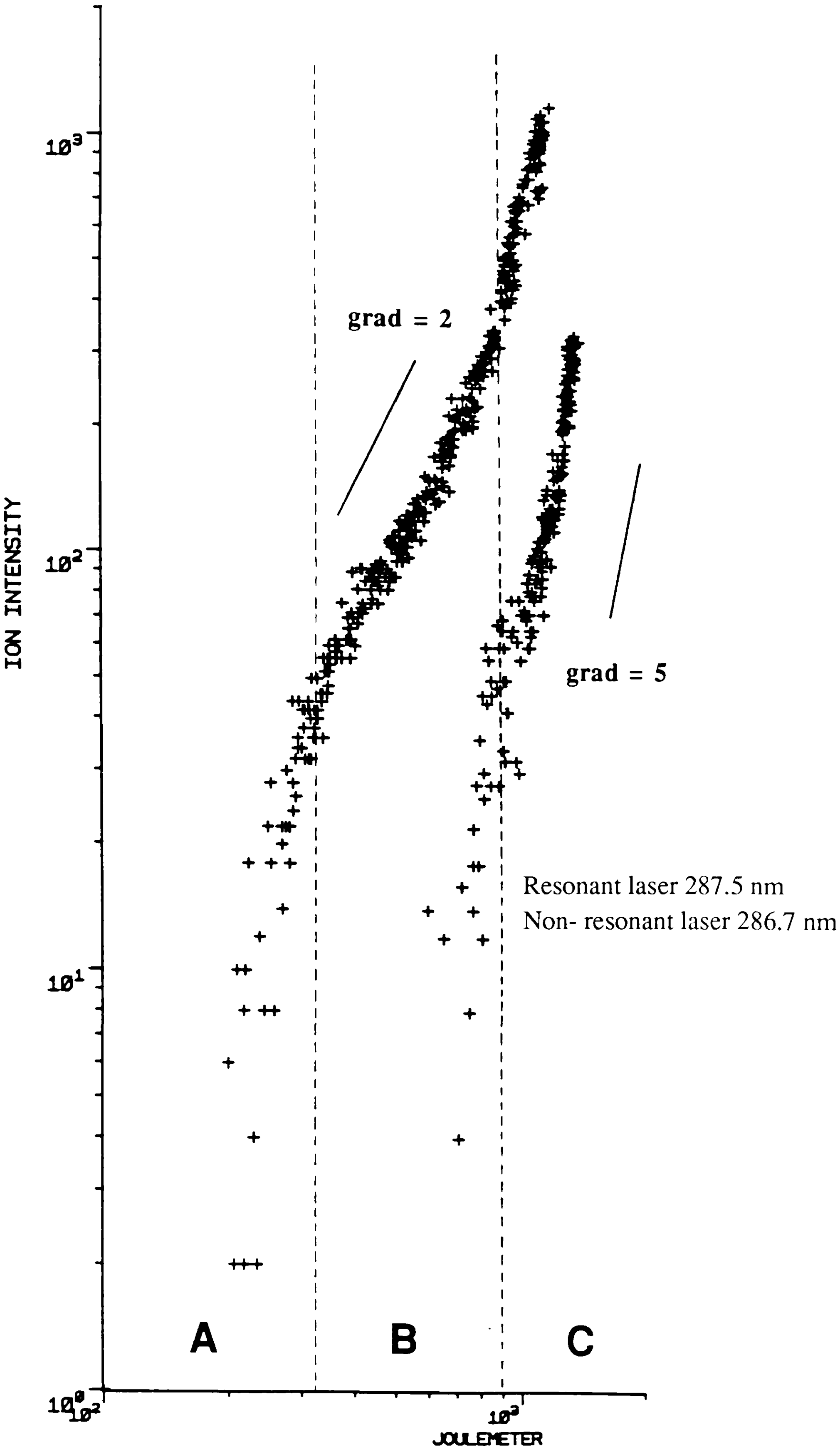

Figure 8.19 Log-log plot for the data of 8.18

With regard to section A of the power curve, let us assume at this stage that the power density of the the laser is insufficient to produce saturation of both photon absorption steps, i.e excitation and ionisation, and consequently, the ionisation probability P can be expressed by a quadratic dependence on the laser intensity I. Also, the number of particles n_0 ablated by the laser as a function of its intensity can be assigned a power dependence of some order m.

The rate of ion production S, dependent on the total number of particles available in the interaction and also the ionisation probability, can then be expressed in a simple fashion by:

$$S \propto n_0 . P \propto I^m . I^2$$

This is assuming that all ionisation is performed by the resonant laser on neutral particles, the contribution of ablated ions to the measured ion intensity being very small.

Clearly, from the observed fifth power dependence of section A, the rate of neutral material ablated follows a **cubic** dependence on laser intensity, i.e. m=3, which is attributed to the continued rise in temperature, and therefore vapour pressure, of the sample material as the energy deposited by the laser onto the sample surface increases.

Retaining the assumption with regard to the ionisation probability, that of a quadratic dependence, the immediate implication of the transition to a quadratic dependence for section B of the curve, is that the ablation yield for neutral particles has become apparently independent of the intensity. Such an effect would only be expected to arise from the attainment of a constant surface temperature, and therefore, since the energy available in the laser continues to increase, one must conclude that another mechanism is interfering with the laser solid interaction preventing energy from being deposited.

From a comparison of sections A and B for the resonant with the non-resonant case, it is clear from the lack of a measurable non-resonant ion signal, that the enhancement in the ionisation rate due to the resonant process is at least several orders of magnitude. This being the case, the ratio of ion to neutral species within the ablation plume should be correspondingly higher, and as a consequence, so too should the density of 'free' electrons. Under such conditions, it is conceivable that the surface of the sample may be shielded to an extent by this plasma [17][114][112].

The plasma mechanism responsible for this shielding is believed to be an inverse-bremsstrahlung process [13][113] or Compton effect where the incident laser photons scatter inelastically from free electrons and ions and thereby lose their energy in a transfer to thermal energy within the plasma. Such an effect is a function of many parameters including the temperature, pressure and charge density of the plasma.

Furthermore, the interaction would also tend to be self stabilising with respect to the temperature of the sample surface, as an increase in the temperature, pressure or charge density within the plasma would result in an increase in the shielding effect, which in turn would reduce the incident energy to the sample, decreasing the temperature at the surface and thereby the ablation yield. This would then result in a reduction in the vapour pressure of the ablated plume, a corresponding decrease in the shielding effect of the plasma, causing the surface temperature to rise and more material to be liberated. The rise in vapour pressure then results in the generation of more free charge which causes an increase in the energy absorption efficiency of the plasma, a rise in plasma temperature, and reiteration of the cycle.

This then may account for the apparently constant ablation rate over the range B, assuming the liberation of material results only from photon interaction with the surface, as opposed to further ion production due to the interaction of existing ions with neutrals in the plume, and with the surface.

Range C, with its overall **fourth** or **fifth** order ion intensity dependence suggests a return to an increasing ablation yield, again assuming at most a quadratic ionisation probability. Even if this assumption is not valid, the shape of the curve still suggests the onset of a process which contributes further to the ablation and/or the ionisation probability.

The mechanisms thought to be responsible are those of collisional ionisation of resonantly excited atoms within the ablation plume as the pressure vapour pressure and temperature rises, and plasma desorption or sputtering of the sample surface by energetic particles.

Finally, with regard to the non-resonant case, the absence of a measurable ion signal up to about 800 (0.65 mJ), implies that the ablated material is predominately neutral, and hence any shielding effect due to the formation of a plasma should not be so pronounced. The temperature of the surface would then rise continuously over this range resulting in the threshold conditions for other forms of ablation (see earlier section) which would account for the high rate of dependence observed after the threshold for detection, up to **sixth** order. The large difference between the ablation yield rates implies also that the apparent correpondence between the non-resonant threshold and the onset of the higher ion yield of section C of the resonant curve may be coincidental or may signify the onset of a separate ablation mechanism.

In the discussion above, the common assumption has been one of a quadratic dependence on intensity for the ionisation probability. Adoption of a linear dependence (i.e assuming saturation of the resonant process) in the highest intensity range would simply require the rate of ablation to be one order higher and would not affect the explanation of the processes involved over each region of the curve.

The effect of varying the laser intensity on the interaction linewidth for RLA is shown in the series of wavelength spectra, Figure 8.20. ındicating a progressive broadening of the linewidth and a reduction in the resonant enhancement as the non-resonant ablation component increases.

(note that this data was acquired in a separate experiment, and as a result, the specified values for pulse energy presented here may not correspond exactly to the conditions at the sample prevailing during the course of those experiments discussed previously.)

For clarity the peak widths have also been plotted as a function of the laser pulse energy in the graph of Figure 8.21, and as can be seen, over the major portion of the range, there is a very gradual increase in the linewidth up to about 600 μJ per pulse, after which the rate of increase is considerably higher. The apparent independence of the width on intensity over a large portion of the total range is evidence of the absence of power broadening effects, which lends further credibility to the assumption of a quadratic ionisation probability, also the power density required to cause such a degree of broadening is two to three orders of magnitude greater than is available in this experiment. The broadening observed is also too great to result from the Doppler effect (see Appendix C). The broadening must therefore be attributed to collisional effects within the plasma.

Since the processes of ablation and ionisation occur effectively simultaneously, i.e. within the 6ns laser pulse, the expansion of the ablated material over this short time scale is restricted to a volume extending only a few micrometres from the sample surface, and hence the particle density in this region can be extremely high, and indeed

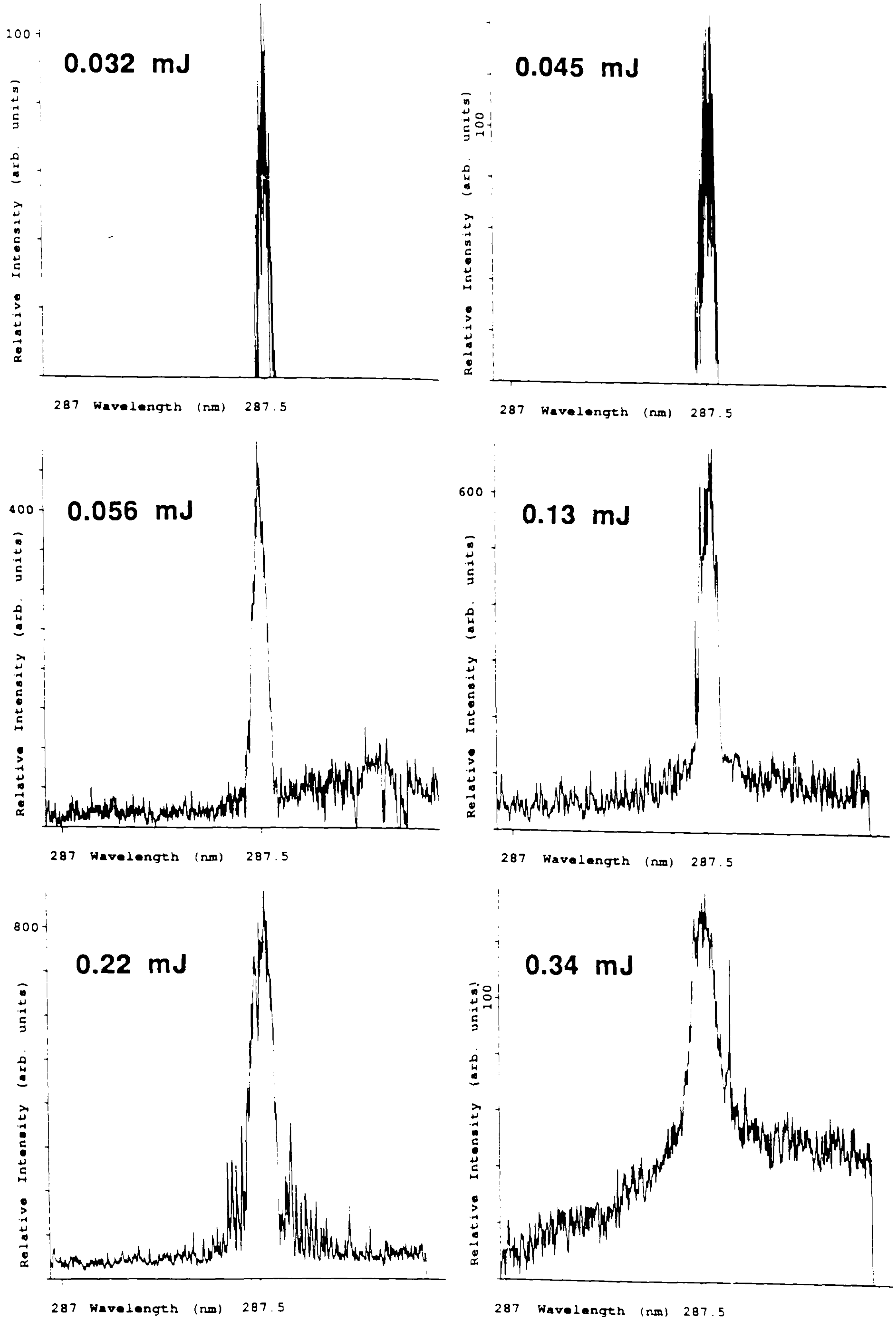

Figure 8.20 This series of diagrams shows the effect on the RLA interaction linewidth as a function of the laser pulse energy (indicated on each plot). Again the data was obtained by delaying the ADC to detect Ga.

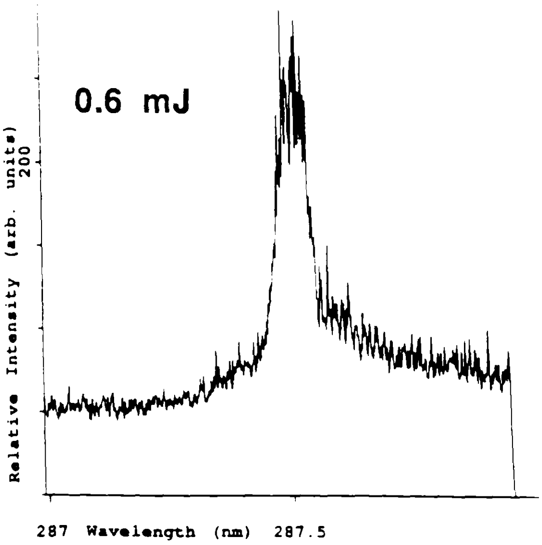
0.6 mJ
Relative Intensity (arb. units)
200
287
Wavelength (nm)
287.5

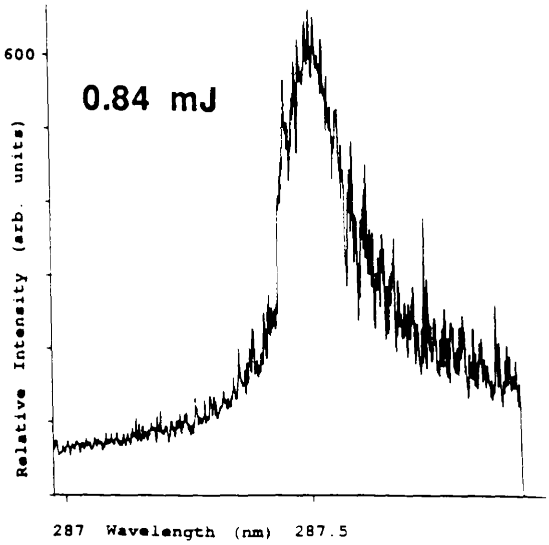
0.84 mJ
600
Relative Intensity (arb. units)
287
Wavelength (nm)
287.5

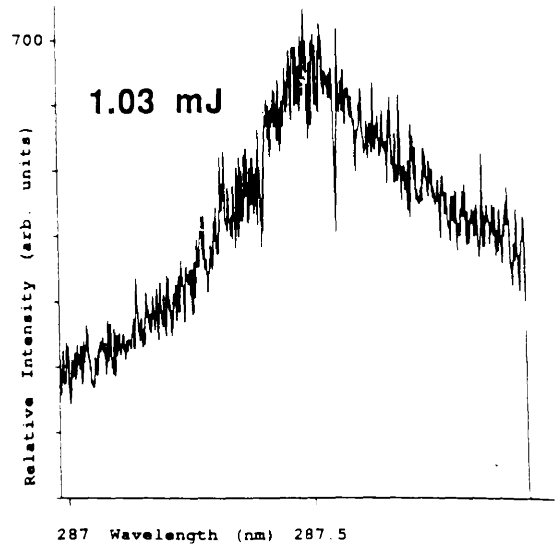
1.03 mJ
700
Relative Intensity (arb. units)
287
Wavelength (nm)
287.5

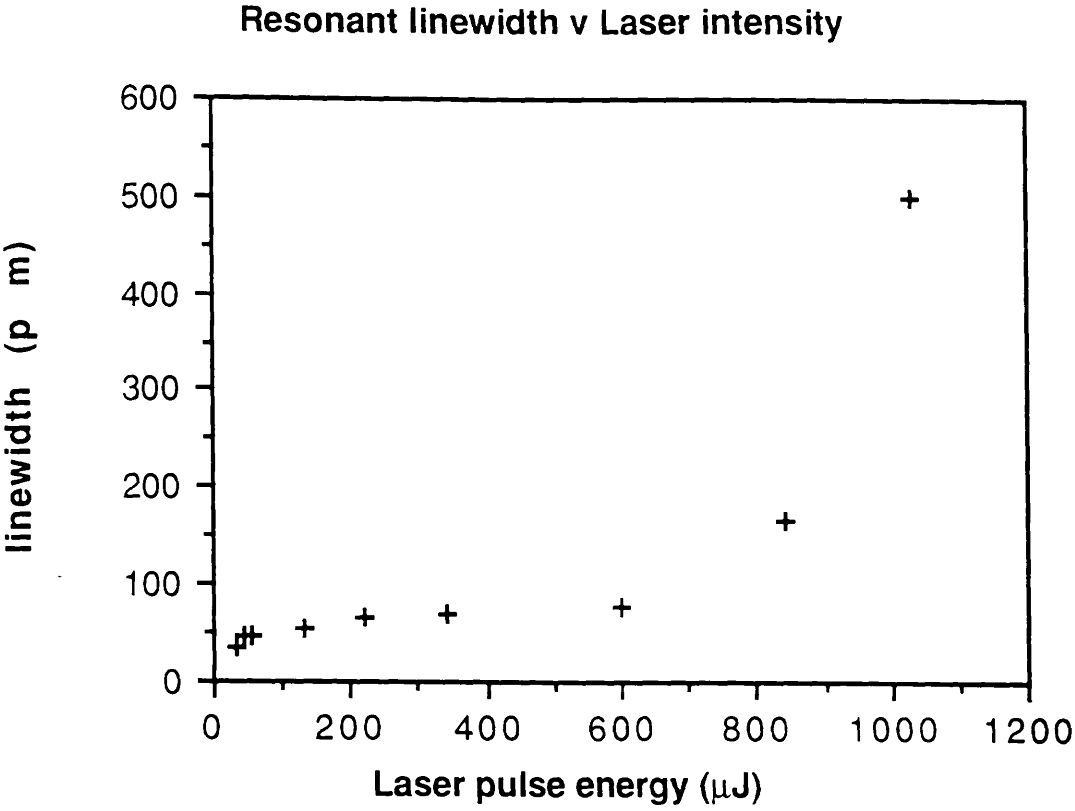

Figure 8.21 Plot of the RLA linewidth as a function of the laser pulse energy, corresponding to the data shown in Fgure 8.20.

the plasma may in many respects exhibit liquid-like qualities, since the density of a liquid is typically 1000 times that of a gas at atmospheric pressure. This suggestion is not unreasonable as the pressure required to induce a broadening of 0.5 nm may be as high as several hundred atmospheres (Appendix C). This pressure effect accounted for the broadening of several nanometres in the experiments of Pang and Yeung [82].

Conclusion.

From the observations made, one may conclude that a two stage process exists during the interaction of a single laser pulse with the solid target. Firstly, the photons in the leading part of the pulse ablate material from the sample causing the formation of a vapour of ions and neutral atoms. Secondly, as the pulse length is very short, the atoms have insufficient time to escape the laser volume before being resonantly ionised by a subsequent part of the same pulse. Hence the geometrical and temporal overlap of the laser with the neutral particles should be effectively 100%, which is probably the main factor contributing to the enhancement of the measured ionisation signal at such comparatively low photon fluxes. It is also important to note that it was not possible to reproduce the extent of resonant transition broadening observed by Verdun et al.[110], which were attributed to the effect of the ablated plasma pressure. This may be a result of the formation of a much lower density plasma during the ablation due to the lower laser flux used here. Another possible reason could be the effect of the system geometry. The transmission sample grid may impose restrictions on the expansion rate of ablated material thereby creating a localised pressure increase. Verification of these theories however, requires further experimentation.

The results presented above would seem to indicate that Resonant Laser Ablation offers the possibility of significant improvements in trace analysis of solids, with the minimum modification to commercially available laser microprobe instruments. Enhancements in sensitivity of several orders of magnitude are readily attainable, along with the added advantage of the atomic selectivity useful in the reduction of isobaric interference, possibly eliminating the usual requirement of such instruments, that of a high mass resolution spectrometer. Furthermore, sensitivity need not be sacrificed in utilising lower primary laser power implying a reduction in the degree of surface damage and fragmentation of surface adsorbed molecules, with the additional prospect of being able to apply higher repetition rate lasers, which generally offer higher standards of pulse to pulse stability, as well as improvements to analysis times.

A consequence of performing resonant ablation is that it may provide a degree of additional and vital information with regard to the temperature of the laser-solid interaction, allowing a comparison with that for ion-solid interaction.

Assuming the absorption probabilities to the excited intermediate state from both ground state levels are equal, then from Equation 5.2, a room temperature interaction at 300 K, would result in near equivalent ionisation probabilities, as observed in the wavelength dependent post-ionisation of Chapter 5. In Figure 8.1, and indeed in the other data on the angular dependence of ion formation, presented in this Chapter (Figure 8.8), the peak corresponding to the transition from the upper level of the ground state is generally more intense by typically a factor of two and as much as a factor of three.

As the separation of this doublet is too small to be resolved in these experiments, the relative transition probabilities from the J=3/2 and J=1/2 ground states are related to the weighting factors of the upper states $g_1=2(3/2)+1$ and $g_2=2(5/2)+1$ by the expression:

$$\frac{g_1+g_2}{g_1}=2\cdot 5 \qquad (8.2)$$

due to single photon absorption occurring between the J=3/2 ground state and both the J=3/2 and 5/2 excited 3d levels. This then can account for a relative intensity of the observed transition peaks up to a factor of 2.5. Any increase over this ratio can be accounted for by a population in the J=3/2 ground state level of more than 50% and therefore a higher temperature than 300 K.

Therefore in comparison with the ion sputtering case (2 eV), it can reasonably be stated that laser ablation occurs at comparatively higher temperatures than ion sputtering.

Under the assumptions already made with regard to the cross-sections, and the lack of any excitation pathways except thermally between J=1/2 and 3/2 ground states, the maximum allowable population ratio between the upper and lower levels is 2:1, which could lead to a possible ratio of transition probabilities of 5:1.

Referring back to the case of ion sputtering, taking into account the above ratio of transition probabilities of 2.5, the observation of equal intensity peaks would tend to imply the sample is much cooler than 300 K. The analysis was carried out at room temperature, however, and therefore it must be assumed that there are other contributing factors to the rate of ionisation from the various levels, such as, possibly differing cross-sections for the states, and/or ionisation probabilities, or perhaps de-excitation mechanisms not considered.

A further interesting consequence of the data plotted in Figure 8.19, is that extrapolation of the off-resonant gradient, assuming the fifth order dependence can be extended over the lower range, back to the lower limit for the resonant case, may yield some information regarding the ratio of ions to neutrals liberated. As can be seen, Figure 8.22, there are approximately two orders of magnitude separating the lowest resonant ion signal and the extrapolated value, point X. Furthermore, assuming there is no saturation of the excitation at the lowest intensity, it is unlikely that more than a few percent of the available neutral particles are ionised, thereby contributing a further two orders of magnitude to the possible ratio, resulting in an estimate of the ion to neutral ratio of 10^{-4} in agreement with accepted values which range from 10^{-2} to 10^{-5} [90][70].

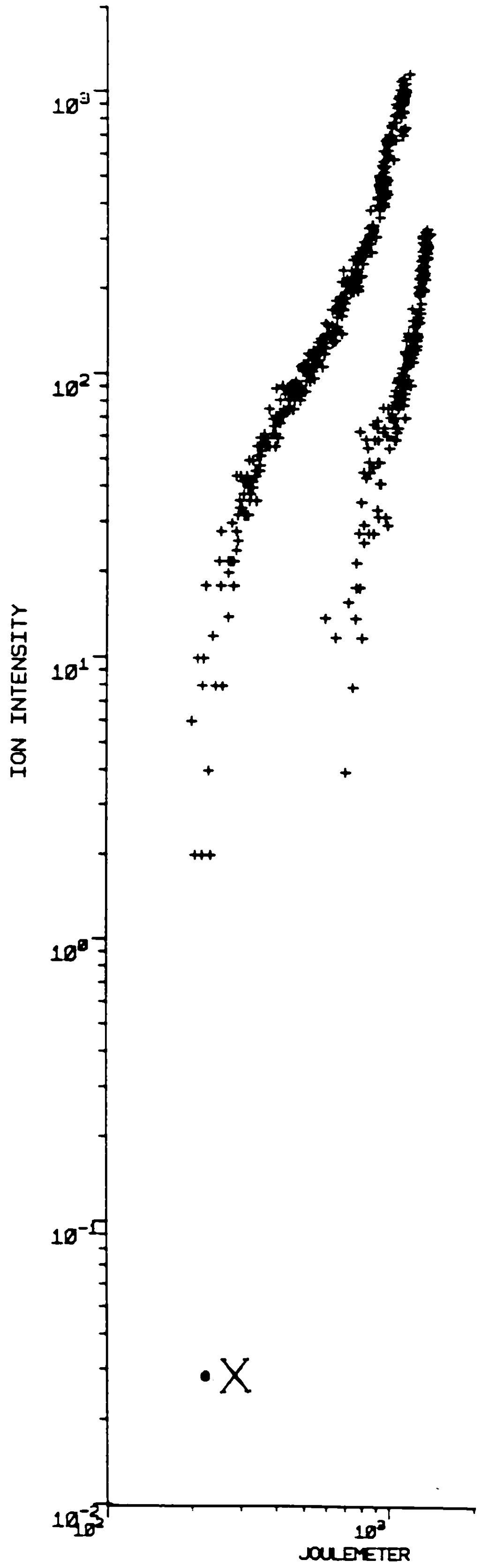

Figure 8.22 Point X is the extrapolation of the non-reonant laser ablation power dependence back to the threshold intensity for RLA ion detection.

Chapter 9

General Discussion and Future Developments.

To reiterate, the major objective of this project was the development of Resonance Ionisation Spectrometery as an analytical tool for the analysis of, principally, III-V semiconductor material.

Resonant Ionisation has been employed in two forms, firstly that of post-ionisation of sputtered material (e.g. **SIRIS** [84]) closely related to the established techniques of **SIMS** and **SNMS** (Chapter 1), and the much more recently observed method of Resonant Laser Ablation (**RLA**), a more sophisticated form of the **LIMA/LAMMA** process.

Primary ion sputtering (Chapter 3) has the great advantage of a high degree of erosion uniformity, particularly when using a rastered ion beam, controllability of the various beam parameters of energy and ion current, and temporal stability, making it ideally suited to depth profiling. In recent years much time and expense has been involved in the development of SIMS technology, in particular the design of primary ion guns, ion extraction lenses, mass filters etc., as well as procedural improvements such as raster gating, in order to obtain the best results, and minimise the instrumental effects prevalent in sputter profiling. Today many commercial, dedicated SIMS instruments are available.

Since RIS is essentially a development of the same analyical procedure, it would be unreasonable to expect comparable performance from relatively unsophisticated apparatus, suffering from similar instrumental problems. For these reasons it was no surprise that the depth resolution observed in the analysis described in Chapter 6 was relatively poor by present SIMS standards. However the results presented, together with others [19][36], give an indication of the possibilities which lie ahead for accurate quantitative depth analysis by this method through further developments in the technologies and procedures applied.

One of the major limiting factors to the depth resolution, in the experiments detailed in this study, was the primary ion gun, which was more suited to large area surface cleaning and was designed specifically to be operated in a straightforward continuous beam mode. Its adaption to pulsed operation, although shown to be possible, was unsatisfactory in that rapid mode switching was impossible, available current was restricted, and the pulse length was long in comparison with the laser pulse, resulting in poor temporal and spatial overlap. A future development at Glasgow will see the implementation of a more advanced ion gun developed by Kratos Analytical, specifically designed for depth profiling applications. Figure 9.1 is a recently acquired scale diagram of the instrument.

The gun incorporates a high brightness Penning ion source, primary mass filtering by a Wien filter to remove undesirable contaminants and isotopes from the beam, and is capable of either continuous or pulsed mode to allow sputter erosion of the sample, and to complement the time-of-flight operation during analysis. Pulsing of the gun is achieved by electronic blanking, which is a rapid deflecting of the beam across an internal aperture, prior to the focusing column. Furthermore, the gun possesses the capability for continuous variation of the primary beam diameter from a few microns to a fraction of a millimetre, depending on the primary energy (variable from 0.5 to 15 eV) and mass. This allows the current density on the sample to be extremely high, which is desirable for rapid sample erosion and to generate a dense secondary sputtered particle plume resulting in an increased number of particles within the influence of the laser. Another important feature of the design, is the incorporation of a 3^0 bend in the internal ion trajectory, in order to suppress the neutral component of the primary beam.

Due to the limitations of the existing analysis chamber, as regards adaptability and additional apparatus, the ion gun will instead be mounted on the Glasgow CMS instrument thereby utilising the advantages of a steeper primary incidence angle (45^0), high resolution spectrometer, and its sophisticated data acquisition system. These additional factors, together with improvements to the existing secondary ion extraction system, such as a more defined extraction focus and incorporation of an aperture to prevent edge effects, should lead to an instrument at least comparable with existing SIMS technology, and with the additional advantages offered by resonant post-ionisation, eventually to a superior instrument. Eventually, it is also expected that the entire procedure will be under computer control.

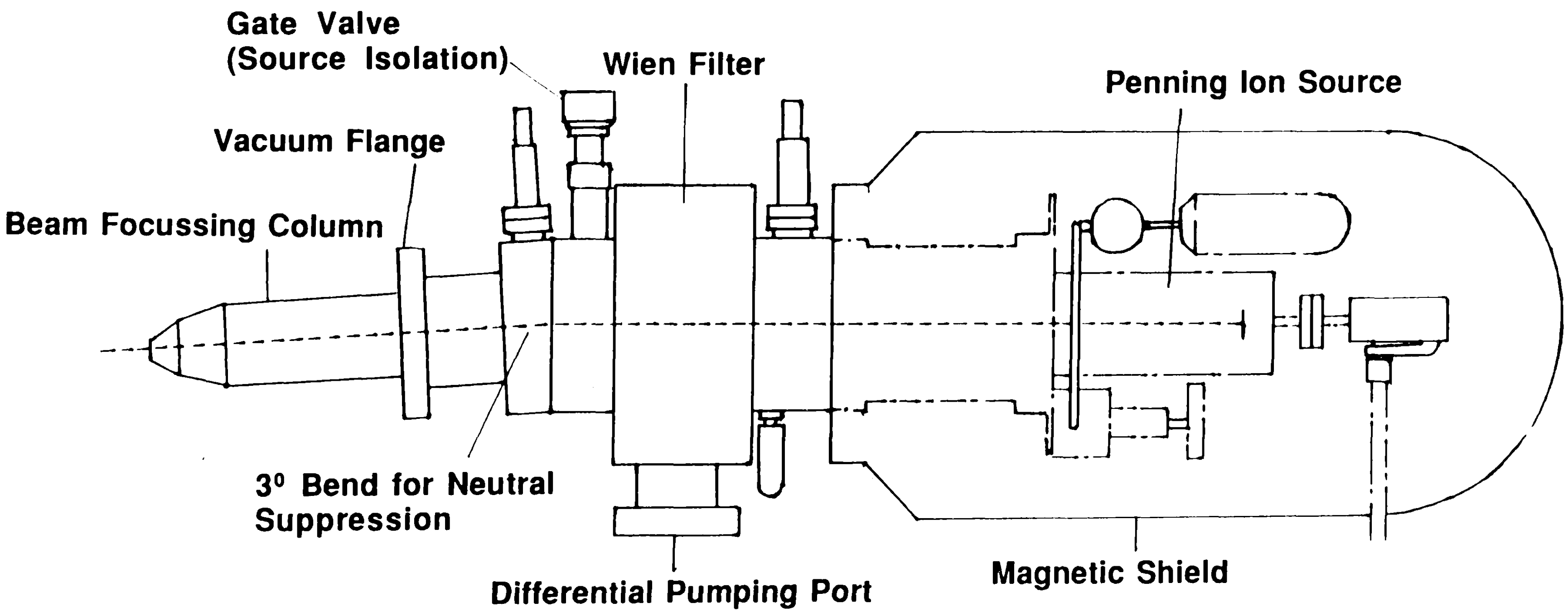

Kratos Profiling Ion Gun SB-262

Gate Valve
(Source Isolation)
Wien Filter
Penning Ion Source
Vacuum Flange
Beam Focussing Column
3⁰ Bend for Neutral
Suppression
Differential Pumping Port
Magnetic Shield

Figure 9.1

An extremely worthwhile exercise was the development of the reverse field extraction optics for secondary ion suppression (Chapter 7), an idea which stemmed intuitively from experience gained during the initial design and construction of the mass spectrometer and was later successfully modelled on computer and effectively applied in a later experiment to assess its capability. Its disadvantage lies in the reduction in overlap with secondary particles due to the volume of laser interaction being distanced from the sample surface. However this problem could possibly be alleviated to an extent by a geometrical scaling down of the interaction volume and the ion extract electrodes and/or increasing the primary current density.

The technique may prove more beneficial in the post-ionisation of laser ablated species as the liberated particles on ablation have typically lower energies than those released due to collisional mechanisms, and hence the suppressing field may be subsequently weakened, allowing post-ionisation closer to the sample, and improved overlap. Also, the angular variation on ablation yield is generally more pronounced in the forward direction with a $\cos^n\theta$ (where $n \sim 8$ [114]) dependence, as opposed to ion sputtering which results in typically a $\cos\theta$ evaporation distribution. This implies a higher density of secondary particles within the laser volume, and within the acceptance angle of the extract system, resulting in a less pronounced effect on overlap of post-ionisation distanced from the surface.

Further instrumental improvements to the post-ionisation and/or laser ablation procedures will see the general introduction of high damage threshold optical fibres for laser transport to the sample region [28]. In this way, multiple beams of different wavelengths may be individually positioned relative to each other for maximum spatial overlap and ionisation efficiency, alleviating the need for complicated beam coupling arrangements. Also, incident angle investigations of the laser ablation yield will be simplified, as the usual restrictions of fixed laser entry windows will be removed, a flexible fibre being mounted instead on a rotating assembly invacuo.

For RIS/RIMS to succeed as a commercially viable analytical technique in the near future, the problems related to the current generation of tunable dye laser sources must be solved. These include the necessity for a multitude of different dyes in order to cover completely the wide spectrum of wavelengths required for resonant excitation of all elements, and associated with these the requirement for periodic dye renewal and replacement. The latter procedures are usually performed manually which is an unsatisfactory arrangement in itself without the additional hazards associated with handling many of the solvents and chemicals involved. Ideally, what is required is an entirely solid-state laser, tunable over the entire range available with dye lasers (typically 350 to 800 nm), and able to provide sufficient power for saturation of the various absorption steps. Only very recently has the technology become available to fill these requirements in the form the Titanium doped Sapphire laser (Ti : Al_2O_3) [75] and Optical Parametric Oscillators (OPO's) [26].

The interest in Ti : Al_2O_3 stems from its broad fluorescence band which ranges from about 660 nm to above 1100 nm (Figures 9.2 and 9.3). Subsequent generation of the various harmonics by frequency doubling and wave mixing can then extend the range down to around 180 nm (Figure 9.4). Figure 9.5 is a schematic of the possible layout of a Nd : YAG pumped Ti : Al_2O_3 laser [59].

With regard to OPO's, when a high intensity pulse of laser light of frequency - ω_p, such as doubled Nd:YAG output, is incident on a birefringent crystal within an optical cavity, scattering of photons with the [illegible] within the [illegible] leads to the creation of two coherent beams known as the signal and the idler waves [26], such that $\omega_p = \omega_s + \omega_i$, the condition for conservation of energy. Maximum Gain from such a parametric amplifier occurs when these waves are all phase matched (i.e. momentum is conserved $\mathbf{k}_p = \mathbf{k}_s + \mathbf{k}_i$). Thus, in order to satisfy the conditions for different signal and idler wave frequencies, the angle between the pump beam and the crystal optic axis is varied. Figure 9.6 shows the variation of signal and idler wavelengths as a function of incidence. The tunability of BBO OPO ranges from 400 nm to 2μm, and once again frequency doubling can extend the lower range further. A typical arrangement for such a laser might be of the form of Figure 9.7 [59].

The output characteristics of such lasers are now within the realms of those demanded by RIMS, and the timescales involved for the production of commercial systems utilising such arrangements or derivatives thereof, is possibly a matter of a few years.

The most interesting phenomena to emerge during the course of experiments was undoubtedly the observation of a resonant enhanced ion yield during laser/solid interaction (Chapter 8). The effect was subsequently named and thereby assigned the acronym **RLA** (or **RELA**, E for Enhanced). Not only does it offer interesting possibilities as a technique for surface analysis, it may also reveal important information with regard to the laser solid interaction and power regimes for various

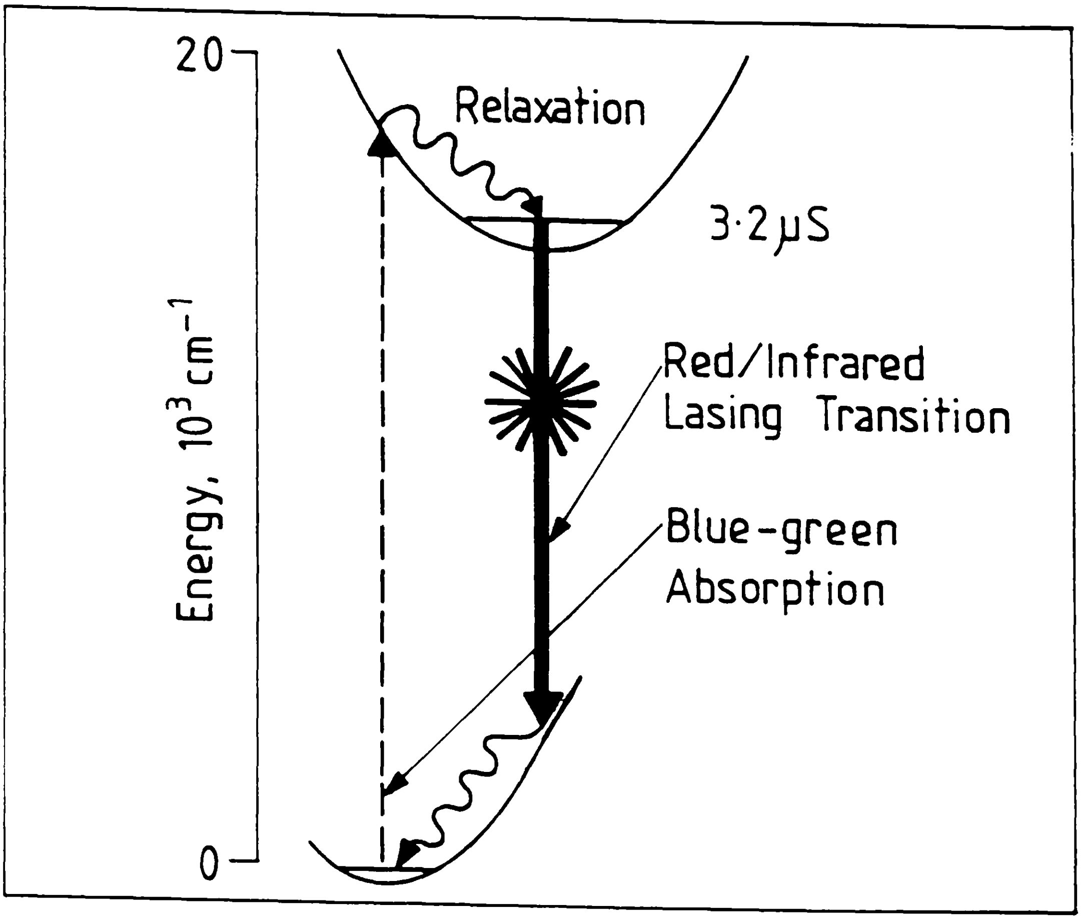
20
0
Energy, 10^3 cm^{-1}
Relaxation
3·2μS
Red/Infrared
Lasing Transition
Blue-green
Absorption

Figure 9.2 Energy Level Diagram for Ti-Sapphire

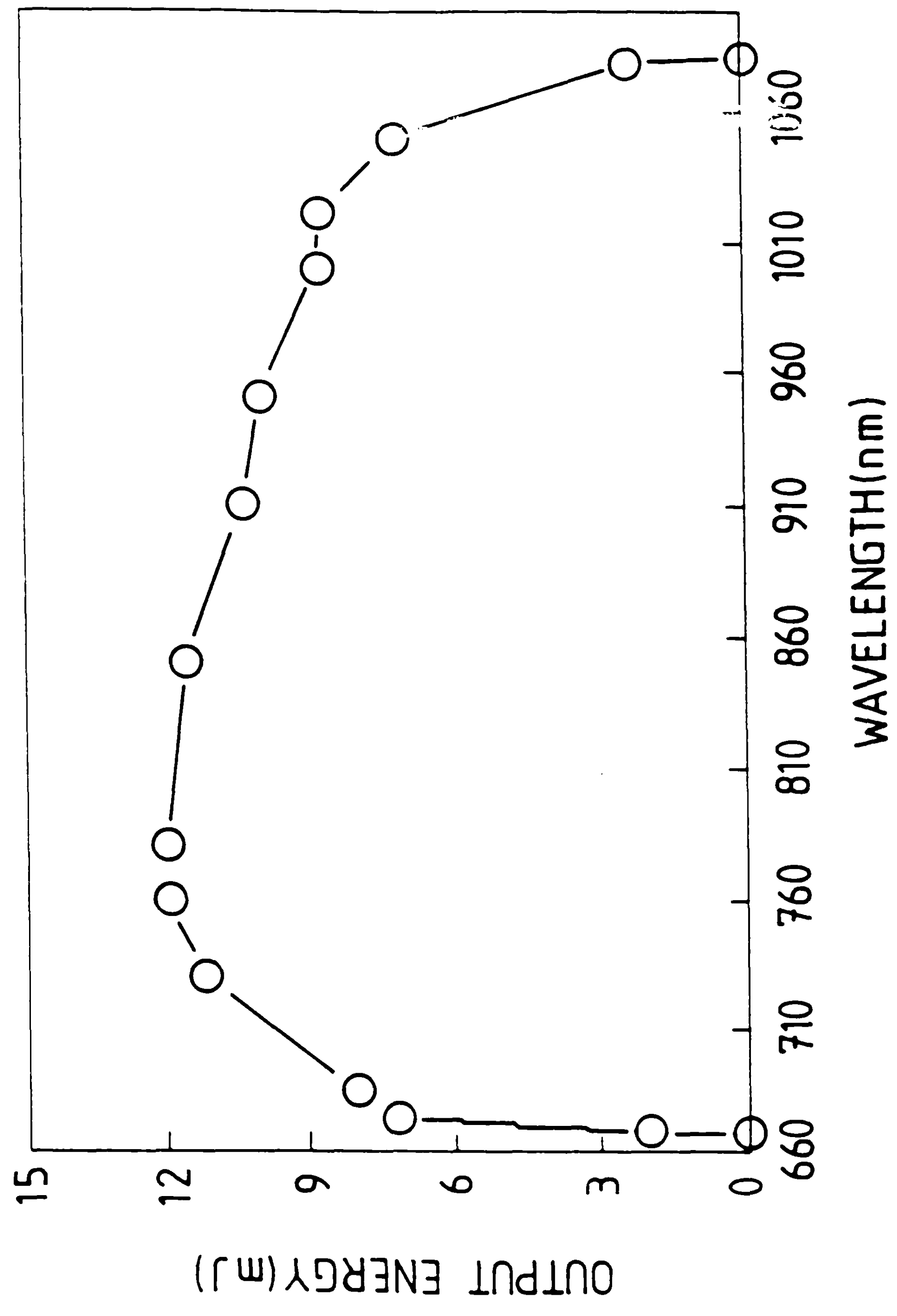

Figure 9.3 Estimated Wavelength Coverage of a Doubled YAG pumped Ti-Sapphire Laser with doubling and mixing.

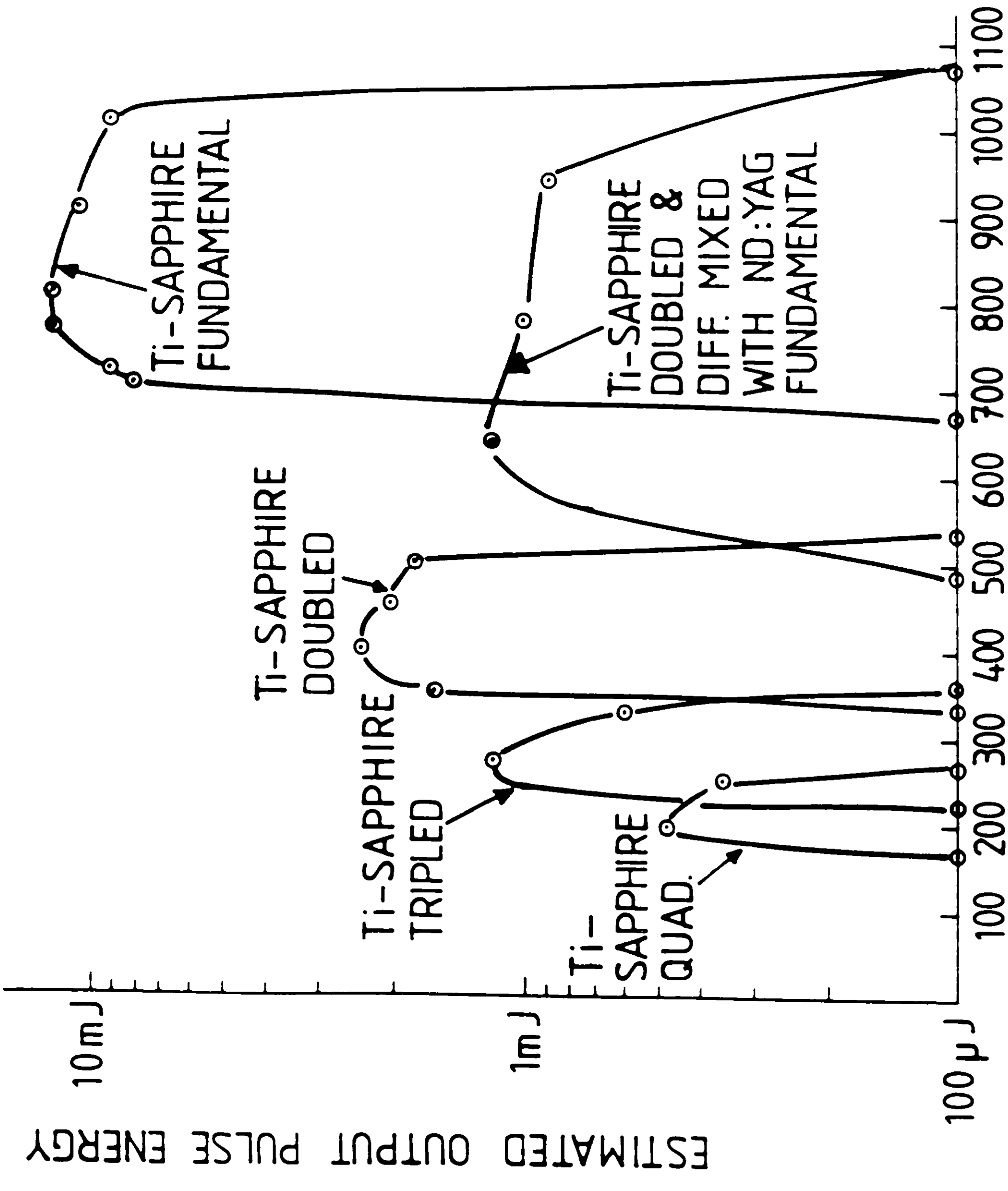

Figure 9.4 Wavelength coverage of douled YAG pumped Ti-Sapphire

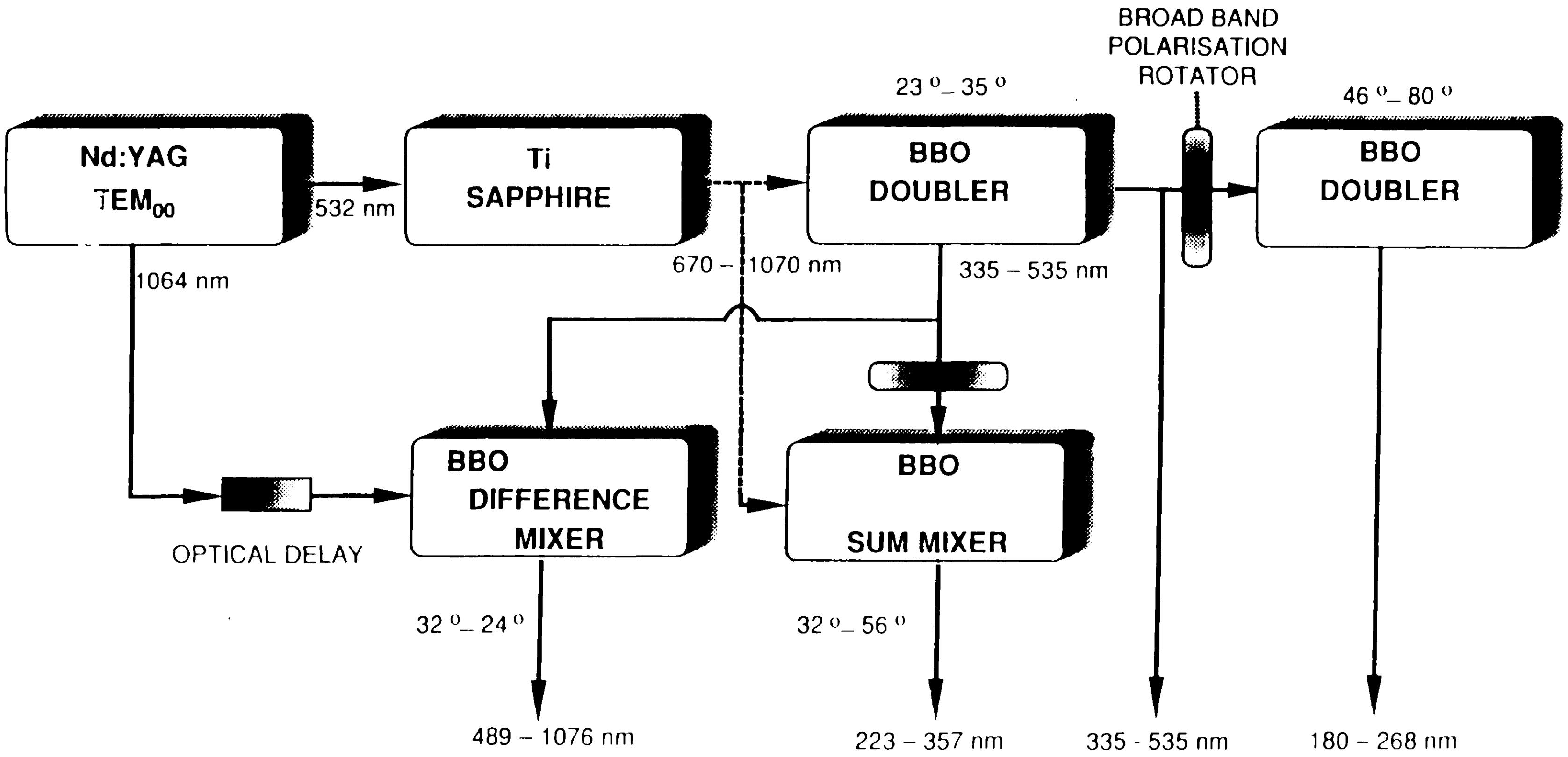
BROAD BAND
POLARISATION
ROTATOR
23 °– 35 °
46 °– 80 °
Nd:YAG
TEM_{00}
532 nm
Ti
SAPPHIRE
BBO
DOUBLER
BBO
DOUBLER
1064 nm
670 – 1070 nm
335 – 535 nm
BBO
DIFFERENCE
MIXER
BBO
SUM MIXER
OPTICAL DELAY
32 °– 24 °
32 °– 56 °
489 – 1076 nm
223 – 357 nm
335 - 535 nm
180 – 268 nm

Figure 9.5 Proposed laser arrangement for laser system covering the wavelengths from 200 to 800 nm

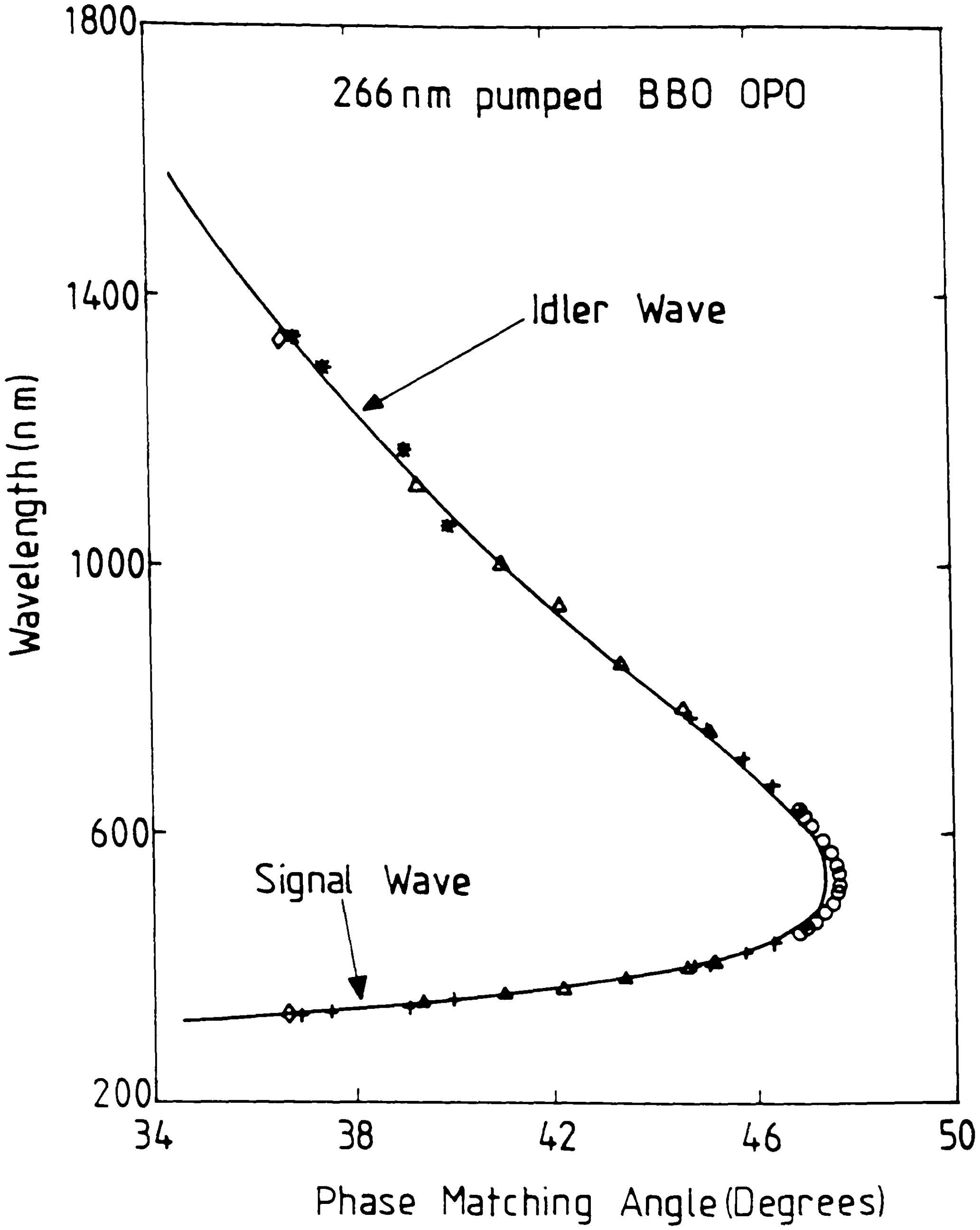

Figure 9.6 Tuning curve of 266 nm pumped BBO OPO

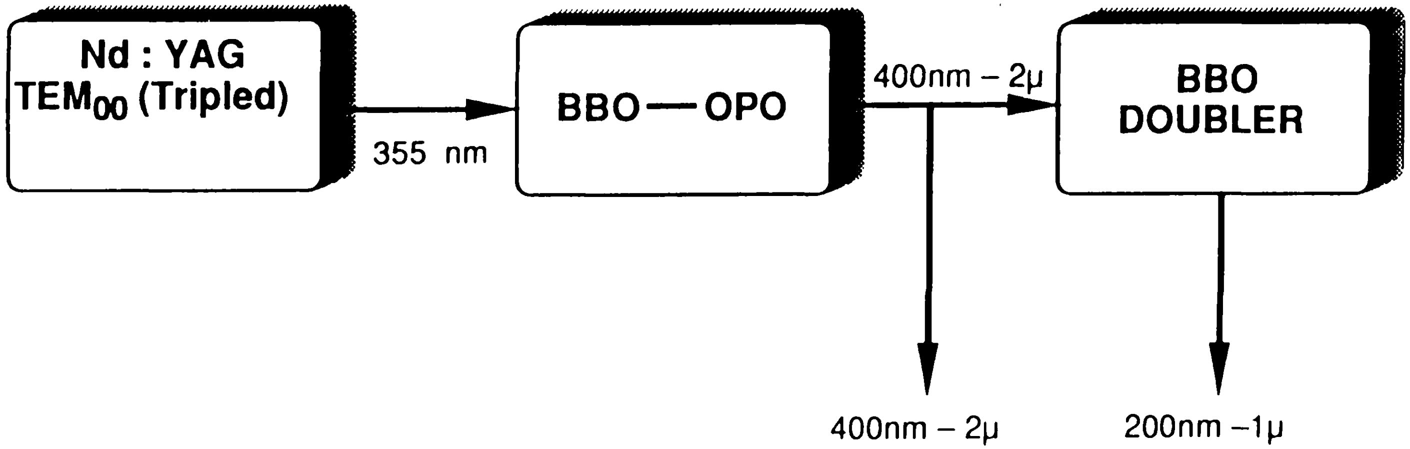
Nd : YAG
TEM$_{00}$ (Tripled)
355 nm
BBO—OPO
400nm – 2μ
BBO
DOUBLER
400nm – 2μ
200nm –1μ

Figure 9.7 Proposed Laser system for OPO with wavelength coverage from 200 to 2000 nm

ion formation processes, due to the combination of coupled mechanisms at solid, plasma, and atomic levels involved.

The process is now the subject of intensive investigation at Glasgow in particular with regard to the effect, on the enhancement ratio and interaction linewidths, of the sample matrix, and also experimental parameters, e.g. the effect of the laser incidence angle and power density on the sample. These experiments will initially concentrate on the resonant ionisation of Ga and Al, conducted on semiconductor samples containing various fractions of the above elements. Eventually, it is hoped, the usefulness of the process can be extended down to analysis at trace levels of a greater range of elements and thereby supercede the current laser ablation/desorption instrumentation.

As well as analysing bulk constituents, there is much interest in extending the process to study surface deposited atomic and molecular layers and adsobants, as the relatively low laser power densities involved should lead to slower sample consumption and a lesser degree of molecular fragmentation. Broad band resonances at a mass comparable with Ga, which could be attributed to molecular energy band structure, have occasionally been observed, although their origin has not as yet been established. The lack of definite reproducibility may be attributed to total removal of the analyte, which is present only as a surface layer. This data however, is not a subject for this work, and will be left to others for interpretation.

Appendix A.

Time-Of-Flight Spectrometer Resolution

The Temporal Resolution R for a mass m with a flight time t is given by:

$$R = \frac{t}{2\sigma} \qquad \text{(A.1)}$$

where σ is the measured peak width. The definition of σ is immaterial in the derivation of a resolution expression, but is usually expressed as the the FWHM or FW at one-tenth Maximum.

If we have 2 neighbouring masses m amd m+1, then we can define them to be just resolved if their difference in flight time $t'-t = \Delta t$, is equal to σ, where t' and t are expressed as:

$$t = k\sqrt{m} \qquad \text{(A.2)}$$

$$t' = k\sqrt{m+1} \qquad \text{(A.3)}$$

m being expressed in atomic mass units and k a constant.

Equation (A.3) can be approximated (assuming m » 1) by a binomial expansion to:

$$t' = k\left(1 + \frac{1}{2m}\right)\sqrt{m} \qquad \text{(A.4)}$$

Therefore, the separation in time can be written as:

$$t' - t = \sigma = \frac{k}{2\sqrt{m}} \qquad \text{(A.5)}$$

In the case of neighbouring masses where $\Delta m = 1$, equation (A.1) can be expresses as:

$$R = \frac{t}{2\sigma} = \frac{m}{\Delta m} = m \qquad (A.6)$$

Now, for 2 known masses m_1 and m_2 the relative flight times are given by:

$$t_1 = k\sqrt{m_1} \qquad (A.7)$$

$$t_2 = k\sqrt{m_2} \qquad (A.8)$$

and their separation by:

$$t_2 - t_1 = n\sigma \qquad (A.9)$$

where n is a factor relating the measured width to the separation. Substituting the values for t_1 and t_2 yields:

$$n\sigma = k(\sqrt{m_2} - \sqrt{m_1}) \qquad (A.10)$$

Substituting for σ from equation (A.5) gives:

$$\sqrt{m} = \frac{n}{2(\sqrt{m_2} - \sqrt{m_1})} \qquad (A.11)$$

Finally the mass resolution given by equation (A.6) can be expressed as:

$$R = m = \frac{n^2}{4(\sqrt{m_2} - \sqrt{m_1})^2} \qquad (A.12)$$

As an example, consider the two isotopes of Gallium which have masses 69 and 71 amu, and have essentially similar natural abundances. Assume that the two mass peaks, in the time-of-flight spectrum, are separated by twice the specified width of a mass peak, i.e. $n = 2$. Substituting the mass values of 69 and 71 for the variables m_1 and m_2 respectively, and the value for n then yields from Equation (A.12) a value for the mass resolution of the spectrometer of ~70. The result is dependent on the choice of measured width, whether at half maximum or tenth maximum, and hence the factor n must be adjusted accordingly, to correspond to the particular definition applied.

Appendix B.

Frequency doubling

When low intensity light propagates through a dense isotropic medium, the induced dipole moment per unit volume **P** is proportional to the electric field. However, when the electric field is extremely high, as is the case in a laser, this polarisation may no longer be directly proportional. Instead it may be expressed as a series expansion of the electric field [124][30]:

$$P = \varepsilon_0\left(\chi_1 E + \chi_2 E^2 + \chi_3 E^3 + \ldots\right) \qquad (B.1)$$

where χ_n are the nonlinear susceptibilities.

For light of the form $E=E_0 \sin \omega t$ incident on the medium, the polarisation can be expressed as:

$$P = \varepsilon_0 \chi_1 E_0 \sin \omega t + \varepsilon_0 \chi_2 E_0^2 \sin^2 \omega t + \varepsilon_0 \chi_3 E_0^3 \sin^3 \omega t + \ldots \qquad (B.2)$$

which can be rewritten as:

$$P = \varepsilon_0 \chi_1 E_0 \sin \omega t + \frac{\varepsilon_0 \chi_2 E_0^2}{2}(1 - \cos 2\omega t) + \frac{\varepsilon_0 \chi_3 E_0^3}{4}(3 \sin \omega t - \sin 3\omega t) + \ldots \qquad (B.3)$$

Part of the second term in this expansion corresponds to dipole oscillation at twice the driving frequency.

For materials with inversion symmetry, a reversal of the E-field results in a reversal of the polarisation vector, and hence the even powers of E in Equation (B.3) must disappear. Therefore, second harmonic generation cannot take place in isotropic media.

The major difficulty with second harmonic generation is that it is governed by dispersive effects in the medium, resulting in the ordinary and extraordinary waves propagating out of phase.

Consider propagation along the z-direction (ref. to diagram) through an anisotropic crystal of thickness *l*. The contribution to the doubled component $dE_{2\omega}$ from a layer of thickness dz at depth z is given by:

$$dE_{2\omega}(z) \propto P_{2\omega}(z)\,dz \qquad (B.4)$$

where $P_{2\omega}$ is the induced dipole moment at frequency 2ω, itself proportional to the square of the incident electric field. Therefore, B.4 can be written as:

$$dE_{2\omega}(z) \propto e^{2i(k_1 z - \omega t)}\,dz \qquad (B.5)$$

Since the second harmonic propagates with a wave number k_2 due to dispersion in the crystal, the second harmonic component at *l* originating from the layer dz is:

$$dE_{2\omega}(l) \propto dE_{2\omega}(z)\,e^{ik_2(l - z)}\,dz \qquad (B.6)$$

which can be expressed as:

$$dE_{2\omega}(l) \propto e^{i(2k_1 - k_2)}\,e^{i(k_2 l - 2\omega t)}\,dz \qquad (B.7)$$

Integrating and squaring then yields the total intensity of the second harmonic as:

$$I_{2\omega} \propto \frac{\sin^2(2\pi\,\Delta n\, l / \lambda_0)}{(2\pi\,\Delta n / \lambda_0)^2} \qquad (B.8)$$

where $\Delta n = n_1 - n_2$, λ_0 the vacuum wavelength, and $k_n = 2\pi n_n / \lambda_n$

The maximum in intensity then occurs at $l = \lambda / (4\,\Delta n)$. This value of *l* is called the coherence length for second harmonic generation and is typically of the propagation through an an-isotropic crystal of thickness l.

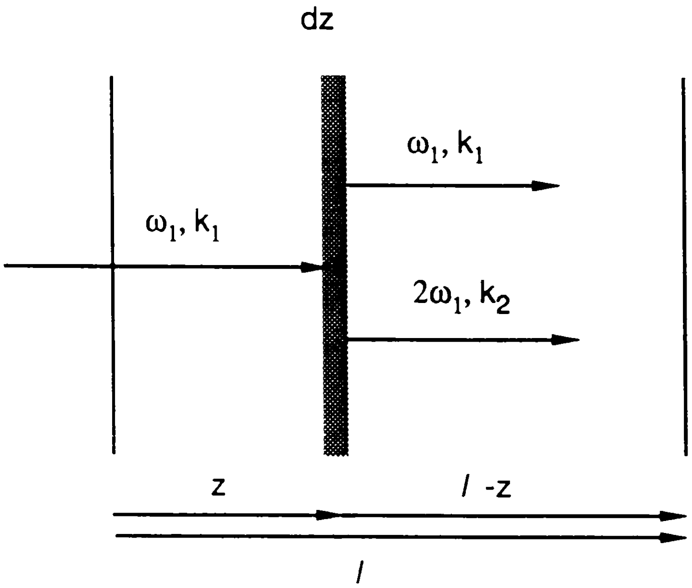
dz
ω_1, k_1
ω_1, k_1
$2\omega_1, k_2$
z
l -z
l

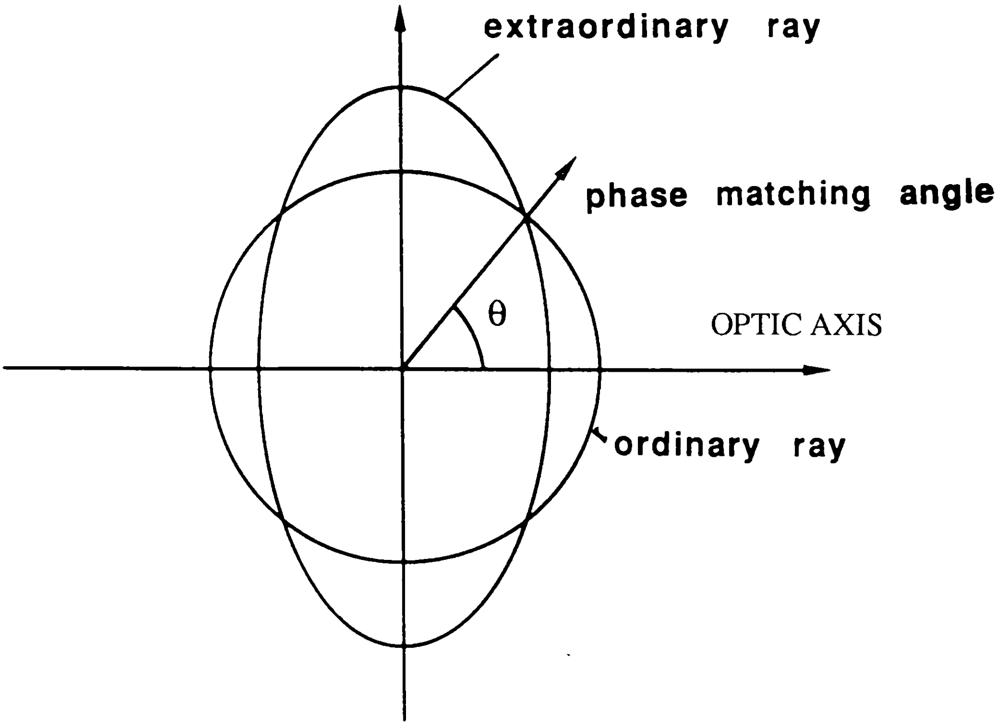
extraordinary ray
phase matching angle
θ
OPTIC AXIS
ordinary ray

Conditions for Phase Matching in
Second Harmonic Generation

Index of refraction for e and o-rays as a function of their angle of propagation wrt the optic axis.

order of a few millimetres for most materials.

In order for the coherence length to be of a realistically applicable size, Δn must be very small. It is possible to achieve these conditions in some anisotropic media where the second harmonic, generated by an incident ordinary wave, is an extraordinary wave. If the fundamental wave is incident at an angle θ_o, corresponding to the angle of intersection of the ellipsoids of the waves at frequency ω and 2ω (refer to figure), the indices of refraction for the two waves will be effectively equal and hence Δn will be very small. This is commonly known as phase matching, and results in both components propagating collinearly.

Appendix C

Transition Broadening Mechanisms.

Doppler Broadening.

The spread in velocities of gaseous atoms leads to a distribution in the frequency of absorption or emission of radiation, via the Doppler effect.

Consider for a two level system, an atom in lower energy level E_1 with a velocity $\mathbf{v}_1$. Absorption of a photon propagating along the z-axis at a frequency ω excites the atom into a level E_2, and causes the atom to recoil to a new velocity $\mathbf{v}_2$. The total momentum of the system before and after the absorption is then given by [63]:

$$M\mathbf{v}_1 + \hbar\mathbf{k} = M\mathbf{v}_2 \tag{C.1}$$

where the photon momentum is given by $\hbar\mathbf{k}$, and $k = \omega/c$.

By energy conservation we have:

$$E_1 + \tfrac{1}{2}Mv_1^2 + \hbar\omega = E_2 + \tfrac{1}{2}Mv_2^2 \tag{C.2}$$

For the condition $v_1 = 0 = v_2$, Equation (C.2) reduces to:

$$\hbar\omega_0 = E_2 - E_1 \tag{C.3}$$

where ω_0 is the transition frequency for the stationary, unperturbed atom.

Eliminating v_2 from Equation (C.2) then leads to:

$$\omega_0 = \omega - (\omega v_1 / c) - (\hbar\omega^2 / 2Mc^2) \tag{C.4}$$

The last term in Equation (C.4) is small by comparison with the second and can usually be neglected to give:

$$\omega = \frac{\omega_0}{(1-(v_1/c))} \approx \omega_0\left(1 \pm \frac{v_1}{c}\right) \qquad \text{(C.5)}$$

with the ± sign allowing for movement in both directions relative to the beam.

The distribution in absorption frequencies then follows the velocity distribution of the gas atoms which is usually regarded as being Maxwellian. The number of atoms in a gas, at a temperature T, with a z-component of velocity between v_z and dv_z is then proportional to

$$\exp\left(-Mv_z^2/2k_BT\right)dv_z$$

$$= \exp\left\{-Mc^2(\omega-\omega_0)^2/2\omega_0^2k_BT\right\}(c/\omega_0)\,d\omega \qquad \text{(C.6)}$$

This is a Gaussian lineshape peaked at ω_0 with a half maximum in intensity at the frequencies which satisfy the condition:

$$\frac{1}{2} = \exp\left\{-Mc^2(\omega-\omega_0)^2/2\omega_0^2k_BT\right\} \qquad \text{(C.7)}$$

Thus, since the absorbed power is proportional to the number density of atoms, the intensity profile follows the form of Equation (C.7).

The FWHM of this lineshape is thus

$$\Delta\omega_D = 2\omega_0\left(2k_BT(\ln 2)/Mc^2\right)^{1/2} \qquad \text{(C.8)}$$

where $\Delta\omega_D = 2\,|(\omega-\omega_0)|$, and since the following holds:

$$\frac{\Delta\lambda}{\lambda} \propto \frac{\Delta\omega}{\omega} \qquad \text{(C.9)}$$

it follows that the contribution to the broadening $\Delta\lambda$ of an absorption line at a wavelength λ is:

$$\Delta\lambda_D = 2\lambda\left(2k_BT(\ln 2)/Mc^2\right)^{1/2} \tag{C.10}$$

Collisional Broadening.

As with Doppler broadening, collisional broadening results from the motion of atoms. Energy levels, on collision, are shifted due to the forces of interaction between the colliding particles [22][63]. The degree of the energy shift is dependent on the electron configuration of the particles and their interatomic separation R. Therefore, an atom with energy levels E_1 and E_2, will, on undergoing a radiative transition at a frequency ω_{12}, between the two levels, satisfy the condition:

$$\hbar\omega_{12} = E_2(R) - E_1(R) \tag{C.11}$$

assuming the transition time is short in comparison with the collision time.

As the atoms within a gas possess a random distribution in position and therefore in atomic separation, which is pressure and temperature dependent, there is a corresponding distribution in transition frequency centred around the unperturbed frequency ω_0. Such collisional behaviour is associated with all atoms within a gas and hence the transition frequency distribution is Lorentzian, with a width proportional to the collision rate:

$$\sim \frac{4d^2 N}{V}\left(\frac{\pi k_B T}{M}\right)^{1/2} = \frac{1}{\tau_0} \tag{C.12}$$

where τ_0 is the mean period of free flight, T and M the mean temperature and atomic mass of the gas particles respectively, N/V the number density of gas particles and d the mean collision radius.

Saturation (Power) Broadening.

In situations where the radiation field interacting with an absorbing medium is not sufficiently intense to alter appreciably the population densities of the atomic energy levels, the population densities can be regarded as constants of the interaction. In the strong field case, if the populations vary significantly as a function of the intensity during the interaction, they can no longer be considered constant and the interaction becomes governed by induced transitions [16][61].

Consider a two level system with population densities N_1 and N_2, and assume equal statistical weights for both levels. The total number density $N = N_1 + N_2$, is a constant of the system, if all decay channels, other than the two levels, are excluded. The rates of change of N_1 and N_2 can be related to the Einstein coefficients for induced emission and absorption, and spontaneous emission. If we also introduce additional collisionally induced transition probabilities, we obtain, under stationary conditions, the expression:

$$\frac{dN_1}{dt} = -\frac{dN_2}{dt} = B_{12}\rho(\omega_{12})(N_2 - N_1) + (A_{21} + C_{21})N_2 - C_{12}N_1 = 0 \qquad \text{(C.13)}$$

where B_{12} and B_{21} are the Einstein coefficients of induced absorption and emission, A_{21} is the spontaneous emission probability, C_{12} and C_{21} are the collisionally induced collision rates, and ρ is the spectral energy density of the radiation field.

The above expression can be rearranged in terms of the population difference

$$\Delta N = N_2 - N_1 \qquad \text{(C.14)}$$

and the total number density

$$N = N_1 + N_2 \qquad \text{(C.15)}$$

to give:

$$\Delta N = \frac{N(R_2 - R_1) / (R_1 + R_2)}{1 + 2B_{12}\rho(\omega_{12}) / (R_1 + R_2)} \qquad \text{(C.16)}$$

where

$$R_1 = A_{21} + C_{21} \tag{C.17}$$

$$R_2 = C_{12} \tag{C.18}$$

are the total emission and absorption rates.

The numerator on the RHS of Equation (C.16) is the population difference for $\rho=0$, and can be simplified to the term ΔN_0.

The second term in the denominator is known as the saturation parameter and is defined as the ratio of the induced transition probability to the mean relaxation probability, and is abbreviated according to:

$$S = \frac{2B_{12}\rho(\omega_{12})}{R_1 + R_2} \tag{C.19}$$

In the case where the only relaxation process is spontaneous emission, S becomes equal to the ratio of the induced to the spontaneous transition rates.

Equation (C.16) can now be simplified to:

$$\Delta N = \frac{\Delta N_0}{1 + S} \tag{C.20}$$

The radiation power absorbed per unit volume by this system is:

$$\frac{dW_{12}}{dt} = \hbar\omega B_{12}\rho(\omega)\Delta N = \hbar\omega B_{12}\rho(\omega)\frac{\Delta N_0}{1 + S} \tag{C.21}$$

Using Equation (C.19) this can be expressed as:.

$$\frac{dW_{12}}{dt} = \frac{\hbar\omega}{2}\frac{(R_1 + R_2)\Delta N_0}{(1 + 1/S)} \tag{C.22}$$

For a homogeneously broadened line, the induced absorption probability follows a Lorentzian profile:

$$B_{12}\rho(\omega)\, L(\omega-\omega_0) \tag{C.23}$$

where:

$$L(\omega-\omega_0)=\frac{(\gamma/2)^2}{(\omega-\omega_0)^2+(\gamma/2)^2} \tag{C.24}$$

for a monochromatic wave with frequency ω and FWHM γ. Therefore a frequency dependent saturation parameter

$$S(\omega)=S_0\frac{(\gamma/2)^2}{(\omega-\omega_{12})^2+(\gamma/2)^2} \tag{C.25}$$

with a FWHM γ can be introduced.

Substituting this expression for the saturation parameter into Equation (C.22) yields:

$$\frac{dW_{12}}{dt}=\frac{1}{2}\hbar\omega(R_1+R_2)\,\Delta N_0 S_0\frac{(\gamma/2)^2}{(\omega-\omega_0)^2+(1+S_0)(\gamma/2)^2} \tag{C.26}$$

which is a Lorentzian profile with FWHM given by:

$$\gamma_S=\gamma\sqrt{1+S_0} \tag{C.27}$$

which is equivalent to:

$$\delta\omega_S=\delta\omega\sqrt{1+S_0} \tag{C.28}$$

In order to quantitatively predict power broadening, the saturation parameter must be related to easily measurable quantities. Assuming no contribution to the transition rates from collisional processes, Equation (C.19) becomes, more simply:

$$S_0 = \frac{2B_{12}\,\rho(\omega)}{A_{21}} \tag{C.29}$$

The spontaneous emission and induced emission coefficients can be related by the expression:

$$A_{21} = \frac{8\pi\, h\nu^3}{c^3} B_{21} \tag{C.30}$$

and the spectral energy density $\rho(\omega)$, can be related to the spectral flux density or irradiance by:

$$I(\omega) = c\,.\ \rho(\omega) \tag{C.31}$$

which in turn is related to the total irradiance by:

$$I = \int_0^\infty I_\nu\, d\nu = \int_0^\infty I_\omega\, d\omega = c \int_0^\infty \rho(\omega)\, d\omega \tag{C.32}$$

Now, assuming that the atomic transition linewidth Γ_{at} is very much smaller than the laser linewidth Γ_L (this is a reasonable assumption since the atomic linewidth is typically 100 MHz, while the laser linewidth, in the present experimental arrangement is of the order of 10 GHz), and assume a Gaussian beam, at line centre ν_0 (refer to diagram), the fractional flux density of the laser dI_ν contributing to the absorption is:

$$dI_\nu = I\ g(\nu_0)\Gamma_{at.} \tag{C.33}$$

where $g(\nu_0)$ is the height of the Gaussian at line centre, and is given by:

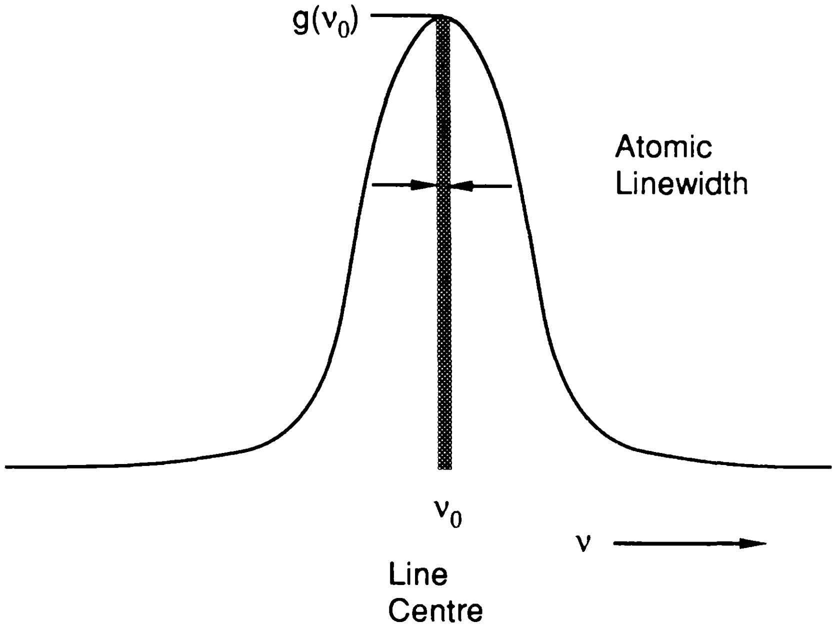
$g(\nu_0)$
Atomic
Linewidth
ν_0
ν
Line
Centre

Gaussian Laser Linewidth

$$g(\nu_0) = \frac{\sqrt{\pi \ln 2}}{\pi \, \Delta\nu_{1/2}} \tag{C.34}$$

where $\Delta\nu_{1/2}$ is the Half Width at Half Maximum (HWHM) of the laser profile and is equivalent to $\Gamma_L/2$.

From Equation (C.32), it is evident that:

$$I_\omega = \frac{I_\nu}{2\pi} \quad \Rightarrow \quad dI_\omega = \frac{dI_\nu}{2\pi} \tag{C.35}$$

Also:

$$g(\omega_0) = \frac{g(\nu_0)}{2\pi} \tag{C.36}$$

and

$$\Gamma_{at.}(\omega) = 2\pi \, \Gamma_{at.}(\nu) \tag{C.37}$$

which implies, from Equation (C.33):

$$dI_\omega = \frac{I \, g(\omega_0) \, \Gamma_\omega}{2\pi} \tag{C.38}$$

where $\Gamma_\omega = \Gamma_{at}(\omega)$, and from (C.32), it is clear that:

$$\rho_\omega = \frac{I}{2\pi c} \frac{\sqrt{\pi \ln 2}}{\pi \, \Delta\omega_{1/2}} \frac{\Gamma_\omega}{d\omega} \tag{C.39}$$

In the approximation $\Gamma_\omega \sim d\omega$, the above can be re-expressed as:

$$\rho_\omega \approx \frac{I}{2\pi c} \frac{\sqrt{\pi \ln 2}}{\pi \, \Delta\omega_{1/2}} \tag{C.40}$$

Using the following expression for the frequency spread in terms of the wavelength spread:

$$\Delta\omega_{1/2} = \frac{2\pi c}{\lambda^2} \Delta \lambda_{1/2} \tag{C.41}$$

Equation (C.40) can be written as:

$$\rho_\omega = \frac{I}{(2\pi c)^2} \frac{\sqrt{\pi \ln 2}}{\pi} \frac{\lambda^2}{\Delta\lambda_{1/2}} \tag{C.42}$$

It then follows from Equation (C.29), that the saturation parameter can be expressed by the relation:

$$S_0 = \frac{\sqrt{\pi \ln 2}}{(2\pi)^4 c^2 h} . I . \frac{\lambda^5}{\Delta\lambda_{1/2}} \tag{C.43}$$

which, on insertion of the various constant values becomes:

$$S_0 = 1 \cdot 59 \times 10^{13} . I . \frac{\lambda^5}{\Delta \lambda_{1/2}} \tag{C.44}$$

References.

[1] Andersen C. A., Hinthorne J. R., "Thermodynamic Approach to the Quantitative Interpretation of Sputtered Ion Mass Spectra", *Anal. Chem.*, **45**, 8, 1421, 1973

[2] Anderson H. H., "The Depth Resolution of Sputter Profiling", *Appl. Phys.*, **18**, 131, 1979

[3] Ambartsumyan R. V., Letokhov V. S.,"Selective Two-Step photoionisation of Atoms and Photodissociation of Molecules by Laser Radiation", *Appli. Opt.*, **11**, 354, 1972

[4] Becker C. H., Gillen K. T., "Surface analysis by Nonresonant Multiphoton Ionisation of Desorbed or Sputtered Species", *Anal. Chem.*, **56**, 1671, 1984

[5] Bekov G., Radaev V., Likonen J., Zilliacus R., Auterinen I., Lakoman E., "Resonance Ionisation Spectrometric Determination of Gallium Using an Electrothermal Graphite Atomiser", *Anal. Chem.*, **59**, 1987

[6] Beekman D. W., Callcott T. A., "Laser ablation studies using RIS", *proceedings RIS 84*, Inst. Phys. Conf. Ser. No. **71**, pp 143-149, 1984

[7] Benninghoven A., Giber J., Laszlo J., Riedel M., Werner H. W., "Secondary Ion Mass Spectometry (SIMS III)", Proceedings of the Third International Conference, *Chemical Physics*, Vol **19**, Springer Verlag,1982

[8] Benninghoven A., Okano J., Shimizu R., Werner H. W., "Secondary Ion Mass Spectometry (SIMS IV)", Proceedings of the Fourth International Conference, *Chemical Physics*, Vol **36**, Springer Verlag,1984

[9] Benninghoven A., Rudenauer F. G., Werner H. W.,"Secondary Ion Mass Spectrometry, Basic Concepts, Instrumental Aspects, Applications and Trends", P. J. Elving, J. D. Winefordner, Ed., *Chemical Analysis*, Vol. **86**, Wiley, 1987

[10] Burgess D., Cavanagh R. R., King D. S., "Laser-induced desorption: Thermal and nonthermal pathways", *J. Chem. Phys.*, **88** (10), 1988

[11] Burgess D. R., Hussla I., Stair P. C., Viswanathan R., Weitz E., "Pulsed laser-induced thermal desorption from surfaces: Instrumentation and procedures", *Rev. Sci. Instrum.*, **55** (11), 1984

[12] Chen G., Yeung E. S., "Acoustic Signal as an Internal Standard for Quantification in Laser-Generated Plumes", *Anal. Chem.*, **60**, 2258, 1988

[13] Clark C. W., Fassett J. D., Lucatorto T. B., Moore L. J., "Enhancement of the isotopic abundance sensitivity of mass spectrometry by Doppler-free resonance ionisation", *proceedings RIS 84*, 107, 1984

[14] Colligon J. S., "Surface compositional analysis using low energy ion bombardment induced emission processes.", *Vacuum,* Vol. **24**, No. 9, 373, 1974

[15] Danielzik B., Harten P., Seeger T., von der Linde D., "Laser photoionisation mass spectrometry with picosecond resolution", *Appl. Phys. Lett.*, **53** (9) 1988

[16] Demtroeder W., "Laser Spectroscopy: Basic Concepts and

Instrumentation"Springer Verlag, chemical physics 5, 1982

[17] Devyatykh G. G., Gaponov S. V., Kovalev I. D., Lapin N. V., Luchin V. I., Maksimiv G. A., Pontus L. I., Suchkov A. I., "Possible chemical analysis of microscopic regions with a laser mass spectrometer", *Sov. Tech. Phys. Lett.*, Vol. **2**, No. 10, Oct. 1976

[18] Dingle R., "Confined carrier quantum states in ultrathin semiconductor heterostructures", Festkorper Probleme XV (Advances in Solid State Physics), H.J. Queisser, Ed. New York: Pergamon, 1975, pp. 21-48

[19] Downey S. W., Hozack R. S., "Reduction of Matrix Effects in SIMS by Resonance Ionisation", *Proceedings SIMS VII,* 1989

[20] Downey S. W., Hosack R. S., "A Hybrid Resonance Ionisation and Secondary Ionisation Mass Spectrometer" unpublished work

[21] Downey S. W., "A Comparison of secondary ion mass spectrometry and resonance ionisation mass spectrometry", unpublished work

[22] Eastham D., "Atomic Physics of Lasers", Taylor and Francis, 1986

[23] Evans C. A.(Jr.), Pemsler J. P., "Analysis of Thin Films by Ion Microprobe Mass Spectrometry", *Anal. Chem.*, **42**, 9, 1060, 1970

[24] Fabbro R., Fabre E., Amiranoff F., Garban-Labaune C., Virmont J., Weinfeld M., Max C.E., "Laser-wavelength dependence of mass-ablation rate and heat-flux inhibition in laser-produced plasmas", *Phys. Rev. A*, Vol. **26**, No. 4, 2289, 1982

[25] Fulghum J. E., McGuire G.E., Musselman I.H., Nemanich R.J., White J.M., Chopra D.R., Chourasia A.R., "Surface Characterisation", *Anal. Chem*, **61**, 243R, 1989

[26] Giordmaine J. A., Miller R. C., "Tunable Coherent Parametric Oscillation in $LiNbO_3$ at Optical Frequencies", *Phys. Rev. Lett.*, Vol. **14**, No. 24, 1965

[27] Gruen D. M., Pellin M. J., Young C. E., Calaway W. F., "Laser spectroscopy of sputtered atoms", *J. Vac. Sci. Technol. A*, Vol. 4, No. 3, 1986

[28] Hand O. W., Emary W. B., Winger B. E., Cooks R. G., "Depth profiling of multilayered samples and comparison of secondary ion and laser desorption spectra in the same instrument", *Int. J. Mass Spectrom. Ion Processes.,* **90**, 1990

[29] Hart R. R., Dunlap H. L., Marsh O. J., "Ion induced migration of Cu into Si", *J. Appl. Phys.*, Vol. 46, No. 5, May 1975

[30] Hecht E., Zajac A., "Optics", Addison-Wesley Publishing Company, Inc. Philippines, 1974

[31] Hein S. J., Piepmeier E. H., "Laser ablation and the laser microprobe", *Trends in anal. chem.*, Vol. **7**, No. 4, 1988

[32] Hofer W. O., Liebl H., "Depth-Profiling of Cu-Ni Sandwich Samples by SIMS", *Appl. Phys.*, **8**, 359, 1975

[33] Hofmann S., "Evalution of Concentration-Depth Profiles by Sputtering in SIMS and AES", *Appl. Phys.*, 9, 59, 1976

[34] Hofmann S., "Depth Resolution in Sputter Profiling", *Appl. Phys.*, 13, 205, 1977

[35] Hofmann S., "Quantitative Depth Profiling in Surface Analysis: A Review", *Surf. Interface Anal.*, Vol. **2**, No. 4, 1980

[36] Hofmann S., "Disturbing Effects in Sputter Profiling", *Proceedings SIMS III*, pp 186-200, 1981

[37] Hofmann S., Erlewein J., Zalar A., "Depth Resolution and Surface Roughness Effects in Sputter Profiling of NiCr Multilayer Sandwich Samples using AES", *Thin Solid Films*, 43, 275, 1977

[38] Hofmann S., Zalar A., "AES depth profiling of Ni / Cr multilayers by sputtering with N^+_2 ions", *Thin Solid Films*, **60**, 201, 1979

[39] Holonyak N. (jr), Kolbas R.M., Dupuis R.D., Dapkus P.D., "Quantum-Well Heterostructure Lasers", *IEEE J. Quantum Electron.*, Vol. **QE-16**, No. 2, February 1980

[40] Houston C. M., Drysdale S. L. T., Jennings R., Land A. P., Ledingham K. W. D., Singhal R. P., Smyth M. H. C., Stewart D. T., Towrie M., "Two and three photon ionisation transitions in caesium vapour", *J. Phys. D: Appl. Phys.*, **21**, 1988

[41] Hurst G. S., Nayfeh M. H., Young J. P., "A demonstration of one-atom detection", *Appl. Phys. Lett.*, **30**, 5, 229, 1977

[42] Hurst G. S., Payne M. G., Kramer S. D., Chen C. H., *Physics Today*, September 1980.

[43] Hurst G. S., Payne M. G., Kramer S. D., Young J. P., "Resonance Ionisation Spectroscopy and One-Atom Detection", *Rev. Mod. Phys.*,Vol. **51**, No. 4, 1979

[44] Ichige K., Matsumoto Y., Namiki A., "Laser- induced Desorption from Compound Semiconductors", *Nuc. Instr. and Meth. Phys. Res.*, **B33**, 820, 1988

[45] Ishitani T., Shimizu R., "Atomic Mixing in Ion Probe Microanalysis", *Appl. Phys.*, **6**, 277, 1975

[46] Ishitani T., Shimizu R., "Computer Simulation of Atomic Mixing during Ion Bombardment.", *Appl. Phys.*, **6**, 248, 1975

[47] Itoh N., Nakayama T., "Mechanisms of Neutral Particle Emission from Electron-Hole Plasma near Solid Surface.", *Physics Lett.*, Vol. **92A**, No. 9, 471, 1982

[48] Kelly N., Kaiser U., "Quantitative depth profiling analysis of (Al,Ga)As structures by Secondary Neutral Mass Spectrometry (SNMS)", *SPIE Vol.946 Spectroscopic Characterisation Techniques for Semiconductor Technology III*, 1988

[49] Kelly R., Cuomo J. J., Leary P. A., Rothenberg J. E., Braren B. E., Aliotta C. F., "Laser Sputtering Part I', *Nucl. Instr. and Meth. Phys. Res.*, **B9**, 329, 1985

[50] Kelly R., Rothenberg J. E., "Laser Sputtering Part III", *Nucl. Instr. and Meth. Phys. Res.*, **B7/8**, 755, 1985

[51] Kimock F.M., Baxter J.P., Pappas D.L., Kobrin P.H., Winograd N., "Solids Analysis Using Energetic Ion Bombardment and Multiphoton Resonance Ionisation with Time-of-Flight Detection", *Anal. Chem.*, **56**, 2782, 1984

[52] Kimock F. M., Baxter J. P., Winograd N., "Ion and Neutral yields from Ion Bombarded Metal Surfaces during Chemisorption using Low Dose SIMS and Multiphoton Resonance Ionisation", *Surf. Sci.*, **124**, L41, 1983

[53] Kittel C., "Introduction to Solid State Physics: 5th Edition", John Wiley and Sons, 1976

[54] Kodama Y., Sumitomo S., Kato I., Jinno M., Yamauchi H., "Combined Spectrometer with the techniques of SIMS, ISS, AES and XPS", *Proceedings SIMS IV*, pp 252-254, 1983

[55] Laser Ionisation Mass Analyser (LIMA), Cambridge Mass Spectrometry Ltd., Spec. Brochure.

[56] LAser Microprobe Mass Analyser (LAMMA), Leybold Heraeus, Spec. brochure.

[57] Ledingham K. W. D., Cahill J. W., Drysdale S. L. T., Raine C., Smith K. M., Smyth M. H. C., Stewart D. T., Towrie M., Houston C. M., "Applications of RIS to accelerator based high energy physics", *proceedings RIS 86*, IOP publishing ,1986

[58] Ledingham K. W. D., Raine C., Smith K. M., Campbell A. M., Houston C. M., Towrie M., Trager C., "Laser induced ionisation in proportional counters seeded with low ionisation potential vapours", *Nucl. Instr. Meth. Phys. Res.*, 225, 1984

[59] Ledingham K. W. D., Singhal R. P., "A Critical Assessment of Ti-Sapphire Lasers and Optical Parametric Oscillators as Sources of Variable Wavelength for Resonant Ionisation Mass Spectrometry", to be published

[60] Letokhov V. S., "Laser Photoionisation Spectroscopy", Academic Press Inc., 1987

[61] Letokhov V. S., Chebotayev V. P., "Nonlinear Laser Spectroscopy", Springer Verlag, 1977

[62] Lewis R. K., Williams P. W., Evans C. A.(Jr), Hanley P. R., "Evaluation of a Caesium Primary Ion Source on an Ion Microprobe Mass Spectrometer", *Anal. Chem.*, **49**, 9, 1399, 1977

[63] Loudon R., "The Quantum Theory of Light", Clarendon Press, Oxford, 1983

[64] Lubman D. M., "Analytical multiphoton ionisation mass spectrometry. Part I. Theory and instrumentation", *Mass Spectrometry Reviews*, **7**, 1988

[65] Lubman D. M., "Analytical multiphoton ionisation mass spectrometry. Part II. Applications", *Mass Spectrometry Reviews*, **7**, 1988

[66] Ludeke R., Esaki L., Chang L. L., "$Ga_{1-x}Al_xAs$ superlattices profiled by Auger electron spectroscopy", *Appl. Phys. Lett.*, Vol. **24**, No. 9, 417, 1974

[67] Magee C. W., Honig R. E., Evans C. A., "Depth Profiling by SIMS: Depth Resolution, Dynamic Range and Sensitivity", *proceedings SIMS III*, p172, 1981

[68] Mathieu H. J., McClure D. E. Landolt D. "Influence of ion bombardment on depth resolution in AES analysis of thin Au films on Ni", *Thin Solid Films*, 38, 281, 1976

[69] McCracken G. M., "The behaviour of surfaces under ion bombardment", *Rep. Prog. Phys.*,**38**, 241, 1975

[70] McCombes P. T., Borthwick I. S., Jennings R., Land A. P., Ledingham K. W. D., Singhal R. P., Towrie M., "Characterisation of the Energy and Spatial Distribution of Neutrals produced by Laser Ablation", *proceedings SPIE 90*, 1990

[71] McCombes P. T., Drysdale S. L. T., Jennings R., Land A. P., Ledingham K. W. D., McLean C. J., Singhal R. P., Smyth M. H. C., Stewart D. T., Towrie M., "The Glasgow Resonant Ionisation Mass Spectrometer", *proceedings IMSC XII*, 1988

[72] McLean C. J., Marsh J. H., Land A. P., Clark A., Jennings R., Ledingham K. W. D., McCombes P. T., Marshall A., Singhal R. P., Towrie M., "Resonant Laser Ablation (RLA)", *Int. J. Mass Spectrom. Ion Processes.*, 1990

[73] McGibbon A. J., Chapman J. N., Cullis A. G., Chew N. G., Bass S. J., Taylor L. L., X-ray microanalysis of InGaAs/InP multilayer structures grown by MOCVD", private communication

[74] Moore C. E., "Atomic Energy Levels", U.S. Deptartment of Commerce, NBS 467 1948

[75] Moulton P. F., "Spectroscopic and Laser Characteristics of Ti:Al_2O_3", *J. Opt. Soc. Am. B*, Vol. **3**, No. 1, 1986

[76] Nagel K., Kuwano H., "FAB-SIMS Study for Analysis of Insulators", *Proceedings SIMS IV*, pp 448-450, 1983

[77] Namiki A., Cho S., Ichige K., "Laser Stimulated Desorption from Compound Semiconductors, Dimerization Enhanced Phase Transition", *Jap. J. Appl. Phys.*, **26**, 1987

[78] Namiki A., Kawai T., Yasuda Y., Nakamura T., "Pulsed-Laser Induced Desorption in GaAs: A Dynamic Pulse Mass Counting Study", *Jap. J. Appl. Phys.*, Vol. **24**, No. 3, 270, 1985

[79] Nogar N. S., Estler R. C., Fearey B. L., Miller C. M., Downey S. W.,"Materials analysis by laser and ion beam sputtering with resonance ionisation mass spectrometry", *Nucl. Instr. Meth. Phys. Res.*, B44, 1990

[80] Oechsner H., "Sputtering - a Review of Some Recent Experimental and Theoretical Aspects", *Appl. Phys.*, **8**, 185, 1975

[81] O'Shea D. C., Callen W. R., Rhodes W. T., "Introduction to Lasers and Their Applications", Addison-Wesley Publishing Company, 1978

[82] Pang H., Yeung E. S., "Laser-Enhanced Ionisation as a Diagnostic Tool in Laser-Generated Plumes", *Anal. Chem.*, **61**, 2546, 1988

[83] Parks J. E., Beekman D. W., Moore H. W., Schmitt H. W., Spaar M. T., Taylor E. H., Hutchinson J. M. R., Fairbanks W. M. (Jr), "Progress in analysis by sputter initiated resonance ionisation spectroscopy", *Proceedings RIS 86*, p157, IOP publishing, 1986

[84] Parks J. E., Beekman D. W., Schmitt H. W., Spaar M. T., "Ultrasensitive Elemental Analysis of Materials Using Sputter Initiated Resonance Ionisation Spectroscopy", presented at the Spring Meeting of the Materials Research Society, April 1985

[85] Parks J. E., Schmitt H. W., Hurst G. S., Fairbanks W. M., Fairbanks W. M., "Sputter initiated RIS (SIRIS) for analysis of semiconductor impurities", *Proceedings RIS 84*, p167, IOP publishing, 1984

[86] Parks J. E., Spaar M. T., Cressman P. J., "Analysis Studies of Semiconductors and Electro-optic Materials Using Sputter Initiated Resonance Ionisation Spectroscopy (SIRIS)", *Proceedings SIMS VI*, 1987

[87] Parks J.E., Spaar M. T., Beekman D. W., Moore L. J., Cressman P. J., "Applications of SIRIS:recent results", *proceedings RIS 88*, IOP publishing 1988

[88] Reuter W., Yu M. L., Frisch M. A., Small M. B., "Charging effects in the SIMS analysis of targets containing low-conductivity regions", *J. Appl. Phys.*, **51** (2), 850, 1980

[89] Rothenberg J. E., Kelly R., "Laser Sputtering Part II", *Nucl. Instr. Meth. Phys. Res.*,**B1**, 291, 1984

[90] Schueler B., Odom W., "Nonresonant multiphoton ionisation of the neutrals ablated in laser microprobe mass spectrometry analysis of GaAs and $Hg_{0.78}Cd_{0.22}Te$",*J. Appl. Phys.* **61** (9), 1 May 1987

[91] Singhal R. P., Land A. P., Ledingham K. W. D., Towrie M., "Population Rate Equations of a Resonant Ionisation Process", *J. Anal. Atomic Spec.*, Vol. 4, 599, October 1989

[92] Singhal R. P., Land A. P., Ledingham K. W. D., Towrie M., "Population Rate Equation Solution of a General Resonant Ionisation Scheme", *Proceedings RIS 88*, p69, 1988

[93] Sigmund P., "Theory of Sputtering. I. Sputtering Yield of Amorphous and Polycrystalline Targets", *Phys. Rev.*, **184**, No. 2, 383, 1969

[94] Sigmund P., "Collision Theory of Displacement Damage, Ion Ranges, and Sputtering", *Rev. Roum. Phys.*, **17**, No. 7, 823, 1972

[95] Sigmund P., "Collision Theory of Displacement Damage, 4. Displacement Cascades", *Rev. Roum. Phys.*, **17**, No. 8, 969, 1972

[96] Sigmund P., "Collision Theory of Displacement Damage, 5. Some Aspects of Sputtering", *Rev. Roum. Phys.*, **17**, No. 9, 1079, 1972

[97] Sigmund P., Gras-Marti A., "Distortion of Depth Profiles During Sputtering", *Nucl. Instr. Meth.*, **168**, 1980

[98] Smith R., Tagg M. A., Walls J. M., "Deterministic models of ion erosion, reflection and redeposition", *Vacuum*, **34**, 175, 1984

[99] Thonnard N., Parks J.E., Willis R. D., Moore L. J., Arlinghaus H. F., "Resonance Ionisation of Neutral Atoms with Applications to Surface Science , Noble Gas Detection and Biomedical Analysis", *Surface and Interface Analysis*, **14**, 1989

[100] Townsend P. D., Kelly J. C., N. Hartley N. E. W., "Ion Implantation Sputtering and their Application", Academic Press, London, 1976

[101] Towrie M., Drysdale S. L. T., Houston C. M., Jennings R., Land A. P., Ledingham K. W. D., McCombes P. T., McLean C. J., Singhal R. P., Smyth M. H. C., Stewart D. T., "The Glasgow resonant ionisation mass spectrometer", *Proceedings RIS 88*, p267, 1988

[102] Towrie M., Drysdale S. L. T., Jennings R., Land A. P., Ledingham K. W. D., McCombes P. T., McLean C. J., Singhal R. P., Smyth M. H. C.,"Trace Analysis using a Commercial Resonant Ionisation Mass Spectrometer", *Int. J. Mass Spectrom. Ion Processes.*, **96**, 1990

[103] Tsang W.T., "Heterostructure Semiconductor Lasers prepared by Molecular Beam Epitaxy", *IEEE J. Quantum Electron.*, Vol. **QE-20**, No. 10, October 1984

[104] Tsong I. S. T., Power G. L., "Edge-Effects Correction in Depth Profiles obtained by Ion-Beam Sputtering", *Nucl. Instr. and Meth.*, **168**, 399, 1980

[105] Tsunoyama K., Suzuki T., Ohashi Y., Kishidaka H., "Sputtering of Metals with 20 keV O_2^+: Characteristic Etch Patterns and Sputtered Atom Yields", *Surf. Int. Anal.*, Vol. **2**., No. 6, 212, 1980

[106] Tsuge H., Esho S., "Angular distribution of sputtered atoms from polycrystalline metal targets", *J. Appl. Phys.*, **52**(7), 4391, 1981

[107] Tumpner J., Wilsch R., Benninghoven A., "Calibration of secondary neutral and secondary ion mass spectrometry: A comparative study", *J. Vac. Sci. Technol.* A, **5** (4), Jul / Aug 1987.

[108] Van Vechten J. A., Tsu R., Saris F. W., "Nonthermal Pulsed Laser Annealing of Si; Plasma Annealing", *Phys. Lett.*, **74A**, 422, 1979

[109] Van Vechten J. A., Tsu R., Saris F. W., Hoonhout D., "Reasons to believe pulsed laser annealing of Si does not involve simple thermal melting", *Phys. Lett.*, **74A**, 417, 1979

[110] Verdun F. R., Krier G., Muller J. F., "Increased Sensitivity in LAMMA by Using Resonant Two-Photon Ionisation Processes', *Anal. Chem.*, **59**, 1383, 1987

[111] Vertes A., Juhasz P., Balazs L., Gijbels R., "Target Heating, Plasma Formation, and Expansion Processes During Laser Ionisation", *Microbeam Analysis*, 273, 1989

[112] Vertes A., De Wolf M., Juhasz P., Gijbels R., "Threshold Conditions of Plasma Ignition in Laser Ionisation Mass Spectrometry os Solids", *Anal. Chem.*, **61**, 1029, 1989

[113] Vertes A., Juhasz P., De Wolf M., Gijebels R., "Hydrodynamic Modelling of Laser Plasma Ionisation Processes", *Int. J. Mass Spectrom. Ion Processes.*, **94**, 1989

[114] Viswanathan R., Hussla I., "Ablation of metal surfaces by pulsed ultraviolet lasers under ultrahigh Vacuum", *J. Opt. Soc. Am. B*, Vol. **3**, No. 5, 1986

[115] Weber K. H., Lawrenz J., Obrebski A., Niemax K., "High Resolution Laser Spectroscopy of Aluminium, Gallium and Thallium" *Physica Scripta.* Vol. **35**, 309-312, 1987.

[116] Werner H. W., "Theoretical and experimental aspects of SIMS", *Vacuum*, Vol. **24**, No. 10, 493, 1974

[117] Werner H. W., Boudewijn P. R., "A comparison of SIMS with other techniques based on ion-beam interactions", proceedings of the 3rd International Conference on Low Energy Ion Beams, *Vacuum*, Vol **34**, 83-101, 1984

[118] Werner H. W., Garten R. P. H., "A comparative study of methods for thin-film and surface analysis", *Rep. Prog. Phys.*, Vol **47**, 221, 1984

[119] Wiley W. C., McLaren I. H., "Time of Flight Mass Spectrometer with Improved Resolution", Rev. Scien. Inst., **26**, No. 12, 1955

[120] Wilson W. D., Haggmark L. G., Biersack J. P., "Calculation of Nuclear stopping, ranges, and straggling in the low-energy region", *Phys. Rev. B*, **15**, 5, 2458, 1977

[121] Winograd N., Baxter J. P., Kimock F. M., "Multiphoton Resonance Ionisation of Sputtered Neutrals: A Novel Approach to Materials Characterisation", *Chem. Phys. Lett.*, **88**, 6, 581, 1982

[122] Wittmack K., "Primary ion charge compensation in SIMS analysis of insulators", *J. Appl. Phys.*, 50 (1). Jan 1979

[123] Woodgate G. K., "Elementary Atomic Structure", Clarendon Press, Oxford, 1983

[124] Young M., "Optics and Lasers", Springer-Verlag, Berlin, Heidelberg, New York, Tokyo, 1986

[125] Young C. E., Pellin M. J., Calaway W. F., Jørgensen B., Schweitzer E. L., Gruen D. M., "Trace surface analysis via RIS/TOF mass spectrometry", *Proceedings RIS 86*, p163, IOP publishing, 1987

[126] Zalm P. C., "Energy dependence of the sputtering yield od silicon bombarded with neon, argon, krypton, and xenon ions", *J. Appl. Phys.*, **54** (5), 2660, 1983

[127] Zalm P. C., "Some useful yield estimates for ion beam sputtering and ion plating at low bombarding energies.", *J. Vac. Sci. Technol.* , **B2**, 1984